
Suitability of atmospheric satellite sensors for ocean color applications

Dissertation
zur Erlangung des wissenschaftlichen Grades
Doktor der Naturwissenschaften
(Dr. rer. nat.)

vorgelegt von

Julia Oelker
geboren am 14.05.1989 in Lüneburg

Institut für Umweltphysik
Fachbereich 1 – Physik und Elektrotechnik
Universität Bremen

Dissertation eingereicht am: 29.06.2021

Tag des Promotionskolloquiums: 03.09.2021

1. Gutachterin: Prof. Dr. Astrid Bracher
2. Gutachter: Prof. Dr. John P. Burrows

Abstract

Global warming is already impacting the modern ocean. To recognize changes and predict the future ocean, ocean color (OC) remote sensing aims at quantifying and monitoring optically active oceanic constituents such as phytoplankton, as well as the underwater light field, on synoptic scales. The underwater light field is typically characterized by the diffuse attenuation coefficient (K_d), which describes how fast the downwelling light diminishes with depth. Phytoplankton diversity is typically assessed by grouping phytoplankton with respect to their function in biogeochemical cycles, which are described as phytoplankton functional types (PFT). Typically, OC sensors record radiometric measurements at several bands, 10-20 nm wide, in the visible and near-infrared. However, direct information of OC variables in the ultraviolet (UV) spectral range is still widely lacking. Also, the coarse spectral resolution of traditional OC sensors hampers the retrieval of information on biodiversity, e.g., represented through PFT, and ecosystems.

While OC sensors have weaknesses in spectral resolution, a suite of atmospheric satellite sensors measures radiation at high spectral resolution (about 0.5 nm) and in spectral ranges (UV) not provided by typical OC sensors. These sensors are designed for the retrieval of atmospheric trace gases using Differential Optical Absorption Spectroscopy (DOAS) and have been utilized for OC retrievals by an adaptation of this method to the ocean domain. PFT, light attenuation and availability, and chlorophyll-a fluorescence have been successfully derived from radiances recorded by the atmospheric sensor SCIAMACHY between 2002 and 2012. So far, only little experience has been gathered with other SCIAMACHY-like sensors, limited to fluorescence retrievals at red wavelengths.

This thesis focuses on retrievals of OC variables in the UV to green spectral range from multiple atmospheric sensors, namely SCIAMACHY, GOME-2, OMI, and TROPOMI. By comparison of OC retrievals from multiple sensors, insight can be gained on retrieval robustness and sources of uncertainty. Merging of data sets from multiple sensors is desirable for creating long time series necessary for observing climate change impacts. Three hypotheses are investigated: (1) OC variables in the blue-green spectral range, such as PFT and the diffuse attenuation coefficient, can be successfully retrieved from multiple SCIAMACHY-like sensors; (2) OC variables from multiple SCIAMACHY-like sensors can

be merged to create long time series; and (3) UV-visible bands of SCIAMACHY-like sensors can be exploited for the retrieval of novel OC products in the UV. The thesis comprises three studies. Two studies concentrate on the diffuse attenuation coefficient with the second study focusing on novel K_d products in the UV. The third study utilizes knowledge from the first two studies to retrieve two key PFT, diatoms and coccolithophores, in the Southern Ocean.

Based on experience gathered with the SCIAMACHY sensor, the retrieval of OC variables was adapted to the other atmospheric sensors and further improved to provide complementary and novel OC information. The mean K_d in the blue spectral range, 390 to around 425 nm, was successfully derived from measurements taken by GOME-2, OMI, TROPOMI (as well as SCIAMACHY). Coccolithophores were successfully retrieved from GOME-2 data in the Southern Ocean, however, diatom retrievals were found to be more challenging and resulting data quality was deemed insufficient. Intersensor biases were found between the derived K_d data sets as well as for the derived PFT data in comparison to the established SCIAMACHY PFT time series prior to this work. Complex instrument-specific corrections would be necessary to remove these biases. Biases were successfully reduced, but unfortunately merging of the multiple data sets is still not possible at this stage. The UV-blue spectral range was exploited for deriving two novel K_d products in the UV, 312.5 to 338.5 nm and 356.5 to 390 nm. Comparison with field measurements and sensitivity analysis of the retrievals showed promising results.

Findings from the third study on Southern Ocean PFT support the Great Calcite Belt hypothesis, which suggests that coccolithophores cause a wide band of enhanced water reflectivity around Antarctica, and indicate that total chlorophyll-a concentration is not an adequate variable for predicting coccolithophore abundance. Spectral-based PFT retrievals, as used in this thesis, are found to be more suitable. Future applications of the data sets derived and characterized in this thesis include: the estimation of the oceanic heat budget and the UV dose rate on marine organisms, the investigation of the sources of colored dissolved organic matter and of phytoplankton photoprotective pigments, as well as residence times of particulate inorganic carbon in the upper ocean.

List of publications

Parts of this thesis, including text passages, tables, and figures, have been previously presented in research articles as well as oral and poster presentations.

Peer-reviewed publications

as first author

Oelker, J., Richter, A., Dinter T., Rozanov, V. R., Burrows, J. P., and Bracher, A. (2019). Global diffuse attenuation derived from vibrational Raman scattering detected in hyperspectral backscattered satellite spectra. *Optics Express*, 27(12):A829-A855. <https://doi.org/10.1364/OE.27.00A829>.

Oelker, J., Richter, A., Losa, S. N., and Bracher, A. TROPOMI-retrieved underwater light attenuation in three spectral regions: ultraviolet to blue. Manuscript in revision for resubmission to *Frontiers in Marine Sciences*.

as a co-author

Losa, S. N., Soppa, M. A., Dinter, T., Wolanin, A., Brewin, R. J. W., Bricaud, A., **Oelker, J.**, Peeken, I., Gentili, B., Rozanov, V., and Bracher, A. (2017). Synergistic Exploitation of Hyper- and Multi-Spectral Precursor Sentinel Measurements to Determine Phytoplankton Functional Types (SynSenPFT). *Frontiers in Marine Science*, 4:203. <https://doi.org/10.3389/fmars.2017.00203>.

Losa, S. N., Dutkiewicz, S., Losch, M., **Oelker, J.**, Soppa, M. A., Trimborn, S., Xi, H., and Bracher, A. (2019). On modeling the Southern Ocean Phytoplankton Functional Types, *Biogeosciences Discuss.* [preprint], <https://doi.org/10.5194/bg-2019-289>.

Selected conference and workshop contributions

Oral Presentations

Oelker, J., Dinter, T., Richter, A., Burrows, J. P., and Bracher, A. Towards improved spatial resolution of hyper-spectral phytoplankton functional type products. Colour and Light in the Ocean from Earth Observation Workshop, 7 September 2016, Frascati: ESA-ESRIN, Italy.

Oelker, J., Dinter T., Rozanov, V. R., Richter, A., Burrows, J. P., and Bracher, A. Global phytoplankton functional type products derived from the Ozone Monitoring Instrument using PhytoDOAS. DPG Frühjahrstagung, 15 March 2017, Bremen, Germany.

Posters

Oelker, J., Dinter, T., Richter, A., Burrows, J. P., and Bracher, A. Phytoplankton functional types derived from different hyper-spectral satellite sensors. Living Planet Symposium, 10-12 May 2016, Prague, Czech Republic.

Oelker, J., Dinter, T., Richter, A., Rozanov, V. R., Burrows, J. P., and Bracher, A. Improved temporal and spatial resolution of hyper-spectral phytoplankton functional type products. International Ocean Color Science Meeting, 16-17 May 2017, Lisbon, Portugal.

Losa, S. N., **Oelker, J.**, Soppa, M. A., Losch, M., Dutkiewicz, S., Dinter, T., Richter, A., Rozanov, V. R., Burrows, J. P., and Bracher, A. Investigating the phytoplankton diversity in the Great Calcite Belt: perspectives from hyper- and multi-spectral satellite retrievals and numerical modeling. Ocean Optics XXIV, 9 October 2018, Dubrovnik, Croatia.

Oelker, J., Richter, A., Dinter T., Rozanov, V. R., Burrows, J. P., and Bracher, A. Towards a long-term data set of diffuse attenuation in the ocean derived from spectral signatures of vibrational Raman scattering in hyperspectral satellite observations. Living Planet Symposium, 16 May 2019, Milan, Italy.

Bracher, A., **Oelker, J.**, Losa, S. N., Soppa, M. A., Richter, A., Rozanov, A., Brotas, V., Brito, A. C., Gomes, M., Costa, M., and Rio, M.-H.. The potential of Sentinel-5P's high spectral resolution for ocean applications. EGU General Assembly, 30 April 2021, online.

Contents

Abstract	iii
List of publications	v
1 Introduction	1
1.1 Motivation	1
1.2 Hypotheses	5
1.3 Main studies	6
1.4 Thesis outline	8
2 Scientific background	9
2.1 Principle of remote sensing	9
2.2 Ocean color remote sensing	10
2.3 Radiometric quantities	10
2.4 Concept of inherent and apparent optical properties	11
2.5 Absorption and scattering	13
2.6 Radiative transfer theory	16
2.7 Radiative transfer model: SCIATRAN	18
2.8 Absorption and scattering processes in the atmosphere	18
2.8.1 Atmospheric absorption	20
2.8.2 Mie and Rayleigh scattering	21
2.8.3 Rotational Raman scattering	21
2.9 Absorption and scattering processes in the ocean	22
2.9.1 Liquid water absorption	22
2.9.2 Phytoplankton absorption	23
2.9.3 NAP absorption	26
2.9.4 CDOM absorption	26
2.9.5 Liquid water scattering	26
2.9.6 Particle scattering	27

2.10 Inelastic processes	28
2.10.1 Phytoplankton fluorescence	28
2.10.2 CDOM fluorescence	29
2.10.3 Vibrational Raman scattering	29
2.10.4 Brillouin scattering	31
2.11 Differential Optical Absorption Spectroscopy	32
2.11.1 Filling-in of Fraunhofer lines	36
2.12 Atmospheric satellite sensors	39
2.13 Ocean color satellite sensors	40
2.13.1 Measurement principle	40
2.13.2 Retrieval principle	41
2.14 Calibration of optical satellite sensors	45

3 Global diffuse attenuation derived from vibrational Raman scattering detected

in hyperspectral backscattered satellite spectra	49
3.1 Introduction	49
3.2 Instrumentation and Methods	52
3.2.1 Satellite Sensors OMI, SCIAMACHY, and GOME-2	52
3.2.2 Vibrational Raman scattering	54
3.2.3 Differential Optical Absorption Spectroscopy	54
3.2.4 Connection between VRS, light availability, and diffuse attenuation	57
3.2.5 Radiative transfer model simulations	58
3.2.6 Retrieval sensitivity	60
3.2.7 OC-CCI as reference data set	62
3.3 Results	63
3.3.1 Global vibrational Raman scattering DOAS fit	63
3.3.2 Agreement between model and satellite data	67
3.3.3 Modification of the VRS fit	68
3.3.4 Derived global diffuse attenuation coefficients	70
3.3.5 Diffuse attenuation coefficient time series	72
3.4 Discussion	74
3.4.1 Correlating cross sections in DOAS	74
3.4.2 Implications of DOAS setting modifications	75
3.4.3 Restricting diffuse attenuation coefficient data sets	76
3.4.4 Spatial and temporal biases in diffuse attenuation coefficients	77
3.5 Conclusion	79

4 TROPOMI-retrieved underwater light attenuation in three spectral regions:	83
ultraviolet to blue	83
4.1 Introduction	83
4.2 Materials and methods	86
4.2.1 Data sets	86
4.2.2 Multispectral satellite data	87
4.2.3 Algorithm	87
4.2.4 Sensitivity analysis	93
4.2.5 K_d product quality evaluation	99
4.3 Results	100
4.4 Discussion	107
4.4.1 VRS retrievability	107
4.4.2 Ultraviolet K_d product quality	108
4.4.3 Blue K_d product quality	109
4.5 Conclusion	111
5 Potential of GOME-2 for monitoring coccolithophores in the Southern Ocean	113
5.1 Introduction	113
5.2 Methods	116
5.2.1 Data sets	116
5.2.2 PhytoDOAS	120
5.2.3 Conversion to PFT Chla	128
5.2.4 Viewing zenith angle correction	130
5.2.5 Offset correction	132
5.2.6 Cloud correction	133
5.3 Results	134
5.3.1 Benefits of cloud correction	134
5.3.2 Satellite product comparisons	136
5.3.3 In-situ comparison	144
5.3.4 Time series	146
5.4 Discussion	150
5.4.1 Diatom identification	150
5.4.2 Coccolithophore identification	151
5.4.3 Coccolithophore quantification	153
5.4.4 Coccolithophore phenology	154
5.4.5 Monitoring coccolithophores in the Southern Ocean	156

5.4.6	Benefits of GOME-2 coccolithophore Chla data	159
5.5	Conclusion	160
6	Concluding remarks	163
6.1	Summary of main conclusions and applications	163
6.2	Hypothesis I	164
6.3	Hypothesis II	167
6.4	Hypothesis III	167
6.5	Outlook	168

1 Introduction

1.1 Motivation

The Earth's climate is changing. Anthropogenic activities, mainly fossil fuel combustion, cement manufacturing, and land use change, have increased greenhouse gas concentrations rapidly since the industrial revolution. The atmospheric carbon dioxide (CO₂) concentration has risen to unprecedented values in the past 800,000 years. As a consequence, the radiative forcing is increasing, causing global warming (IPCC, 2014).

The ocean acts as a buffer in the climate system. It has taken up more than 90% of the excess heat caused by increased greenhouse gas emissions (IPCC, 2013). It additionally acts as a carbon sink. About 25% of the released anthropogenic CO₂ was taken up by the ocean (Friedlingstein et al., 2019). As a consequence, the ocean is warming, sea levels are rising, sea ice concentrations are declining, and ocean acidity is enhancing (IPCC, 2019).

The role of the marine biosphere for planetary future predictions has been recognized, but is still not fully understood and difficult to parameterize in Earth system models (Boman and Doney, 2018). Complex coupling and feedback mechanisms between the marine biosphere and global climate have been identified (Hense et al., 2017) and phytoplankton play a key role (Hays et al., 2005; Sweeney et al., 2005; Jochum et al., 2010).

Phytoplankton are single-celled free-floating algae. They are the basis of the oceanic food web (Fenchel, 1988) and provide life on Earth with a source of oxygen (Harris, 1986). About half of global primary production is due to primary production by phytoplankton (Field et al., 1998). Through photosynthesis, phytoplankton sequester CO₂. The partial pressure of CO₂ is lowered in the upper ocean which increases the uptake of atmospheric CO₂ due to a steeper CO₂ gradient (Falkowski et al., 2000). Some of the fixed carbon is transported to the deeper ocean through gravitational sinking of dead phytoplankton cells or fecal pellets of higher trophic organisms or through particle-injection pump mechanisms (Boyd et al., 2019). This process known as the biological carbon pump removes CO₂ from the Earth system's carbon cycle on long time scales (Passow and Carlson, 2012).

The phytoplankton community structure affects the efficiency of the biological carbon pump (Basu and Mackey, 2018), biogeochemical cycling (Litchman et al., 2015; Jin et al.,

(2006) and air-sea gas exchange (Carpenter et al., 2012), as well as nutrition supply for higher trophic levels (Karl et al., 2001). Phytoplankton can be grouped with respect to their physiological traits or function in the biogeochemical cycles into so-called phytoplankton functional types (PFT) (Reynolds et al., 2002; Le Quéré et al., 2005). Grouping is usually done with respect to size or taxa. For instance, diatoms are mainly micrometer-sized (microphytoplankton) silicifying phytoplankton associated also with large carbon export rates. In contrast, cyanobacteria are small, photosynthetically active, and nitrogen-fixing bacteria, which belong to the picophytoplankton group. Coccolithophores are calcifiers belonging to the intermediate size group, the nanophytoplankton.

Phytoplankton and other dissolved and particulate oceanic substances, both organic and inorganic, influence the underwater light field and determine how much light at different wavelengths is absorbed or backscattered to the atmosphere (Dierssen and Randolph, 2013). Absorbed radiation impacts the overall global heat budget (Sathyendranath et al., 1991; Morel and Antoine, 1994; Frouin and Iacobellis, 2002) and affects physical processes such as mixed layer dynamics (Ohlmann et al., 1996). Radiation can have both harmful as well as beneficial effects on marine organisms. Ultraviolet radiation can inhibit phytoplankton photosynthesis (Cullen and Neale, 1994), but also degrades colored dissolved organic matter (CDOM), which increases light and nutrient availability, but also allows exposure to harmful levels of radiation (Zepp et al., 2003, 2007). Visible radiation is essential for photosynthesis (McCree, 1981). A key variable for characterizing the underwater light field is the diffuse attenuation coefficient for downwelling irradiance: K_d . It describes how fast the light penetrating the ocean diminishes with depth z and is defined as (Gordon et al., 1980):

$$K_d(z, \lambda) = -\frac{d \ln E_d(z, \lambda)}{dz}, \quad (1.1.1)$$

with downwelling irradiance E_d and wavelength λ .

Ocean color (OC) remote sensing retrieves information on oceanic variables such as the total phytoplankton chlorophyll-a concentration (Chla) on regional to global scales, on temporal resolutions of multiple hours to multiple days, and on spatial resolutions from 10 m to a few kilometers (Groom et al., 2019), providing valuable information, amongst others (IOCCG, 2008), for the (climate) modeling community (IOCCG, 2020). Typical OC satellite sensors record backscattered radiances from the ocean-atmosphere system at multiple spectral bands at visible and near-infrared wavelengths. After removal of the atmospheric and surface contributions to the satellite measurements, most OC algorithms derive OC variables from band ratios of water-leaving radiances or reflectances (e.g.,

O'Reilly et al., 1998; O'Reilly and Werdell, 2019). The relationships between band ratios and OC variables are obtained empirically from field measurements. Other algorithms are semi-analytic (e.g., IOCCG, 2006). Relationships between radiance signals and optical properties of the water are obtained from radiative transfer theory.

The Global Climate Observing System (GCOS) recognized total Chla and the water-leaving radiance or reflectance at multiple wavelengths as essential climate variables (GCOS, 2011, 2016). Within a conducted survey, remote sensing scientists and climate modelers indicated other variables as additionally useful including spectral information on absorption and scattering coefficients of seawater and its particulate and dissolved constituents, primary production, and phytoplankton community structure (Sathyendranath, 2011; Sathyendranath et al., 2019). A survey on photosynthetically available radiation (PAR) further revealed user needs for a whole suite of spectral radiation products, including information in the ultraviolet spectral range (Frouin et al., 2018). Some of these desired OC variables are already operationally provided, have been presented as validated data products, or have been explored in feasibility studies. The variables typically provided on an operational basis are (<https://oceancolor.gsfc.nasa.gov/>): total Chla, fluorescence line height, (instantaneous) PAR, remote sensing-reflectance at all spectral bands, total absorption and backscattering at all spectral bands, absorption by colored dissolved organic matter (CDOM) and detritus as well as phytoplankton at a blue waveband, particle backscattering at a blue waveband, diffuse attenuation coefficient at 490 nm, and particulate organic and inorganic carbon. Many approaches for determining phytoplankton community structure from space have been presented (Mouw et al., 2017) and even implemented as downloadable products in online services (e.g., Xi et al., 2020). Many more approaches have been presented for deriving OC information from satellites that did not make it to operational level (yet), but information is still lacking in some areas. Some information is difficult to obtain with OC remote sensing, including information on vertical profiles of OC variables and information from below the first optical depth requiring lidar and polarimetry technologies (Jamet et al., 2019), information on diurnal cycles usually requiring geostationary satellites (Ruddick et al., 2014), etc. The spectral range and spectral resolution of current OC satellite missions limits the retrieval of some OC variables of interest. For instance, the ultraviolet spectral range is typically not included in common OC satellite sensors (Frouin et al., 2018) with the exception of two recent OC sensors which have bands placed at 355 and/or 380/385 nm (SGLI, Okamura et al., 2019; HY-1C UVI, <http://www.nsoas.org.cn/eng/item/204.html>). The first hyperspectral satellite sensors that record spectra continuously with a resolution of about 2 to 5 nm have been explored in the past (e.g., Hyperion, Flores-Anderson et al., 2020; HICO, Corson et al.,

[2008]), are now in space (e.g., DESIS, [Krutz et al., 2019]; PRISMA, [Guarini et al., 2017]), or are planned for launch in the near future (e.g., PACE OCI, [Werdell et al., 2019]; EnMAP, [Guanter et al., 2015]). Higher spectral resolution is thought to enable better detection of phytoplankton functional types and ecosystem mapping ([Giardino et al., 2019]). The Ocean Color Instrument of the PACE mission, planned to be launched at the end of 2023, will also start recording radiances at 340 nm, partially covering the ultraviolet spectral range.

For observing climate trends in OC variables, data sets with observation periods around 40 years ([Henson et al., 2010]) are needed due to decadal and multi-decadal sources of variability ([Schlesinger and Ramankutty, 1994]; [Trenberth and Hurrell, 1994]). Planned satellite mission lifetimes are typically five years. Although some sensors greatly exceed this period (e.g., MODIS-Aqua has been recording data from 2002 to date), merging several satellite sensors is required for creating a time series suitable for monitoring climate change impacts ([IOCCG, 2007]). Merged time series from multispectral OC missions have been created within the Global ocean Colour project (GlobColour, www.globcolour.info), by the Making Earth Science Data Records for Use in Research Environments initiative (MEaSUREs, wiki.icess.ucsb.edu/measures/), and by the Ocean Colour Climate Change Initiative (OC-CCI, www.esa-oceancolour-cci.org/), of which the latter is the most internally consistent and stable with respect to inter-sensor biases so far ([Couto et al., 2016]; [Sathyendranath et al., 2019]).

Several studies have shown that OC variables can also be retrieved from satellite sensors which were designed for the retrieval of atmospheric trace gases ([Bracher et al., 2009]; [Sadeghi et al., 2012a]; [Dinter et al., 2015]; [Wolanin et al., 2015b]). Due to their much higher spectral resolution (about 0.5 nm), different retrieval methods are applied than for multispectral OC data, offering independent OC products. Retrievals are based on Differential Optical Absorption Spectroscopy (DOAS). In a single step, atmospheric and oceanic absorption spectra are fitted to top-of-atmosphere (TOA) backscattered radiances together with a low-order polynomial which accounts for all broadband effects, such as elastic scattering. A higher spectral resolution is beneficial for discriminating PFT based on their subtle differences in absorption spectra (e.g., [Wolanin et al., 2016]). Based on spectrally highly-resolved data of these DOAS-type sensors, cyanobacteria, diatoms, coccolithophores and, to some extent, dinoflagellates have been successfully quantified in terms of Chla ([Bracher et al., 2009]; [Sadeghi et al., 2012a]). The higher spectral resolution of atmospheric sensors also offers the opportunity to exploit optical properties such as vibrational Raman scattering which are not accessible with standard OC sensors ([Vountas et al., 2007]). Besides the difference in spectral resolution, atmospheric and OC sensors

usually cover different spectral ranges, optimized for their respective applications. Many atmospheric sensors do not record radiances between 500 and 600 nm (OMI, [Levelt et al., 2006](#); TROPOMI, [Veefkind et al., 2012](#)), which may limit OC applications, but on the other hand, atmospheric sensors generally record radiances in the ultraviolet wavelength range, which may offer new opportunities for OC applications. Investigations of vibrational Raman scattering in the ocean have already been carried out in this spectral region and show reasonable spatial patterns ([Vountas et al., 2007](#)).

The Scanning Imaging Absorption Spectrometer for Atmospheric Chartography (SCIAMACHY) is a satellite sensor designed for atmospheric applications which recorded data from 2002 until 2012 ([Bovensmann et al., 1999](#)). PFT ([Bracher et al., 2009](#); [Sadeghi et al., 2012a](#)), light availability and diffuse attenuation ([Dinter et al., 2015](#)), as well as marine chlorophyll-a fluorescence ([Wolanin et al., 2015b](#); [Joiner et al., 2016](#)) have been successfully retrieved from the spectrally high-resolved backscattered radiances measured by SCIAMACHY. [Losa et al. \(2017a\)](#) have produced a PFT time series from the 10-year data set. Few examples exist for OC retrievals on data measured by other atmospheric satellite sensors. [Wolanin et al. \(2015b\)](#) and [Joiner et al. \(2016\)](#) also applied their chlorophyll-a fluorescence retrieval to data measured by the Global Ozone Monitoring Experiment 2 (GOME-2). Differences in variability and biases between fluorescence results from SCIAMACHY and GOME-2 were observed, but results are generally similar. Due to the similar sensor design of various atmospheric satellite sensors, other OC variables are also likely retrievable from multiple atmospheric satellite sensors. The 10-year time series covered by SCIAMACHY can potentially be complemented and extended by current and future atmospheric satellite sensors to obtain long-term time series of OC variables which are not necessarily retrievable from traditional OC sensors or are retrieved with independent methods. For atmospheric applications, merging time series from these atmospheric satellite sensors has already been proven successful for different sensor combinations and different atmospheric trace gases (e.g., [Hilboll et al., 2013](#); [Pastel et al., 2014](#); [Coldewey-Egbers et al., 2015](#); [Heue et al., 2016](#)).

1.2 Hypotheses

Based on the knowledge gaps identified above, this thesis investigates three major hypotheses:

- I. Ocean color variables in the blue-green spectral range (such as phytoplankton functional types or the diffuse attenuation coefficient) can be successfully retrieved from multiple SCIAMACHY-like satellite sensors (GOME-2, OMI, TROPOMI).

- II. Ocean color variables from multiple SCIAMACHY-like sensors can be merged to create long time series.
- III. Ultraviolet-visible bands of SCIAMACHY-like sensors can be exploited for the retrieval of novel ultraviolet OC products.

1.3 Main studies

To investigate the above overarching hypotheses, three main studies were conducted. Each of these studies focuses on different objectives which, when combined, contribute to examining the overarching hypotheses. All studies give insight into hypotheses I and II, whereas hypothesis III is mainly addressed in study 2.

Study 1: Global diffuse attenuation derived from vibrational Raman scattering detected in hyperspectral backscattered satellite spectra

This study investigates diffuse attenuation of the underwater downwelling light-field inferred from satellite data from the three sensors, SCIAMACHY, GOME-2, and OMI. The diffuse attenuation coefficient is derived from retrievals of vibrational Raman scattering using Differential Optical Absorption Spectroscopy on satellite-measured backscattered radiances based on the method presented in [Dinter et al. \(2015\)](#). Nearly one year of data is examined within a time period in which satellite missions overlap and data quality is optimal. Resulting diffuse attenuation coefficients are intercompared between sensors with respect to temporal and spatial differences. The operationally-provided diffuse attenuation coefficient from common OC sensors is used as a reference. The study has two objectives: (1) it investigates if vibrational Raman scattering can be found in TOA radiances of OMI and GOME-2 and be adequately retrieved using Differential Optical Absorption Spectroscopy, and (2) if and how a product derived from vibrational Raman scattering (the diffuse attenuation coefficient) can be merged from different sensors.

While study 1 focuses on an established vibrational Raman scattering retrieval which has already been used for deriving light availability and diffuse attenuation in the blue spectral range ([Dinter et al., 2015](#)), study 2 explores retrievals at shorter wavelengths for deriving novel diffuse attenuation products.

Study 2: TROPOMI-retrieved underwater light attenuation in three spectral regions: ultraviolet to blue

The potential of the TROPOMI sensor for OC applications is explored in this study. Based on the established vibrational Raman scattering retrieval in the blue spectral region (Dinter et al., 2015; Losa et al., 2017a; study 1) and on a vibrational Raman scattering retrieval in the ultraviolet spectral region (Vountas et al., 2007; Bracher et al., 2009), vibrational Raman scattering is retrieved in three spectral regions in the ultraviolet and blue spectral ranges for deriving two novel ultraviolet diffuse attenuation coefficients, next to the formerly presented blue diffuse attenuation coefficient. The study is designed as a feasibility study investigating one month of TROPOMI data which coincides with a ship campaign. Field measurements from the ship campaign as well as operational diffuse attenuation products are used for evaluation of derived diffuse attenuation coefficients. Objectives of this study are the exploitation of TROPOMI's ultraviolet-visible wavelength bands for deriving novel diffuse attenuation coefficients in the ultraviolet spectral region as well as their evaluation.

The first two studies focus on vibrational Raman scattering for two main reasons: (1) interesting OC variables, the light availability and diffuse attenuation coefficients, can be derived from vibrational Raman scattering, offering the possibility for new OC products, especially in the ultraviolet spectral region, and (2) adequate retrievals of vibrational Raman scattering are necessary to estimate the underwater light path needed for calculating the chlorophyll-a concentration of PFT retrievals. Knowledge from the first two studies is used in the third study for improving the estimation of PFT-specific chlorophyll-a concentration.

Study 3: Potential of GOME-2 for monitoring coccolithophores in the Southern Ocean

Coccolithophore and diatom chlorophyll-a concentrations are retrieved from backscattered radiances measured by GOME-2 using Differential Optical Absorption Spectroscopy based on (Bracher et al., 2009; Sadeghi et al., 2012a). The study focuses on the Atlantic and Indian sectors of the Southern Ocean. PFT concentrations are retrieved for two austral summers, 12 months in total. Data are compared to field measurements conducted in the same time period and area, as well as several other OC satellite products, including coccolithophore and diatom concentrations from SCIAMACHY (Losa et al., 2017a). Objectives of this study are to assess the performance of PFT retrievals from GOME-2 measurements

and consider its suitability for long-term monitoring of diatoms and coccolithophores in the Southern Ocean.

1.4 Thesis outline

Studies 1 to 3 can be found in chapters [3](#) to [5](#), respectively. Each study comprises an introduction, methods, results, discussion and conclusion section and can, in principle, be read separately from the others. If needed, information required from one of the other studies is shortly summarized and the reader is referred to the corresponding section for more details. A more detailed scientific background for the methods used here is given in chapter [2](#). Chapter [5](#) concludes the thesis. Main conclusions and applications of the three studies are presented. Studies 1 to 3 are then discussed in combination to address the overarching hypotheses I to III.

2 Scientific background

2.1 Principle of remote sensing

Remote sensing comprises Earth observation techniques which infer information on geophysical parameters such as soil moisture, sea surface temperature, atmospheric composition, sea ice concentration, and many more from measurements taken at a distance. In contrast, in-situ measurements span those measurements where the instrument is taken either to the field to directly measure the target medium at a certain location or samples are taken in the field and brought to the lab for analysis. In remote sensing, electromagnetic radiation is measured which interacted with the parameter of interest. The radiometric measurements need to be interpreted by inversion techniques to retrieve information on the target parameter (Liou, 2002). The electromagnetic signal is collected by the detector after it interacted with the target medium, which contains the target observable and also other molecules, particles, and surfaces. The target medium T determines the signal S , which can be expressed in terms of an unknown function F ,

$$S = F(T). \quad (2.1.1)$$

This equation describes the forward model. If the state of T is known as well as F , namely all the physical processes that determine S based on T , S can be calculated. Radiative transfer theory is used to model S given T . It is introduced in section 2.6.

Remote sensing techniques deal with the inverse problem. T has to be determined based on S ,

$$T = F^{-1}(S). \quad (2.1.2)$$

Due to complexity of the Earth system, F is generally complex and inversion not straightforward. In general, the problem is not unique. The target medium usually consists of many parameters. Multiple conditions of the medium can result in the same S . Usually Equation 2.1.2 is solved by finding the parameters that combinedly best describe S . The retrieval method used in this work is introduced in section 2.11.

2.2 Ocean color remote sensing

Ocean color (OC) remote sensing (Mobley, 1994; Mobley et al., 2021) refers to the discipline that infers information on the ocean from optical measurements. Remote sensing techniques can be active or passive. In passive remote sensing, measured light originates from natural sources such as the sun or other stars. Passive OC satellite sensors measure sunlight that entered the ocean and is backscattered through the atmosphere to the detector, which is looking down on the ocean, so-called nadir viewing geometry. The sunlight propagates through the atmosphere where it is partly scattered and absorbed before it reaches the sea surface. At the sea surface, a fraction of the sunlight is reflected back to the sky. Some light penetrates the ocean where it interacts with the ocean constituents. Through backscattering, multiple forwardscattering, and maybe sea bottom reflection, light reaches back to the sea surface. Some of it is transmitted to the atmosphere. A fraction of this light makes it all the way back through the atmosphere and into the satellite sensor. Due to all these processes, the percentage of the signal which contains information on the ocean interior is small. The majority of the signal measured by the satellite sensor, typically more than 90%, has only interacted with the atmosphere or the surface.

Many passive satellite sensors are in sun-synchronous orbits (Burrows et al., 2011). The satellite moves in accordance with the sun such that it always views the sunlit ocean. Such a viewing geometry can be reached in lower Earth orbits, which have an altitude of about 800 km and an inclination angle between orbital plane and equator of $\sim 98^\circ$. Due to the non-sphericity of the Earth, at this inclination and height, the orbit precesses at the same rate as the Earth moves around the sun. The angle between orbital plane and sun-Earth line is kept constant, ensuring that the satellite crosses the equator always at the same local time. Satellites in these orbits circle the Earth about 14 times per day. The swath is the area of the Earth which is observed by the satellite per orbit. Depending on the width of the swath, the satellite can reach daily global coverage meaning that it measures every point on Earth within one day. Measurement principles of optical sun-synchronous satellite sensors are introduced in sections 2.12 and 2.13.

2.3 Radiometric quantities

Light is electromagnetic radiation which propagates as waves of perpendicular electric and magnetic fields described by the Maxwell equations (Maxwell, 1865). For quantifying the amount of light, e.g., reaching a satellite detector, different quantities can be defined (Liou, 2002). The radiance or intensity I is the radiant energy Q per time t and wavelength λ

in a differential solid angle $d\Omega$ oriented at an angle θ normal to the surface element dA , intercepting an effective area $\cos\theta dA$:

$$I(\lambda) = \frac{dQ(\lambda)}{\cos\theta d\Omega d\lambda dt dA} [\text{Jm}^{-2}\text{nm}^{-1}\text{s}^{-1}\text{sr}^{-1}]. \quad (2.3.1)$$

The plane irradiance is the normal component of the radiance integrated over the entire hemispheric solid angle above dA :

$$E(\lambda) = \int_{\Omega} I(\lambda) \cos\theta d\Omega. \quad (2.3.2)$$

For isotropic radiation, the irradiance is $\pi I(\lambda)$. The total flux density of radiant energy is obtained by integrating the irradiance over all wavelengths:

$$E = \int_0^{\infty} E(\lambda) d\lambda. \quad (2.3.3)$$

The total flux or radiant power W incident onto a surface is:

$$W = \int_A E dA. \quad (2.3.4)$$

For optical oceanography, it is useful to define the upwelling plane irradiance, E_u , and downwelling irradiance, E_d , as the irradiances measured by an instrument pointing downward or upward, respectively, which captures light from the respective hemisphere (Mobley, 1994; Mobley et al., 2021):

$$E_d(\lambda) = \int_{\phi=0}^{2\pi} \int_{\theta=0}^{\pi/2} I(\lambda) |\cos\theta| \sin\theta d\theta d\phi, \quad (2.3.5)$$

$$E_u(\lambda) = \int_{\phi=0}^{2\pi} \int_{\theta=\pi/2}^{\pi} I(\lambda) |\cos\theta| \sin\theta d\theta d\phi, \quad (2.3.6)$$

with azimuthal angle θ and polar angle ϕ .

2.4 Concept of inherent and apparent optical properties

The concept of inherent and apparent optical properties is widely used in the field of optical oceanography (Mobley, 1994; Mobley et al., 2021). Inherent optical properties (IOPs) only depend on the properties of the medium, i.e., composition, size and shape of particles, and concentration of the medium's constituents. Apparent optical properties (AOPs), on the

other hand, additionally depend on viewing geometry and surface properties.

The most prominent IOPs are the absorption and the scattering coefficients of a medium. When a monochromatic and collimated light beam, with spectral radiant power $W(\lambda)$, passes through a small volume of a medium, some of the incident radiant power will be scattered out of the direction of the light beam, some will be absorbed and some will exit the volume unchanged. The absorptance is defined as the ratio of the absorbed radiant power within the volume $W_a(\lambda)$ to the incident radiant power $W_i(\lambda)$,

$$A(\lambda) = \frac{W_a(\lambda)}{W_i(\lambda)}. \quad (2.4.1)$$

Similarly, the scatterance can be defined as the ratio of scattered radiant power by the volume $W_b(\lambda)$ to the incident radiant power,

$$B(\lambda) = \frac{W_b(\lambda)}{W_i(\lambda)}. \quad (2.4.2)$$

The transmittance is the ratio of the radiant power that exits the volume unchanged in direction and wavelength, $W_t(\lambda)$, to the incident radiant power

$$T(\lambda) = \frac{W_t(\lambda)}{W_i(\lambda)}. \quad (2.4.3)$$

Due to conservation of energy, $A(\lambda) + B(\lambda) + T(\lambda) = 1$. The absorption coefficient $a(\lambda)$ of the medium is the change in absorptance with distance ds propagated through the medium:

$$a(\lambda) = \frac{dA}{ds} [\text{m}^{-1}], \quad (2.4.4)$$

which can also be expressed as the product of absorption cross section σ_a (in units of area) and the number density n (in units per volume), $a(\lambda) = \sigma_a(\lambda)n$. Analogously, the scattering coefficient is given by

$$b(\lambda) = \frac{dB}{ds} = \sigma_b(\lambda)n [\text{m}^{-1}], \quad (2.4.5)$$

where σ_b is the scattering cross section. The sum of these two coefficients is the beam attenuation coefficient $c(\lambda) = a(\lambda) + b(\lambda)$. In optical oceanography, the term attenuation is commonly used for the sum of absorption and scattering, whereas the atmospheric community usually refers to it as extinction. Absorption and scattering are introduced in more detail in the next section, [2.5](#), introducing also other IOPs such as the scattering

phase function.

AOPs are those optical properties that can be determined via remote sensing, whereas the IOPs are usually indirectly derived from these. IOPs give insight on the medium's constituents in a straightforward manner, however, they can only be measured in-situ with technically demanding instrumentation. AOPs on the other hand are derived from rather easily measurable radiometric quantities such as the radiance. To be acknowledged as an AOP, a radiometric quantity is required to depend strongly on IOPs and only weakly on the viewing geometry and other environmental parameters such as cloudiness and wind speed such that valuable information on the medium can be gained. Ratios and gradients of irradiances and radiances generally fulfill these criteria. AOPs can be reflectances such as the irradiance reflectance $R(z, \lambda) = E_u(z, \lambda)/E_d(z, \lambda)$ at depth z as well as mean cosines such as $\bar{\mu} = (E_d(z, \lambda) - E_u(z, \lambda))/E_o(z, \lambda)$, where $E_o(z, \lambda)$ is the scalar spectral irradiance. Logarithmic depth derivatives of irradiances or radiances, also known as diffuse attenuation coefficients or K functions, are also AOPs. The diffuse attenuation coefficient of downwelling irradiance is (Gordon et al., 1980)

$$K_d(z, \lambda) = -\frac{d \ln[E_d(z, \lambda)]}{dz} = -\frac{1}{E_d(z, \lambda)} \frac{dE_d(z, \lambda)}{dz}. \quad (2.4.6)$$

The K functions depend on the angular distribution of the light field and therefore change with depth near the surface even for homogeneous media. Far from boundaries, the K functions only depend on the IOPs. In contrast, the beam attenuation coefficient is the same for all depths. K_d is generally smaller than the beam attenuation coefficient, because the downwelling irradiance can gain photons from neighboring beams through single-scattering events, whereas in case of the beam attenuation coefficient, a multi-scattering event of photons from neighboring beams that go exactly into the incident beam direction is rather unlikely.

2.5 Absorption and scattering

When light interacts with particles, it can either be absorbed or scattered. Absorption (Mobley, 1994; Burrows et al., 2011; Mobley et al., 2021) describes the process in which the energy of a photon is passed to an atom or molecule leaving it in an excited state. An atom consists of a nucleus with surrounding electrons, which occupy discrete energetic states. The energy of a photon $E_{ph} = h\nu$ is determined by its frequency ν and the Planck constant h . To be absorbed, the photon's energy has to correspond to the difference in energy $E_i - E_j$ between two atomic energy levels i and j . These electronic transitions are

therefore associated with sharp absorption lines for specific wavelengths. Typical energies are in the ultraviolet and visible wavelength range. A molecule consists of several atoms which can move as a unit or with respect to each other. Vibration and rotation of a molecule are associated with energies one to four orders of magnitude less than electronic transitions. For each electronic energy level, a fine structure of energy levels, corresponding to different vibrational and rotational modes, appears. The ground state corresponds to a certain occupation of electronic states and vibrational and rotational modes which are described by a set of quantum numbers. In the process of absorption, a molecule is excited from its ground state to a higher energetic state corresponding to a different set of quantum numbers. Selection rules depending on spin and angular momentum of photon and electrons within the molecule determine allowed transitions. The manifold energy levels in a molecule due to vibration and rotation explain that a large molecule like chlorophyll-a has broad absorption peaks.

Elastic scattering (Mobley, 1994; Mobley et al., 2021) occurs when light encounters a change in index of refraction from one location to another. The index of refraction is defined as the ratio of the speed of light in vacuum to the speed of light in a medium and can be changed locally, e.g., by a particle along the light path or by density fluctuations of a medium. Elastic scattering does not change the energy of the incoming light, only its direction. The volume scattering function (VSF) describes the angular distribution of unpolarized light scattered from its initial direction \vec{x}' into direction \vec{x} at wavelength λ . Most media in the aquatic environment are isotropic, i.e., scattering only depends on the angle ξ between \vec{x}' and \vec{x} . The VSF can be defined as

$$\beta(\xi, \lambda) = \frac{1}{E(0, \lambda)} \frac{dI(\xi, \lambda)}{dV} [\text{m}^{-1}\text{sr}^{-1}] \quad (2.5.1)$$

with the incoming irradiance $E(0, \lambda)$, the radiant intensity $dI(\xi, \lambda)$ scattered to angle ξ , and infinitesimal volume element dV . The scattering coefficient is the integral of the VSF over all angles

$$b(\lambda) = 2\pi \int_0^\pi \beta(\xi, \lambda) \sin \xi d\xi. \quad (2.5.2)$$

The phase function is the VSF normalized to the scattering coefficient:

$$\tilde{\beta}(\lambda, \xi) = \frac{\beta(\lambda, \xi)}{b(\lambda)}. \quad (2.5.3)$$

Since light reaching a satellite sensor is either backscattered or multiply forward scattered,

backscattering is an important process. The backscattering coefficient b_b is calculated from the VSF only considering angles larger 90° :

$$b_b(\lambda) = 2\pi \int_{\pi/2}^{\pi} \beta(\xi, \lambda) \sin \xi d\xi. \quad (2.5.4)$$

The backscattering ratio is the amount of backscattering relative to the amount of total scattering: $\tilde{b} = b_b/b$.

Scattering on particles can be theoretically described by Mie theory. Mie theory covers the situation of a plane electromagnetic wave interacting with a spherical particle with complex refractive index, i.e., the particle scatters and absorbs, embedded in a non-absorbing medium. The problem can be parameterized with a size parameter x ,

$$x = \frac{2\pi r n_m}{\lambda}, \quad (2.5.5)$$

where λ is the wavelength in vacuum, r the particle's radius, and n_m the real refractive index of the medium. The second parameter needed is the complex refractive index of the particle relative to the refractive index of the medium,

$$m = \frac{n_s}{n_m} + \frac{ik_s}{n_m}, \quad (2.5.6)$$

where n_s and k_s are the real and imaginary part of the particle's refractive index, respectively.

The size parameter is a measure for the particle's size in comparison to the incident light's wavelength and determines the scattering regime. If the size of the particle is much smaller than the wavelength, $x \ll 1$, the Rayleigh approximation can be used. If the size of the particle is much larger than the wavelength, $x \gg 1$, geometric optics can be used. In all other cases, when particle size and wavelength are similar, full Mie theory has to be considered. However, Mie theory is for spherical particles and therefore an approximation for real particles in the atmosphere and in the ocean, which are often non-spherical. Non-sphericity has a large effect on the backscattering, which can easily differ by a factor of three due to particle shape (Curtis et al., 2008).

In inelastic processes, the excitation state of the molecule is changed upon interaction, consequently also changing the energy of the incident light. An inelastic process is therefore always associated with a shift in wavelength. An important inelastic process in the atmosphere and ocean is Raman scattering. Light is scattered inelastically to longer or shorter wavelengths which is caused by an instantaneous change of the molecule's vibra-

tional or rotational state or both. Scattered light to longer wavelengths is referred to as Stokes line whereas the Anti-Stokes line appears due to scattering to shorter wavelengths. Another important inelastic process is fluorescence that occurs when light is absorbed by a molecule and re-emitted at longer wavelengths. Raman scattering and fluorescence occur on different time scales. Raman scattering is an instantaneous process on time scales of 10^{-13} - 10^{-12} s compared to fluorescence being a process of absorption and later reemission on the order of 10^{-9} s. In the framework of radiative transfer, both processes can be described by an absorption process at λ' and a reemission at λ . The inelastic scattering coefficient,

$$b^i(\lambda' \rightarrow \lambda) = b^i(\lambda')f^i(\lambda' \rightarrow \lambda), \quad (2.5.7)$$

is a product of the total inelastic scattering coefficient $b^i(\lambda')$ and a wavelength distribution function $f^i(\lambda' \rightarrow \lambda)$, which contains information on the wavelength shift. Emission due to fluorescence is generally isotropic, whereas Raman scattering has an angular dependence.

2.6 Radiative transfer theory

Radiative transfer theory is the mathematical framework for describing the propagation of radiation through a medium. Radiance measured by a satellite sensor is from sunlight which propagates, at least partly, through the atmosphere and ocean and back into the sensor. Several processes occur on the way which cause an increase or decrease in radiation along the light path (Mobley, 1994; Mobley et al., 2021). Considering a monochromatic light beam traveling a distance ds , radiative energy can be lost by absorption and turned into chemical energy or heat. Photons can be elastically scattered out of the beam. Energy can also be lost by inelastic processes, i.e., photons are absorbed by molecules and re-emitted at longer wavelengths in the process of fluorescence or phosphorescence and photons can be scattered to wavelengths differing from the incident light's wavelength. The inelastically scattered photons may be additionally out of the direction of the light beam. Energy can be gained by elastic scattering from other directions into the light beams direction or by inelastic processes, scattering or emitting light at the beam's wavelength and direction. In emission processes such as bioluminescence, chemical energy is converted to radiative energy, which can also cause a gain in energy of the light beam.

Mathematically, the loss and gain processes of light propagating through a medium can be expressed as follows (Liou, 2002). The reduction in intensity of the light beam is determined by the absorption and scattering coefficient whose sum is the beam attenuation

coefficient c :

$$dI(\lambda) = -c(\lambda)I(\lambda)ds = -\sigma_c(\lambda)nI(\lambda)ds, \quad (2.6.1)$$

where $\sigma_c = \sigma_a + \sigma_b$ is the attenuation cross section in units of area and n is the number density of the medium. Similarly, the source term can be defined as:

$$dI(\lambda) = j(\lambda)ds = \sigma_j(\lambda)nds, \quad (2.6.2)$$

with the source function coefficient $j(\lambda)$ or cross section σ_j having the same physical meaning as the attenuation coefficient or cross section, respectively. Source terms accounting for different physical processes can be formulated. For example, the source term for contributions from elastic scattering is

$$dI = \int_0^{2\pi} \int_0^\pi I(s, \theta', \phi', \lambda) \beta(s, (\theta', \phi') \rightarrow (\theta, \phi), \lambda) \sin \theta' d\theta' d\phi' ds, \quad (2.6.3)$$

for scattering from direction (θ', ϕ') to (θ, ϕ) . The basic monochromatic, one-dimensional, time-independent radiative transfer equation (RTE) is given by the sum of the loss and gain terms:

$$dI(\lambda) = -\sigma_c(\lambda)nI(\lambda)ds + \sigma_j(\lambda)nds. \quad (2.6.4)$$

By solving the RTE, the radiation field can be determined at any point in the medium.

Polarization is an inherent property of light which describes the orientation of the electric field vector of an electromagnetic wave with respect to its direction of propagation. To account for polarization of light, the RTE needs to be in a vectorial form. For most oceanic applications, this is not required because of the following reasons (Mobley et al., 2021):

- Oceanic particles are usually much larger than λ . The induced polarization by particles upon scattering is largest for particles much smaller than λ .
- Multiple scattering is usually present under water which decreases the degree of polarization introduced by single scattering events.
- Often, irradiances are considered in optical oceanography. Integration over direction tends to cancel out different polarization in different directions.

The RTE has to be solved for boundary conditions. The upper boundary is usually given by the incident solar irradiation at the top of atmosphere and the lower boundary by

the sea bottom. Even the basic RTE in Equation 2.6.4 has no analytic solution except for simplified cases, e.g., no scattering. Accurate solutions of the RTE for realistic atmospheric and oceanic conditions therefore require numerical solutions. In this work, the radiative transfer model (RTM) SCIATRAN is used for solving the RTE.

2.7 Radiative transfer model: SCIATRAN

The radiative transfer model SCIATRAN (Rozanov et al., 2014, 2017) is used for solving the radiative transfer equation based on the discrete ordinates technique. The method of discrete ordinates was developed by Subrahmanyam Chandrasekhar (Chandrasekhar, 1960) and discretizes the xyz-domain as well as the angular variables to approximately solve the RTE numerically. Different modes can be used depending on the required results. In this work, either intensities are calculated at the TOA as seen for a specific satellite sensor or in-water fluxes are calculated at discrete depths. The model solves the RTE for a coupled ocean-atmosphere system by an iterative approach until convergence is reached for the radiation penetrating into the ocean and for the water-leaving radiation. Scattering and absorption properties of the atmosphere and oceanic constituents as well as the sea surface roughness need to be defined. Relevant physical processes in the ocean-atmosphere systems are introduced in the next sections. Chosen parameterizations and settings are described in each study (chapters 3-5), specific for each application.

2.8 Absorption and scattering processes in the atmosphere

The atmosphere (Liou, 2002) can be divided into four distinctly different layers based on the temperature change with altitude: the troposphere, stratosphere, mesosphere, and thermosphere. Relevant absorption and scattering processes occur in the troposphere and stratosphere. The troposphere is closest to the Earth's surface and reaches up to about 12 km. The temperature decreases with altitude. All water vapor, clouds and precipitation are confined in this layer. The stratosphere is adjacent to the troposphere and reaches to an altitude of roughly 50 km. The temperature increases with altitude in this layer.

The chemical composition of the atmosphere is made up of several gases with permanent or varying concentrations. Nitrogen, oxygen and argon are the biggest contributors to the permanent gases and make up 99.6% of the atmosphere by volume. Other well-known permanent gases are carbon dioxide and methane, although their concentrations have risen

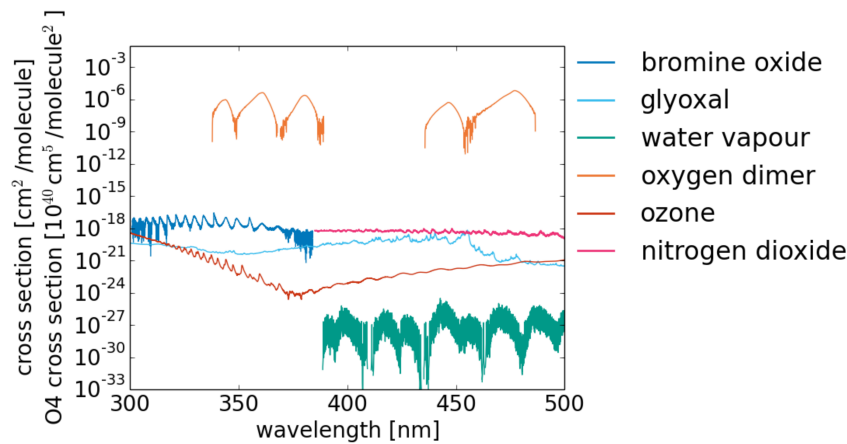


Figure 2.8.1: Absorption cross section of atmospheric absorbers used within ocean color retrievals in this work: ozone (Serdyuchenko et al., 2014), nitrogen dioxide (Vandaele et al., 1998), glyoxal (Volkamer et al., 2005), bromine monoxide (Fleischmann et al., 2004), water vapor (Rothman et al., 2013, using HITRAN 2009), and the oxygen dimer (Thalman and Volkamer, 2013).

in the past decades due to human activities. Concentrations of permanent gases have stable volume ratios up to 60 km. Important variable constituents with respect to contribution by volume are water vapor, ozone, sulfur dioxide, nitrogen dioxide, and ammonia. Most of the ozone is found in the ozone layer at 15 to 30 km altitude with a maximum at 20 to 25 km, however, ozone is also present in the troposphere due to anthropogenic activities. Nitrogen oxides NO_x (NO , NO_2) are also found in both layers. The main source of NO_x in the troposphere originates from transportation and combustion processes at the surface. Aircrafts cause an increase in NO_x at the upper troposphere and lower stratosphere. The main source for NO_x in the stratosphere is the dissociation of nitrous oxide (N_2O).

The atmosphere also contains larger particles, aerosols, with sizes on the order of 10^{-3} to $20 \mu\text{m}$. Aerosols are produced in natural processes such as volcanic eruptions, sand storms, forest fires, wave motion, but also in anthropogenic activities, mainly combustion. Clouds cover more than 50% of the sky on the global scale.

Absorption and scattering of the atmospheric constituents is briefly discussed in the following for the UV and visible spectral regions with a focus on 300 to 600 nm. Absorption cross sections of atmospheric absorbers above the sunlit ocean, relevant for OC applications, are shown in Figure 2.8.1.

2.8.1 Atmospheric absorption

Ozone absorbs most strongly in the Hartley bands from 200 to 300 nm. Medium absorption is found for the Huggins bands between 300 and 360 nm and weak absorption in the Chappuis bands in the visible spectral range (e.g., [Gorshelev et al., 2014](#); [Serdyuchenko et al., 2014](#)).

Nitrogen dioxide absorbs in the UV and visible wavelength range between 200 and 700 nm ([Vandaele et al., 1998](#); [Solomon et al., 1999](#)).

Molecular oxygen has absorption bands in the visible and infrared. The most important bands at visible wavelengths are the A band (762 nm), the B band (688 nm), the γ band (628 nm), and the δ band (580 nm) ([Newnham and Ballard, 1998](#)).

The oxygen dimer, referred to as O_4 , is induced by collision of two oxygen molecules. O_4 absorbs in broad spectral bands in the UV and visible spectral regions (e.g., [Wagner et al., 2002](#)). The intensity of the O_4 bands varies with the square of the oxygen pressure.

Water vapor H_2O (e.g., [Eldridge, 1967](#)) has three fundamental vibrational modes in the infrared. Some H_2O lines are also present in the visible as overtones and combinations of the vibration modes.

Bromine monoxide (BrO) absorbs in the UV wavelengths. Enhanced concentrations of BrO can be found, amongst others, in the marine boundary layer ([Leser et al., 2003](#); [Sander et al., 2003](#); [Saiz-Lopez et al., 2004](#)), especially in polar sea ice regions (e.g., [Simpson et al., 2007](#)).

Iodine monoxide (IO) absorbs in the blue spectral range and exhibits sharp absorption features. Similar to BrO, it is present in the marine boundary layer (e.g., [Peters et al., 2005](#)). Concentrations are generally low, however, have been detected with remote sensing techniques ([Schönhardt et al., 2008](#)).

Glyoxal (CHOCHO) and formaldehyde (HCHO) originate from oxidation of the majority of volatile-organic compounds. Sources are vegetation, fossil fuel consumption, biomass burning, and to a lesser extent, the ocean ([Guenther et al., 1995](#); [Andreae and Merlet, 2001](#); [Vrekoussis et al., 2010](#)). Direct production is also possible, mainly from anthropogenic emissions for formaldehyde and from fires in the case of glyoxal ([Stavrakou et al., 2009](#); [Zhang et al., 2016](#)). They are short-lived species, although evidence of transport has been found recently ([Behrens et al., 2019](#); [Alvarado et al., 2020](#)). Glyoxal absorbs at visible wavelengths. The concentration of glyoxal over open ocean areas should be negligible and was therefore also not further considered in chapters [4](#) and [5](#). Formaldehyde absorbs in the UV. The main source for global background concentrations is the oxidation of methane. Concentrations over ocean regions are generally low ([Wittrock et al., 2006](#)).

Furthermore, species such as sulfur dioxide (SO_2), chlorine dioxide ($OCIO$), chlorine

monoxide (ClO), and nitrate (NO₃) absorb in the UV wavelength range. However, these are only relevant in certain situations or areas. SO₂ is usually associated with volcanic eruptions or anthropogenic activities such as coal burning. Satellite observations of SO₂ show that concentrations over open ocean areas are usually low (e.g., [Theys et al., 2015](#)). OClO and ClO are only significantly present in the dark polar vortex ([Wagner et al., 2001](#)) and NO₃ is rapidly photolyzed by sunlight ([Orlando et al., 1993](#)).

2.8.2 Mie and Rayleigh scattering

Atmospheric molecules are much smaller than UV-VIS wavelengths. Their scattering falls in the Rayleigh regime, $x \ll 1$. Rayleigh scattering ([Rayleigh, 1899](#)) can be derived from Mie theory or derived in the picture of interaction between light and an air molecule ([Liou, 2002](#)). An applied electric field induces an oscillating dipole in the molecule which produces plane-polarized radiation, the scattered electromagnetic wave. The total scattered intensity of unpolarized light incident on a molecule in the direction of ξ is given by:

$$I = \frac{I_0}{s^2} \alpha^2 \left(\frac{2\pi}{\lambda} \right)^4 \frac{1 + \cos^2 \xi}{2}, \quad (2.8.1)$$

with polarizability α . The scattered intensity is proportional to the incident intensity I_0 and inversely proportional to the square of the distance s between the molecule and the observer. The strong wavelength dependence, $\sim \lambda^{-4}$, is related to the blue color of the sky. The phase function of Rayleigh scattering is

$$\tilde{\beta} = \frac{3}{4}(1 + \cos^2 \xi). \quad (2.8.2)$$

Forward scattering and backscattering are of equal magnitude, $\tilde{b} = 0.5$.

Scattering on aerosols and cloud particles is described by full Mie theory since $x \approx 1$. It is similar to scattering on oceanic particles described in detail in section [2.9.6](#). The scattering is predominantly in forward direction. The wavelength dependence is rather weak and depends on particle size. Clouds and non-absorbing particles therefore appear white.

2.8.3 Rotational Raman scattering

Raman scattering in the atmosphere ([Burrows et al., 2011](#)) is predominantly associated with a change in rotational state of air molecules. Rotational Raman Scattering (RRS) on N₂ and O₂ leads to a Raman shift up to $\pm 200 \text{ cm}^{-1}$. Additionally, the vibrational mode

can be changed. For changes in vibrational state, the Raman shift is $2,331\text{ cm}^{-1}$ for N_2 and $1,555\text{ cm}^{-1}$ for O_2 . Rotational-vibrational Raman scattering (RVRS) coefficients are one order of magnitude weaker than RRS coefficients and RRS is one order of magnitude weaker than Rayleigh scattering.

2.9 Absorption and scattering processes in the ocean

Particulate and dissolved organic and inorganic substances as well as liquid water itself define the optical properties of oceanic water. Absorption and scattering properties of oceanic constituents are introduced in the next sections following (Mobley, 1994; Mobley et al., 2021).

2.9.1 Liquid water absorption

Liquid water absorption is at its minimum in the blue and increases towards shorter and longer wavelengths. The absorption spectrum is broad band with absorption plateaus visible in the red and longer wavelengths. Vibrational modes of the water molecule originate from bending and stretching of O-H bonds. In the liquid state, water molecules are not free to rotate due to hydrogen bonding between molecules. Rotational modes are therefore reduced to so-called libration modes. The absorption features seen in the red are caused by harmonics of these vibration and libration modes. The water absorption coefficient is challenging to measure in the laboratory (e.g., Buiteveld et al., 1994), especially in the UV (e.g., Fry, 2000). Several literature values have been reported (e.g., Quickenden and Irvin, 1980; Smith and Baker, 1981; Pope and Fry, 1997; Cruz et al., 2009; Kröckel and Schmidt, 2014; Mason et al., 2016). Figure 2.9.1 shows two water absorption coefficients (Pope and Fry, 1997; Mason et al., 2016), which are commonly used. The coefficients agree in the green to red wavelength range, however, larger discrepancies are found in the UV and blue spectral regions.

Temperature and dissolved ions change the structure of the water molecule cluster, leading to a temperature and, to a lesser degree, salinity dependence of the harmonics. Temperature and salinity dependencies have been determined in laboratory measurements (Kou et al., 1993; Buiteveld et al., 1994; Langford et al., 2001; Sullivan et al., 2006; Larouche et al., 2008; Röttgers et al., 2014). Röttgers et al. (2014) find that below 500 nm, temperature effects are negligible for visible wavelengths. Small effects are seen up to 575 nm. Larger effects appear at longer wavelengths which should be taken into account for accurate optical simulations and measurements. At visible wavelengths, the salinity effects are

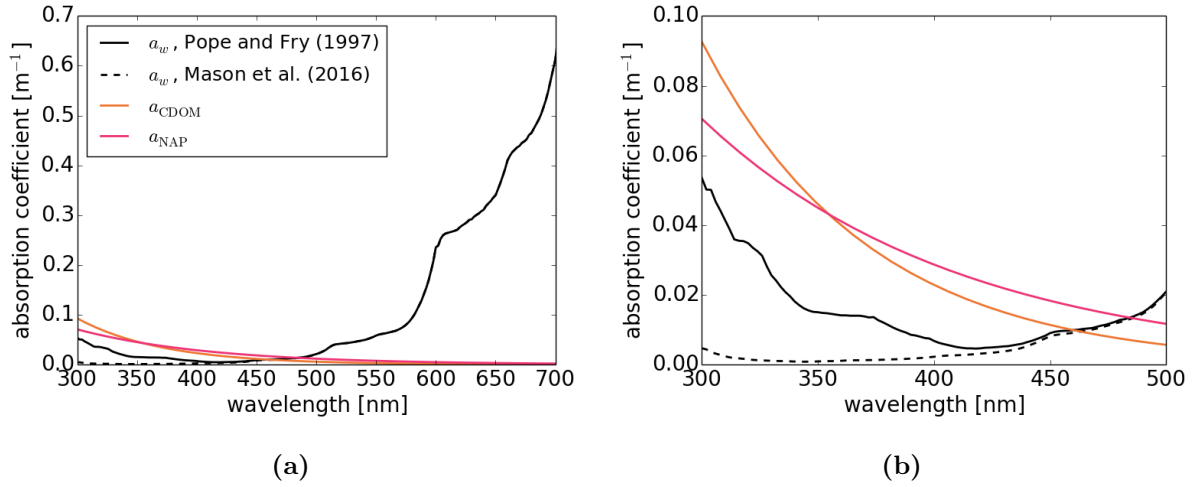


Figure 2.9.1: Absorption coefficients for colored dissolved organic matter (a_{CDOM}), non-algal particles (a_{NAP}), and liquid water (a_w) in the wavelength range (a) 300 to 700 nm and (b) 300 to 500 nm. Two absorption spectra are shown for liquid water absorption measured by Pope and Fry (1997) and Mason et al. (2016). The CDOM absorption coefficient was calculated based on the parameterization of Morel and Maritorena (2001) for a chlorophyll-a concentration of 1 mg/m^2 , corresponding to $S_{\text{CDOM}} = 0.014 \text{ nm}^{-1}$ and $a_{\text{CDOM}}(440) = 0.013 \text{ m}^{-1}$. a_{NAP} was calculated for a medium slope of $S_{\text{NAP}} = 0.009 \text{ nm}^{-1}$ and $a_{\text{NAP}}(440) = 0.02 \text{ m}^{-1}$.

only relevant for wavelengths larger 600 nm.

2.9.2 Phytoplankton absorption

Phytoplankton contain different types of pigments (Mobley et al., 2021; Blankenship, 2002) that are used for photosynthesis and photoprotection. Chlorophyll-a is the main pigment for photosynthesis contained in all phytoplankton. Other chlorophylls, carotenoids, and phycobilipigments are other main pigments typically found in phytoplankton. Chlorophylls have a tetrapyrrole ring and a carbon chain tail, except chlorophyll-c which only has the ring structure. These molecules have two absorption bands, one in the blue and one in the red wavelengths. Carotenoids are long double-bonded carbon chains, often with a ring structure at each end. Their absorption spectra show a broad absorption band in the blue-green wavelengths. Phycobilipigments are chains of pyrrole rings that absorb in the spectral region from 550 to 650 nm. Figure 2.9.2 (a) shows absorption spectra of different pigments. Each phytoplankton species has a specific pigment composition and the overall absorption coefficient is generally the sum of the pigment absorption coefficients weighted according to the phytoplankton's pigment composition. Phytoplankton absorption coefficients, $a_\phi(\lambda)$,

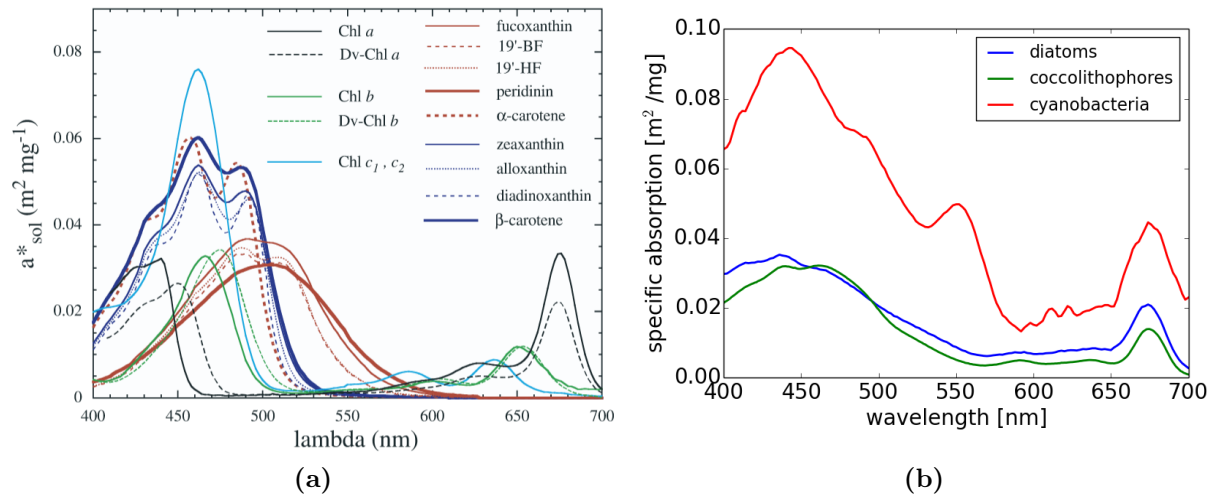


Figure 2.9.2: (a) Estimated in-vivo weight-specific absorption coefficients of different pigments. Pigment absorption spectra were measured in solvent by High Performance Liquid Chromatography in relative values and scaled to weight-specific absorption coefficients following [Goericke and Repeta \(1993\)](#) and then shifted to in vivo positions of absorption maxima as in [Bidigare et al. \(1990\)](#) (Figure was taken from [Bricaud et al. \(2004\)](#)). Dv : divinyl, 19'-HF: 19'-hexanoyloxyfucoxanthin, 19'-BF: 19'-butanoyloxyfucoxanthin. (b) Specific absorption coefficients of three phytoplankton functional types: cyanobacteria, diatoms, coccolithophores as in [Bracher et al. \(2009\)](#); [Sadeghi et al. \(2012a\)](#).

are usually measured on bulk samples giving the absorption coefficient of a culture or natural water sample. Normalization to the chlorophyll-a concentration yields the specific absorption coefficient $a_{\phi}^*(\lambda)$.

The pigment composition varies naturally within one species and therefore variations in phytoplankton absorption spectra are found within one species. The formation of pigments other than chlorophyll-a and the overall pigment concentrations are influenced by light and nutrient conditions in the growth phase (Johnsen et al., 1994; Henriksen et al., 2002; Staehr and Henriksen, 2002). At the level of phytoplankton functional types, where multiple species are clustered, large variations in phytoplankton absorption, but also large similarities are found. Most pigments are found in several phytoplankton functional types. However, the same groups of pigments can be found in phytoplankton with similar evolutionary lineages (Falkowski et al., 2004). Different phytoplankton functional types therefore have absorption spectra with similar broad absorption bands, but distinctly different small absorption peaks as shown in Figure 2.9.2 (b). Variability in phytoplankton absorption is not only due to pigment concentration and composition, but also due to pigment packaging. The light absorbing material in a phytoplankton cell is packaged which reduces the absorption coefficient in relation to the absorption coefficient of the same light absorbing material in an unpackaged state. A package effect index (Bricaud et al., 2004), $Q_a^*(\lambda)$, can be defined as the ratio of phytoplankton absorption coefficient, $a_{\phi}(\lambda)$, to the absorption coefficient of the corresponding phytoplankton cells' content dispersed into a solvent, $a_{\text{sol}}(\lambda)$:

$$Q_a^*(\lambda) = a_{\phi}(\lambda)/a_{\text{sol}}(\lambda). \quad (2.9.1)$$

$a_{\text{sol}}(\lambda)$ can be calculated as the sum of weight-specific absorption spectra of individual pigments, $a_{\text{sol},i}^*(\lambda)$, and their concentrations C_i in the solvent, $a_{\text{sol}}(\lambda) = \sum a_{\text{sol},i}^*(\lambda)C_i$. The package effect index lies between 0 and 1, with 1 indicating no pigment packaging and 0 maximal pigment packaging. Bricaud et al. (2004) found that pigment packaging increases with Chla. Since large phytoplankton are associated with higher algal biomass, the pigment package effect increases with phytoplankton size.

Phytoplankton can also produce UV-absorbing pigments for protection from damaging radiation. The mycosporine-like amino acids absorb between 320 and 350 nm peaking around 330 to 340 nm (Vernet et al., 1994; Bracher and Wiencke, 2000). Production of UV-absorbing pigments depends on UV irradiation and species and is highly variable (Vernet et al., 1994).

2.9.3 NAP absorption

Non-algal particles (NAP) are operationally defined as a fraction of particulate matter, i.e., does not pass a filter of 0.7 mm pore size. It is not extracted by methanol in spectrophotometric measurements of particles on a filter pad (Kishino et al., 1985). It is composed of bacteria, other protists, zooplankton, detrital organic matter, and suspended inorganic particles. NAP absorption, $a_{\text{NAP}}(\lambda)$, depends on wavelength. It is highest in the UV-blue and exponentially decays to the red spectral range (see Figure 2.9.1):

$$a_{\text{NAP}}(\lambda) = a_{\text{NAP}}(440) \exp(-S_{\text{NAP}}(\lambda - 440)). \quad (2.9.2)$$

The spectral slope S_{NAP} varies between 0.006 to 0.013 nm⁻¹ (Roesler et al., 1989; Babin et al., 2003) depending on composition.

2.9.4 CDOM absorption

Colored dissolved organic matter (CDOM) is operationally defined as the absorbing matter that passes through a filter of 0.2 mm pore size (Bricaud et al., 1981). This fraction contains organic substances and inorganic salts. The inorganic salts are optically active in the UV, whereas the fraction that absorbs in the visible is dominated by organic matter, hence the name CDOM. Similar to NAP absorption, CDOM absorption, $a_{\text{CDOM}}(\lambda)$, decays exponentially with wavelength (see Figure 2.9.1):

$$a_{\text{CDOM}}(\lambda) = a_{\text{CDOM}}(440) \exp(-S_{\text{CDOM}}(\lambda - 440)). \quad (2.9.3)$$

However, spectral slopes are larger than for NAP. The spectral slope, S_{CDOM} , varies naturally in the range 0.007 to 0.026 nm⁻¹ (e.g., Twardowski et al., 2004). Variations in spectral slope are due to composition of the organic substances and are an indicator of their origin. Fulvic material of terrestrial origin, e.g., degrading plants introduced by river run-off, has generally smaller slopes than the humic material of marine origin, e.g., degrading phytoplankton. Depending on the spectral range used for determining S_{CDOM} , S_{CDOM} varies. In the UV, generally larger values of S_{CDOM} are found (Aurin et al., 2018).

2.9.5 Liquid water scattering

Pure water scatters elastically and inelastically. Inelastic scattering by pure water is introduced in section 2.10. Elastic scattering by water can be understood as caused by density fluctuations causing short term variations in refractive index. Density fluctuations are due

to thermal movement of water molecules. [Einstein \(1910\)](#) and [v. Smoluchowski \(1908\)](#) first described optical scattering due to thermodynamical fluctuations. Their theory was later modified to include polarization and yields for water following VSF (e.g., [Buiteveld et al., 1994](#)):

$$\beta(\lambda, \xi) = \frac{2\pi kT}{\lambda^4 \beta_T} n^2 \left(\frac{\partial n}{\partial P} \right)_T^2 \frac{6 + 6\rho}{6 - 7\rho} \left(1 + \frac{1 - \rho}{1 + \rho} \cos^2 \xi \right) \quad (2.9.4)$$

with temperature T , Boltzman constant k , isothermal compressibility of water β_T , isothermal pressure derivative of index of refraction $\left(\frac{\partial n}{\partial P}\right)_T$, and depolarization ratio ρ . Similar to Rayleigh scattering on atmospheric molecules, scattering on water molecules inversely depends on the wavelength to the power of 4. This analogy originates from the fact that the spatial extent of the density fluctuations is, just as atmospheric molecules, much smaller than the wavelength of visible light. The backscattering ratio of water is 0.5, half of the incoming light is scattered forward and half is scattered backward. The scattering coefficient of sea water depends on temperature and salinity ([Zhang et al., 2009](#)). Variations on the order of 30% are observed for typical salinity ranges in the ocean. The temperature dependence is with 4% significantly weaker.

2.9.6 Particle scattering

Oceanic particles scatter in the Mie regime. Various particles of different sizes are present in oceanic waters, including organic particles ranging from bacteria to large phytoplankton or zooplankton and inorganic particles such as storm-induced terrestrial dust. Small particles are much more abundant than large particles. Particle size distributions follow a hyperbolic shape, so-called Junge distributions. The number of particles per unit volume with size greater than r is proportional to $r^{-\mu}$ with $\mu = 3 - 5$ for typical oceanic size distributions ([Kostadinov et al., 2009](#)). [Fournier and Forand \(1994\)](#) derived an approximate analytic phase function from Mie theory for a Junge particle distribution, given in its latest form ([Fournier and Jonasz, 1999](#)) as:

$$\tilde{\beta}_{FF}(\xi) = \frac{1}{4\pi(1 - \delta)^2 \delta^\eta} [\eta(1 - \delta) - (1 - \delta\eta) + [\delta(1 - \delta^\eta) - \eta(1 - \delta)] \sin^2(\xi/2)] \quad (2.9.5)$$

$$+ \frac{1 - \delta_{180}^\eta}{16\pi(\delta_{180} - 1)\delta_{180}^\eta} (3 \cos^2 \xi - 1) \quad (2.9.6)$$

$$\eta = \frac{3 - \mu}{2}, \quad \delta = \frac{4}{3(n - 1)^2} \sin^2(\xi/2) \quad (2.9.7)$$

with δ_{180} being δ evaluated at 180° . The backscattering fraction is:

$$\tilde{b} = 1 - \frac{1 - \delta_{90}^{\eta+1} - 0.5(1 - \delta_{90}^\eta)}{(1 - \delta_{90})\delta_{90}^\eta} \quad (2.9.8)$$

with δ_{90} being δ evaluated at 90° . Typical oceanic \tilde{b} range between 0.001, very large phytoplankton, to 0.1, very small mineral particle (Mobley et al., 2021). This analytically derived phase function best matches field measurements of phase functions of natural waters. The exact choice of μ and η for a given backscattering fraction is not crucial. The backscattering fraction can be wavelength dependent and is usually parameterized as a power law decreasing with wavelength.

The strength of the total scattering coefficient is decreasing weakly with wavelength as typical for the Mie scattering regime. The scattering coefficient can be parameterized in terms of chlorophyll-a concentration C :

$$b = b_0 C^\epsilon \left(\frac{500}{\lambda} \right)^\gamma \quad (2.9.9)$$

b_0 , ϵ , and γ are constants that were empirically determined by, e.g., (Gordon and Morel 1983) as $b_0 = 0.3$, $\epsilon = 0.62$, $\gamma = 1$.

2.10 Inelastic processes

2.10.1 Phytoplankton fluorescence

Phytoplankton use light and water to convert carbon dioxide by photosynthesis to sugars and oxygen. Photosynthesis consists of a light-dependent and a light-independent reaction. During the light-dependent reaction, light is absorbed and transferred to electrons. In the dark reaction, this energy is used to build sugars from carbon dioxide and water. Oxygen is released as a waste-product. Light is absorbed by chlorophyll-a and other light-harvesting pigments and transferred to the reaction centers, photosystems (PS) I and II (Kirk, 1994). PS I and II consist of components needed for charge separation and electron transfer as well as pigment-proteins (containing chlorophyll) for light-harvesting. The excited PS I and II can return to ground state via three different mechanisms: photochemistry, fluorescence, or heat release. Through photochemical quenching, the absorbed energy is used in the photosynthesis reactions to ultimately produce sugars. Under stressful conditions or high light intensity, when photochemical reactions saturate, fluorescence and heat release yields increase. Chlorophyll-a fluoresces in two broad peaks around wavelengths 683 nm and

736 nm, referred to as red and far-red peaks. From the ocean, only the red peak can be sensed, because liquid water absorption is too strong in the far-red (e.g., [Wolanin et al., 2015b](#)).

2.10.2 CDOM fluorescence

A fraction of CDOM fluoresces. Since CDOM consists of many different dissolved organic compounds of terrestrial and marine origin, the fluorescent compounds are also diverse. Generally, CDOM fluoresces at wavelengths from UV to blue-green (e.g., [Hudson et al., 2007](#)).

2.10.3 Vibrational Raman scattering

Vibrational Raman scattering (VRS) is a significant process in water. [Sugihara et al. \(1984\)](#) discovered that measurements of upwelling irradiance E_u are unexpectedly high at depths below 50 m and wavelengths larger 520 nm, considering the absorption by water at these wavelengths, and postulated that the contributions to E_u at these wavelengths are from Raman scattered light in the blue-green wavelength range. VRS describes the light-water interaction in which the vibrational excitation state of a water molecule is altered, yielding scattered light at longer and shorter wavelengths λ than the incident light's wavelength λ' . The mean Raman shift for water is about $\Delta\nu \approx 3400 \text{ cm}^{-1}$ at room temperature. The VRS scattering coefficient

$$b^{\text{VRS}}(\lambda' \rightarrow \lambda) = b^{\text{VRS}}(\lambda') f^{\text{VRS}}(\lambda' \rightarrow \lambda) \quad (2.10.1)$$

is given by the product of the total VRS scattering coefficient $b^{\text{VRS}}(\lambda')$ and the wavelength distribution function $f^{\text{VRS}}(\lambda' \rightarrow \lambda)$, which can be understood as a probability density function for light with wavelength λ' being scattered to wavelength λ .

The total VRS scattering coefficient can be calculated from [\(Kattawar and Xu, 1992\)](#)

$$b^{\text{VRS}}(\lambda') = \frac{800N\pi}{3} \left[\frac{d\sigma(\lambda')}{d\Omega} \right] \left(\frac{1+2\rho}{1+\rho} \right), \quad (2.10.2)$$

with the VRS scattering cross section at a scattering angle of 90° , $\frac{d\sigma(\lambda')}{d\Omega}$, the number of molecules per cubic centimeter, N , and the depolarization ratio, ρ . $\frac{d\sigma(\lambda')}{d\Omega}$ has been measured in several studies for a reference wavelength of $\lambda_0 = 488 \text{ nm}$. Resulting $b^{\text{VRS}}(\lambda_0) = b^{\text{VRS}}(488)$ ranges between $2.4 \cdot 10^{-4}$ and $2.9 \cdot 10^{-4} \text{ m}^{-1}$ ([Romanov and Shuklin, 1975](#); [Kondilenko et al., 1977](#); [Marshall and Smith, 1990](#); [Bartlett et al., 1998](#); [Desiderio, 2000](#)).

The wavelength dependence of $b^{\text{VRS}}(\lambda')$ can be either described as an inverse power law

$$b^{\text{VRS}}(\lambda') = b^{\text{VRS}}(\lambda_0) \left(\frac{\lambda_0}{\lambda'} \right)^\gamma, \quad (2.10.3)$$

with $\gamma = 4$ derived theoretically (Placzek, 1934), or a resonance model (Bischel and Black, 1983; Faris and Copeland, 1997),

$$b^{\text{VRS}}(\lambda') = b^{\text{VRS}}(\lambda_0) \frac{1}{N_r} \frac{\nu^4}{(\nu_i^2 - \nu'^2)^2}, \quad (2.10.4)$$

with incident wave number ν' and normalization factor

$$N_r = \frac{(\nu^2 - \nu_0'^2)^2}{\nu_0^4} \text{ with } \nu_0' = \nu_0 + \Delta\nu, \quad (2.10.5)$$

where ν_0 is the reference wave number corresponding to $\lambda_0 = 488 \text{ nm}$. The resonance model is expected to better describe the wavelength dependence close to the absorption band of water, located at 130 nm , corresponding to $\nu_i = 76923 \text{ cm}^{-1}$.

The wavelength distribution function $f^{\text{VRS}}(\lambda' \rightarrow \lambda)$ can be described as a sum of four Gaussian functions (Walrafen, 1967), see Figure 2.10.1 (a), which was parameterized in Haltrin and Kattawar (1993),

$$f^{\text{VRS}}(\lambda' \rightarrow \lambda) = \frac{10^7}{\lambda'^2} \frac{1}{\sqrt{2\pi} \sum_{i=1}^4 (\alpha_i \sigma_i)} \sum_{i=1}^4 \alpha_i \exp \left(-\frac{(\frac{10^7}{\lambda'} - \frac{10^7}{\lambda} - \Delta\bar{\nu}_i)^2}{2\sigma_i^2} \right), \quad (2.10.6)$$

where the three parameters, α_i , σ_i , $\Delta\bar{\nu}_i$, define the shape of the Gaussian functions. The spectral shift of VRS is constant in terms of frequency. In terms of wavelength, the shift increases with increasing wavelength and $f^{\text{VRS}}(\lambda' \rightarrow \lambda)$ broadens and flattens, see Figure 2.10.1 (b). For incident light in the UV-VIS with wavelengths between 300 and 700 nm , the wavelength shift ranges between 33 and 100 nm . The shape parameters are temperature and salinity dependent. The hydrogen bonds break and reform constantly between water molecules which is thought to be the reason for the temperature dependence (Hare and Sorensen, 1990). The temperature and salinity dependence are small (Bartlett et al., 1998). Nevertheless, temperature and salinity dependencies of VRS are detectable with specific instrumentation and were suggested to be exploited for remotely measuring temperature and salinity of water bodies with a lidar-compatible Raman spectrometer system (Artlett and Pask, 2015; de Lima Ribeiro and Pask, 2020).

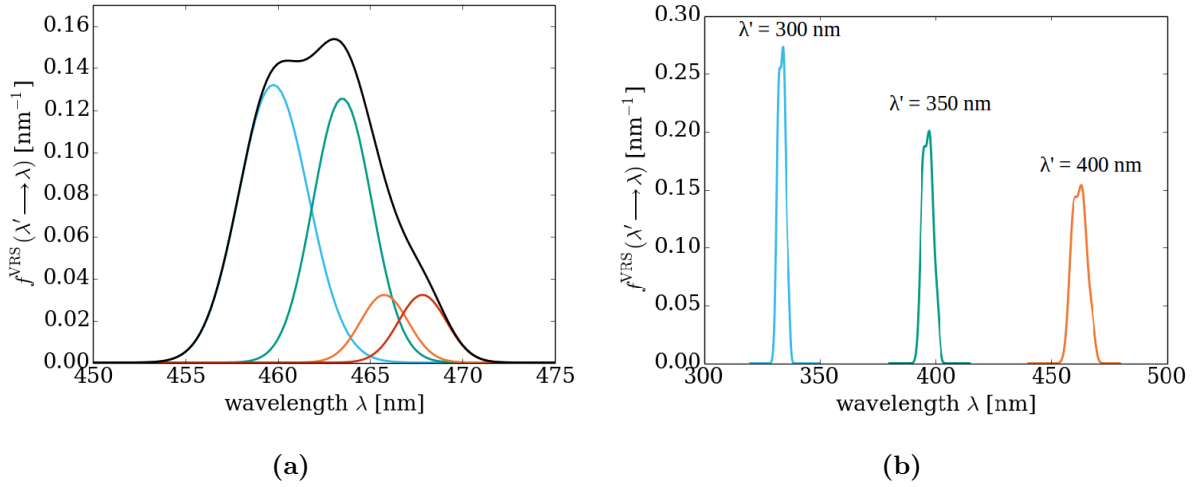


Figure 2.10.1: (a) Wavelength distribution function as made up of four Gaussian functions for a single VRS excitation wavelength of $\lambda' = 400$ nm. (b) Wavelength distribution functions for vibrationally Raman scattered light at three different wavelengths, $\lambda' = 300$, 350 , and 400 nm.

The phase function of VRS is given by

$$\tilde{\beta} = \frac{3}{16\pi} \frac{1+3\rho}{1+2\rho} \left[1 + \left(\frac{1-\rho}{1+3\rho} \right) \cos^2 \xi \right] \quad (2.10.7)$$

with scattering angle ξ . It is similar to the shape of elastic scattering of liquid water.

2.10.4 Brillouin scattering

Einstein-Smoluchowski theory was introduced in section 2.9.5 which describes elastic scattering in water due to density fluctuations. Later it was discovered that the elastic scattering component is not a single spectral line, but actually a triplet. Brillouin proposed the existence of two frequency-shifted lines due to scattering on dynamic fluctuations (Brillouin, 1922). Interaction of electromagnetic radiation with these propagating acoustic phonons leads to a Doppler shift. The red- and blue-shifted lines are referred to as Mandelstam-Brillouin (MB) doublet which are analogous to the Stokes and Anti-Stokes line for Raman scattering. The center line of the triplet is not shifted with respect to the incident light's wavelength. It is caused by scattering on static fluctuations and called Gross line (Gross, 1930). The ratio of the Gross line intensity to the MB doublet intensity is called Landau Placzek ratio (Landau, L. D. and Placzek, G, 1934) and is about 1% for water at 25°C (O'Connor and Schlupf, 1967).

In conclusion, almost all scattering in water is inelastic. However, at an incident wave-

length of 450 nm, the wavelength shift is $\Delta\lambda \approx \pm 0.006$ nm for the MB doublet (Peters, 2013). This wavelength shift is so small that it is not relevant for the spectral resolution usually considered in optical oceanography. Brillouin scattering is treated in the RTM as an elastic component in the framework of Einstein-Smoluchowski theory. This assumption is further discussed in section 2.11.1.

2.11 Differential Optical Absorption Spectroscopy

Differential Optical Absorption Spectroscopy (DOAS) (Platt and Stutz, 2008) has been first used for determining trace gas concentrations of weak atmospheric absorbers in the UV-VIS spectral range from ground-based spectroscopic measurements (Noxon, 1975; Platt et al., 1979; Perner and Platt, 1979; Solomon et al., 1987). The method identifies spectral features of the target's absorption cross section in the measured spectra. DOAS-type instruments therefore record radiances over broad spectral ranges (on the order of 50-200 nm) with moderate spectral resolution such that the rather broad band absorption features in the UV-VIS, as opposed to line absorption features, can be resolved. The first space-borne DOAS-type instrument was the Global Ozone Monitoring Experiment (GOME) (Burrows et al., 1999). The DOAS method has since been applied to satellite-recorded backscattered radiances from GOME and other DOAS-type satellite sensors and yielded global observations of concentrations of weak atmospheric absorbers such as nitrogen dioxide, bromine monoxide, chlorine dioxide, formaldehyde, glyoxal, iodine monoxide, the oxygen dimer, and sulfur dioxide.

DOAS is based on Beer-Lambert's law which follows from the radiative transfer equation (Liou, 2002). The RTE presented in Equation 2.6.4 can be solved analytically, if the source term is neglected. The emission by atmospheric molecules and Earth's surface is negligible in the UV-VIS wavelength range. In the case of parallel incident sunlight and no multiple scattering, the scattering contribution to the source term becomes zero as well. The RTE at UV-VIS and near-infrared wavelengths is reduced to

$$dI(\lambda) = -\sigma_c(\lambda)nI(\lambda)ds, \quad (2.11.1)$$

where n is the number density of absorbing molecules along the light path. With the incident intensity $I_0(\lambda)$ at $s = 0$, the solution is

$$I(\lambda) = I_0(\lambda) \exp\left(-\int_0^{s_1} \sigma_c(\lambda)nds\right). \quad (2.11.2)$$

If $\sigma_c(\lambda)$ is independent of distance s , the slant column density SCD can be introduced as

$$SCD = \int_0^{s_1} n ds. \quad (2.11.3)$$

It follows Beer-Lambert's law

$$I_{s_1}(\lambda) = I_0(\lambda) \exp(-\sigma_c SCD) = I_0(\lambda) \exp(-\tau) \quad (2.11.4)$$

which states that the intensity after traveling a distance s_1 through a homogeneously attenuating medium can be described by an exponential decay of the initial intensity which decreases with the product of the attenuation cross section and the SCD . This product is the optical depth τ .

The DOAS equation (Platt and Stutz, 2008; Richter and Wagner, 2011) is derived from Beer-Lambert's law. Each absorbing and/or scattering constituent i of the medium adds to the optical depth:

$$I(\lambda) = c_{\text{eff}} I_0(\lambda) \exp(-\tau) = c_{\text{eff}} I_0(\lambda) \exp\left(-\sum_i [\sigma_{a,i}(\lambda) + \sigma_{b,i}(\lambda)] SCD_i\right) \quad (2.11.5)$$

$$\ln \frac{c_{\text{eff}} I_0(\lambda)}{I(\lambda)} = \tau(\lambda) = \sum_i [\sigma_{a,i}(\lambda) + \sigma_{b,i}(\lambda)] SCD_i. \quad (2.11.6)$$

The efficiency factor c_{eff} was introduced here to account for the fact that the DOAS method is applied to scattered light and therefore the initial intensity is not just the extraterrestrial solar irradiance I_0 . It needs to be corrected by taking into account the scattering efficiency. The DOAS method separates high frequency spectral features from broad band features. For this purpose, a low order polynomial is introduced to combine all broad band contributions to the optical depth in one term. Since the wavelength dependencies of elastic scattering in the atmosphere and ocean generally follow power laws, their contribution is approximated by the polynomial. Assuming that the logarithm of the scattering efficiency has a polynomial wavelength dependence, $\ln(c_{\text{eff}})$ also vanishes in the polynomial,

$$\ln \frac{I_0(\lambda)}{I(\lambda)} = \tau(\lambda) = \sum_i \sigma_{a,i}(\lambda) SCD_i + \sum_m w_m \lambda^m, \quad (2.11.7)$$

with polynomial coefficients w_m . Equation 4.2.2 is a general form of the DOAS equation. It is generally only valid for weak absorbers, because for strong absorbers, the light path differs for light of different wavelengths. The absorption structure in the measured radiance can then not be approximated by a scaling of the absorption cross section with a single

factor (SCD). How to account for inelastic processes in the DOAS equation is discussed in section [2.11.1](#). The DOAS equation is often formulated by introducing the concept of differential cross sections. The differential cross section $\sigma'_{a,i}$ is the high-frequency component of the cross section. The broad band component of the cross section is then also included in the polynomial,

$$\tau(\lambda) = \sum_i \sigma'_{a,i}(\lambda)SCD_i + \sum_m w'_m \lambda^m, \quad (2.11.8)$$

consequently, with polynomial coefficients w'_m differing in value from w_m .

The concentration of an atmospheric absorber is usually targeted in a certain wavelength range, the fit window, where its absorption cross section shows distinct features easily separable from those of other atmospheric contributions in this wavelength range. Cross sections of atmospheric gases are determined prior, usually in laboratory measurements. DOAS-type satellite sensors usually also record I_0 . With the measured τ as input from instruments, Equation [4.2.2](#) is solved for the slant column densities SCD_i and the polynomial coefficients w_m by minimization at several wavelengths. Since I_0 and I are measured at spectral resolution of the instrument, the cross sections are convolved with the slit function of the instrument prior to the fit. This procedure is mathematically not strictly correct, because the mathematical order of the convolution and the exponential function in Equation [2.11.5](#) can not be switched and requires correction in case of strong or structured absorption ([Aliwell et al., 2002](#)).

The DOAS retrieval yields the SCD for the target species, which needs to be converted to a concentration in a second step. For atmospheric applications, slant column densities SCD are usually in units of molecules per area. The light path, the actual distance s that the light traveled to the instrument, needs to be known for converting SCD into an absorber gas concentration. For realistic atmospheric conditions, obtaining n_i from SCD_i is not so straight-forward, because the scattered light reaching the detector originates from multiple paths. The effective path is influenced by multiple-scattering on air molecules and aerosols. The relationship between slant column density and vertical column density VCD , which is the vertically integrated absorber concentration above the satellite ground pixel, is given by the air mass factor AMF ,

$$VCD = SCD/AMF. \quad (2.11.9)$$

The AMF expresses the effective light path and depends on multiple parameters that influence the light path such as vertical profile of the absorber, position of the sun, aerosol

loading and vertical distribution, and surface albedo. It can be calculated with the help of an RTM.

The DOAS method was extended for targeting concentrations of oceanic constituents (PhytoDOAS) (Bracher et al., 2009; Sadeghi et al., 2012a). For satellite remote sensing applications, absorption cross sections of oceanic absorbers σ_a^{oc} are fitted to measured optical depths next to cross sections of atmospheric absorbers σ_a^{atm}

$$\frac{I_0}{I(\lambda)} = \tau = \sum_i \sigma_{a,i}^{\text{atm}} SCD_i + \sum_j \sigma_{a,j}^{\text{oc}} SCD_j + \sum_m w_m \lambda^m. \quad (2.11.10)$$

Generally, a lower order polynomial is chosen for oceanic than for atmospheric applications, because oceanic absorption cross sections are rather broad band as compared to atmospheric ones due to different rotational and vibrational degrees of freedom in liquids compared to gases. The exponentially decaying absorption by CDOM and NAP with wavelength can be approximated and is therefore accounted for by the polynomial, when rather short fit windows are considered. Main oceanic absorbers that need to be specifically considered are therefore liquid water and phytoplankton. As introduced in section 2.9.2, the absorption of phytoplankton is usually determined as specific absorption coefficient a^* normalized to Chla (usually in units m^2/mg). The sum in Equation 2.11.10 can then be expressed as $\sum_j \sigma_{a,j}^{\text{oc}} SCD_j = \sum_j a_j^* SCD_j^*$, where the slant column density is now defined in terms of concentration C_j in units of mg/m^3 , $SCD_j^* = \int C_j ds$.

In earlier studies (Bracher et al., 2009; Sadeghi et al., 2012a,b), the concentration C_j of the target oceanic constituent was directly inferred from SCD_j^* by estimating the underwater light path. In recent studies (Dinter et al., 2015; Losa et al., 2017a), the conversion of SCD_j^* to concentrations of oceanic quantities is achieved with the help of an RTM and a look-up table (LUT) approach. The RTM is used to simulate radiances as seen by the satellite sensor. Results of PhytoDOAS fits on these simulated radiances with known oceanic concentrations can then be used to map the relationship between SCD_j^* and C_j in form of a LUT. The LUT is then applied to retrieved SCD_j^* from actual measurements. By comparing DOAS fits on simulated satellite measurements with fits on actual satellite measurements, introduced errors due to violation of assumptions on weak absorption as well as low degree of structuring of absorption features are mostly compensated.

Uncertainties of DOAS retrievals are mainly caused by insufficient calibration of the sensor (see section 2.14), uncertainties in measured absorption cross sections, and spectral correlation (Richter and Wagner, 2011). An additional source for uncertainty in the final DOAS product is the conversion from the retrieval output to the physical unit of the target using an RTM. Exact wavelength calibration of the sensor is important for the DOAS

retrieval due to the spectrally narrow Fraunhofer lines (see also next section, 2.11.1) in the solar spectrum. If wavelength alignment between I_0 and I is not exact, large spectral artifacts can result when the ratio of I_0 and I is taken. Prior to solving Equation 2.11.10, I_0 is numerically aligned with respect to a reference solar spectrum (Fraunhofer atlas) (Chance and Kurucz, 2010) to compensate for any residual wavelength calibration errors (van Geffen, 2004). Additionally, I is allowed to shift and squeeze in the fitting routine to ensure optimal wavelength alignment (Richter, 1997). Largest uncertainties in DOAS retrievals arise from spectral correlation of the absorption cross section of the target species with those of other absorbing species, and spectral features caused by inelastic scattering (see next section, 2.11.1) or by instrumentation, e.g., by stray light. The fit window can be optimized such that spectral correlation is minimized. The impact of remaining spectral interferences on the fit result is reduced by taking into account cross sections for all spectral effects, e.g., empirically determined pseudo-cross sections which characterize instrumental stray light. Although less spectral information is contained in short fit windows, they usually yield better results. In short fit windows, the distortion of absorption structures due to the wavelength dependence of the light path is less pronounced, inaccuracies in cross sections are better compensated by the polynomial, and wavelength dependence of broad band effects following different power laws or even exponential decay, as is the case for CDOM absorption, are better approximated by the polynomial.

2.11.1 Filling-in of Fraunhofer lines

Sharp lines of reduced intensity are present in the solar spectrum. These so-called Fraunhofer lines (Fraunhofer, 1817) are absorption lines, caused by absorption of sunlight by gases in the sun's photosphere (Kirchhoff, 1860). In measurements of the solar spectrum, it has been observed that these lines are less pronounced when scattered sunlight is measured as compared to direct sunlight measurements. The lines are filled-in. This effect is known as the Ring effect first observed by Grainger and Ring (1962). The filling-in of Fraunhofer lines is caused by inelastic processes. The Ring effect is caused by RRS and, to some extent, Brillouin scattering in the atmosphere (Kattawar et al., 1981) and has also been observed in the ocean by (Kattawar and Xu, 1992) where it is caused by VRS and also, to some extent, Brillouin scattering. Inelastic processes redistribute light to wavelengths different from the incident light's wavelength. More Raman scattering events occur at wavelengths where light intensity is high compared to wavelengths of low light intensity such as the Fraunhofer lines. Due to the wavelength shift associated with inelastic processes, more light is scattered to wavelengths at the Fraunhofer lines than out of the

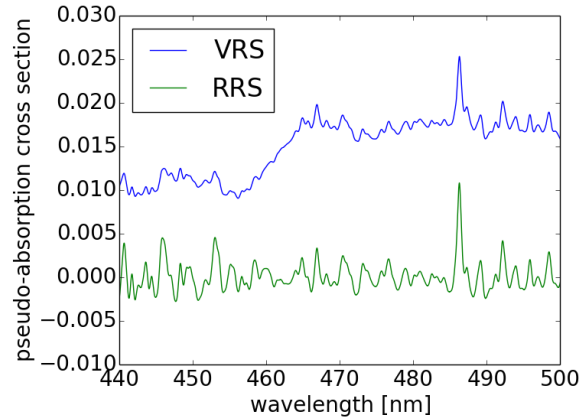


Figure 2.11.1: Pseudo-absorption cross sections for VRS and RRS between 440 and 500 nm at instrumental resolution of GOME-2. The cross sections were calculated based on Equation 2.11.11 from modeled radiances which were convolved with the GOME-2 slit function prior to taking the natural logarithm. The model run for VRS contained a chlorophyll-a concentration of 0.1 mg/m³.

Fraunhofer lines. Consequently, the Fraunhofer lines become less deep. They are filled-in with light from adjacent wavelengths. Fluorescence also leads to filling-in of Fraunhofer lines at the emission wavelengths. Inelastic processes can be incorporated into the DOAS equation as so-called pseudo-absorbers. The pseudo-absorption cross section that accounts for the filling-in by inelastic process k can be determined as (Vountas et al., 1998)

$$\sigma_{f,k}(\lambda) = \ln \frac{I^+(\lambda)}{I^-(\lambda)}, \quad (2.11.11)$$

where I^+ and I^- are modeled radiances for a reference scenario calculated with and without considering inelastic process k in the RTM, respectively. The PhytoDOAS Equation 2.11.10 becomes

$$\tau = \sum_i \sigma_{a,i}^{\text{atm}} S_i + \sum_j \sigma_{a,j}^{\text{oc}} S_j + \sum_k \sigma_{f,k} S_k + \sum_m w_m \lambda^m. \quad (2.11.12)$$

The SCD was exchanged with S , referred to as the fit factor, since the physical meaning of the fit factors for inelastic processes S_k generally differs from the SCD . For consistency, all SCD retrieved with DOAS in this work are referred to as fit factors independent of their physical meaning. Pseudo-absorption cross sections as defined in Equation 2.11.11 have been proven successful to account for RRS, VRS, and chlorophyll-a fluorescence in backscattered radiances measured by different satellite sensors (Vountas et al., 1998, 2003,

2007; Dinter et al., 2015; Wolanin et al., 2015b).

Just as for atmospheric and oceanic absorbers, all relevant inelastic processes within a fit window should be considered. In this work, DOAS fits are performed for fit windows within the wavelength range 349 to 560 nm. Only two inelastic processes are considered in the PhytoDOAS equation, RRS in the atmosphere and VRS in the ocean. Pseudo-absorption cross sections of VRS and RRS are exemplarily shown for the wavelength range of 440 to 500 nm in Figure 2.11.1. Other inelastic processes are not considered for following reasons:

- VRS in the atmosphere: Lampel et al. (2015) investigated the effect of VRS in the atmosphere on the DOAS method. They found that the effect is negligible for DOAS fits with a root mean square (RMS) larger than $4 \cdot 10^{-4}$, which is usually the case for PhytoDOAS fits.
- Brillouin scattering: The wavelength shift of Brillouin scattering by liquid water is small compared to VRS and RRS, but partial-filling in of Fraunhofer lines by Brillouin scattering in the ocean has been reported by Xu and Kattawar (1994). Peters (2013) investigated if Brillouin scattering needs to be taken into account for DOAS measurements from instruments with slit functions of different full width at half maximum (FWHM). For an instrument with a slit function of roughly 0.5 nm FWHM, the optical depth for Brillouin scattering is $4 \cdot 10^{-5}$ as estimated by RTM corresponding to an RMS of $1.4 \cdot 10^{-5}$. Peters (2013) concluded that for instruments with spectral resolution of 0.5 nm, the influence of Brillouin scattering can be neglected, because its optical depth is an order of magnitude lower than the residuals obtained for DOAS fits with best fit quality. Brillouin scattering can also occur in the atmosphere, however, the filling-in of Fraunhofer lines in satellite-measured backscattered radiances with spectral resolution on the order of typically 0.5 nm can be sufficiently accounted for by only considering RRS (Joiner et al., 1995).
- CDOM fluorescence: CDOM fluorescence is detectable using DOAS in CDOM-rich waters, however, RRS and VRS are usually the dominant contributors to filling-in of Fraunhofer lines depending on wavelength and on attenuation in the ocean (Wolanin et al., 2015a). Pseudo-absorption cross sections for CDOM fluorescence σ_{fCDOM} were found to differ significantly in spectral shape from those for VRS and RRS (Wolanin et al., 2015a). Due to the wide range of fluorescent CDOM compounds and difficulties in modeling their fluorescence, it is difficult to define σ_{fCDOM} for global applications (Wolanin et al., 2015a). Neglecting CDOM fluorescence in the PhytoDOAS fit might be a potential source of uncertainty in areas of high CDOM abundance. Since the spectral dependence of σ_{fCDOM} and σ_{VRS} are distinctly different, the influence on

retrieved VRS fit factors should be small. Furthermore, this work concentrates on open ocean scenes, where CDOM abundance is generally low.

- chlorophyll fluorescence: Emission wavelengths are at red and near-infrared wavelengths, consequently, out of the considered wavelength range.

2.12 Atmospheric satellite sensors

A number of satellite sensors have been dedicated for determining atmospheric trace gases using Differential Optical Absorption Spectroscopy. In this work, measurements from the sensors SCIAMACHY (Bovensmann et al., 1999), GOME-2 (Munro et al., 2016), OMI (Levelt et al., 2006), and TROPOMI (Veefkind et al., 2012) are used. Their measurement principles are briefly presented in this section. All sensors are on satellites in sun-synchronous orbits, recording backscattered radiances in nadir geometry and measuring the extraterrestrial solar irradiance as reference once per day. For atmospheric applications, the spectral resolution of these instruments in the UV-VIS spectral range is required to be around 0.5 nm. High signal-to-noise ratios (around 1000) are needed for accurate retrievals. Table 2.12.1 summarizes instrumental parameters of the four sensors.

SCIAMACHY and GOME-2 are whisk-broom sensors. Their instrument design is very similar. Whisk broom sensors scan the swath across track with a scan mirror. Consequently, across-track ground pixels are measured subsequently, not simultaneously. Backscattered radiation is collected by the scan mirror which directs the radiation through an aperture to the entrance slit of the instrument. The dimension of the entrance slit is small for these types of sensors leading to a narrow Instantaneous Field of View (IFOV). The light is spectrally pre-dispersed by a prism and then directed to the spectral channels, of which each has a grating for further dispersion. The resulting spectrum is then recorded with photodiodes (1024 pixels). The light path to the detectors and the detectors themselves are polarization sensitive. The prism not only pre-disperses the light, but also directs a fraction of the light which is perpendicularly polarized with respect to the instrument's optical plane to the Polarization Measurement Device (PMD) by Brewster angle reflection. Together with pre-flight calibration data and data from the spectral detectors, the polarization of the light can be determined from the PMD data.

OMI and TROPOMI are push-broom sensors. TROPOMI inherited the design of OMI. These sensors have a wide IFOV. The full swath is measured at the same time. For this purpose, the sensors are equipped with large 2-dimensional charge-coupled device (CCD) arrays. One dimension is used for recording the spectral information, the other one for the

Table 2.12.1: A selection of sensor parameters for SCIAMACHY, GOME-2, OMI, and TROPOMI. The spatial resolution for GOME-2 and TROPOMI was reduced in July 2013 and August 2019, respectively.

	SCIAMACHY	GOME-2	OMI	TROPOMI
mission period/launch year	2002-2012	2006	2004	2017
spectral channels	UV-SWIR	UV-NIR	UV-VIS	UV-VIS, NIR, SWIR
used spectral ranges [nm]	424-525	397-604	350-504	320-405, 405-500
spectral resolution [nm]	0.47	0.51	0.63	0.55
spatial resolution [kmxkm] (across- x along-track)	30x60	80x40 40x40	13x24	3.5x7 3.5x5.5
local overpass time	10:00	09:30	13:45	13:30
node	descending	descending	ascending	ascending
global coverage [days]	6	1.5	1	1

spatial information. Upon entrance, the light first passes a polarization scrambler. The unpolarized backscattered light is then subdivided and directed to different spectrometers where the light is dispersed by gratings and measured by CCD arrays.

For the atmospheric science community, the spectral resolution of about 0.5 nm of these sensors is only moderately high. In the context of optical oceanography, this spectral resolution is much higher than those of recent or planned ocean color satellite sensors, and also higher than the spectral resolution of most radiometers used for in-situ measurements. These atmospheric sensors are referred to as hyperspectral sensors throughout this work. Hyperspectral, in the context of optical oceanography, means that a continuous spectrum is recorded over a broad spectral region. In contrast, multispectral sensors record radiances at a number of wavelength bands. Their measurement principles are described in the next section.

2.13 Ocean color satellite sensors

2.13.1 Measurement principle

Typical ocean color satellite sensors are multispectral sensors. Radiances are recorded at a number of wavelength bands in the visible with typically 10-20 nm bandwidth. Data from the Sea-Viewing Wide Field-of-View Sensor (SeaWiFS) (Barnes and Holmes, 1993), the Medium Resolution Imaging Spectrometer (MERIS) (Bezy et al., 1997), the Moderate Resolution Imaging Spectroradiometer (MODIS) (Barnes and Salomonson, 1992), the Vis-

Table 2.13.1: A selection of sensor parameters for the ocean color sensors SeaWiFS, MODIS, MERIS, VIIRS, and OLCI. The bandwidth is given for the ocean color bands of each sensor.

	SeaWiFS	MODIS	MERIS	VIIRS	OLCI
operation period/ launch year	1997-2010	1999 (Terra), 2002 (Aqua)	2002-2012	2011	2016 (S3A), 2018 (S3B)
number of bands	8	36	15	22	21
spectral range [nm]	410-865	410-14400	390-1040	400-1250	400-1020
bandwidth [nm]	20	10	10	20	10
spatial resolution [m]	1100	1000	1200	750	300

ible Infrared Imager Radiometer Suite (VIIRS) (Welsch et al., 2001), and the Ocean and Land Colour Instrument (OLCI) (Nieke et al., 2012) are used for comparative purposes in this work. Most of these instruments are also used for land applications and therefore also record at spectral bands in the infrared. SeaWiFS, MODIS, and VIIRS are scanning radiometers similar to GOME-2 and SCIAMACHY. For example, SeaWiFS has eight spectral bands. Incoming radiation is collected by a folded telescope and reflected on a rotating half-angle mirror. Dichroic beam splitters separate the incoming radiation into four wavelength intervals of which each comprises two spectral bands. The bands are separated by two spectral bandpass filters and imaged onto detectors. On the contrary, MERIS and OLCI have a push-broom sensor design. The swath is covered by five cameras of which each consists of a CCD array simultaneously measuring the incoming radiation across the entire swath. Some OC sensors as SeaWiFS are tilted out of the nadir viewing geometry to reduce sun glint. For a given spectral range and spectral resolution, the spatiotemporal resolution of the sensors is limited by the data rate, which can be downlinked from the satellite to the ground. Since the spectral resolution is much lower than for atmospheric sensors, the spatial resolution is much higher. The introduced multispectral sensors have a spatial resolution of about 1200 m or better. OLCI is the newest sensor with full resolution of 300 m. Table 2.13.1 summarizes parameters of the five OC sensors.

2.13.2 Retrieval principle

Most ocean color algorithms use remote sensing reflectances or normalized water-leaving radiances as input. The water-leaving radiance L_w is the radiance that is upwelled in the water and crosses the sea-air interface. The remote sensing reflectance R_{rs} is the ratio of L_w to the downwelling irradiance E_d that is incident on the water surface, $R_{rs} = L_w/E_d$. OC algorithms often use band ratios of these quantities to derive OC variables from empirical

relationships which are derived from large match-up data bases of in-situ and satellite data. A whole suite of such band ratio algorithms was developed for the retrieval of Chla (O'Reilly et al., 1998; O'Reilly and Werdell, 2019). The most widely used empirical algorithm for Chla retrievals from CZCS data, for example, uses the ratio of the normalized water-leaving radiance of the band at 443 nm to that of the band at 550 nm for Chla smaller 1.5 mg/m³. It switches to the ratio of normalized L_w at bands 520 nm and 550 nm for higher Chla, when the blue-green band ratio is too low (Gordon et al., 1983; Feldman et al., 1989; Evans and Gordon, 1994).

Satellite sensors measure the total radiance I_t reaching the instrument independent of whether the electromagnetic radiation interacted with the ocean or not. An atmospheric correction is used for obtaining L_w from I_t . In the following, the idea behind the atmospheric correction is described and the normalization of derived L_w introduced.

Atmospheric correction

The goal of the atmospheric correction (Mobley et al., 2021) is to convert the satellite-measured I_t to L_w which is needed as a starting point for OC retrievals. The ocean color community typically uses L for radiances, whereas the atmospheric community typically uses I . To be consistent with usual terminology in both fields, the notation with I is used for atmospheric applications in this work and L for oceanic applications. In the following, I is therefore used for atmospheric contributions and L for oceanic or sea-surface related radiances. As briefly outlined in section 2.2, the radiance that is measured by the satellite consists of different contributions from the atmosphere, the surface, and the ocean,

$$I_t = I_{\text{atm}} + L_{\text{surf}}^{\text{TOA}} + L_w^{\text{TOA}} \quad (2.13.1)$$

I_{atm} and L_{surf} are the radiance contribution from the atmosphere and the surface, respectively. Angle and wavelength dependencies are omitted for brevity. Since L_w is traditionally defined just above the water surface, the superscripts TOA denote that these are L_w and L_{surf} at the top of atmosphere (TOA). I_{atm} shall always be defined at TOA. The atmospheric contribution originates from scattering on atmospheric gases (Rayleigh contribution I_R) and aerosols (I_a) as well as multiple scattering between aerosols and gases (I_{aR}) (Gordon and Wang, 1994b). The surface contribution consists of a contribution from specular reflection on the ocean surface (Wang and Bailey, 2001), known as sun glint, L_g^{TOA} , reflection of diffuse sunlight by the ocean surface $L_{\text{sky}}^{\text{TOA}}$, and reflection of diffuse and direct sunlight by white caps and foam L_{wc}^{TOA} (Gordon and Wang, 1994a; Frouin et al.,

1996). I_t can be written as

$$I_t = I_R + I_a + I_{aR} + L_g^{\text{TOA}} + L_{\text{sky}}^{\text{TOA}} + L_{wc}^{\text{TOA}} + L_w^{\text{TOA}}. \quad (2.13.2)$$

L_{sky} is usually accounted for as part of I_R . Transmittances are introduced to relate the contributions from the surface and the water-leaving radiance at TOA to their values at sea level where they are usually defined and measured in-situ,

$$I_t = I_R + I_a + I_{aR} + TL_g + tL_{wc} + tL_w, \quad (2.13.3)$$

where T is the direct and t the diffuse transmittance (Yang and Gordon, 1997; Wang, 1999). All the contributions to I_t in Equation 2.13.3 need to be estimated to obtain L_w . Ancillary data from other satellites or climatologies, empirical parameterizations of contributions, and radiative transfer modeling are used to tackle this challenge.

Normalization

The water-leaving radiance as determined from satellite measurements generally depends on SZA, viewing geometry, atmospheric conditions, and wave state at the time of measurement. L_w is normalized (Mobley et al., 2021) in order to compare the satellite-measured L_w to in-situ measurements for validation and algorithm development. The influence of the sun's position and atmospheric attenuation are removed in the normalized water leaving radiance

$$[L_w(\theta_V, \phi)]_N = \left(\frac{R}{R_0}\right)^2 \frac{L_w(\theta_S, \theta_V, \phi)}{\cos \theta_S t(\theta_S)} \quad (2.13.4)$$

with θ_V as VZA, θ_S as SZA, and $t(\theta_S)$ as atmospheric diffuse transmittance for irradiance in sun's direction for atmospheric conditions at time of measurement. The factor (R/R_0) corrects for the influence of the Earth-sun distance at the time of measurement. R is the Earth-sun distance at time of measurement and R_0 the mean Earth-sun distance. The non-dimensional normalized water-leaving radiance is defined as

$$[\rho_w(\theta_V, \phi)]_N = \frac{\pi}{F_0} [L_w(\theta_V, \phi)]_N \quad (2.13.5)$$

where F_0 is the extraterrestrial solar irradiance at R_0 . The remote sensing reflectance R_{rs} is the ratio of L_w and E_d just above the surface (denoted by 0^+) which depends on SZA

$$R_{rs}(\theta_V, \phi) = \frac{L_w(\theta_S, \theta_V, \phi)}{E_d(0^+, \theta_S)} \quad (2.13.6)$$

$E_d(0^+, \theta_S)$ can be expressed in terms of the parameters introduced for normalization,

$$E_d(0^+, \theta_S) = F_0 \left(\frac{R_0}{R} \right)^2 \cos \theta_{St}(\theta_S), \quad (2.13.7)$$

which shows that the non-dimensional normalized water-leaving radiance and the remote sensing reflectance are related by

$$[\rho_w(\theta_V, \phi)]_N = \pi R_{rs}(\theta_V, \phi). \quad (2.13.8)$$

The dependence on viewing geometry is known as the BRDF effect. The bidirectional reflectance distribution function (BRDF) is the radiance which is reflected by the surface divided by the incident plane irradiance onto the surface. For a perfect Lambertian surface, the reflected radiance is isotropic and the BRDF is $1/\pi$. $[\rho_w]_N$ can be understood as the BRDF of the ocean, L_w/E_d , normalized to the BRDF of a perfect Lambertian surface

$$[\rho_w]_N = \frac{L_w/E_d}{1/\pi} = \pi R_{rs}. \quad (2.13.9)$$

The BRDF effect (Morel, 1991; Morel and Gentili, 1993, 1996) describes how the angular distribution of the upwelling radiance depends on the sky radiance distribution, the viewing geometry, and water optical properties and needs to be removed to the greatest possible extent to obtain a fully normalized satellite measurement. The correction requires three parameters \mathcal{R} , f , and Q . \mathcal{R} is dimensionless and corrects for all transmission and reflection effects of the wavy sea surface in the case of transmission of $E_d(0^+)$ downward and $L_u(0^-, \theta'_V, \phi)$ upward through the surface. θ'_V is the angle below the sea surface which is refracted by the surface to the viewing direction θ_V above surface. f is also dimensionless and relates the irradiance reflectance just below the sea surface, $E_u(0^-)/E_d(0^-)$, to the most relevant IOPs, $E_u(0^-)/E_d(0^-) = f \cdot b_b/a$. Q has units of steradian and expresses the angular distribution of the upwelling radiance. Morel et al. (2002) incorporated these factors to yield what they call the exact normalized water-leaving radiance,

$$[L_w]_N^{ex} = [L_w(\theta_V, \phi)]_N \frac{\mathcal{R}_0(W)}{\mathcal{R}(W, \theta'_V)} \frac{f_0(\text{ATM}, W, \text{IOP})}{Q_0(\text{ATM}, W, \text{IOP})} \frac{Q(\theta_S, \theta'_V, \phi, \text{ATM}, W, \text{IOP})}{f(\theta_S, \text{ATM}, W, \text{IOP})}, \quad (2.13.10)$$

where \mathcal{R}_0 , f_0 , and Q_0 are reference values for normal conditions. W is the wind speed and IOP and ATM denote, respectively, the ocean IOPs and atmospheric conditions at the time of measurement.

2.14 Calibration of optical satellite sensors

Calibration of a radiometric sensor (IOCCG, 2013) is required to relate the electrical response of the detector in units of voltage or digital numbers to the radiant power incident on the detector. An ideal sensor is only sensitive to radiation within a small wavelength range $\lambda \pm \Delta\lambda/2$ and has a linear relationship between electrical output and radiometric input signal. The electrical signal $V_c(\lambda)$ that the detector measures when the input signal is generated by a calibration source of known radiance $I_c(\lambda)$ is given by

$$V_c(\lambda) = k_I(\lambda)I_c(\lambda), \quad (2.14.1)$$

where k_I is the calibration constant in terms of radiance. Measurement of an unknown source gives

$$V(\lambda) = k_I(\lambda)I(\lambda) = [V_c(\lambda)/I_c(\lambda)]I(\lambda). \quad (2.14.2)$$

Calibration of a radiometric sensor is generally complex, since sensors are not ideal. The non-ideal behavior of the sensor needs to be characterized. Typical effects for multispectral OC color sensors are out-of-band response, polarization sensitivity, bright-target response, and non-linearity. A full characterization of the sensor performance is conducted in the laboratory on ground before launch. This pre-launch calibration data is a first basis for interpreting the electric output signal of the sensor when in space. However, during launch and due to outgassing processes when in orbit as well as degradation of the sensor with time, sensor characteristics change and pre-launch calibration data is not sufficient to meet required radiometric accuracy. Satellite sensors are therefore also calibrated when in orbit. This in-flight calibration is achieved with on-board calibration devices such as lamps, extraterrestrial targets such as the moon and sun, and/or well-characterized Earth targets. The sun is the gold standard for calibration since its spectrum is well-known. Satellite sensors usually have different observation modes used for calibration. Radiation from different calibration sources can be directed to the detector. On the dark side of the orbit, all shutters are closed to determine the dark current of the sensor. Although a lot of effort is made for calibration of the sensor and constant monitoring of its performance throughout its mission lifetime, calibration is usually not perfect. On-board calibration

devices also degrade. Often, different measurements are carried out for correcting the same effect or the performance of calibration devices themselves is monitored by measurements of moonshine spectra for example. The sun is a stable and well-known calibration source, however, due to its high intensity, it can only be measured via a diffuser. Diffusers are also non-perfect and therefore characterized prior to launch, but are also subject to degradation which is difficult to perfectly monitor and characterize (Hilsenrath et al., 1995). Residual calibration errors therefore remain in measured backscattered radiances.

The radiometric accuracy for OC satellite missions is especially demanding, because, on average, 90% of the signal measured by the sensor only contains information on the atmosphere and surface. Based on experience with the first OC sensor in space, the Coastal Zone Color Scanner (CZCS), radiometric requirements of OC satellite sensors were formulated. OC sensors should achieve an accuracy of normalized water-leaving radiances within $\pm 5\%$ at 443 nm and retrieved Chla within $\pm 30\%$ in oligotrophic waters. The atmospheric correction introduces uncertainties on the order of 2.5% for normalized water-leaving radiances. At 443 nm, the water-leaving radiance is highest and contributes about 20% to the measured signal at the TOA for oligotrophic ocean scenes. Consequently, calibration uncertainty can not exceed about 0.5%. This requirement is challenging to reach even in laboratory conditions and can only be fulfilled using vicarious calibration (IOCCG, 2013).

Vicarious calibration (IOCCG, 2013; Mobley et al., 2021) means that calibration data are adjusted such that measured TOA radiance yields correct water-leaving radiance after atmospheric correction. It is assumed that the sensor calibration is optimal and only residual calibration errors need to be corrected. Two different types of vicarious calibration exist, system and radiometric. Radiometric vicarious calibration requires accurate measurements of atmospheric pressure, sky irradiance, and L_w as well as sunphotometer measurements at the surface at the time of the satellite measurement. These measurements are used to calculate I_t . Correction factors are then determined to match the predicted I_t to the satellite-measured I_t . In the system approach, the sensor and the atmospheric correction are combinedly calibrated. A system vicarious calibration is consequently specific for a certain sensor and atmospheric correction approach. For a system vicarious calibration, the general idea is that the atmospheric correction that would be applied for a certain ground pixel is reversed. Let's assume that the true water-leaving radiance L_w^t is the water-leaving radiance that is measured in-situ at this ground pixel location. By reversing the atmospheric correction, L_w^t can be propagated to I_t^t , the radiance that the satellite measures under given conditions. The ratio of this true satellite measurement to

the actual satellite measurement is the gain factor

$$g(\lambda) = \frac{I_t^t(\lambda)}{I_t(\lambda)}. \quad (2.14.3)$$

When a satellite measurement is multiplied by the gain factor, the correct water-leaving radiance is retrieved. Gain factors are determined from match-up comparisons of satellite and in-situ measurements. Usually, in-situ L_w are normalized for this purpose, because measurement conditions can differ between the satellite and the in-situ measurement. Furthermore, a band-pass correction factor has to be considered to account for different spectral responses of satellite and in-situ measurement.

Calibration of hyperspectral atmospheric sensors usually comprises pre-launch and in-flight calibrations correcting for polarization sensitivity, etalon spectral interference patterns, stray light, pixel-to-pixel gain, etc. (e.g., [Noël et al., 2003](#); [Veefkind et al., 2012](#); [Munro et al., 2016](#); [Dirksen et al., 2017](#)). Exact wavelength calibration is essential for DOAS-type retrievals that target high-frequency spectral structures. Which detector pixel measures which wavelength depends on the instrument's temperature. A spectral light source that generates light with well-known spectral lines is carried on-board for the wavelength calibration. All calibrations can be applied in the processing of the original level 0 data to generate level 1b data which is used as input for DOAS retrievals. The hyperspectral atmospheric sensors are usually not vicariously calibrated. Remaining residual calibration errors can be removed, at least partly, within the DOAS methods. Imperfect wavelength calibration, for example, is corrected by adjusting Fraunhofer lines to their known spectral positions as well as shift and squeeze methods, as described in section [2.11](#). Absolute radiometric requirements are not so high, since the DOAS method uses the ratio of I/I_0 , which are both measured by the same instrument.

3 Global diffuse attenuation derived from vibrational Raman scattering detected in hyperspectral backscattered satellite spectra

This chapter has been published in Optics Express in 2019, DOI 10.1364/OE.27.00A829 (Oelker et al., 2019). Notation has been changed slightly to be in accordance with the other parts of this document and cross-references have been added. Author contributions are as follows: I conceptualized the study, ran all PhytoDOAS retrievals, post-processed the data (including building of look-up-table and conversion to K_d), made all the RTM simulations for which I incorporated new parameterizations, wrote the first draft of this chapter and incorporated all revisions. Andreas Richter provided the DOAS software used for the retrievals. He gave many ideas for retrieval settings and helped discussing the results. Valuable discussions on retrieval settings and interpretation of results with Tilman Dinter also significantly contributed to the study. Vladimir Rozanov helped with RTM parameterizations. John P. Burrows and Astrid Bracher conceptualized the bigger scientific frame this study is part of. They gave ideas for the focus of this study through discussion of results. All co-authors revised the first draft of manuscript and the submitted and revised versions and gave valuable comments on presentation of results and their discussion as well as structure of the manuscript.

3.1 Introduction

Vibrational Raman scattering (VRS) in water is an inelastic scattering process occurring when photons interact with water molecules. It leads to filling-in of Fraunhofer lines (Vasilkov et al., 2002a) and a general spectral redistribution of the radiation in the ocean and in water-leaving radiance. VRS needs to be taken into account to accurately determine the underwater light field and to exploit this information in oceanic

remote sensing applications, especially if the spectral resolution of measurements is high. Not considering oceanic Raman scattering in radiative transfer modeling affects the determination of inherent-optical-properties (IOPs) using inversion models on hyperspectral in-situ data (Westberry et al., 2013) and atmospheric trace gas retrievals on hyperspectral top-of-atmosphere (TOA) radiances (Vountas et al., 2003). With upcoming ocean colour satellite missions planned to record radiances at higher spectral resolution (e.g., PACE, <https://pace.gsfc.nasa.gov/>), VRS is going to play an increasingly important role for satellite-based ocean color retrievals.

The VRS signal in water-leaving radiances carries information about the number of inelastic scattering events in the water and consequently the number of photons in the ocean. Since the VRS contribution from the atmosphere can be considered negligible (Vountas et al., 1998), the VRS signal in TOA radiances can be exploited to estimate light levels in the ocean (Dinter et al., 2015). Global data sets with good spatio-temporal resolution that characterize the underwater light field are needed for estimating primary productivity from satellite derived chlorophyll-a concentrations (Sathyendranath and Platt, 1993) and heat budget (Lewis et al., 1990). At present, planar photosynthetically available radiation (PAR) above surface, ultraviolet irradiance above surface, and diffuse attenuation coefficient at one wavelength are operationally provided from earth observations (Frouin et al., 2018). An independent global data set could be provided by exploiting the VRS signal in satellite-measured TOA radiances to spectrally derive the light availability and diffuse attenuation coefficient in the ocean.

Several hyperspectral satellite sensors designed for the retrieval of atmospheric trace gases have been used not only for quantifying the VRS contribution to TOA radiances and assessing its retrieval-influence but also for inferring information about environmental parameters. Using VRS, information on cloud pressure (Joiner et al., 2004) and ocean parameters linking VRS to chlorophyll-a concentration and light penetration depth (Joiner et al., 2004; Vountas et al., 2007; Bracher et al., 2009) have been derived.

These earlier studies investigated VRS in the ultraviolet (UV) region whereas more recent publications analyzed VRS in the visible region to directly investigate the light used for photosynthesis. Dinter et al. (2015) derived the light availability in the ocean from VRS as the depth and wavelength integrated scalar irradiance in the wavelength range from 390 to 444.5 nm. Through coupled ocean-atmosphere radiative transfer modeling, they related the VRS signal in TOA radiances to light availability in the ocean which was built into a look-up-table (LUT). Using Differential Optical Absorption Spectroscopy (DOAS), VRS was first retrieved from TOA radiances measured by the Scanning Imaging Absorption Spectrometer for Atmospheric Chartography (SCIAMACHY) and converted

to the amount of light in the ocean using the LUT. As evaluation of their light availability product, the diffuse attenuation coefficient is additionally determined using radiative transfer modeling. For one month of data, it was compared to the diffuse attenuation coefficient at a wavelength of 490 nm $K_d(490)$ from the merged ocean color product GlobColour (<http://www.globcolour.info/>).

The connection between phytoplankton biomass and the VRS signal is more straightforward in the visible than in the UV, since this is the spectral region where chlorophyll-a absorbs. VRS retrieved in the visible with DOAS from TOA radiances measured by SCIAMACHY has been used as a proxy for the light penetration depth to calculate chlorophyll-a concentrations of different phytoplankton functional types (PFT) (Losa et al., 2017a).

SCIAMACHY measurements are only available until April 2012. Newer satellite sensors with improved temporal coverage and spatial resolution can be explored. The Ozone Monitoring Instrument (OMI) (Levelt et al., 2006) provides data with significantly improved spatial resolution and daily global coverage from 2004 to date. The Global Ozone Monitoring Experiment 2 (GOME-2) (Munro et al., 2016) provides global coverage within one and a half days and long data time series being an operational mission with the first sensor launched in 2006 on Metop-A, the second sensor in 2012 on Metop-B, and the third sensor in 2018 on Metop-C. So far, the VRS signature has not been explicitly investigated in TOA radiances measured by OMI or GOME-2, especially not in the visible wavelength region. For both sensors, spectral structures caused by VRS in TOA radiances were pointed out to be interfering with atmospheric signals in various trace gas DOAS retrievals although often not explicitly accounted for (Vrekoussis et al., 2009; Lerot et al., 2010; Richter et al., 2011; Peters et al., 2014). Merely, vibrational and rotational Raman scattering have been simultaneously included in a model in the UV to retrieve cloud pressure for OMI (Joiner and Vasilkov, 2006). Like SCIAMACHY, OMI and GOME-2 can potentially be used for phytoplankton functional type retrievals. DOAS retrievals on hyperspectral satellite data generally require an estimation of the light penetration depth to calculate PFT chlorophyll-a concentrations. Adequate retrieval of VRS from OMI and GOME-2 are therefore required. The approach developed by Dinter et al. (2015) to derive the amount of light in the ocean from VRS can also be transferred to other sensors such as OMI and GOME-2. Their study was a feasibility study showing one month of results. Combining VRS from different satellite sensors could give a time series of global light availability since 2002.

This study therefore has two objectives. First it is investigated, if VRS can be found in TOA radiances recorded by OMI and GOME-2 and be adequately retrieved using DOAS. Second it is investigated, if and how a VRS derived product, in this case the diffuse

attenuation coefficient, can be merged from different hyperspectral satellite sensors. The study focuses on the diffuse attenuation coefficient as VRS derived product instead of the light availability. For this quantity, better possibilities exist to compare with established ocean color products from multispectral sensors. It is also easier to intercompare diffuse attenuation coefficients from different satellite sensors with differing overpass times and viewing geometries, since the diffuse attenuation coefficient is regarded as a quasi-inherent optical property of ocean water (Baker and Smith, 1980).

Diffuse attenuation coefficients are calculated from VRS retrieved from TOA radiances measured by SCIAMACHY, OMI and GOME-2 closely following the approach presented by Dinter et al. (2015). The quality of the resulting diffuse attenuation coefficient product is evaluated by comparison with the diffuse attenuation coefficient at 490 nm provided by the Ocean Colour Climate Change Initiative (OC-CCI) data set for nearly one year of data. The same time series data are explored in different Longhurst biogeochemical provinces to illustrate their broader comparability and possibility for a merged product.

3.2 Instrumentation and Methods

3.2.1 Satellite Sensors OMI, SCIAMACHY, and GOME-2

VRS signals are retrieved from three different hyperspectral satellite sensors, the Ozone Monitoring Instrument (OMI), the Scanning Imaging Absorption Spectrometer for Atmospheric Chartography (SCIAMACHY), and the Global Ozone Monitoring Experiment 2 (GOME-2) on Metop-A. All three sensors are on satellites in sun-synchronous orbits and have the mission goal to monitor atmospheric trace gases. GOME-2 and SCIAMACHY have a more similar instrument design compared to OMI, since they are both whisk-broom instruments whereas OMI is a push-broom sensor.

OMI (Levelt et al., 2006) onboard the satellite Aura operated by NASA was launched on 15 July 2004 and is still in operation. It has a local overpass time at the equator at 1:45 pm in ascending node. OMI is designed as a nadir-viewing imaging spectrometer with 60 across track ground pixels that are measured simultaneously. Ground pixel size is 13 km by 24 km at nadir becoming significantly larger at the swath edges. With a swath of 2600 km, OMI achieves daily global coverage. It records spectra in the UV/Vis from 264-504 nm. Only level 1b data (version 003) from the visible channel (350 to 500 nm) were used for the VRS retrievals. The spectral resolution of this VIS channel is 0.63 nm. OMI measures the extraterrestrial irradiance spectrum and the upwelling earthshine spectrum. Daily measured OMI irradiance spectra are of poor quality due to low signal. For the OMI

retrieval, a solar irradiance spectrum averaged over all irradiance measurements recorded in the year 2005 was used as reference (OMI, 2005).

The ESA instrument SCIAMACHY (Bovensmann et al., 1999) onboard ENVISAT collected data from 2002 until April 2012. Local overpass time at the equator was 10:00 am in descending node. The instrument had a spatial resolution of 30 km by 60 km for nadir ground pixels. With a swath width of 960 km and alternating nadir-limb mode, global coverage was reached within six days. Level 1b data (version 7.04.) from cluster 15 (424 to 525 nm) of channel 3 with a spectral resolution of 0.47 nm were used for the VRS retrievals. SCIAMACHY daily recorded solar spectral irradiances.

The first GOME-2 (Munro et al., 2016) is hosted by the Metop-A satellite operated by EUMETSAT. It was launched in 2006 providing data from January 2007 until date. The spatial resolution was 40 km by 80 km for nadir ground pixels until 15 July 2013 when it was changed to 40 km by 40 km at reduced coverage. The sensor has a swath width of 1920 km and reaches global coverage in 1.5 days. Local overpass time at the equator is 9:30 am in descending node. Level 1b data (version 5.3) from visible channel 3 (397 to 604 nm) were used for the retrieval which have a spectral resolution of 0.51 nm. Solar spectral irradiances are recorded daily.

Ground pixel selection

Only ground pixels with solar zenith angle (SZA) smaller than 70° were used. Reflectance thresholds and operationally provided cloud products were used to filter cloud, glint, and ice affected ground pixels. An average reflectance R over the wavelength window used in the VRS fit was calculated as $R = \pi I_{\text{TOA}} / (F_0 \cdot \cos(\text{SZA}))$ using the spectrally averaged TOA intensity I_{TOA} and spectrally averaged solar irradiance F_0 as input. Reflectance thresholds were set to around 0.3. OMI and GOME-2 data were additionally cloud filtered using the O₂-O₂ (Acarreta et al., 2004) and the FRESCO (Munro et al., 2016) cloud products, respectively. Cloud fractions were set to 0.05. Backscans were excluded in SCIAMACHY and GOME-2 data. OMI suffers from a row anomaly which varies with time (<http://projects.knmi.nl/omi/research/product/rowanomaly-background.php>). It is assumed to be caused by a blocking object in front of the nadir port leading to changes in radiation level and wavelength shift. It first appeared in June 2007 affecting CCD rows 53 and 54 (0-based). From May 2008 on, the number of affected rows increases. Operationally provided flagging was used to filter affected ground pixels (Schenkeveld et al., 2017).

Observation period

The year 2007 is chosen as time period for our investigations. This year appears to be optimal for an intercomparison of the three hyperspectral sensors since all three sensors were measuring and OMI measurements are not severely affected by the row anomaly yet. GOME-2 measurements do not exist for the full month of January. For simplicity, the entire analysis for all three sensors was performed for 01 February 2007 to 31 December 2007.

3.2.2 Vibrational Raman scattering

Vibrational Raman scattering occurs in liquid water when vibrational modes of the water molecules are excited by inelastic scattering with photons. The wavelength of the photon is shifted in this process. In this work, we considered only the shift to a longer wavelength (Stokes line) around which radiation is emitted in a broad band. Based on experimental work by Walrafen (1967), Haltrin and Kattawar (1993) formulated a function to describe the broad band VRS emission by a combination of four Gaussian functions. In terms of wavelength, the shift and broad band width is wavelength dependent. In the spectral range from 400 nm to 700 nm, which phytoplankton use for photosynthesis, the light that has been Raman scattered in water originates from the wavelength region 352 to 567 nm and the emission band width ranges between 31 and 41 nm. This study evaluated the VRS emission in a spectral window from 450 to 497 nm which corresponds to an excitation wavelength range from 390 to 426 nm.

VRS leads to filling-in of Fraunhofer lines. It can be treated as a pseudo-absorber. Following Vountas et al. (2003), a VRS pseudo-absorption, also called VRS compensation spectrum σ_{VRS} , can be defined as

$$\sigma_{\text{VRS}} = \ln(I^+/I^-) \quad (3.2.1)$$

where I^+ and I^- are modeled TOA radiance spectra from a model run including VRS processes and excluding VRS processes, respectively. The spectral signature of this pseudo-absorption can be found in hyperspectral TOA radiances measured by satellites and can be retrieved using Differential Optical Absorption Spectroscopy.

3.2.3 Differential Optical Absorption Spectroscopy

Differential Optical Absorption Spectroscopy (DOAS) is a technique commonly used for the retrieval of atmospheric trace gases by distinguishing their high frequency absorption

features (Perner and Platt, 1979) (see section 2.11 for details). The DOAS method has been extended for investigating oceanic parameters. The amount of VRS (Vountas et al., 2007), light availability (Dinter et al., 2015), chlorophyll-a concentration of different phytoplankton functional types (Bracher et al., 2009; Sadeghi et al., 2012a), and chlorophyll-a fluorescence (Wolanin et al., 2015b; Joiner et al., 2016) have been successfully retrieved from SCIAMACHY and partly (chlorophyll-a fluorescence) from GOME-2 measurements.

Starting from Beer-Lambert's law, the optical depth τ is separated into broadband and high frequency components by introducing a low-order polynomial.

$$\ln(I_0/I) = \tau = \sum_j \sigma'_j S_j + \sum_i b_i \lambda^i \quad (3.2.2)$$

where I_0 is a background spectrum, e.g., extraterrestrial solar spectrum, I is a measured intensity, e.g., TOA radiance, and σ'_j are differential absorption cross sections of j components in the observed system. The differential cross section is only the high frequency component of the cross section. The broadband component is included in the polynomial. All relevant absorbing atmospheric gases and absorbing ocean constituents plus inelastic scattering processes in the atmosphere and ocean are considered. In the DOAS fit, Equation (3.2.2) is solved for the fit factors S_j of j components and the polynomial coefficients b_i at multiple wavelengths λ using a Levenberg-Marquardt least-squares minimization. The polynomial accounts for broadband signals such as elastic scattering and absorption by colored dissolved organic matter (CDOM) and suspended particulate matter. Retrieved S_j of target components are converted to physical values, e.g. trace gas concentration, by comparison with radiative transfer model (RTM) simulations. Theoretical TOA radiances are modeled using an RTM and the same DOAS fit is performed on these.

In this study, the diffuse attenuation coefficient in the ocean was derived from the VRS fit factor by comparison with theoretical VRS fit factors from modeled data. Details on the comparison and radiative transfer modeling are elaborated below. Settings for the VRS DOAS fit were chosen based on the latest SCIAMACHY VRS DOAS fit results as in (Losa et al., 2017a). Cross sections for following components were included in the DOAS VRS fit

- absorption cross sections for ozone (O_3) (Serdyuchenko et al., 2014), nitrogen dioxide (NO_2) (Vandaele et al., 1998), water vapor (H_2O) (Rothman et al., 2013), oxygen dimer (O_4) (Thalman and Volkamer, 2013), glyoxal (CHOCHO) (Volkamer et al., 2005).
- pseudo-absorption cross section for rotational Raman scattering (RRS) accounting

for the Ring effect (Grainger and Ring, 1962) in the atmosphere. RRS pseudo-absorption cross sections were calculated on the same principle as the VRS pseudo-absorption cross section (Vountas et al., 1998).

- pseudo-absorption cross section for VRS that was calculated from modeled case-1 TOA radiances for a chlorophyll-a concentration of 0.1 mg/m^3 and a SZA of 40° .
- ocean weighting function wf_{oc} defined as in Dinter et al. (2015) calculated from case-1 TOA radiances for a SZA of 40° . This weighting function describes the spectral change in TOA radiances when the chlorophyll-a concentration in the model scenario changes from 0.1 mg/m^3 to 0.11 mg/m^3 . It combinedly accounts for phytoplankton and liquid water absorption.

Although no weighting function DOAS (WF-DOAS) was used in this study, the ocean weighting function from Dinter et al. (2015) was kept as cross section in the retrieval. Fit factors for wf_{oc} were not used for deriving any oceanic quantities, so their magnitude was not of importance in this study. The advantage of using wf_{oc} is that it combines the effect of absorbing oceanic constituents and liquid water in a single spectrum, avoiding the fit of multiple correlating absorption cross sections.

Pseudo-absorption cross sections for RRS and VRS as well as the ocean weighting function were calculated (see section 3.2.5) for each OMI CCD row separately and fitted for each row specifically. The row-specific solar spectrum was used as background spectrum for each CCD row. Daily recorded solar spectra were used as background spectra for GOME-2 and SCIAMACHY (Azimuth Scan Mirror).

As in Losa et al. (2017a), instrumental artifacts were characterized by analyzing residual structures over the Sahara region (Soppa et al., 2016b). A DOAS fit was made over a small region in the Sahara (2°E to 6°E , 23.5°N to 34.5°N) where no VRS signal is expected. In this pre-fit, only atmospheric components were considered and the resulting residuals were analyzed using a principal component analysis (PCA). The first two eigenvectors from this PCA were calculated on a monthly basis and included as cross sections in the DOAS fit. This method was only used for SCIAMACHY and GOME-2. No correction of instrumental effects through eigenvectors was used for OMI. As a test, the first two eigenvectors from a PCA over the Sahara region were calculated as for SCIAMACHY and GOME-2 for each CCD row separately and included in the VRS fit, however, no significant improvement of the fit was obtained. The global VRS fit factors calculated with and without eigenvectors had a correlation of $r=0.99$. To reduce the amount of retrievals and computation time, we decided not to include eigenvectors in the VRS fit for OMI.

The wavelength window for the fit was set to 450 nm to 497 nm which is slightly larger than in [Losa et al. \(2017a\)](#) and significantly shorter than in [Dinter et al. \(2015\)](#). The upper boundary is limited by OMI's visible channel. The fit window was set the same for all three sensors, since this simplifies comparison between the sensors and merging of the data sets.

The only significant difference in the DOAS settings used here in comparison to [Losa et al. \(2017a\)](#) is that a second order polynomial was used instead of a third order polynomial. Due to the modifications in the RTM settings for calculating the pseudo-absorption cross sections (see section [3.2.5](#)), a second order polynomial quickly proved to be more optimal.

3.2.4 Connection between VRS, light availability, and diffuse attenuation

This study exploits the VRS signal to derive the light availability in the ocean. An increased number of photons in the ocean leads to an increased number of inelastic scattering events. Since the VRS contribution from the atmosphere is negligible ([Vountas et al., 1998](#)), the VRS signal in the TOA radiances is closely linked to the light availability in the ocean. This section summarizes the approach presented in [Dinter et al. \(2015\)](#) on how to derive light availability and diffuse attenuation coefficient from VRS. They formulated a relationship between the change in VRS signal at TOA and the amount of radiation energy in the ocean. For a given wavelength region, the amount of radiation energy in the ocean \bar{u} is the depth and wavelength integrated scalar irradiance \bar{E}_o divided by the speed of light c given as

$$\bar{u} = \frac{1}{c} \bar{E}_o = \frac{1}{c} \int_0^H \int_{\lambda_1}^{\lambda_2} E_o(z, \lambda) dz d\lambda. \quad (3.2.3)$$

The integration is performed from the surface $z = 0$ to the ocean bottom $z = H$. We followed their approach to connect the VRS signal, retrieved as VRS fit factor S_{VRS} using DOAS, to \bar{E}_o . We established a look-up-table (LUT) relating \bar{E}_o to S_{VRS} using a radiative transfer model. To derive such a function,

$$\bar{E}_o = f(S_{\text{VRS}}), \quad (3.2.4)$$

two types of radiative transfer calculations are needed. On the one hand, TOA radiances need to be calculated to obtain S_{VRS} . On the other hand, in-water flux calculations are needed to obtain \bar{E}_o . A DOAS fit was performed on the modeled TOA radiances to get the theoretical VRS fit factor for a certain ocean scenario. For the same ocean scenario, in-

water fluxes were calculated to give \bar{E}_o . For this ocean scenario, a single point in the LUT was obtained. Various ocean scenarios were modeled to build up the whole LUT covering situations found in the global oceans. Most of the global ocean can be considered as case-1 waters where chlorophyll-a is the main driver for the underwater light field (Morel and Prieur, 1977). A range of typical chlorophyll-a concentrations was therefore used to generate the LUT. As shown in (Dinter et al., 2015), \bar{E}_o depends strongly on SZA. Model runs were made for a variety of SZAs giving a two-dimensional LUT $\bar{E}_o(S_{\text{VRS}}, \text{SZA})$. Retrieved DOAS VRS fit factors together with the corresponding SZA for each satellite ground pixel were then converted into a global \bar{E}_o map by interpolating the LUT.

It is difficult to evaluate the quality of the resulting \bar{E}_o data set, since no comparable ocean color satellite product for the depth integrated scalar irradiance in the investigated wavelength range from 390 to 426 nm exists. However, the diffuse attenuation coefficient at 490 nm $K_d(490)$ is often retrieved from ocean color satellite data. It is closely linked to the light availability in the ocean and was thus used for comparison in this study.

The diffuse attenuation coefficient can be calculated as a mean value over distant depths z_1 and z_2 from the change in downwelling irradiance $E_d(z)$ (Lee et al., 2005a)

$$K_d(z_1 \longleftrightarrow z_2, \lambda) = \frac{1}{z_2 - z_1} \ln \left(\frac{E_d(z_1, \lambda)}{E_d(z_2, \lambda)} \right). \quad (3.2.5)$$

which gives $K_d(z_{90}, \lambda) = 1/z_{90}(\lambda)$ for the attenuation depth z_{90} defined as the depth at which the downwelling irradiance has reduced to 1/e of its subsurface value (Gordon and McCluney, 1975). From the flux calculations, $K_d(z_{90}, \lambda)$ was calculated for all modeled case-1 scenarios. As for \bar{E}_o , a LUT relating K_d with S_{VRS} and SZA was established. Since the S_{VRS} were retrieved in a certain wavelength range (450 - 497 nm), corresponding diffuse attenuation coefficients were averaged over the excitation wavelength range $K_d(z_{90}, \lambda_{\text{ext}})$, $\lambda_{\text{ext}} = 390 - 426$ nm. The relationship $K_d(z_{90}, \lambda_{\text{ext}}) = f(S_{\text{VRS}}, \text{SZA})$ was used to create global $K_d(z_{90}, \lambda_{\text{ext}})$ maps which were compared to $K_d(490)$ products from ocean color satellites. In the following, the dependence on z_{90} was omitted for brevity.

3.2.5 Radiative transfer model simulations

Modeled TOA radiances were used to calculate VRS pseudo-absorption cross sections and to perform comparative DOAS retrievals whereas underwater fluxes were used to calculate the light availability and diffuse attenuation coefficient. The model should accurately describe radiative transfer processes, especially inelastic processes, in the atmosphere and in the ocean at high spectral resolution matching the spectral resolution of the satellites of

about half a nanometer. We used the ocean-atmosphere coupled RTM SCIATRAN (Blum et al., 2012; Rozanov et al., 2014, 2017) version 4.0.8 to model various case-1 scenarios. The theoretical description of VRS is based on the above described formulation of VRS by Haltrin and Kattawar (1993). Correct implementation of the VRS in SCIATRAN has been evaluated by comparison with other radiative transfer models and experimental data from satellite, ship-based, and underwater instruments (Rozanov et al., 2017).

TOA radiances were modeled for 23 different case-1 scenarios with chlorophyll-a concentrations ranging between 0 and 30 mg/m³. A standard case-1 model was used based on Morel and Maritorena (2001) parameterization for chlorophyll and CDOM absorption. Model settings follow Dinter et al. (2015) with some changes:

- a more recent clear water absorption spectrum by Mason et al. (2016) was used.
- particle scattering was described using a wavelength-independent Fournier-Forand scattering function as in the widely used Hydrolight case-1 water model (Mobley and Sundman, 2013). The phase function was parameterized using the backscattering ratio as input (Mobley et al., 2002). The change in backscattering ratio with chlorophyll-a concentration is not robust, but as a first estimate for our global open ocean retrieval, we used the relationship between backscattering ratio and chlorophyll-a concentration found for case-1 stations by Twardowski et al. (2001). The relationship between mass-specific scattering coefficient and chlorophyll-a was taken from Gordon and Morel (1983).
- instead of an aerosol-free atmosphere, a background maritime aerosol was assumed with aerosol optical depth (AOD) of 0.1 at 550 nm. AOD was taken from annual mean AOD measured over the tropical South East Pacific by MODIS-Aqua (Remer et al., 2008).
- atmospheric profiles for temperature, pressure, and ozone were set according to the mid-latitude standard atmosphere model (Sinnhuber et al., 2009). As default, results for April and latitude 45°N were chosen arbitrarily.

Instrument-specific extraterrestrial solar spectra were used for each sensor for the TOA radiance calculations, since spectral alignment is very important for the DOAS retrieval. For SCIAMACHY, a solar irradiance measured by SCIAMACHY was used (Skupin et al., 2005). For OMI, an average over solar irradiance spectra recorded by OMI in the year of 2005 was used as mentioned above (OMI, 2005). For GOME-2, SCIATRAN calculations were made at high spectral resolution of 0.01 nm using a Kurucz solar spectrum (Chance and Kurucz, 2010). Resulting radiances were convolved to instrument spectral resolution

using the GOME-2 slit function. Underwater fluxes were calculated instrument-unspecific at a spectral resolution of 0.5 nm also using the Kurucz solar spectrum since they should be insensitive to the exact spectral resolution.

Geometry settings were chosen as follows:

- TOA radiances were modeled for 13 different SZAs, i.e. 5° steps between 15° and 70°.
- viewing zenith angle (VZA) was set instrument-specific. For SCIAMACHY and GOME-2, a nadir-viewing geometry was chosen $VZA = 0^\circ$. For OMI, the VZA of the different CCD rows was determined by averaging for each CCD row the VZA as recorded in the level 1 data for globally distributed ground pixels.
- relative azimuth angle was set to 90°.

DOAS fit settings for the retrieval of theoretical VRS fit factors from the modeled TOA radiances were the same as for the retrieval on satellite radiances (see section 3.2.3) except for atmospheric cross sections. Only ozone was included as trace gas in the modeled atmosphere, so only the ozone absorption cross section was used when fitting modeled TOA radiances.

3.2.6 Retrieval sensitivity

The LUT used to convert VRS fit factors to $K_d(\lambda_{\text{ext}})$ was kept simple with SZA as only additional input parameter. In the following, the sensitivity of our retrieval with respect to model assumptions on AOD and CDOM absorption was investigated. Four new sets of model simulations were calculated. In two of these sets, AOD was increased or reduced to 0.2 or 0.05 at 550 nm, respectively. The other two sets were calculated with increased or reduced CDOM absorption. The coefficient for CDOM absorption in the Morel and Maritorena (2001) parameterization was changed from 0.2 to 0.4 or 0.1, respectively. VRS retrieval as described in section 3.2.3 was performed for each of these four synthetic TOA radiance sets. Retrieved VRS fit factors were then converted to $K_d(\lambda_{\text{ext}})$ using the LUT. For each set, resulting $K_d(\lambda_{\text{ext}})$ for each scenario were compared to the expected $K_d^{\text{exp}}(\lambda_{\text{ext}})$ in this scenario calculated from flux simulations with the four modified settings, i.e. higher or lower AOD and higher or lower CDOM absorption. Figure 3.2.1 shows the relative deviation of derived $K_d(\lambda_{\text{ext}})$ from expected $K_d^{\text{exp}}(\lambda_{\text{ext}})$, $(K_d(\lambda_{\text{ext}}) - K_d^{\text{exp}}(\lambda_{\text{ext}}))/K_d^{\text{exp}}(\lambda_{\text{ext}})$, as function of $K_d^{\text{exp}}(\lambda_{\text{ext}})$. The analysis is shown in a $K_d^{\text{exp}}(\lambda_{\text{ext}})$ range from 0 to 0.15 m^{-1} , since our retrieval is only applicable in this range due to too low VRS signals for higher attenuating waters as discussed in section 3.4. For most SZAs, an increase in AOD leads to an overestimation of $K_d^{\text{exp}}(\lambda_{\text{ext}})$ whereas a reduction leads to an underestimation. The

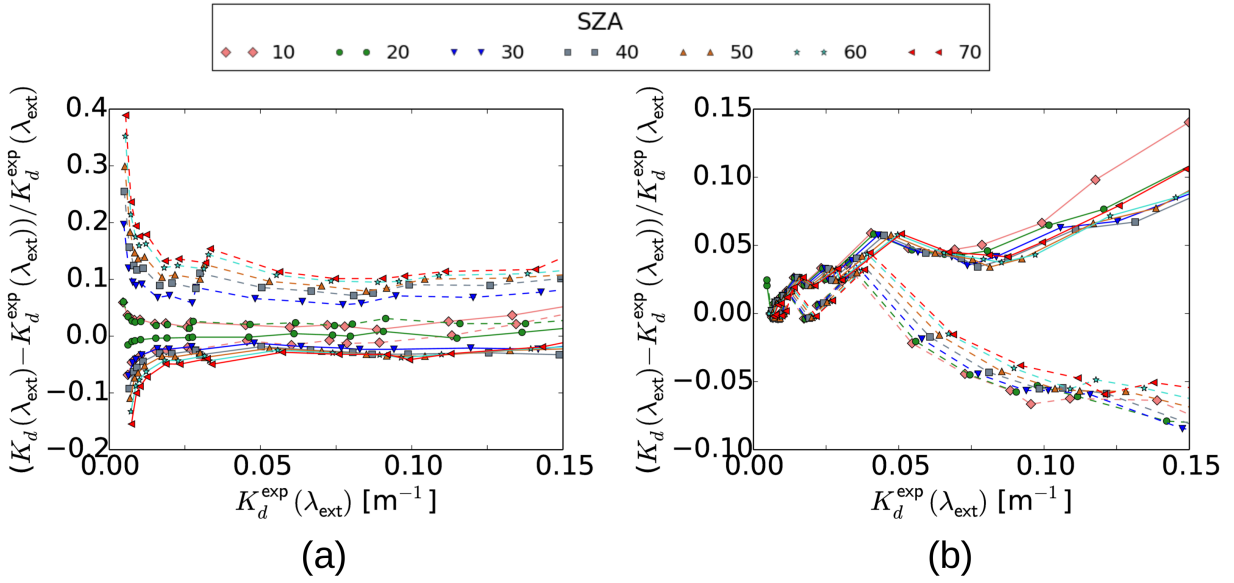


Figure 3.2.1: Retrieval sensitivity analysis: relative deviation of derived $K_d(\lambda_{\text{ext}})$ from expected $K_d^{\text{exp}}(\lambda_{\text{ext}})$, $(K_d(\lambda_{\text{ext}}) - K_d^{\text{exp}}(\lambda_{\text{ext}})) / K_d^{\text{exp}}(\lambda_{\text{ext}})$, in modeled open ocean scenarios with reduced (solid lines) and increased (dashed lines) (a) AOD and (b) CDOM absorption. Compared to the average global open ocean scenario used for the retrieval and described in section 3.2.5, AOD and CDOM absorption were reduced and increased by a factor of two. Deviations are shown for a range of SZAs.

retrieval is especially sensitive to AOD when $K_d^{\text{exp}}(\lambda_{\text{ext}}) < 0.01 \text{ m}^{-1}$. For these extremely clear waters, deviations are significantly larger than in the range 0.01 m^{-1} to 0.15 m^{-1} . Here, deviations from $K_d^{\text{exp}}(\lambda_{\text{ext}})$ are nearly constant and less than -5% in case of reduced AOD and less than $+20\%$ in case of increased AOD. Higher or lower CDOM absorption in the RTM simulations leads to underestimated or overestimated $K_d^{\text{exp}}(\lambda_{\text{ext}})$ for most scenarios, respectively. Deviations increase with increasing $K_d^{\text{exp}}(\lambda_{\text{ext}})$. In the investigated $K_d^{\text{exp}}(\lambda_{\text{ext}})$ range, derived $K_d(\lambda_{\text{ext}})$ deviate from $K_d^{\text{exp}}(\lambda_{\text{ext}})$ by less than $+15\%$ in case of a reduced CDOM absorption and between -10% and $+5\%$ in case of an increased CDOM absorption.

The retrieval sensitivity to AOD and CDOM absorption is rather low, but not negligible. Regarding AOD, the method could be improved by adding another dimension to the LUT and taking AOD from a data base as third input parameter. Wolanin et al. (2015a) calculated the average polynomial, resulting from the DOAS fit, to evaluate the brightness of each ground pixel. They used this estimate of all broadband effects as input parameter in a LUT. This approach could be implemented for the method presented here to reduce the sensitivity to broadband effects such as AOD and CDOM absorption. We decided to keep the LUT simple, since it turned out that the noise introduced by mismatches between

model scenarios and observed scenes is a secondary effect. As discussed in section 3.4, spectral features caused by instrumentation have a larger effect on the results.

Other model settings additionally influence the retrieval. Further sensitivity analyses on the choice of phytoplankton spectra and vertical profiles of chlorophyll-a concentration can be found in Dinter et al. (2015). The approaches are not one-to-one comparable, but the sensitivity analyses presented there give an impression what to expect in our particular approach.

3.2.7 OC-CCI as reference data set

Diffuse attenuation coefficients were taken from the release version 3.1 of the OC-CCI (Sathyendranath et al., 2018) of the European Space Agency (<http://www.esa-oceancolour-cci.org/>) for evaluating the quality of the diffuse attenuation coefficients derived from VRS fit factors. OC-CCI provides the diffuse attenuation coefficient at 490 nm merged from three different multispectral sensors MODIS, MERIS, and SeaWiFS.

Since OC-CCI diffuse attenuation coefficients are given at a wavelength of 490 nm $K_d^{\text{OC}}(490)$, diffuse attenuation coefficients from the OC-CCI data set were converted to the wavelength range of our retrieval output. SCIATRAN flux calculations were performed for wavelengths up to 500 nm to investigate K_d 's wavelength dependence. The modeled diffuse attenuation coefficient in the excitation wavelength region $K_d^{\text{mod}}(\lambda_{\text{ext}})$ was related to the modeled diffuse attenuation coefficient at 490 nm $K_d^{\text{mod}}(490)$. $K_d^{\text{mod}}(490)$ was calculated by integrating fluxes between 485 nm and 495 nm. A 10 nm integration width was chosen here to best resemble the band width of multispectral ocean color sensors used to calculate $K_d^{\text{OC}}(490)$. A linear relationship between $K_d^{\text{mod}}(490)$ and $K_d^{\text{mod}}(\lambda_{\text{ext}})$ was found,

$$K_d^{\text{mod}}(\lambda_{\text{ext}}) = a \cdot K_d^{\text{mod}}(490) + b, \quad (3.2.6)$$

for all modeled SZA with r^2 values above 0.99. Averaging over the slope and intercept found by linear least squares regression for each SZA gave $\bar{a} = 1.30 \pm 0.02$ and $\bar{b} = -0.018 \pm 0.002 \text{ m}^{-1}$ with standard deviations as uncertainties. The relationship was used to wavelength-convert the OC-CCI $K_d^{\text{OC}}(490)$ product to $K_d^{\text{OC}}(\lambda_{\text{ext}})$ through

$$K_d^{\text{OC}}(\lambda_{\text{ext}}) = \bar{a} \cdot K_d^{\text{OC}}(490) + \bar{b}. \quad (3.2.7)$$

Since we modeled different case-1 ocean scenarios to change the diffuse attenuation in the model, the impact of the change in chlorophyll concentrations can clearly be seen in the wavelength conversion function. For simulations with low diffuse attenuation, in

our model a scenario with low chlorophyll content, the diffuse attenuation coefficient at 490 nm is larger than the diffuse attenuation coefficient in the excitation wavelength range. With increasing chlorophyll concentration this difference becomes less until it is reversed. For high chlorophyll concentrations, the diffuse attenuation coefficient in the excitation wavelength range is larger than at 490 nm due to stronger absorption by chlorophyll at shorter wavelengths. Other studies derived similar relationships between $K_d(490)$ and, e.g., $K_d(412)$ from experimental measurements of the spectral diffuse attenuation coefficient. Linear relationships between $K_d(490)$ and $K_d(412)$ were estimated with a slope around 1.7 for measurements from a variety of different water types (Austin and Petzold, 1986, 1990; Wang et al., 2008a). Regional studies predict lower slopes closer to the value found here around 1.28 for the Arctic (Wang and Zhao, 2014) and 0.95 for the Southern Bay of Bengal (Ashraf et al., 2013). Generally, differences in these studies show that relating $K_d(490)$ and $K_d(\lambda_{\text{ext}})$ through a linear relationship is too simple to globally describe all open ocean cases. The shape and magnitude of the specific absorption of the phytoplankton in the water will certainly change the relation between $K_d(490)$ and $K_d(\lambda_{\text{ext}})$. The wavelength conversion found here is merely an average value for a standard case-1 scenario which adds uncertainty in the comparison between $K_d(\lambda_{\text{ext}})$ from hyperspectral sensors and from OCCI. This stresses the importance of directly determining diffuse attenuation coefficients from satellite measurements over a wider spectral range and not just at 490 nm.

3.3 Results

Here, we present the results of the DOAS fits and diffuse attenuation coefficient derivation. A separate discussion follows in section 3.4.

3.3.1 Global vibrational Raman scattering DOAS fit

Fit residuals and global distributions of VRS fit factors were analyzed for May 2007 as a first quality check of the DOAS fit. Examples of the differential optical depth (second term in Equation (3.2.2)) for VRS and the ocean weighting function accounting for absorption by phytoplankton and liquid water are shown in Figure 3.3.1. Results are shown for ground pixels from the South Pacific Gyre where a strong VRS signal is expected. The residual has about the same magnitude as the reference indicating that the signals from VRS and other ocean parameters are found moderately well by the DOAS fit in the TOA radiances. The mean absolute residual of all cloud-free pixels in a small region in the South Pacific Gyre (22-30°S, 115-125°E) during the month of May 2007 amounts to 0.0009 for SCIAMACHY,

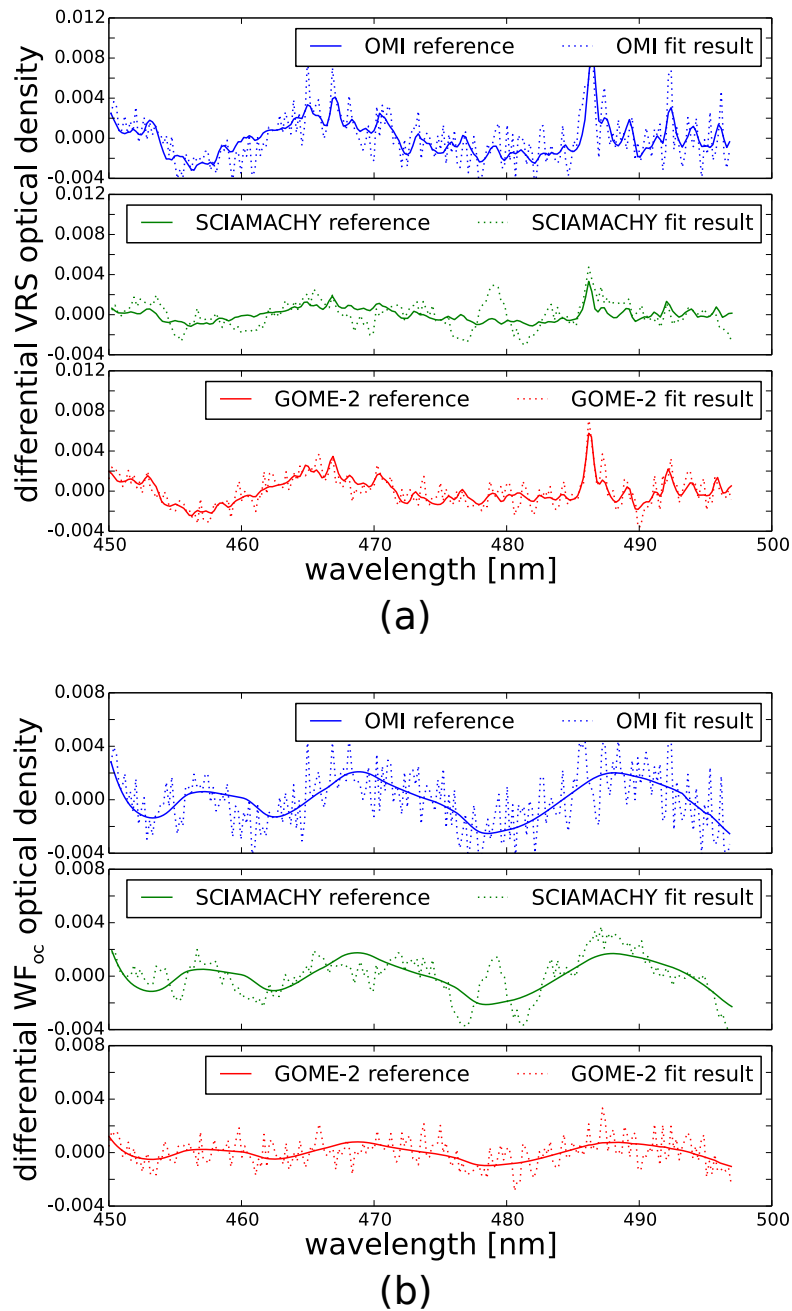


Figure 3.3.1: Resulting differential optical depth for (a) VRS and (b) other oceanic parameters from the spectral fit on OMI (upper panel), SCIAMACHY (center panel), and GOME-2 (lower panel) TOA radiances. The solid lines are the references which are the differential cross sections multiplied by the retrieved fit factor for the corresponding ground pixel. The dashed line is the retrieval result showing the reference plus the overall fit residual. Results are from ground pixels in the South Pacific Gyre obtained on 19 May 2007 (OMI: 24.29°S, 235.03°E; SCIAMACHY: 24.25°S, 235.03°E; GOME-2: 24.68°S, 235.34°E).

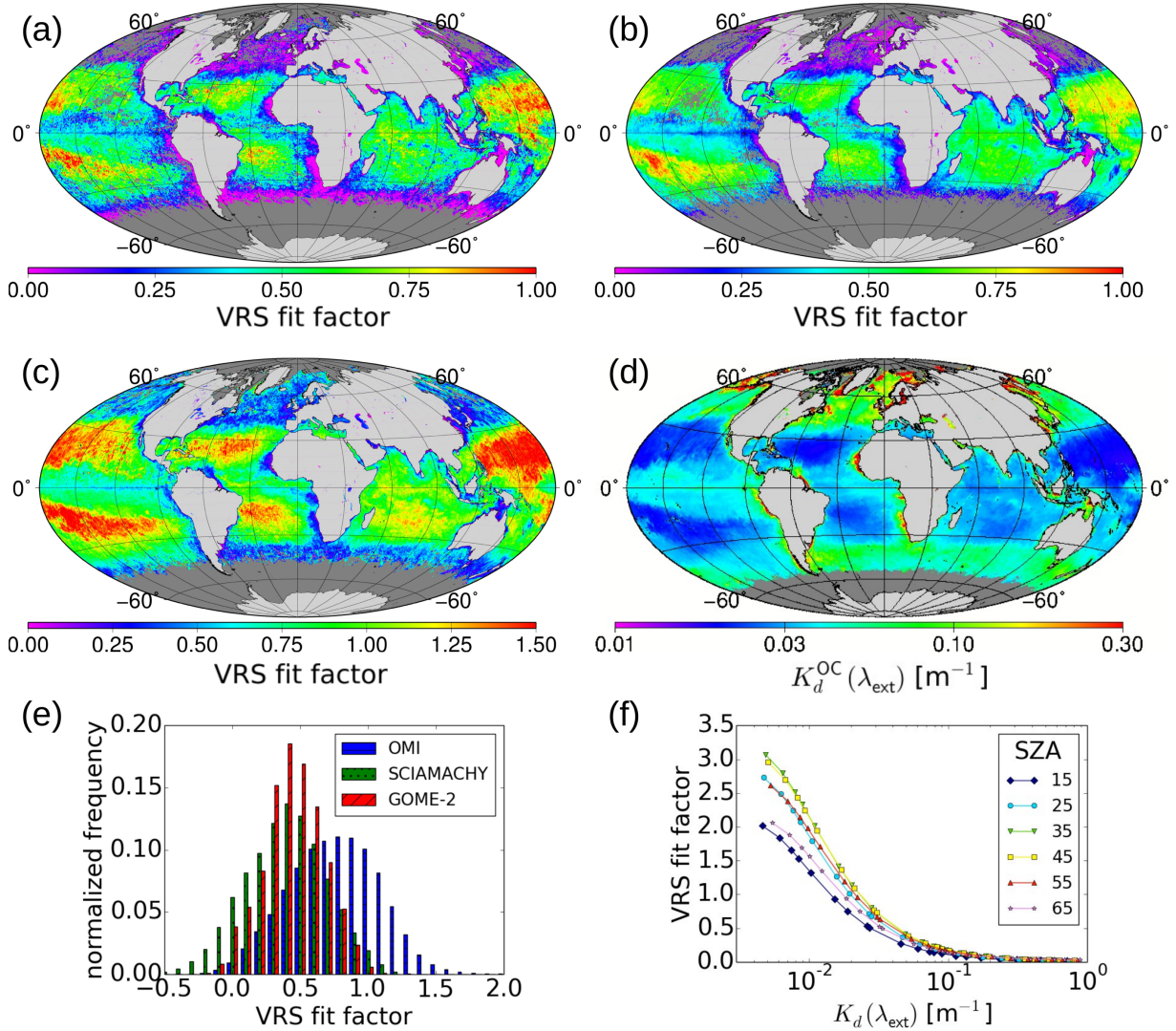


Figure 3.3.2: Global VRS fit factors retrieved using DOAS on TOA radiances from (a) SCIAMACHY, (b) GOME-2, (c) OMI for May 2007. (d) $K_d^{OC}(\lambda_{ext})$ from OC-CCI. (e) Global normalized frequency of VRS fit factors excluding land and coast pixels for May 2007 for OMI (blue, horizontally striped), SCIAMACHY (green, dotted), and GOME-2 (red, diagonally striped). For OMI, only ground pixels of the two nadir rows in the middle of the CCD are included (row 29 and 30 starting to count at 0). (f) Average VRS fit factor for OMI's two nadir CCD rows (see (e)) as retrieved from synthetic TOA radiances simulated with SCIATRAN for different diffuse attenuation coefficients $K_d(\lambda_{ext})$. Only results for every second simulated SZA are shown for clarity.

0.0006 for GOME-2, and 0.0013 for OMI.

Figure 3.3.2 shows monthly gridded global VRS fit factors for May 2007 from (a) OMI, (b) SCIAMACHY, and (c) GOME-2. For comparison, Figure 3.3.2 (d) shows the diffuse attenuation coefficient $K_d^{\text{OC}}(\lambda_{\text{ext}})$ from the OC-CCI data set for the same month. Due to the definition of the VRS pseudo absorption cross section, VRS fit factors are usually negative. We defined them as positive here for easier understanding by multiplying with -1 . Now, high VRS fit factors correspond to high VRS signals. VRS fit factors show similar global patterns among the different sensors. These patterns are in agreement with regions generally known to have high and low amount of light in the water. Clearly, there is an anti-correlation between high/low VRS fit factors corresponding to regions with high/low diffuse light attenuation for all three instruments.

Figure 3.3.2 (e) shows the normalized frequency of global VRS fit factors for the month of May 2007 excluding land and coast pixels. Only ground pixels from OMI's nadir CCD rows 29 and 30 were considered roughly enabling comparison with distributions from GOME-2 and SCIAMACHY. VRS fit factor ranges are significantly different between the three sensors which is expressed in a difference in mean value of 0.81 for OMI, 0.44 for SCIAMACHY, and 0.49 for GOME-2 and standard deviation of 0.35 for OMI, 0.31 for SCIAMACHY, and 0.22 for GOME-2. For all three instruments, negative VRS fit factors are present in the global distribution. Among the three sensors, SCIAMACHY has the highest amount of negative values. About 4% of all ground pixels have negative VRS fit factors. Figure 3.3.2 (f) shows the VRS fit factor $S_{\text{VRS}}^{\text{mod}}$ as function of $K_d(\lambda_{\text{ext}})$ as calculated from SCIATRAN simulations for different SZAs. Since SCIATRAN simulations were calculated instrument-specific, i.e., for each sensor individually, this relationship varies among the sensors. Displayed is the averaged result for OMI's two center CCD rows 29 and 30 (0-based) for every second SZA that was simulated. The relationship $K_d(\lambda_{\text{ext}}) \leftrightarrow (S_{\text{VRS}}^{\text{mod}}, \text{SZA})$ looks very similar to the one for OMI's nadir rows if SCIAMACHY and GOME-2 settings were used. VRS fit factors retrieved on instrument-specific simulated TOA radiances for SCIAMACHY and GOME-2 deviate by less than 3% from those in Figure 3.3.2 (f) for the lowest simulated diffuse attenuation coefficients.

VRS fit factors are not directly comparable among the sensors, mostly, because they depend on SZA which differs among the sensors due to different local overpass times, and, minorly, because of different instrument design. A one-to-one comparison of the VRS fit factors between the different hyperspectral sensors might not be meaningful. But, through roughly comparing the theoretically expected VRS fit factor range as presented in Figure 3.3.2 (f) with the global VRS fit factor frequencies in Figure 3.3.2 (e), differences in fit factor frequencies are expected, but appear to be large. As seen in Figure 3.3.2 (f),

the model predicts only positive VRS fit factors over the entire simulated $K_d(\lambda_{\text{ext}})$ range, but negative VRS fit factors are seen in the satellite data. This disagreement between retrieval results on model and satellite data indicates a correlation between cross sections as discussed in section [3.4.1](#).

3.3.2 Agreement between model and satellite data

A thorough comparison of the VRS fit performance between the three hyperspectral sensors and quality estimation of each single sensor can only be made when VRS fit factors are converted to a physical quantity, here, the diffuse attenuation coefficient in the excitation wavelength region. A correct conversion from VRS fit factor to diffuse attenuation coefficient requires that the VRS fit on modeled data accurately represents the VRS fit on real satellite data. The robustness of the conversion can be estimated from comparing the hyperspectral satellite derived diffuse attenuation coefficient to an independent data set.

Starting from the retrieved VRS fit factors, the diffuse attenuation coefficient for the excitation wavelength range $K_d(\lambda_{\text{ext}})$ was derived using a LUT built up by SCIATRAN calculations (details in section [3.2.5](#)) relating $S_{\text{VRS}}^{\text{mod}}$, SZA, and $K_d(\lambda_{\text{ext}})$ based on the relationship shown exemplarily in Figure [3.3.2](#) (f). Figure [3.3.3](#) shows retrieved $K_d(\lambda_{\text{ext}})$ from (a) SCIAMACHY, (b) GOME-2, and (c) OMI in comparison to the wavelength-converted $K_d^{\text{OC}}(\lambda_{\text{ext}})$ using $K_d^{\text{OC}}(490)$ from OC-CCI as input (details in section [3.2.7](#)). The scatter plot contains data from 01 Feb 2007 to 31 Dec 2007. The comparison was calculated on a daily basis using data gridded to 0.5° . $K_d(\lambda_{\text{ext}})$ derived from SCIAMACHY and GOME-2 are much larger than $K_d^{\text{OC}}(\lambda_{\text{ext}})$ from the OC-CCI data set. Linear total least squares regression shown by the dash-dotted black line yielded a slope of 3.02 for SCIAMACHY and 2.05 for GOME-2 which indicates that their $K_d(\lambda_{\text{ext}})$ are roughly 3 and 2 times, respectively, larger than OC-CCI values. OMI shows a different behavior. $K_d(\lambda_{\text{ext}})$ derived from OMI is smaller than $K_d^{\text{OC}}(\lambda_{\text{ext}})$ over the entire data range expressed in a slope of 0.30. Regression statistics are summarized in Table [3.3.1](#).

In summary, the slopes found in comparison with the OC-CCI data differ significantly from one and indicate a disagreement between the VRS fit factors found by fitting global satellite data and those found by fitting model data. High slopes for SCIAMACHY and GOME-2 express a lower VRS fit factor range in satellite data than in model data. Conversely, underestimation of $K_d(\lambda_{\text{ext}})$ by OMI indicates a higher VRS fit factor range than the model predicts.

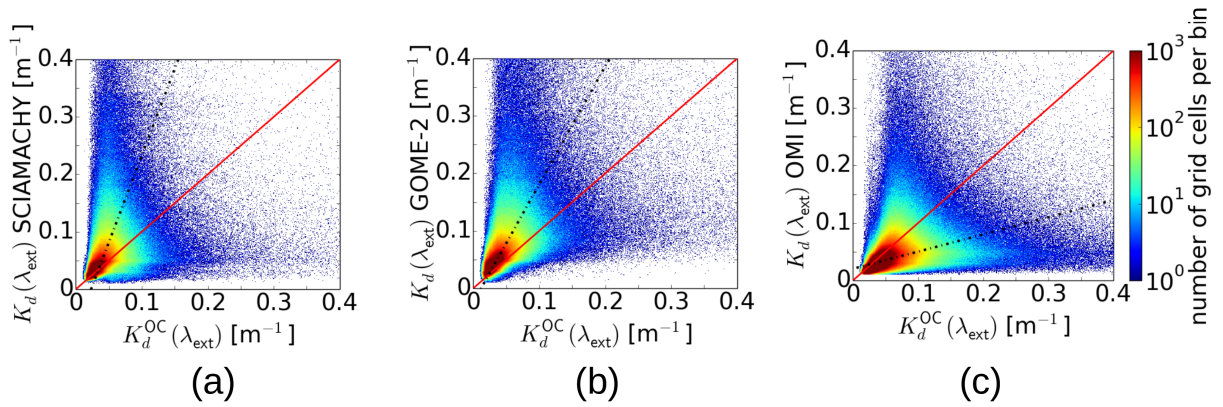


Figure 3.3.3: Scatter plots show $K_d(\lambda_{\text{ext}})$ from VRS obtained with the DOAS fit settings as in [Losa et al. \(2017a\)](#) from (a) SCIAMACHY, (b) GOME-2, and (c) OMI in comparison to $K_d^{\text{OC}}(\lambda_{\text{ext}})$ which was wavelength converted from OC-CCI $K_d^{\text{OC}}(490)$. The solid red line is the 1:1 line. The dash-dotted black line is a linear total least squares regression through the global data set. Daily gridded data with 0.5° grid cell size were used as input. The comparison contains all data from 01 Feb 2007.

3.3.3 Modification of the VRS fit

Modifications of the VRS fit were tested to improve the agreement between VRS fit factor ranges from fits on model and satellite data. For SCIAMACHY, including zeta and eta functions was tested which were taken from calibration key data ([Lichtenberg et al., 2006](#)) for correcting polarization structures. For GOME-2 and SCIAMACHY, the number of eigenvectors accounting for instrumental artifacts were reduced from two to one eigenvector in the DOAS fit. Since no eigenvectors were used in the DOAS fit on OMI data, no further modifications of the DOAS fit were tested for OMI in this study. We merely tested if reducing the number of CCD rows to the inner 20 CCD rows closest to nadir improves the results. Looking at the 11 month comparison between $K_d(\lambda_{\text{ext}})$ and $K_d^{\text{OC}}(\lambda_{\text{ext}})$, a slightly different slope was found, but no change in correlation of the data set. Since no significant improvement was achieved, diffuse attenuation coefficients from all CCD rows were kept in the data set.

For GOME-2, reducing the number of cross sections from two to one eigenvector significantly improved the derived diffuse attenuation coefficient product. Changing this fit setting, shifted the globally retrieved VRS fit factor distribution towards higher values. For example for May, the global distribution has now a higher mean value of 0.56 while the standard deviation stayed the same.

For SCIAMACHY, best results were found when two eigenvectors were included for correcting instrumental effects and additionally the zeta function was fitted. VRS fit

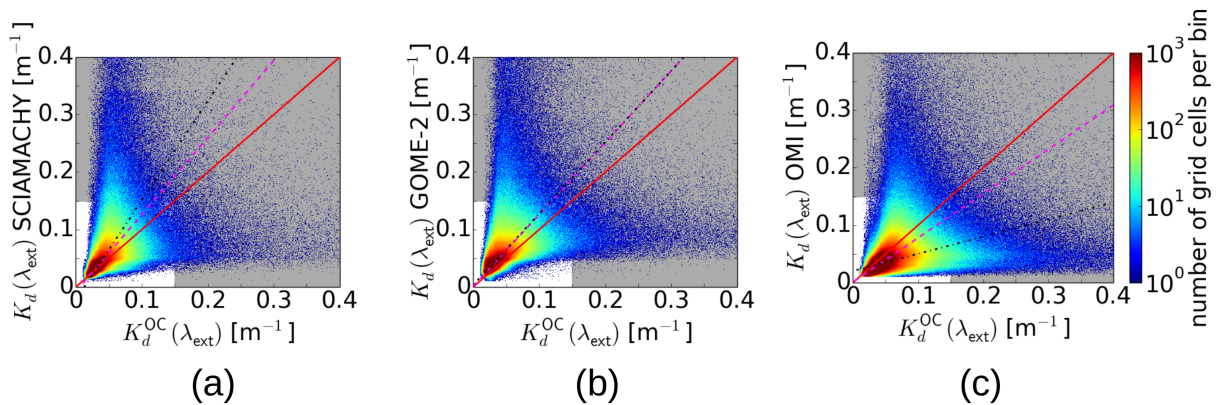


Figure 3.3.4: Scatter plots showing $K_d(\lambda_{\text{ext}})$ from VRS obtained with the modified DOAS fits from (a) SCIAMACHY, (b) GOME-2, and (c) OMI in comparison to $K_d^{\text{OC}}(\lambda_{\text{ext}})$ wavelength converted from OC-CCI $K_d^{\text{OC}}(490)$. The solid red line is the 1:1 line. The dash-dotted black line is a linear total least squares regression through the global data set and the dashed magenta line is a linear total least squares regression through the global data set where values above 0.15 m^{-1} were filtered out (grey area). Daily gridded data with 0.5° grid cell size were used as input. The comparison contains all data from 01 Feb 2007 until 31 Dec 2007.

factors generally increased and the number of negative VRS fit factors decreased. Similar behavior to GOME-2 was found for the example month May. The global distribution has a similar standard deviation of 0.30, but a higher mean value of 0.51 compared to the old DOAS settings without zeta function.

Figure 3.3.4 shows $K_d(\lambda_{\text{ext}})$ derived from VRS fit factors resulting from the modified DOAS fit on (a) SCIAMACHY and (b) GOME-2 in comparison to the wavelength-converted OC-CCI diffuse attenuation coefficient product $K_d^{\text{OC}}(\lambda_{\text{ext}})$. Regression results can be found in Table 3.3.1 (middle column). Considering all global ground pixels, linear total least squares regression yielded slopes of 1.73 for SCIAMACHY and 1.24 for GOME-2. For large values, the spread in the scatter plots becomes large for both instruments. Especially for SCIAMACHY, two pronounced wings are observed in the scatter plot, where values from OC-CCI are very large when values derived from SCIAMACHY are small and vice versa. We decided to restrict the retrieval of $K_d(\lambda_{\text{ext}})$ from hyperspectral satellite data to waters with diffuse attenuation coefficients below 0.15 m^{-1} given by $K_d^{\text{OC}}(\lambda_{\text{ext}})$. Additionally, values of $K_d(\lambda_{\text{ext}})$ above 0.15 m^{-1} were discarded. This filtering left only data outside the grey area in Figure 3.3.4. Linear total least squares regression is shown as dashed magenta line. Reducing the data set increased the correlation between $K_d(\lambda_{\text{ext}})$ and $K_d^{\text{OC}}(\lambda_{\text{ext}})$ from 0.27 to 0.66 for SCIAMACHY and from 0.25 to 0.66 for GOME-2. The slopes changed for SCIAMACHY from 1.73 to 1.34 and for GOME-2 from

Table 3.3.1: Slope, intercept, and Pearson correlation of the total linear least-squares regression between $K_d(\lambda_{\text{ext}})$ and $K_d^{\text{OC}}(\lambda_{\text{ext}})$ comparing 11 months of diffuse attenuation coefficients derived with the original DOAS settings on the full data set (left column: orig., full), with the modified DOAS settings on the full data set (middle column: mod., full), and with modified (SCIAMACHY and GOME-2) or original (OMI) DOAS settings on the reduced data set ($K_d(\lambda_{\text{ext}})$ and $K_d^{\text{OC}}(\lambda_{\text{ext}}) < 0.15\text{m}^{-1}$) (right column: mod.,red. or orig.,red.).

	SCIAMACHY			GOME-2			OMI	
	orig., full	mod., full	mod., red.	orig., full	mod., full	mod., red.	orig., full	orig., red.
slope	3.02	1.73	1.34	2.05	1.24	1.25	0.30	0.77
intercept	-0.070	-0.022	-0.008	-0.024	0.003	0.001	0.020	0.001
correlation	0.22	0.27	0.66	0.34	0.25	0.66	0.35	0.65

1.24 to 1.25. The same filtering approach was applied to results for OMI displayed in Figure 3.3.4 (c). Correlation increased here from 0.35 to 0.65 and the slope increased from 0.30 to 0.77. Regression results for the reduced data sets can also be found in Table 3.3.1 (right column).

All results presented below were obtained using modified VRS fit settings and data filtering as described in this section. The hyperspectral satellite $K_d(\lambda_{\text{ext}})$ was filtered in waters where $K_d^{\text{OC}}(\lambda_{\text{ext}})$ predicts values above 0.15m^{-1} by gridding both data sets to the same grid of 0.5° gridsize.

3.3.4 Derived global diffuse attenuation coefficients

Global $K_d(\lambda_{\text{ext}})$ maps derived from VRS fit factors obtained with modified DOAS settings are shown in Figure 3.3.5 for (a) SCIAMACHY, (c) GOME-2, and (e) OMI after $K_d(\lambda_{\text{ext}})$ was filtered as described in section 3.3.3. Systematic differences between the three sensors can already be deduced from these global maps. Diffuse attenuation coefficients derived from OMI VRS fit factors are globally lower than those derived from SCIAMACHY and GOME-2 VRS fit factors. Higher values in the northern hemisphere are the most prominent difference between SCIAMACHY and GOME-2 derived $K_d(\lambda_{\text{ext}})$.

To identify regional differences between the hyperspectral satellite and the OC-CCI products, the difference $K_d(\lambda_{\text{ext}}) - K_d^{\text{OC}}(\lambda_{\text{ext}})$ is shown as global map in Figure 3.3.5 for (b) SCIAMACHY, (d) GOME-2, and (f) OMI. As the pronounced difference between GOME-2 and SCIAMACHY in the northern hemisphere suggested, a difference between northern and southern hemisphere is observed for SCIAMACHY. In the northern hemisphere, $K_d(\lambda_{\text{ext}})$ is smaller than $K_d^{\text{OC}}(\lambda_{\text{ext}})$ for most ground pixels, whereas in the southern

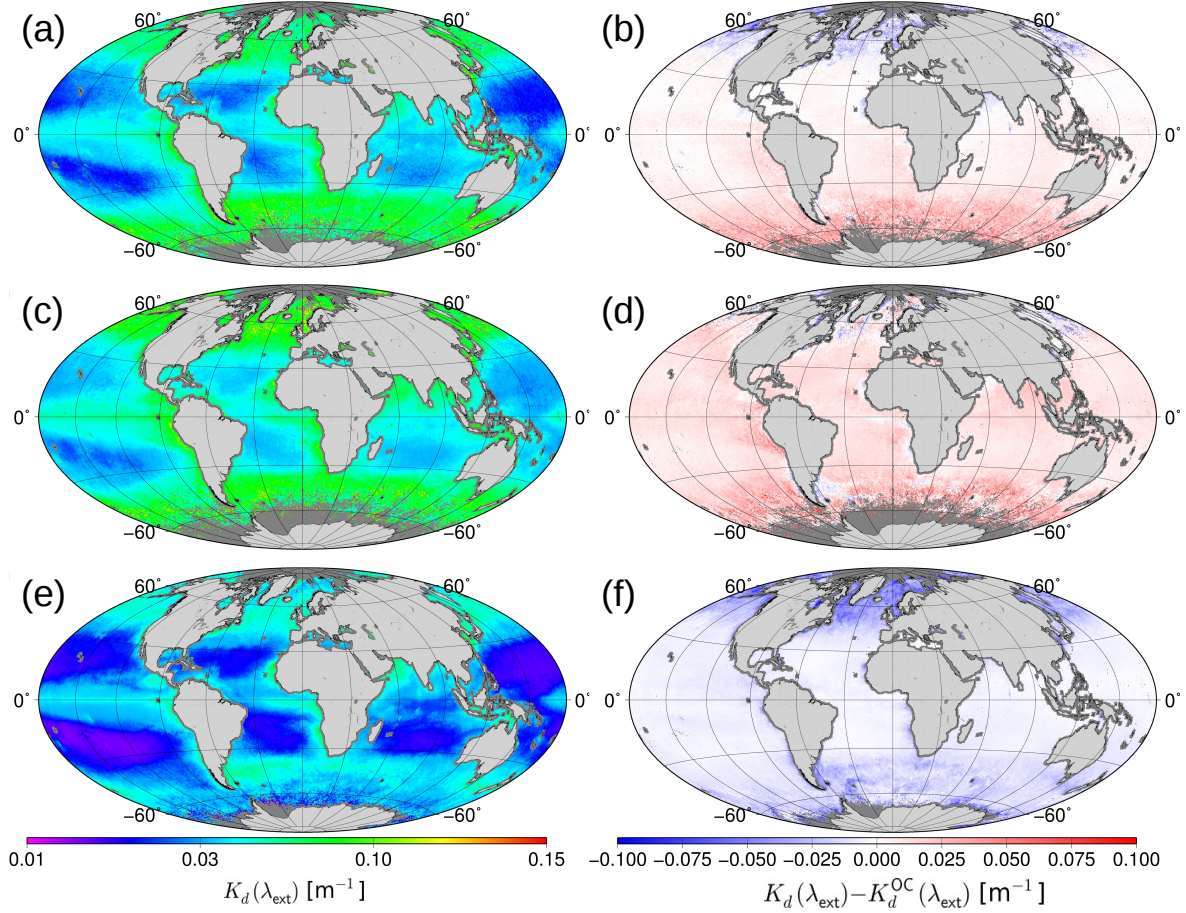


Figure 3.3.5: Global distribution of the diffuse attenuation coefficient at the excitation wavelength region $K_d(\lambda_{\text{ext}})$ derived from (a) SCIAMACHY, (c) GOME-2, and (e) OMI VRS fit factors gridded for the time period 01 Feb 2007 to 31 Dec 2007. Data was gridded to 0.5° grid cell size. Globally mapped distribution of the difference between the OC-CCI and the hyperspectral satellite data sets $K_d(\lambda_{\text{ext}}) - K_d^{\text{OC}}(\lambda_{\text{ext}})$ for (b) SCIAMACHY, (d) GOME-2, and (f) OMI. In all six images, $K_d(\lambda_{\text{ext}})$ was filtered below 0.15 m^{-1} and restricted to waters where $K_d^{\text{OC}}(\lambda_{\text{ext}}) < 0.15 \text{ m}^{-1}$.

hemisphere $K_d(\lambda_{\text{ext}})$ is larger than $K_d^{\text{OC}}(\lambda_{\text{ext}})$ for most ground pixels. The observed spread in the scatter plot in Figure 3.3.4 (a) as two wings, where $K_d^{\text{OC}}(\lambda_{\text{ext}})$ is large when $K_d(\lambda_{\text{ext}})$ is small and vice versa, is mainly caused by a north-south trend in $K_d(\lambda_{\text{ext}})$ originating from a north-south trend in SCIAMACHY VRS fit factors. For GOME-2, no significant north-south trend is observed. In low latitudes, $K_d^{\text{OC}}(\lambda_{\text{ext}})$ is larger than $K_d(\lambda_{\text{ext}})$ in the Mauretanian, Benguela, and Malvinas upwelling regions where diffuse attenuation coefficients are the highest. For open ocean situations such as the Southern Ocean, GOME-2 derived attenuation coefficients tend to be smaller than the OC-CCI product. However, especially in the high latitudes in the north, spatial patterns are not so clear. As seen from the global $K_d(\lambda_{\text{ext}})$ map, averaged over one year, OMI derived $K_d(\lambda_{\text{ext}})$ are generally smaller than $K_d^{\text{OC}}(\lambda_{\text{ext}})$. Largest differences between the two data sets can be found in northern high latitudes.

3.3.5 Diffuse attenuation coefficient time series

Figure 3.3.6 (a) shows mean diffuse attenuation coefficients in the excitation wavelength range for SCIAMACHY, GOME-2, OMI, and OC-CCI in five different Longhurst provinces (Longhurst et al., 1995) over the course of 2007, starting 01 Feb 2007. Mean $K_d(\lambda_{\text{ext}})$ were calculated as 7-day composites. Relative differences $(K_d(\lambda_{\text{ext}}) - K_d^{\text{OC}}(\lambda_{\text{ext}}))/K_d^{\text{OC}}(\lambda_{\text{ext}})$ between hyperspectral satellites and OC-CCI in the five provinces are shown in Figure 3.3.6 (b). In general, largest differences between $K_d(\lambda_{\text{ext}})$ and $K_d^{\text{OC}}(\lambda_{\text{ext}})$ are observed in the NADR and ARCT region where a significant amount of data points deviates by up to $\pm 60\%$. Positive and negative deviations are observed for GOME-2 in all five provinces showing a seasonal behavior. E.g., large positive deviations up to $+120\%$ are observed in the winter months February, March, and December. During the other months, GOME-2 deviates from $K_d^{\text{OC}}(\lambda_{\text{ext}})$ by less than $\pm 30\%$ in the ISSG, ARAB, and BENG provinces and less than $\pm 40\%$ in the NADR and ARCT provinces. OMI and SCIAMACHY diffuse attenuation coefficients are mostly smaller than $K_d^{\text{OC}}(\lambda_{\text{ext}})$. This trend becomes more striking with increasing latitude. Although SCIAMACHY and OMI generally have a significant bias, they tend to be more stable with time than GOME-2. E.g., for the ARCT province, OMI time series has a large bias, but is relatively stable in time in comparison to $K_d^{\text{OC}}(\lambda_{\text{ext}})$. Deviations range between -40% to -65% for most data points while they range between -10% to -60% for SCIAMACHY and -40% to $+40\%$ for GOME-2 (excluding winter months).

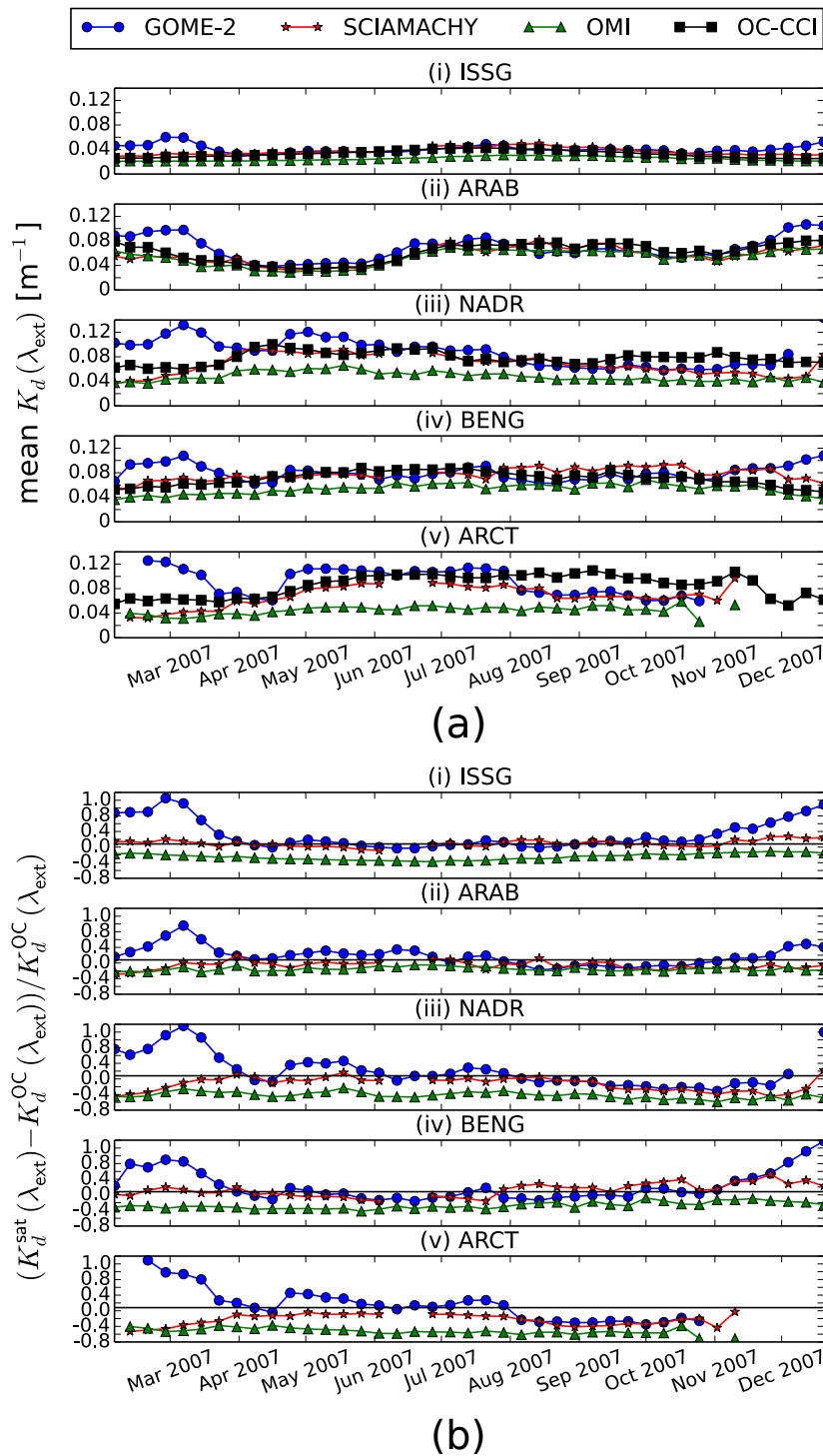


Figure 3.3.6: (a) Mean $K_d(\lambda_{\text{ext}})$ from SCIAMACHY, GOME-2, OMI, and OC-CCI and (b) relative deviation of SCIAMACHY, GOME-2, and OMI $K_d^{\text{sat}}(\lambda_{\text{ext}})$ from OC-CCI $K_d^{\text{OC}}(\lambda_{\text{ext}})$ in five different Longhurst provinces (Longhurst et al., 1995) over the course of the year 2007. 7-day composites were calculated starting 01 February 2007. Naming convention follows the original naming by Longhurst et al. (1995). (i) ISSG - Indian S. Subtropical Gyre Province, (ii) ARAB - NW Arabian Upwelling Province, (iii) NADR - N. Atlantic Drift Province, (iv) BENG - Benguela Current Coastal Province, (v) ARCT - Atlantic Arctic Province.

3.4 Discussion

3.4.1 Correlating cross sections in DOAS

The spectral signature of VRS was identified in all three satellite sensors OMI, SCIAMACHY, and GOME-2. Global VRS maps can be retrieved from TOA radiances measured by the three sensors and resulting global patterns agree with regions of high and low diffuse light attenuation. However, a disagreement in VRS fit factor range between model and satellite data was found. For nadir viewing geometry, VRS fit factors retrieved from satellite data were lower than predicted by the model in case of SCIAMACHY and GOME-2, whereas they were slightly higher than predicted by the model in case of OMI. This discrepancy hints at a correlation between cross sections in the DOAS fit.

The difficulty of separating VRS from liquid water absorption spectral features in DOAS is known. For circumventing this problem in phytoplankton DOAS retrievals, Bracher et al. (2009) performed a PCA over clear water regions and included the first two eigenvectors in the DOAS fit instead of including a separate VRS cross section. Peters et al. (2014) tried to experimentally determine a VRS cross section to improve DOAS NO_2 fits, but were not able to separate liquid water absorption from VRS. They obtained the best NO_2 results over water regions when using a combined spectrum. Since we are particularly interested in the VRS signal, we need it as separate cross section in the DOAS fit. In principle, a combined spectrum of VRS and liquid water absorption could also be used as a proxy for the diffuse attenuation coefficient in the ocean. However, the interpretation of such an approach is more difficult, since the VRS excitation is in a different wavelength region than the DOAS fit window where liquid water absorbs. It is not straightforward for which wavelength range the light availability should be calculated.

To a certain extent, the comparison with model results accounts for the correlation between the spectra, since the same DOAS fit is performed on modeled TOA radiances. A theoretical correlation between cross sections also impacts retrieved fit factors from modeled data. The VRS fit factors retrieved from satellite data are directly related to those retrieved from modeled data to derive the diffuse attenuation coefficient in our approach. Correlating spectra affect the model retrieval and the satellite retrieval in the same way and the direct comparison of the two should compensate for this effect. However, in real world applications with satellite spectra that are noisy and show spectral features caused by the instrumentation, model and satellite results are not one-to-one comparable.

Differences in VRS fit factors between the three sensors suggest that not only the correlation between cross sections, but primarily the instrument itself influences the fit results. Major differences are that GOME-2 and SCIAMACHY are whisk-broom sensors whereas

OMI is a push-broom sensor, that SCIAMACHY and GOME-2 provide higher quality daily sun spectra than OMI for which a fixed sun spectrum has to be used, and that SCIAMACHY and GOME-2 have no polarization scramblers. All these differences in instrument design plus differences in light path in the instrument interior cause different spectral signatures in the recorded TOA radiances and sun spectra, e.g. caused by stray light in the instrument or structures on the diffuser used for recording sun spectra. The eigenvectors that were used in the DOAS fit in this study to account for instrumental spectral artifacts that are not removed during the calibration differ between GOME-2 and SCIAMACHY. The eigenvectors could also correlate with the VRS pseudo-absorption cross section and change the theoretically expected VRS fit factor. In general, SCIAMACHY and GOME-2 have a more similar instrument design in comparison to OMI. This may explain, why the retrieved VRS fit factor ranges are more similar for these instruments and why including eigenvectors in the DOAS fit for OMI hardly affects the result.

We want to note that the discrepancy found here between VRS results from simulations and measurements determined with the DOAS settings as in [Losa et al. \(2017a\)](#) does not mean that their results on SCIAMACHY measurements suffer from the same issues. For converting their fit factors into PFT chlorophyll-a concentrations, they use a ratio of fit factors for two quantities, i.e. PFT and VRS, while here only one fit factor is used in combination with model results. Ratios of fit factors are more robust providing that instrumental artifacts affect the two quantities similarly.

3.4.2 Implications of DOAS setting modifications

Modifications of the DOAS fit for GOME-2 and SCIAMACHY were tested and significantly improved resulting diffuse attenuation coefficients. Evaluating the results by comparison with wavelength-converted diffuse attenuation coefficients from OC-CCI data sets yielded slopes close to one in the scatter plots ([Figure 3.3.4](#)). Through modifying the DOAS fit for GOME-2 and SCIAMACHY, we were able to bring together fit performance on modeled radiances with that on satellite-recorded radiances.

Including zeta and eta functions for polarization corrections in DOAS fits has been suggested by [McLinden et al. \(2002\)](#) and shown to improve DOAS fit results on SCIAMACHY radiances for various atmospheric trace gas retrievals ([Kühl et al., 2008](#)). In the VRS DOAS fit studied here, only including the zeta function worked best. For other retrieval targets, other combinations of zeta and eta function were found beneficial. E.g., for BrO vertical profile retrievals from SCIAMACHY limb measurements, including the eta function improved the fit, but including the zeta function destabilized the fit ([Rozanov](#)

et al., 2011).

For OMI, DOAS fit settings were not modified. No significant improvement was achieved through CCD row filtering for the 20 middle CCD rows which are closest to nadir and have more optimal viewing geometries for ocean observations than the outer CCD rows. It can be concluded that for OMI the viewing angle dependence in the model accurately describes the situation found in measurements.

3.4.3 Restricting diffuse attenuation coefficient data sets

Large spreads in the scatter plots were observed for high diffuse attenuation coefficients, especially for OMI and SCIAMACHY, leading to wings in the scatter plot. Such a butterfly-shape has been already observed by Dinter et al. (2015) when comparing one month of derived diffuse attenuation coefficients from SCIAMACHY to $K_d(490)$ from GlobColour. They suggested the following reasons for the wings. The horizontal wing is possibly caused by cloud-contaminated SCIAMACHY ground pixels leading to an overestimation of $K_d(\lambda_{\text{ext}})$ and the vertical wing is caused by deviations of vertical chlorophyll-a profiles and specific chlorophyll-a absorption from those set in the model. They restricted their statistical analysis of the comparison to diffuse attenuation coefficients below 0.06 m^{-1} and improved the correlation from 0.42 to 0.69. One-to-one comparison for SCIAMACHY results found here with those published in Dinter et al. (2015) is not possible since DOAS fit settings, observed time period, and multispectral reference product used for the comparison differ. However, it can be stated roughly that, when comparing correlations found here and in their study, a similar degree of agreement was found, when $K_d(\lambda_{\text{ext}})$ from SCIAMACHY is compared to diffuse attenuation coefficients from multispectral sensor data sets.

We similarly restricted our retrieval for all three hyper-spectral sensors to $K_d^{\text{OC}}(\lambda_{\text{ext}}) < 0.15 \text{ m}^{-1}$ to improve data quality justifying and adding general suggestions here for reasons behind the observed spread in the scatter plots. Waters with high diffuse attenuation coefficients have a low VRS signal. The sensitivity of the VRS DOAS fit in these waters is therefore low and the fit is expected to be less accurate there (Vountas et al., 2007). OC-CCI diffuse attenuation coefficients by the Lee method (Lee et al., 2005a) have better accuracies for waters with high diffuse light attenuation (Lee et al., 2005b; Shang et al., 2011). The VRS method is expected to be more sensitive to waters with low diffuse light attenuation.

Additionally, derived diffuse attenuation coefficients from the hyperspectral sensors were cut-off at 0.15 m^{-1} even if OC-CCI predicts values below 0.15 m^{-1} . This filtering was

necessary to improve the data quality sufficiently and was easy to apply. From a physical point of view it is more difficult to understand though: considering OC-CCI values as correct, the VRS fit gives wrong results for filtered out ground pixels, although the VRS fit sensitivity should have been high. Partially this can be caused by noise in the recorded TOA radiances. Cloud-contamination of ground pixels can significantly reduce the VRS signal as already pointed out by [Dinter et al. \(2015\)](#). Other possible causes are a mismatch between average ocean scenario used in the model simulations and the true state of the ocean during the measurement, e.g. extremely high wind speeds or aerosol loads. By restricting derived diffuse attenuation coefficients to waters where OC-CCI predicts values below 0.15 m^{-1} and additionally cutting off all remaining values above 0.15 m^{-1} , reduces the data sets by less than four percent. It is unfortunate that these scenes have to be removed from the data set, since biological activity is high and significantly contributes to the overall primary production in open oceans, however, valuable information on open ocean primary productivity may still be drawn from the remaining data points.

3.4.4 Spatial and temporal biases in diffuse attenuation coefficients

Despite the DOAS fit modifications, issues in the VRS DOAS fit remained. Possible origins of these issues and impacts on the quality of the derived diffuse attenuation coefficient became apparent when looking at spatial and temporal patterns of the derived diffuse attenuation coefficient.

For SCIAMACHY, a clear north-south trend was found in the data which is most likely caused by spectral features arising from polarization sensitivity of the instrument. Scatter geometries differ from North to South causing differences in spectral features due to polarization ([Liebing et al., 2018](#)). If these spectral features, included as eigenvectors in the fit, correlate with the VRS pseudo-absorption cross section, the north-south trend in these spectral features is passed on to the VRS fit factors. The zeta function was included to account for polarization. Including the zeta function in the fit reduced but did not fully remove the north-south trend.

For OMI, agreement with OC-CCI becomes worse with increasing latitude. This finding suggests that the model predicts a different SZA dependence of the VRS fit factor than found in the DOAS retrieval results on measured TOA radiances. Detailed investigations on this behavior have not been performed in this study.

For GOME-2, spread does not arise from spatial trends, but mainly from temporal variations in the fit factors. Seasonal variations as observed here have been identified in trace gas columns retrieved with DOAS from GOME and attributed to the diffuser plate

causing spectral artifacts in the irradiances that correlate with absorber cross sections (Richter and Wagner, 2001). This effect of seasonal variation has also been observed for the weak signal of glyoxal in DOAS columns from GOME-2 measurements (Lerot et al., 2010). Using a constant solar spectrum instead of daily solar spectra could improve the situation for 2007, but is not a solution for the whole GOME-2 mission period due to significant instrumental drifts (Richter et al., 2011; Dikty et al., 2012). Another option as background spectrum (e.g. Meier et al., 2017; Dikty2012) is to use daily earthshine spectra measured by GOME-2 over a region where no VRS signal is expected, e.g. over the Sahara. We have quickly tested this option for the month of December 2007. Resulting diffuse attenuation coefficients were closer to OC-CCI compared to results obtained with daily solar spectra but still too high with a slope in the monthly scatter plot of 0.57 (filtered below 0.15 m^{-1}). Other correlating spectral features seem to be introduced that disturb the fit results. The seasonal variation could also be empirically corrected, e.g., through adjusting retrieved fit factors by forcing the fit factors in a certain region to a known value (Hewson et al., 2013). The seasonal variation dominates the time series in the five Longhurst provinces. To build up a consistent time series over the entire GOME-2 mission period and analyze trends in diffuse attenuation coefficients from this series, a correction for this variation is required.

Although we clearly saw that biases and seasonal variations in the three hyperspectral sensors dominate the time series in the Longhurst provinces, also a difference between OC-CCI data set and hyperspectral data sets arises due to a difference in data coverage in the five Longhurst provinces. Coverage was calculated for all five provinces by dividing the number of unique gridded ground pixels in one Longhurst province within one 7-day composite by the total amount of gridded ground pixels fitting into the Longhurst province. Largest differences in coverage between OC-CCI and the hyperspectral sensors were found for NADR and ARCT which are strongly impacted by cloud occurrence (e.g. King et al., 2013). In combination with a spatial inhomogeneity in biomass in these provinces due to the occurrences of phytoplankton blooms, this may explain, why the diffuse attenuation coefficients from hyperspectral sensors compare less well with the $K_d^{\text{OC}}(\lambda_{\text{ext}})$ data set in these two provinces than in the other three provinces.

Due to the large ground pixel sizes of hyper-spectral satellite sensors and the associated inhomogeneity within a ground pixel, in combination with the rather complex retrieval method presented in this study, we expect diffuse attenuation coefficients derived from hyperspectral sensors to be associated with larger uncertainties and regard OC-CCI $K_d(490)$ as a solid data set to evaluate our retrieval performance. However, also the OC-CCI diffuse attenuation coefficients are associated with uncertainties. $K_d^{\text{OC}}(490)$ was determined using

the semianalytical method by Lee et al. (2005a). This method is a two step process. First, inherent optical properties are derived with a Quasi-Analytical Approach from remote sensing reflectances (Lee et al., 2002). Extensive radiative transfer simulations have been made to relate these inherent optical properties, i.e., absorption and backscattering, in a second step, to an apparent optical property, the diffuse attenuation coefficient. Model runs were made with a whole range of different inherent optical properties found in different water classes. Other conditions were set to standard values describing the average global scenario, though, limiting the accuracy of the approach. Similar settings as chosen for the simulations in this study were used, e.g., a mean wind speed of 5 m/s, vertically homogeneous waters, and clear sky conditions. The OC-CCI data set has been validated in comparison with in-situ matchups. On regional scales, the performance quality of the Lee method can vary (Shang et al., 2011; Soppa et al., 2013). The DOAS-based method presented here and the method by Lee et al. differ fundamentally in determining diffuse attenuation coefficient, but both approaches are rather analytical with a similar degree of assumptions that have to be made. One advantage of the DOAS-based method is that it effectively removes the atmospheric signal from the TOA radiances. No atmospheric correction is needed as additional step before the VRS retrieval.

As discussed above, the time series analysis showed that biases and seasonal variations are significant in the five Longhurst provinces. As the diffuse attenuation products are now, the agreement between the three hyperspectral sensors and overall data quality are not robust enough for merging the three data sets. Several studies have pointed out how intermission differences affect trend analysis on merged ocean color time series (Gregg and Casey, 2010; Beaulieu et al., 2013; Mélin, 2016). Based on the findings in this study, the intersensor consistency of the diffuse attenuation coefficient product should now be increased, e.g. through empirical corrections of the seasonal variations in GOME-2 as mentioned above, statistical bias correction (Bai et al., 2016), better calibration of the level 1 data (Lerot et al., 2014), or a combination of several correction schemes.

3.5 Conclusion

We evaluated the possibility of exploiting the VRS signal in radiances measured by hyperspectral satellite sensors for assessing the diffuse light attenuation over long time scales building up on the work by Dinter et al. (2015). VRS signals were retrieved and diffuse light attenuation coefficients were derived for nearly one year of earth observations from three different hyperspectral satellite sensors, SCIAMACHY, GOME-2, and OMI.

VRS signals were detected in radiances from all three hyperspectral sensors. Starting

with the latest published DOAS VRS retrieval settings, VRS fit factors were found to be sensitive to spectral structures in the measured radiances caused by instrumentation. For example, SCIAMACHY VRS fit factors were highly influenced by polarization features. Modifying the DOAS retrieval for SCIAMACHY and GOME-2 by changing how instrumental effects are accounted for in the retrieval, resulted in significantly improved diffuse attenuation coefficients. For SCIAMACHY, the zeta function was included to better correct for spectral features caused by polarization sensitivity of the sensor. For GOME-2, the amount of cross sections accounting for instrumental effects determined through a PCA on fit residuals over the Sahara were reduced from two to one eigenvector.

Through these DOAS fit setting modifications, VRS fit factor ranges from DOAS fits on satellite measurements were brought in agreement with VRS fit factor ranges predicted by fits on synthetic radiances calculated by radiative transfer modeling. In comparison to the established diffuse attenuation coefficient product from OC-CCI, robust correlations and slopes close to unity were found for all three sensors when only diffuse attenuation coefficients below 0.15 m^{-1} were used. Highest correlation was found for GOME-2 data.

For further evaluating the quality of the derived diffuse attenuation coefficients from GOME-2, SCIAMACHY, and OMI, spatial and temporal deviations from the OC-CCI product were investigated by assessing global maps and time series of 7-day composites in five different Longhurst provinces. SCIAMACHY and OMI both showed latitudinal trends in derived diffuse attenuation coefficients. A north-south trend was found for SCIAMACHY indicating that spectral structures caused by polarization sensitivity could not be completely corrected despite including the zeta function in the DOAS fit. For OMI, biases with respect to the OC-CCI product become larger with increasing latitude indicating a disagreement between the SZA dependence of the VRS fit factor found in measurements in comparison to that predicted by radiative transfer modeling. This effect was not further investigated here. GOME-2 shows spatially a more homogeneous agreement with OC-CCI, but exhibits periodic changes in VRS fit factors over time which are probably caused by spectral structures in recorded solar measurements changing over the course of one year due to altering measurement geometries.

This first intercomparison of the performance of DOAS ocean retrievals on radiances from three different hyperspectral satellites revealed how challenging it is to accurately calibrate hyperspectral sensors to reliably and consistently retrieve small ocean signals. Merging the data sets is difficult since significant biases between the sensors were found. This study provides a good basis for further improving overall data quality and intersensor consistency to create a long-term diffuse attenuation coefficient time series in the blue spectral range. Based on the results of this study, it is unlikely that diffuse attenuation

coefficients derived from measurements of the particular hyperspectral sensors presented here could compete in quality with the diffuse attenuation coefficient from multispectral sensors. However, since the method presented here is independent and offers assessing diffuse attenuation in a different spectral range, it is worth further developing this approach, especially with respect to upcoming satellite missions. Better calibration of hyperspectral satellite sensors with respect to ocean applications could improve this situation. Building up on this study, empirical corrections could be introduced to reduce biases and stabilize the time series of hyperspectrally derived diffuse attenuation coefficients. A more complex LUT could be build to reduce noise as shown by the presented sensitivity analysis. A thorough uncertainty estimation is desired. Comparison with in-situ measurements becomes possible for the most recent or upcoming sensors that provide measurements at much higher spatial resolution. For example since October 2017, TROPOMI (TROPOspheric Monitoring Instrument) [Veefkind et al. \(2012\)](#), similar in mission goal and design as OMI, provides global hyperspectral radiances at a spatial resolution of 7 km by 3.5 km. Validating 7 km by 3.5 km large pixels with in situ point measurements would still be difficult, but becomes more feasible for in situ measurements from towed systems yielding transects of in situ data. With increased spatial resolution, DOAS fit quality is also expected to improve due to increased homogeneity in satellite scenes. The suitability of TROPOMI for ocean color applications is investigated in chapter [4](#).

4 TROPOMI-retrieved underwater light attenuation in three spectral regions: ultraviolet to blue

This chapter is the basis for a research article that is in revision for resubmission to Frontiers in Marine Science (Oelker et al., 2021). Author contributions are as follows: I extended the DOAS algorithm to the UV domain, performed the DOAS retrievals and RTM simulations, conceptualized and carried out the algorithm sensitivity analysis, and calculated the resulting K_d product as well as the comparisons with in-situ and multispectral data. I wrote the first draft of the manuscript and incorporated suggestions from the co-authors. Svetlana Losa supported the comparisons of TROPOMI-derived K_d products to multispectral and in-situ data sets and their discussion. Andreas Richter provided the software for the DOAS retrievals and gave advice with respect to retrieval settings and use of cloud products. Astrid Bracher initiated the project and gave the idea for the K_d -UV retrievals based on the results of Dinter et al. (2015) and chapter 3 as well as provided the in-situ K_d data set. All co-authors reviewed the first draft and the revised version presented in this thesis and gave valuable comments on the presentation of results and their discussion as well as structure of the manuscript.

4.1 Introduction

Light governs large-scale biological, physical, and chemical processes in the ocean. Incoming radiation heats the ocean thereby influencing mixed layer dynamics (Ohlmann et al., 1996) and ocean circulation, which in turn is coupled to atmospheric temperature and circulation (Lewis et al., 1990; Miller et al., 2003; Shell et al., 2003). Optically active biological and chemical constituents influence the heat and radiation budget of the ocean (Sathyendranath et al., 1991; Morel and Antoine, 1994; Frouin and Iacobellis, 2002). Visible radiation controls primary productivity of phytoplankton and higher aquatic plants (Sathyendranath et al., 1989) and thus the base of almost all life in the ocean. In contrast,

ultraviolet (UV) radiation damages phytoplankton cells and other microorganisms (Cullen and Neale, 1994; Sinha and Häder, 2002). Interactions between climate change and UV radiation penetrating the ocean and its effect on biogeochemical cycles are complex (Zepp et al., 2003, 2007). Upon photodegradation of colored dissolved organic matter (CDOM), the primary absorber of UV radiation in the ocean (Siegel et al., 2002), light penetration and nutrient availability increase. UV radiation also affects bioavailability of iron, copper, and other trace metals and the exchange of trace gases across the air-sea interface, changing atmospheric chemistry.

Adequately describing these light-ocean interaction processes and their role in biogeochemical cycling and climate change feedback mechanisms requires measurements of radiation parameters on a regular basis and large scales (IOCCG, 2008). Ocean color satellite missions routinely monitor the global ocean from space providing some insight into radiation in the ocean (Frouin et al., 2018). Standard products that are operationally provided are the photosynthetically available radiation above the surface (PAR) and the diffuse attenuation coefficient (K_d) at 490 nm ($K_d(490)$). K_d describes how fast the incoming light diminishes with depth. The mean K_d over distant depths z_1 and z_2 can be calculated from the downwelling plane irradiance E_d as (Lee et al., 2005a)

$$K_d(z_1 \leftrightarrow z_2, \lambda) = \frac{1}{z_2 - z_1} \ln \left(\frac{E_d(z_1, \lambda)}{E_d(z_2, \lambda)} \right). \quad (4.1.1)$$

From passive remote sensing, the average K_d of the surface ocean can be retrieved. It contains information of the first optical depth, i.e. the depth at which the incoming radiation below the ocean surface has decreased to around 37% (Gordon and McCluney, 1975). Despite these limitations, it is a valuable parameter used for estimating, e.g., heat budget (Lewis et al., 1990; Morel and Antoine, 1994; Kara et al., 2004) and primary productivity (Platt, 1986; Sathyendranath et al., 1989). $K_d(490)$ and K_d at other wavelengths ($K_d(\lambda)$) can be calculated from ocean color satellite data using empirical (based on band ratios) (Austin and Petzold, 1981; Morel, 1988; Mueller, 2000; Morel and Maritorea, 2001; Chauhan et al., 2003; Werdell and Bailey, 2005; Doron et al., 2007; Zhang and Fell, 2007; Kratzer et al., 2008; Shen et al., 2017), semi-analytical (Lee et al., 2005a; Morel et al., 2007a; Wang et al., 2009), or neural network (Jamet et al., 2012) approaches.

Current and planned upcoming ocean color satellites can only provide limited information on light penetration in the UV. For most ocean color sensors, the shortest wavelength band lies around 412 nm, some reach down to 380 nm. The only recent OC sensor with a band at shorter wavelengths, 355 nm, is the Ultraviolet Imager on HaiYang-1C satellite launched in 2018 (<http://www.nsoas.org.cn/eng/item/204.html>). The Ocean Color

Instrument of the upcoming PACE mission is planned to record radiances from 340 nm with spectral resolution of 5 nm. However, the PACE mission will not be launched before November 2023 (<https://pace.oceansciences.org/>). So far, the only existing UV product for ocean color applications is the above-surface planar spectral UV irradiance at noon from the hyperspectral Ozone Monitoring Instrument (OMI) (Tanskanen et al., 2006). Information on K_d in the UV has been indirectly obtained from ocean color information at visible wavelengths in several studies. K_d in the UV is empirically related to K_d or absorption at visible wavebands (Smyth, 2011; Lee et al., 2013), blue-green reflectance ratios (Johannessen et al., 2003), or principle components of visible reflectances (Fichot et al., 2008) or it is estimated using an ocean case-1 UV model with the chlorophyll-a concentration (Chla) from ocean color sensors as input (Vasilkov et al., 2005). All of these approaches rely on the rather weak relationship of optical properties between the UV and visible wavelength range (Vasilkov et al., 2002b; Morel et al., 2007b). Wang et al. (2021) developed a deep-learning system to obtain the remote-sensing reflectance (R_{rs}) and from this K_d at 360, 380, and 400 nm from R_{rs} at visible bands. They demonstrate the non-linearity between R_{rs} at UV and visible wavelengths and do not apply their approach to shorter wavelengths than 360 nm because there is no clear relationship between the phytoplankton absorption coefficient below 350 nm and that at visible wavelengths (due to UV pigments). Frouin et al. (2018) have summarized user needs for radiometric satellite products, revealing a need for information on ocean radiation in the UV. They suggest to fill parts of this knowledge gap by utilizing current satellite missions such as Sentinel-5P for UV products.

In this study, Sentinel-5P Tropospheric Monitoring Instrument's (TROPOMI) UV and visible bands are exploited for deriving two novel K_d products in the UV. These products describe the average K_d in the wavelength regions 312.5 to 338.5 nm and 356.5 to 390 nm for the first optical depth. In addition, the average K_d is derived in the range 390 to 423 nm. The approach is based on (Dinter et al., 2015) further adapted in chapter 3, where this latter K_d in the blue spectral range was derived from SCIAMACHY (Scanning Imaging Absorption Spectrometer for Atmospheric CHartography), GOME-2 (Global Ozone Monitoring Experiment 2), and OMI satellite data. Differential Optical Absorption Spectroscopy (DOAS) is used to target the vibrational Raman scattering (VRS) signal in the ocean. The number of these inelastic scattering processes depends on the number of photons in the ocean and causes filling-in of absorption structures such as Fraunhofer lines in the solar spectrum. Because VRS is negligible in the atmosphere, the VRS signal found in backscattered radiances measured by satellites can be linked to the radiation in the ocean using radiative transfer simulations.

This study is conceptually showing the feasibility by presenting first results of the novel K_d -UV products and the K_d -blue product. It focuses on one month of TROPOMI data in 2018, 11 May to 9 June, for which in-situ $K_d(\lambda)$ data are available from a R/V Polarstern cruise transecting the Atlantic Ocean from Punta Arenas, Chile, to Bremerhaven, Germany. The quality of these K_d products is evaluated against this in-situ data set and wavelength-converted multispectral K_d products from the Ocean Colour Climate Change Initiative (OC-CCI) data set and the Sentinel-3A Ocean and Land Colour Instrument (OLCI).

4.2 Materials and methods

4.2.1 Data sets

TROPOMI data

The satellite Sentinel-5 Precursor (S5P) hosts the Tropospheric Monitoring Instrument (TROPOMI) (Veefkind et al., 2012). It is in a low Earth orbit and its standard level 2 products provide daily global measurements of atmospheric trace gases and aerosols. The satellite was launched in October 2017. Local solar time at ascending node is 13:30. TROPOMI measures backscattered radiances at a spatial resolution of 3.5 km by 7 km at nadir which was reduced to 3.5 km by 5.5 km in August 2019 due to high signal-to-noise performance. Once per day the solar irradiance is recorded. Measurements are taken in push-broom configuration at a swath width of 2600 km providing daily global coverage. TROPOMI has spectral bands in the UV, visible (VIS), near-infrared, and the shortwave infrared. Band 3 (UV) from 310 nm to 405 nm and band 4 (VIS) from 405 nm to 500 nm are relevant for developing the K_d products in this study. Spectral resolution of these bands is around 0.55 nm. Level 1b TROPOMI radiances V01.00.00 and corresponding daily UVN (bands 1 to 6) irradiances (Vonk, 2018) were used. Clouds shield the radiance signal from the ocean, so the TROPOMI data set was filtered for cloud-free scenes using a cloud fraction of 0.01 as threshold. Cloud fractions were taken from FRESCO type cloud retrieval in the nitrogen dioxide fit window (van Geffen et al., 2019). Pixels over land and inland waters were removed from the data set.

In-situ data

Radiometric data were collected from 11 May to 9 June 2018 on Polarstern expedition PS113, crossing the Atlantic from Punta Arenas, Chile, to Bremerhaven, Germany. K_d

was determined at 19 discrete stations distributed along a transect between the Malvinas upwelling region and the English channel. An irradiance sensor (RAMSES ACC-2-VIS, TriOS GmbH, Germany) covering the wavelength region from 320 nm to 950 nm with a spectral sampling of 3.3 nm, resolution of 10 nm, and accuracy of 0.3 nm was used. It is additionally equipped with an inclination and pressure sensor. The sensor was mounted to a steel frame for vertical profiling of the underwater downwelling irradiance $E_d(z, \lambda)$ at a distance of 5 m to the ship. The general measurement procedure followed [Taylor et al. \(2011\)](#). A second RAMSES ACC-2-VIS sensor mounted on top of the ship recorded the incident downwelling irradiance above the surface $E_d(\lambda, 0^+)$, to correct for incident sunlight variations. Mean K_d was calculated from $E_d(z, \lambda)$ profiles mostly over the depth interval 7 to 22 m. Details on measurement procedure and determination of K_d can be found in [Bracher et al. \(2020\)](#).

4.2.2 Multispectral satellite data

Derived K_d products from TROPOMI were compared to $K_d(490)$ from Sentinel-3A OLCI and the OC-CCI data set. OLCI onboard Sentinel-3A has a spatial resolution of 300 m. Ocean color information is obtained from 21 spectral bands. The operational $K_d(490)$ product is calculated based on the OK2-555 algorithm ([Morel et al., 2007a](#)) which combines a semi-analytical relationship between Chla and R_{rs} ratios with an empirical relation between Chla and $K_d(490)$. OLCI data were downloaded via EUMETSAT Streaming Service. As second multispectral data set, the OC-CCI data set ([Sathyendranath et al., 2019](#)) version 4.2 ([Sathyendranath et al., 2020](#)) (<http://www.esa-oceancolour-cci.org>) was used. It is a merged product consisting of information from MODIS-Aqua and VIIRS sensor for 2018. Data are provided on a sinusoidal grid with 4 km spatial and daily temporal resolution. $K_d(490)$ is retrieved semi-analytically ([Lee et al., 2005a](#)). Absorption and backscattering are first obtained in a quasi-analytical approach ([Lee et al., 2002](#)) and then related to $K_d(490)$ using look-up tables (LUTs) established with radiative transfer modeling.

4.2.3 Algorithm

Vibrational Raman scattering (VRS) is an inelastic scattering process which occurs in the ocean when photons scatter off water molecules ([Walrafen, 1966](#)). It therefore contains information of the amount of photons in the ocean. Photons are scattered to longer wavelengths with a wavelength shift of 33 to 99 nm in the UV-VIS ([Haltrin and Kattawar, 1993](#)). Absorption features such as Fraunhofer lines in the solar spectrum are filled-in by

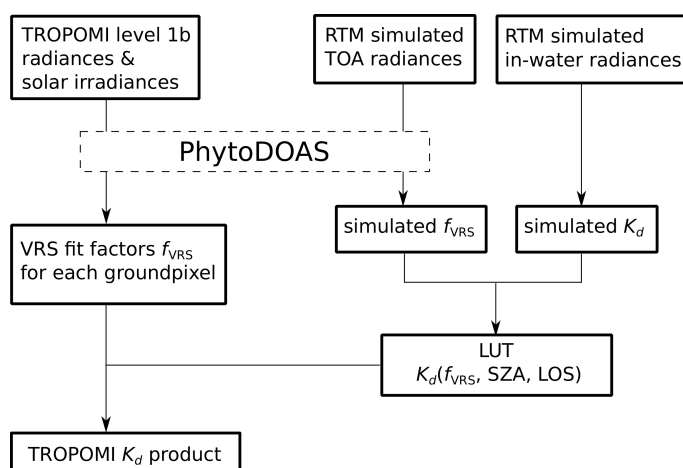


Figure 4.2.1: Flow chart illustrating TROPOMI K_d algorithm.

these photons detectable in backscattered radiances recorded by satellites, appearing as a so-called pseudo-absorption, known as the Ring effect (Grainger and Ring, 1962). Using Differential Optical Absorption Spectroscopy (DOAS), the VRS signal can be identified in backscattered radiances from satellite sensors with sufficient spectral resolution (~ 0.5 nm) (Vasilkov et al., 2002a; Vountas et al., 2003, 2007). Since VRS is negligible in the atmosphere (Vountas et al., 1998), Dinter et al. (2015) exploited these spectral features to infer the light availability and K_d in the ocean via radiative transfer modeling from SCIAMACHY backscattered radiances. Chapter 3 closely followed this approach with some modifications on DOAS and RTM settings to derive K_d from SCIAMACHY and additionally OMI, and GOME-2 for nearly one year of data in 2007. Here, the algorithm is based on these earlier works with minor modifications. In the following, the retrieval steps for deriving K_d from VRS are summarized, see also the flowchart in Figure 4.2.1.

PhytoDOAS

Differential Optical Absorption Spectroscopy (DOAS) (Perner and Platt, 1979) is a method for inferring atmospheric trace gas concentrations from high-frequency absorption features in backscattered radiances (see section 2.11 for details). The optical depth τ is calculated from backscattered radiances I divided by a reference spectrum, e.g., an extra-terrestrial solar spectrum I_0 . Low-frequency features are removed by subtracting a low-order polynomial. Absorption spectra of atmospheric trace gases are fitted to the high-frequency part of the optical depth to infer their concentrations. DOAS has been extended to the ocean domain (PhytoDOAS) for retrieving phytoplankton functional types (Bracher et al., 2009; Sadeghi et al., 2012a), light availability (Dinter et al., 2015), K_d (Dinter et al., 2015, study 1), through VRS (Vountas et al., 2003, 2007), and phytoplankton fluorescence (Wolanin

et al., 2015b) by including (pseudo-) absorption spectra for oceanic constituents and inelastic processes. Pseudo-absorption spectra σ can be calculated from RTM radiances, which are calculated from a model run including (I^+) and excluding (I^-) inelastic processes (Vountas et al., 1998):

$$\sigma = \frac{I^+}{I^-}. \quad (4.2.1)$$

For this study, three VRS fits were performed in three spectral regions 349.5 to 382 nm, 405 to 450 nm, and 450 to 493 nm, in the following referred to as UV, short-blue, and blue window, respectively. The blue and short-blue windows lie in TROPOMI's band 4, whereas the UV window lies in band 3. VRS fit factors have been successfully retrieved in the UV window using data from the GOME and SCIAMACHY sensor (Vountas et al., 2003, 2007). The blue window is slightly shorter than in Losa et al. (2017a) and chapter 3, because TROPOMI's band 4 ends before 497 nm. VRS fits in the short-blue window are tested here for the first time. Considering all relevant processes in these fit windows for targeting VRS, the DOAS equation can be formulated as:

$$\tau = \ln \frac{I_0}{I} = \sum_{j=1}^J S_{a,j} \sigma_{a,j}(\lambda) + S_{VRS} \sigma_{VRS}(\lambda) + S_{OC} \sigma_{OC}(\lambda) + S_R \sigma_R(\lambda) + \sum_{m=0}^M x_m \lambda^m. \quad (4.2.2)$$

with atmospheric absorption cross sections $\sigma_{a,j}(\lambda)$ of J trace gases and pseudo-absorption cross section $\sigma_R(\lambda)$ for Rotational Raman Scattering (RRS) in the atmosphere based on Equation 4.2.1. The pseudo-absorption cross section for VRS (σ_{VRS}) was calculated based on Equation 4.2.1 from modeled case I TOA radiances for Chla of 0.1 mg/m³ and solar zenith angle (SZA) of 40° (see Figure 4.2.2). The ocean weighting function (σ_{OC}) was defined as in Dinter et al. (2015) calculated from case I TOA radiances for a SZA of 40°. The weighting function was calculated for a change in Chla from 0.1 mg/m³ to 0.11 mg/m³. For the blue and short-blue window, following atmospheric absorbers were fitted: absorption cross sections for ozone (O₃) (Serdyuchenko et al., 2014), nitrogen dioxide (NO₂) (Vandaele et al., 1998), water vapor (H₂O) (Rothman et al., 2013, using HITRAN 2009), and oxygen dimer (O₄) (Thalman and Volkamer, 2013). The VRS fits in the blue and short-blue window only differ in fit window, whereas the UV window fit additionally differs in fitted atmospheric absorbers. In the UV window, the absorption cross section for bromine monoxide (BrO) was additionally fitted, but water vapor was removed from the list of absorbers. For all three fit windows, a second order polynomial was chosen ($M = 2$). Equation 4.2.2 is solved for the fit factors S and the polynomial coefficients x_m .

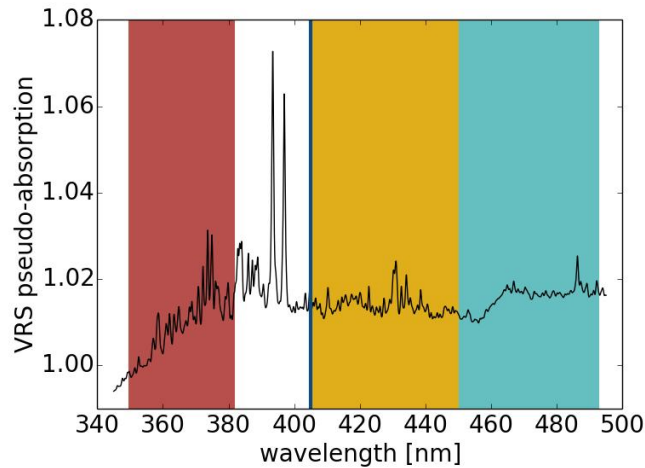


Figure 4.2.2: VRS pseudo-absorption spectrum as function of wavelength. Colored areas indicate UV (red), short-blue (yellow) and blue (light-blue) DOAS fit window. The thick blue line marks the end/start of band 3/4.

RTM SCIATRAN

The ocean-atmosphere coupled RTM SCIATRAN (Blum et al., 2012; Rozanov et al., 2014, 2017, <https://www.iup.uni-bremen.de/sciattran/>) version 4.0.8 was used for radiance simulations to calculate pseudo-absorption cross sections and LUTs. Two types of RTM simulations have to be performed for the LUTs used to convert VRS fit factors to K_d . On the one hand top-of-atmosphere (TOA) radiances and on the other hand underwater radiant fluxes for various ocean scenarios are needed. 23 different case-1 scenarios (Morel and Maritorena, 2001) were modeled with Chla ranging between 0 and 30 mg/m³, i.e., optical properties of the ocean are driven by Chla, other optically active constituents such as CDOM change proportionally. Similar to the case-1 model in Hydrolight (Mobley and Sundman, 2013), the phytoplankton absorption spectrum (Prieur and Sathyendranath, 1981) was extrapolated into the UV range as an exponentially decaying function leading to a CDOM-dominated UV case-1 model. A background maritime aerosol was assumed with aerosol optical depth (AOD) of 0.1 at 550 nm (LOWTRAN, Kneizys et al., 1988). Detailed model settings can be found in section 3.2.5 adapted from Dinter et al. (2015).

TROPOMI-specific adaptations were made for this study. Since spectral alignment is very important for the DOAS retrieval, a TROPOMI-measured extraterrestrial solar spectrum was used for the TOA radiance calculations. A solar spectrum measurement from a middle row of the charge-coupled device (row 225, 0-based) from May 2018 was chosen. Underwater fluxes were simulated at a spectral resolution of 0.5 nm using a Fraunhofer atlas (Chance and Kurucz, 2010) since they are insensitive to the exact spectral resolution.

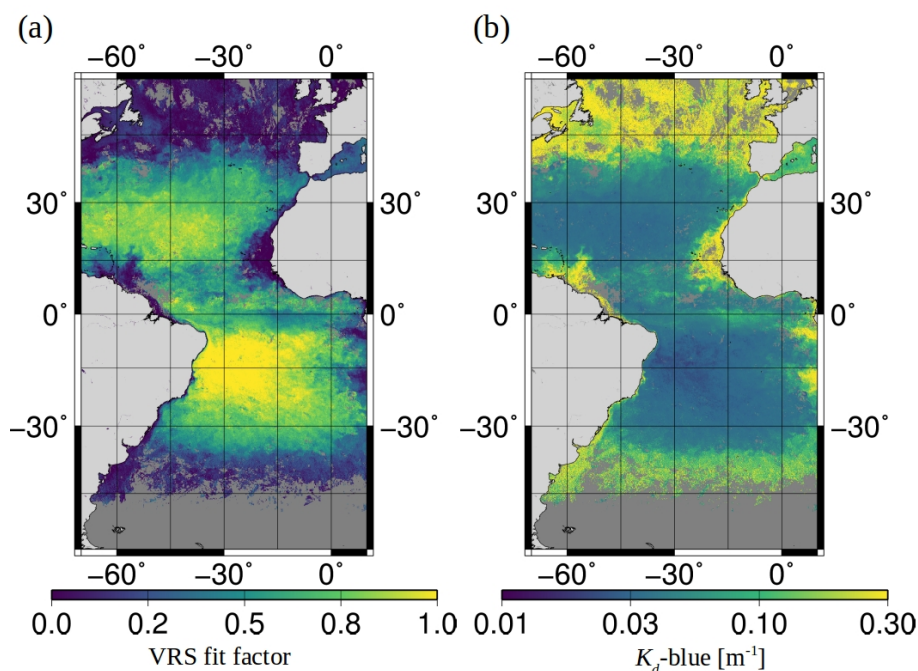


Figure 4.2.3: (a) Original VRS fit factors and correspondingly derived (b) K_d -blue, both, gridded at 0.083° as mean for 11 May to 9 June.

Geometry settings were chosen to cover all of TROPOMI’s viewing geometries (5° steps for SZA and viewing zenith angle (VZA)), except for the azimuth angle which was held constant (90°).

Look-up-table for deriving K_d from VRS

The LUT for deriving K_d from VRS was built by combining VRS PhytoDOAS fits on simulated TOA radiances with K_d calculated from simulated underwater radiant fluxes. PhytoDOAS fit settings for the retrieval of theoretical VRS fit factors from the modeled TOA radiances are the same as for the retrieval on satellite radiances (see above) except for atmospheric cross sections. Water vapor was not fitted, since it was not included in the SCIATRAN simulation. K_d was calculated according to Equation 4.1.1 for each wavelength from the underwater radiant flux simulations, which give, amongst others, the downwelling irradiance at discrete depths z . The first optical depth, z_{90} , was determined via linear interpolation of the log-transformed downwelling irradiance E_d at depth. Taking into account the wavelength shift of the VRS process, resulting K_d were then averaged over wavelength between 312.5 nm and 338.5 nm for K_d -UVAB, between 356.5 nm and 390 nm for K_d -UVA, and between 390 nm and 423 nm for K_d -blue. K_d calculations and VRS PhytoDOAS retrievals were performed for each SZA and each VZA separately. VRS

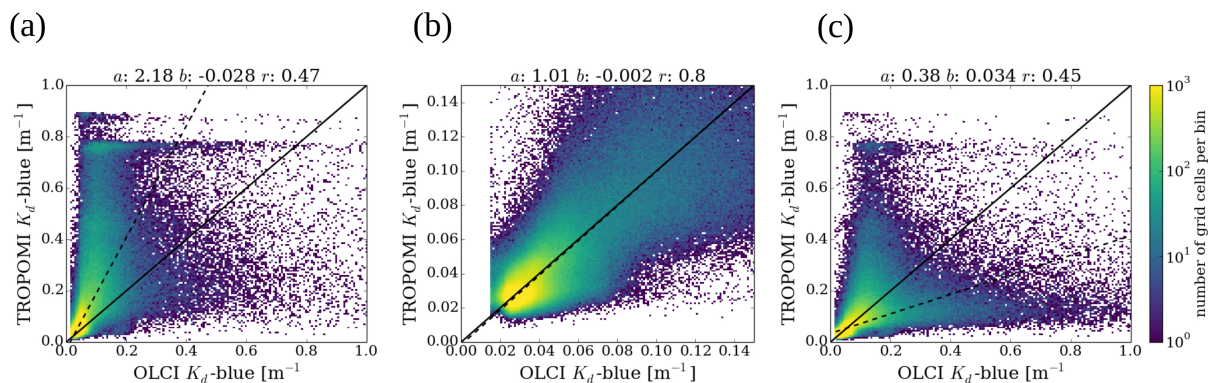


Figure 4.2.4: K_d -blue derived from (a) original VRS fit factors and (b), (c) offset-corrected VRS fit factors in comparison to OLCI K_d -blue as mean for 11 May to 9 June. The comparison was calculated on a daily basis taking data sets gridded at 0.083° as input. (b) shows the comparison for a reduced data set, K_d -blue $< 0.15 \text{ m}^{-1}$, used to optimize the applied offset such that the slope of an orthogonal linear regression is equal to unity. (c) shows the comparison for the full data set. Total least-squares regression results (shown as black-dashed line) can be found on top of the figure, together with the Pearson correlation coefficient r . The black solid line is the 1:1 line.

fit factors were matched with K_d calculated from scenarios with the same Chla. As an update to the two-dimensional LUT in chapter 3, a three-dimensional LUT was created where K_d is a function of VRS fit factor, SZA, and (newly added) VZA.

Offset correction

TROPOMI-derived K_d -blue was much higher than expected (discussed in section 4.4.1), necessitating an empirical offset correction, see Figures 4.2.3 and 4.2.4. K_d -blue much better agreed with the wavelength-converted $K_d(490)$ from OLCI and OC-CCI when a constant was added to the VRS fit factors. Generally, TROPOMI K_d -blue is closer to the OLCI K_d -blue than the OC-CCI K_d -blue and correlation is highest for low K_d values (see Table 4.3.2). Hence, we concentrated on comparing the low values ($K_d < 0.15 \text{ m}^{-1}$) from the TROPOMI K_d -blue to those from the OLCI K_d -blue data set to determine the offset that best corrects the data. The comparison was calculated for the entire study time period using 5 minute gridded daily K_d data as input. The offset correction was optimized such that a linear total-least-square regression on this comparison data set (limited to $K_d < 0.15 \text{ m}^{-1}$) yielded a slope close to one. The optimal offset was found to be 0.186. Regression statistics for this setting were a slope of 1.01, intercept of -0.002 m^{-1} , and Pearson correlation coefficient of 0.80. The offset was used to correct all VRS fit factors

and by that the whole K_d range.

4.2.4 Sensitivity analysis

The algorithm sensitivity was evaluated with respect to model settings similar to the sensitivity analysis presented in section 3.2.6. Here, next to aerosol and CDOM settings, the sensitivity analysis was extended to the parameters: CDOM slope, UV-absorbing pigments, liquid water absorption, wind speed, and ozone concentration.

For each parameter, the sensitivity was analyzed as follows. An RTM simulation was performed to calculate radiances and radiant fluxes in which one parameter is increased or decreased with respect to the standard scenario used to build the LUT as described in section 4.2.3. The PhytoDOAS fit was performed on this modified scenario. Resulting VRS fit factors were converted to K_d using the LUT. The resulting K_d , K_d^{der} , was compared to the expected K_d , K_d^{exp} , calculated from the radiant fluxes of the modified scenario. The deviation of derived from expected K_d was determined, $(K_d^{\text{der}} - K_d^{\text{exp}})/K_d^{\text{exp}}$.

Since mainly only a change in inherent optical properties changes K_d , the parameters can be separated in two groups. One group comprises the atmospheric and surface parameters which have no or only a minimal effect on the mean K_d over the first optical depth, but may influence VRS since scattering is proportional to light intensity. The second group comprises the oceanic parameters which affect both, K_d and VRS. For the second group, K_d changes can be large, however, VRS changes accordingly, and K_d is retrieved correctly within an uncertainty which is only a fraction of the change in K_d .

Atmospheric and surface parameters

Parameters within the first group were varied as follows: wind speed was reduced to 1 m/s and increased to 8 m/s (standard: 4.1 m/s); aerosol optical depth (AOD) was reduced to 0.05 and increased to 0.2 (standard: 0.1); ozone profile was changed to one with reduced total ozone column of 290 DU (standard: 420 DU). Figure 4.2.5 shows the influence of these selected atmospheric and surface parameters on the filling-in by VRS as determined by Equation 4.2.1 for Chla of 0.1 mg/m³. The influence of AOD and wind speed is largest for the blue fit window and decreases with decreasing wavelength. It is negligible for wavelengths smaller 360 nm. The influence of the ozone concentration is largest at the short wavelengths. It is negligible for wavelengths larger 370 nm. Results for changes in AOD and wind speed are therefore only presented for the short-blue and blue fit window and in ozone for the UV fit window. The influence of aerosols on the K_d -blue retrieval was already presented in section 3.2.6. A constant deviation over the K_d -blue range was

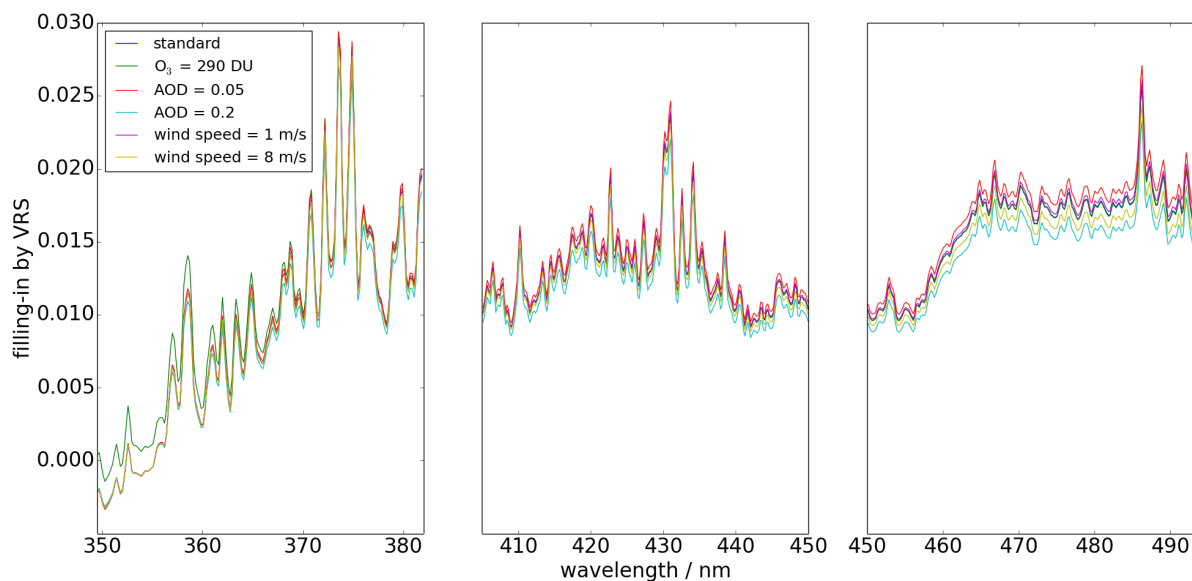


Figure 4.2.5: Filling-in by vibrational Raman scattering for different model parameterizations in comparison to the standard simulation for the three wavelength ranges of the PhytoDOAS VRS fits.

found which was less than -5% for the reduced AOD scenario and less than $+20\%$ for the increased AOD scenario. Figures 4.2.6 (a) and (b) show that the influence of aerosols on the K_d -UVA retrieval is similar in magnitude. The effect of aerosols on the K_d -UVAB retrieval (not shown) is significantly lower with only $+5\%$ deviation for the increased AOD scenario. Figures 4.2.6 (c) and (d) show the K_d -blue retrieval sensitivity with respect to wind speed. For most SZA, an altered wind speed causes deviations from the expected K_d -blue well below 5% . Larger deviations of up to $\pm 10\%$ are found for specific SZA at the lower SZA range depending on wind speed. The influence on K_d -UVA was even smaller as expected from the behavior of the filling-in by VRS. For the same specific SZA, deviations up to $\pm 5\%$ can be found (not shown). The influence of the ozone column on the K_d -UVAB retrieval is shown in Figure 4.2.6 (e) and is below 5% .

It can be seen that the retrieval performance is not robust for $K_d > 0.3 \text{ m}^{-1}$, outside of grey-shaded area in Figure 4.2.6. Later on, results will show that TROPOMI K_d can not be well retrieved for scenes with $K_d > 0.3 \text{ m}^{-1}$, discussed in section 4.4.3. Also, the retrieval is less robust at high SZA and at high VZA, which causes large error bars in the plots. This effect should be kept in mind, when the algorithm is applied in high latitudes. In the investigated Atlantic region, SZA are only moderately high and satellite pixels with high VZA are often screened out by the cloud filter due to their larger pixel size.

In summary, the influence of atmospheric and surface parameterizations is generally

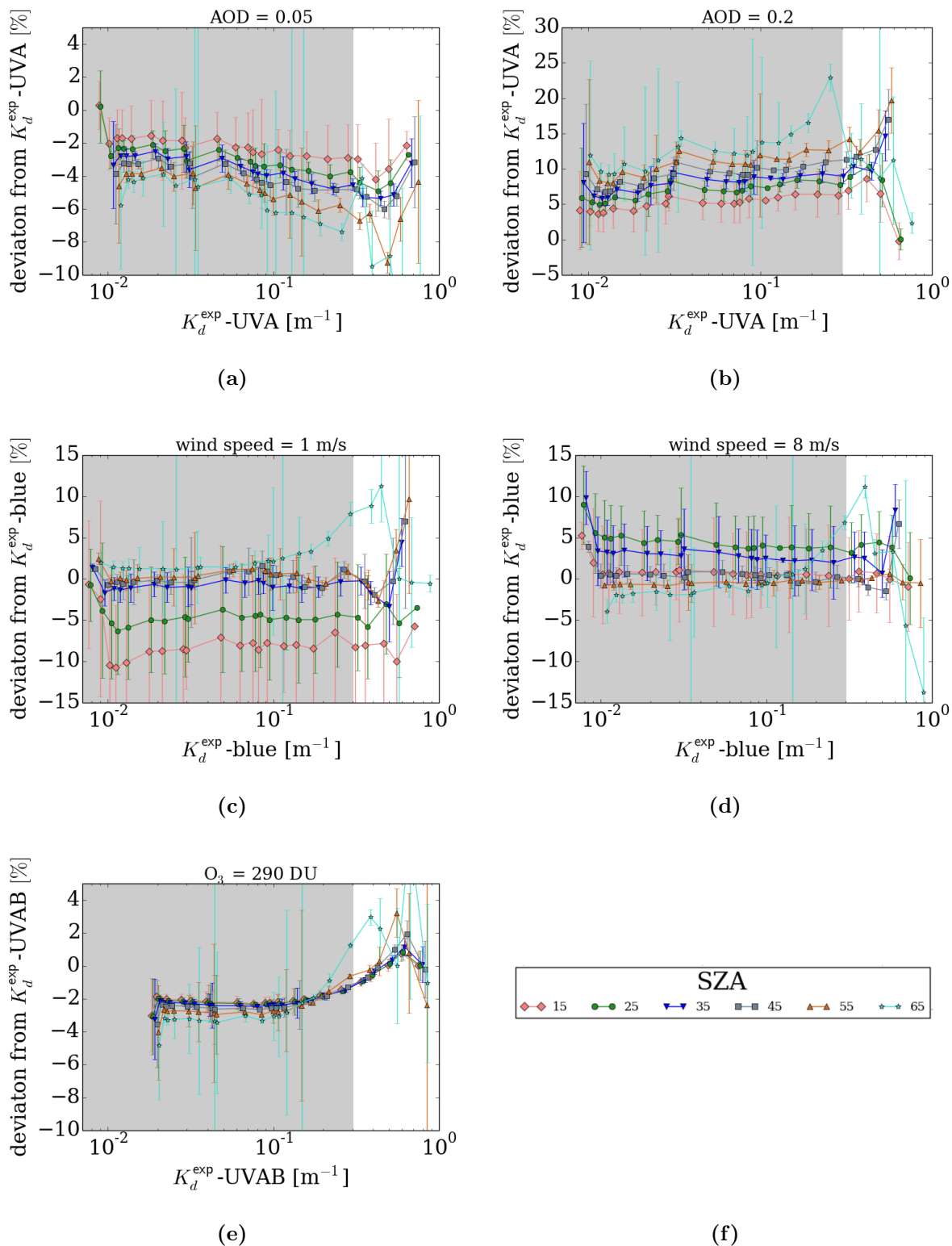


Figure 4.2.6: Deviation of derived from expected K_d in case of (a) reduced AOD, (b) increased AOD, (c) reduced wind speed, (d) increased wind speed, and (e) reduced ozone column for different SZA. Results were averaged for different VZA with the standard deviation given as error bar. (a), (b) show results for K_d -UVA, (c), (d) for K_d -blue, and (e) for K_d -UVAB.

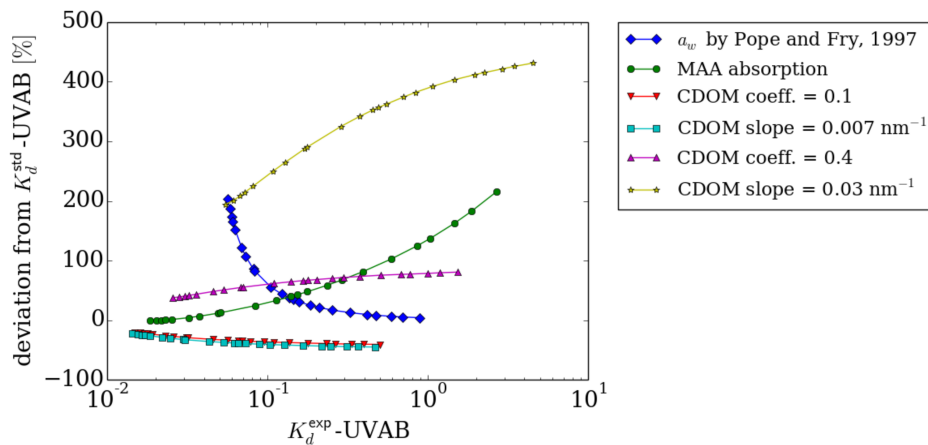


Figure 4.2.7: Deviation of $K_d^{\text{exp}}\text{-UVAB}$ as in the modified scenario from $K_d\text{-UVAB}$ in the standard scenario as function of $K_d^{\text{exp}}\text{-UVAB}$ for tested variations in oceanic parameters.

low on the K_d retrievals. Uncertainties increase with the difference between conditions found for an actual satellite scene and the average ones used in the simulated standard scenario. Largest uncertainties can be expected for scenes with high aerosol loadings, which only occur in specific regions and times of the year (Remer et al., 2008). For the Atlantic region, Saharan dust storms can have a significant influence (e.g. van der Does et al., 2016). Maritime aerosols were investigated here, terrestrial dust might have even stronger impacts. These critical scenes are largely removed through the strict cloud filter criterion used in this study (cloud fraction of 0.01). In the future, the dimensionality of the LUT can be increased, when confidence in performance of K_d retrievals has been gained by comparison with larger in-situ data sets than available for this study. The total ozone column, AOD, and wind speed can be included in the LUT and taken from ancillary data (some variables also available from TROPOMI) to further reduce uncertainty in TROPOMI K_d data sets.

Oceanic parameters

The case-1 assumption is generally not valid in the UV domain. The absorption coefficient can not be accurately described using Chla (Vasilkov et al., 2002b; Morel et al., 2007b). The influence of the case-1 parameterization used for the optical constituents in the ocean on the ultraviolet K_d retrievals needs to be checked carefully. As introduced in section 4.2.3, the case-1 parameterization for the visible wavelength range was used in combination with a recent pure water absorption spectrum accurately measured for UV wavelengths (Mason et al., 2016). Nevertheless, the influence of the choice of water absorption spectrum was checked. A modified scenario was simulated with liquid water absorption coefficients

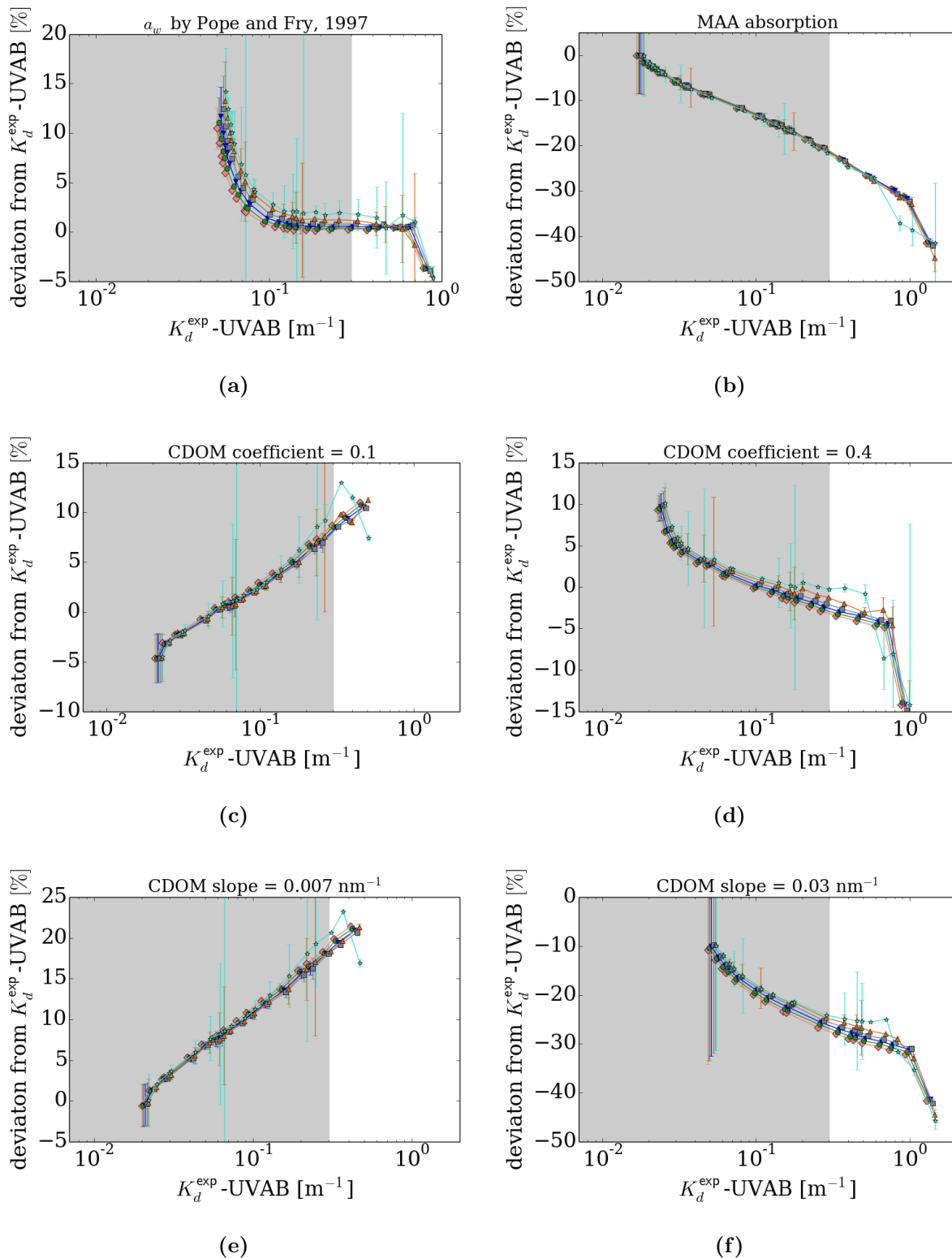


Figure 4.2.8: Deviation of derived from expected K_d -UVAB in case of (a) reduced and (b) increased CDOM coefficient, (c) reduced and (d) increased CDOM slope, (e) liquid water absorption by [Pope and Fry \(1997\)](#), and (f) MAA absorption as function of expected K_d -UVAB. Results were averaged for different VZA with the standard deviation given as error bar. See [Figure 4.2.6](#) for symbol legend.

from Pope and Fry (1997) which significantly differ at short wavelengths from those measured by Mason et al. (2016), see section 2.9.1. High uncertainty also lies within the settings for phytoplankton and CDOM absorption. Presence of mycosporine amino acids (MAA) causes higher UV absorption than prescribed in the standard case-1 parameterization. MAA absorb between 320 and 350 nm with a peak around 330 to 340 nm (Vernet et al., 1994; Bracher and Wiencke, 2000). Presence of these UV-absorbing pigments should therefore mainly influence K_d -UVAB (Wang et al., 2021). A modified scenario was simulated using a phytoplankton absorption spectrum with medium MAA absorption (S9 from Bracher and Wiencke (2000)). High variability can also be expected for the CDOM slope, 0.01 to 0.03 nm^{-1} (Vodacek and Blough, 1997) as compared to 0.014 nm^{-1} in the standard case-1 scenario. Modified RTM simulations were made with a reduced CDOM slope of 0.007 nm^{-1} and an increased CDOM slope of 0.03 nm^{-1} . Also the CDOM coefficient was modified as in section 3.2.6, while keeping the CDOM slope at 0.014 nm^{-1} .

Figure 4.2.7 shows the change in K_d -UVAB caused by the altered parameterizations with respect to the standard scenario (K_d^{std}), calculated as $(K_d^{\text{exp}} - K_d^{\text{std}})/K_d^{\text{std}}$. Implemented changes cause drastic changes in K_d -UVAB. The influence of the water absorption coefficients, MAA absorption, and a high CDOM slope is especially large. For the clearest waters, the water absorption by Pope and Fry (1997) leads to an increase in K_d -UVAB by 200%. A similar increase is found for MAA absorption for waters with highest Chla. Since the reference wavelength for CDOM absorption is in the visible spectral region, an increase in CDOM slope causes extreme changes in K_d -UVAB (about 200-430%). The other tested variations in CDOM parameterization lead to comparably moderate changes in K_d -UVAB below 100%.

Figure 4.2.8 shows retrieval sensitivity results for the oceanic parameters for K_d -UVAB. The focus here lies on the K_d range below 0.3 m^{-1} . The change in water absorption spectrum results in an overestimation of 15% for clear water scenarios which reduces to zero for high Chla scenarios, see Figure 4.2.8 (a). The overestimation is counter-intuitive, since K_d^{exp} is higher than K_d^{std} . A changed parameterization often also causes a spectral change in K_d which impacts the VRS fit quality and can result in this unexpected behavior. MAA absorption leads to an underestimation which increases to 20% at K_d -UVAB = 0.3 m^{-1} and can be significantly higher for higher K_d -UVAB (Figure 4.2.8 (b)). A change in CDOM coefficient causes deviations of $\pm 10\%$ (Figures 4.2.8 (c) and (d)). A reduced CDOM slope results in an overestimation of up to 20% and an increased CDOM slope in an underestimation of up to 30% depending on Chla as shown in Figures 4.2.8 (e) and (f). The influence on the K_d -UVA retrieval was also evaluated with respect to water absorption and CDOM (results not shown). Results are qualitatively similar, however, the

influence is generally smaller. Overestimation up to 10% for the change in water absorption, overestimation of up to 10% in case of reduced CDOM slope, and underestimation up to 25% in case of increased CDOM slope are found. A change in CDOM coefficients leads to similar deviations of $\pm 10\%$.

In conclusion, the K_d -UV retrievals are rather insensitive to the chosen RTM parameterization compared to the large variability that this parameterization causes in K_d in the ultraviolet spectral range.

4.2.5 K_d product quality evaluation

K_d products were evaluated against in-situ and multispectral K_d data sets. For all comparisons, we provide metrics typically used for ocean color variables (Brewin et al., 2015; Seegers et al., 2018): the slope and intercept of least-square regressions, the Pearson correlation coefficient, the bias, the mean absolute error (MAE), root-mean-square difference (RMSD), and, where useful, the unbiased RMSD, calculated as $\sqrt{\text{RMSD}^2 - \text{bias}^2}$.

Wavelength conversion for $K_d(490)$

To compare the TROPOMI-derived K_d products to $K_d(490)$ from OLCI and OC-CCI, $K_d(490)$ needs to be wavelength-converted first. The spectral relationship between K_d -blue, K_d -UVA, K_d -UVAB and $K_d(490)$ was investigated based on the in-situ $K_d(\lambda)$ from 19 stations of PS113. K_d -blue, K_d -UVA, K_d -UVAB were determined from the in-situ $K_d(\lambda)$ by averaging over the corresponding wavelength ranges. They were then plotted against the in-situ $K_d(490)$. Linear regression results can be found in Table 4.2.1. There is a tight relationship between K_d -blue and $K_d(490)$. Correlation with $K_d(490)$ decreases with decreasing wavelength. Based on these results, OLCI and OC-CCI $K_d(490)$ were wavelength-converted using

$$K_d\text{-blue/-UVA/-UVAB} = a \cdot K_d(490) + b \quad (4.2.3)$$

with slope a and intercept b from Table 4.2.1.

Match-up analysis

Match-ups between geolocation of PS113 stations and TROPOMI ground pixels were calculated using a loose criterion given the low number of stations ($N = 19$). For each station, TROPOMI match-ups were searched within ± 2 days and a radius of 5.5 km. If several match-ups were found in this time period, the mean TROPOMI K_d was calculated from all

Table 4.2.1: Linear least-square regression results for in-situ K_d -blue, K_d -UVA and K_d -UVAB compared against in-situ $K_d(490)$ from 19 stations during PS113.

K_d	slope a	intercept b [m^{-1}]	Pearson correlation r
blue	1.40	-0.008	0.98
UVA	1.58	0.000	0.93
UVAB	2.57	0.012	0.84

match-ups per station. The standard deviation was noted as uncertainty of the TROPOMI K_d . Using this loose criterion, match-ups were found for 8 stations. OLCI and OC-CCI data were used to further quality control these 8 match-ups. The same spatial and temporal collocation criteria were applied to high-resolution OLCI data to find the corresponding OLCI data for each match-up. Following the Sentinel-3 ocean color validation protocol (EUMETSAT, 2021), OLCI match-ups were only considered valid if half of the pixel box was filled and if the coefficient of variation was not larger than 0.2. In addition, OC-CCI match-ups were determined with spatial collocation criterion of 1 by 1 (corresponding to TROPOMI criterion) and 3 by 3 pixel box to additionally check the spatial homogeneity as for OLCI. 7 of the TROPOMI match-ups were confirmed to be valid.

4.3 Results

Figure 4.3.1 shows VRS fit factors for the three PhytoDOAS fit windows in the (a) UV, (b) short-blue, and (c) blue in the Atlantic Ocean for the time period 11 May to 9 June. VRS fit factors in the blue window are presented offset-corrected. The data were gridded to 0.083° (~ 9 km). For all three fit windows, high and low VRS fit factors are found in typically low and high Chla regions corresponding to low and high light penetration into the ocean, respectively. As expected, the VRS signal decreases with decreasing wavelength. Fit quality is similar for the PhytoDOAS fits in all three fit windows. The average root mean square (RMS) of all fit residuals in this area and time period and its standard deviation were evaluated to $1.0 \cdot 10^{-3} \pm 3 \cdot 10^{-4}$ for the UV (excluding 26 outliers with $\text{RMS} > 4$), $0.9 \cdot 10^{-3} \pm 2 \cdot 10^{-4}$ for the short-blue, and $1.0 \cdot 10^{-3} \pm 3 \cdot 10^{-4}$ for the blue fit window. VRS fit factors from different fit windows are not strictly correlated, e.g., differences appear around Newfoundland and Great Britain.

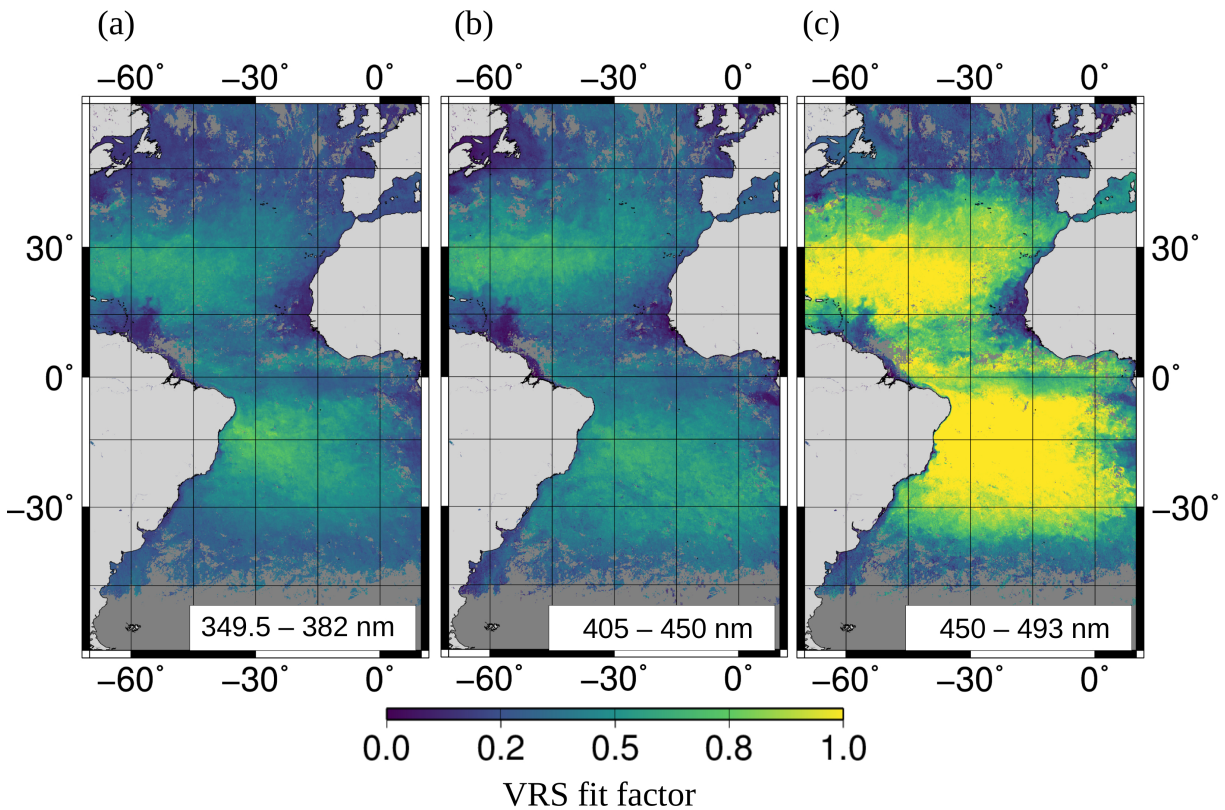


Figure 4.3.1: VRS fit factors in the (a) UV, (b) short-blue, and (c) blue fit window in the Atlantic Ocean gridded at 0.083° as mean for 11 May to 9 June 2018.

K_d was derived from these VRS fit factors using separate LUTs for each wavelength region. Figure 4.3.2 shows the resulting (a) K_d -UVAB, (b) K_d -UVA, and (c) K_d -blue in the Atlantic Ocean gridded to 0.083° over the time period from 11 May to 9 June 2018. Lowest K_d are found in the North and South Atlantic Gyres, highest K_d in the upwelling regions along the African coast and the Amazon river plume. With decreasing wavelength, K_d increases. However, K_d -UVAB is not generally larger than K_d -UVA. In the upwelling regions off the coast of West African, the Amazon river plume, around Newfoundland, and around Great Britain the ratio K_d -UVA/ K_d -UVAB is larger than 1 (roughly 1.25 on average, 2 in extreme cases). K_d -blue is strikingly larger than K_d -UVA and UVAB in the productive areas north of the Northern Atlantic Gyre.

Derived TROPOMI K_d products were compared to in-situ K_d measurements taken during expedition PS113. In general, the monthly mean satellite K_d matches well the in-situ point data values. For a direct comparison, match-ups between TROPOMI and station data were evaluated (Figure 4.3.2). Match-ups for TROPOMI K_d -UVAB, K_d -UVA, and K_d -blue plotted against the corresponding in-situ K_d (Figure 4.3.3) show an overall good

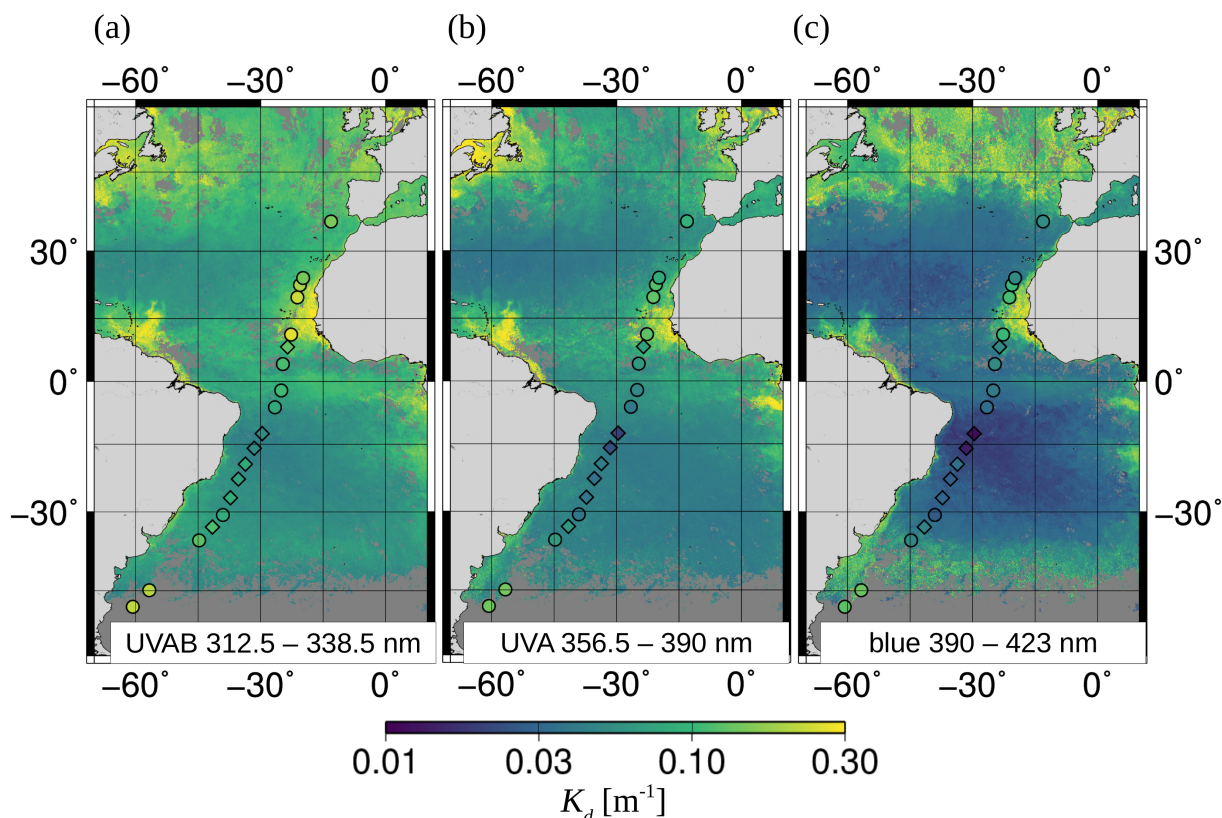


Figure 4.3.2: TROPOMI (a) K_d -UVAB, (b) K_d -UVA, and (c) K_d -blue in the Atlantic Ocean gridded at 0.083° as mean for 11 May to 9 June 2018. Accordingly, K_d -UVAB, K_d -UVA, and K_d -blue measured in-situ at 19 stations during expedition PS113 are overlaid as diamonds (match-ups) and circles (unmatched stations).

agreement for all three spectral wavelength regions (correlation between $r = 0.51$ and 0.85), considering the low number of match-ups and loose match-up criterion. TROPOMI K_d -blue shows good agreement with the in-situ K_d -blue, which might not be so surprising since the VRS fit factors were offset-corrected for this wavelength range such that agreement is maximized for low K_d -blue with OLCI K_d -blue. Linear regression obtains a slope of 0.83 and an intercept of 0.01 m^{-1} . A slightly lower slope is obtained for TROPOMI K_d -UVAB and a higher one for K_d -UVA (Table 4.3.1). TROPOMI K_d -UVAB covers a larger range of K_d values than the other two K_d , yielding the highest correlation coefficient. For high K_d -UVAB values, TROPOMI tends to underestimate K_d -UVAB. Bias, RMSD, and MAE increase with decreasing wavelength (Table 4.3.1). Considering the unbiased RMSD, performance of TROPOMI K_d -blue and K_d -UVAB is similar and worse for K_d -UVA.

TROPOMI K_d -blue was compared to K_d data from the multispectral OLCI and OCCI data sets. For the latter, $K_d(490)$ was converted to K_d -blue via a linear wavelength

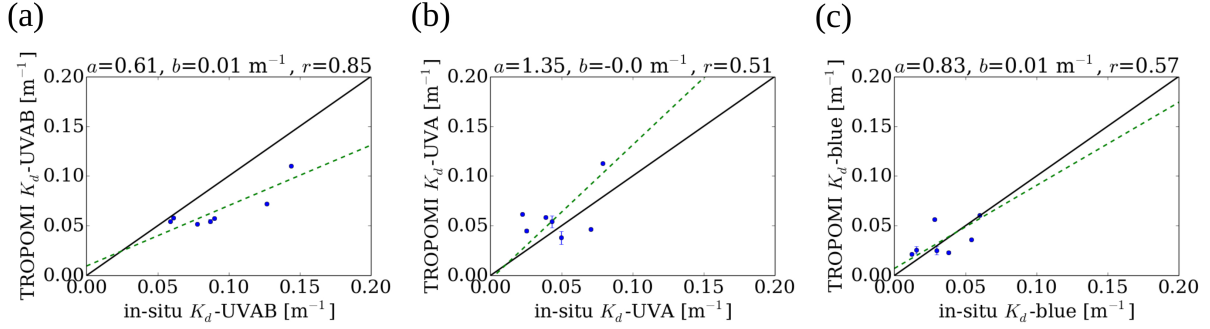


Figure 4.3.3: TROPOMI (a) K_d -UVAB, (b) K_d -UVA, and (c) K_d -blue against in-situ K_d -UVAB, K_d -UVA, and K_d -blue. Match-ups between TROPOMI K_d data and PS113 in-situ data were searched for within ± 2 days and 5.5 km radius of the in-situ measurement. If more than one match-up was found within these search criteria, the mean TROPOMI K_d was calculated with standard deviation shown as error bar.

Table 4.3.1: Metrics for the match-ups between TROPOMI against in-situ K_d -UVAB, K_d -UVA, and K_d -blue. Given are slope a and intercept b from linear least-square regression, Pearson correlation coefficient r , bias, mean absolute error (MAE), and (unbiased) root mean square difference (RMSD).

K_d	a	b [m^{-1}]	r	bias [m^{-1}]	MAE [m^{-1}]	RMSD [m^{-1}]	unbiased RMSD [m^{-1}]
UVAB	0.61	0.01	0.85	-0.027	0.027	0.031	0.015
UVA	1.35	-0.002	0.51	0.013	0.023	0.025	0.021
blue	0.83	0.01	0.57	0.002	0.012	0.015	0.015

conversion scheme (Table 4.2.1). Since this wavelength conversion is principally valid for relating $K_d(490)$ to K_d -blue, the comparison was restricted to K_d -blue and not extended to the UV K_d . For the study period and on the same grid as in Figures 4.3.1 and 4.3.2, Figure 4.3.4 shows K_d -blue for (a) TROPOMI in comparison to (b) OLCI and (c) OC-CCI. Overall, TROPOMI K_d -blue patterns resemble the multispectral ones (e.g., gyres and productive areas around the Amazon river plume, Mauretanian upwelling system, English Channel). Regional differences are observed between TROPOMI and the multispectral K_d -blue, but also among the multispectral products. In the Atlantic gyres, OC-CCI K_d -blue is significantly higher than the other two products. Similar to OLCI, OC-CCI K_d -blue is lower in the North than in the South Atlantic Gyre, whereas TROPOMI K_d -blue is lower in the South. In the productive areas in the North Atlantic, the TROPOMI K_d -blue product appears noisier than the multispectral products. A distinct difference again is visible near Newfoundland. OLCI and OC-CCI show similar high- K_d patterns north of Newfoundland whereas this pattern does not fully occur in the TROPOMI K_d -blue product. Differences appear in maximum values south of 40°S, where SZAs are large and data coverage is low and differs between sensors. Despite these differences between the three data sets, comparison with RMSD (Figure 4.3.4 (d)) as provided in the OC-CCI data set (converted to the blue spectral region) shows that these differences are on the order of the uncertainty of the OC-CCI product (see Figure 4.3.5).

All above mentioned data sets were gridded to 0.083° on a daily basis for the study period. Then, the satellite K_d -blue products were intercompared (TROPOMI *vs.* OLCI, TROPOMI *vs.* OC-CCI, and OLCI *vs.* OC-CCI) as well as the three TROPOMI K_d products among each other either based on the full data set or on a masked data set, where values above 0.3 m⁻¹ were excluded (Table 4.3.2). As can be seen from Figure 4.3.2, most satellite scenes are within this masked data set. Correlations between masked data sets are generally much larger than for full data sets. Significant correlation is found between TROPOMI K_d -blue and the multispectral K_d -blue, with slightly better agreement between TROPOMI and OLCI, $r = 0.77$ for masked data set, than between TROPOMI and OC-CCI, $r = 0.74$ for masked data set. We note that the VRS fit factors underlying the K_d -blue product were corrected such that TROPOMI *vs.* OLCI yields a slope of one for an even smaller data set (K_d -blue < 0.15 m⁻¹). For the larger masked data set (K_d -blue < 0.3 m⁻¹), a slope of unity is still found. Higher correlation is found between the multispectral data sets ($r = 0.92$). However, biases are observed depending on K_d range. OC-CCI is larger than OLCI for small K_d -blue values, lower for medium K_d -blue values and again larger for the highest K_d -blue values in the data set. The hyperspectral UV K_d were only compared to TROPOMI K_d -blue and not to the multispectral data sets, since

the wavelength conversion is less valid for the shorter wavelengths and the intercomparison indirectly contains information of the UV K_d with the multispectral products. The correlation between K_d -blue and K_d -UVA is lower than the one between K_d -blue and K_d -UVAB, contrasting the finding on the relationship between the K_d from the in-situ $K_d(\lambda)$.

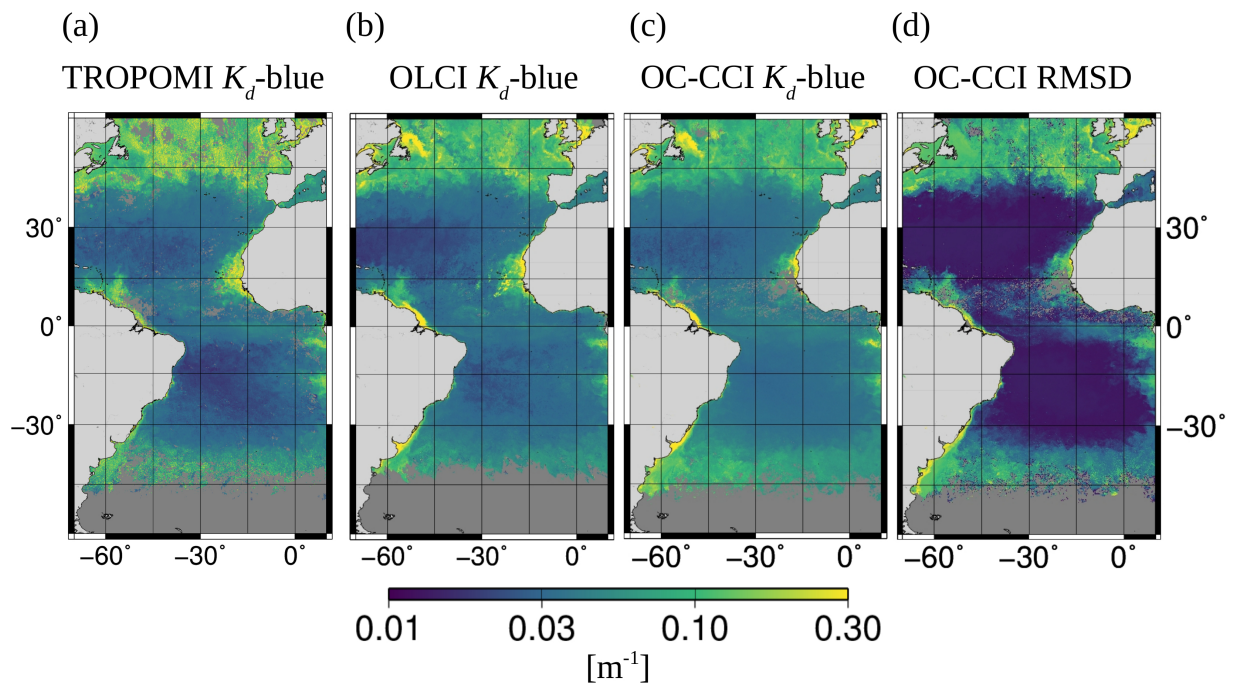


Figure 4.3.4: (a) TROPOMI, (b) OLCI, and (c) OC-CCI K_d -blue gridded at 0.083° as mean for 11 May to 9 June 2018. (d) RMSD provided in the OC-CCI product which was wavelength-converted to blue spectral range.

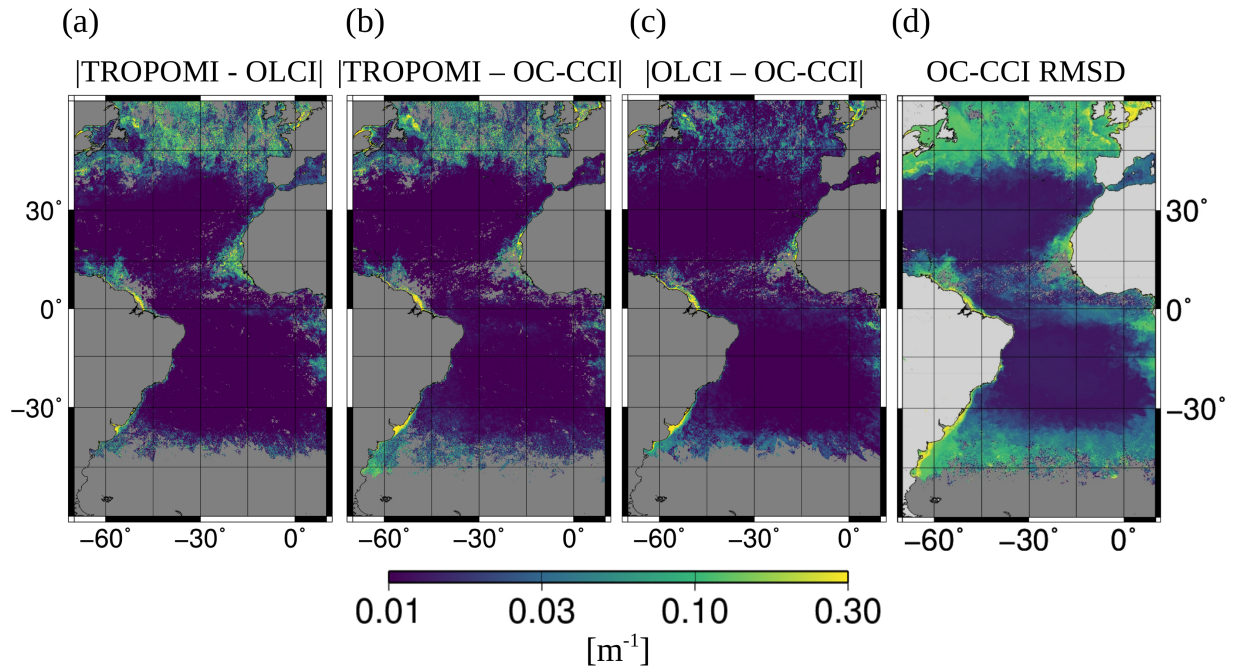


Figure 4.3.5: Mean absolute difference between (a) TROPOMI and OLCI, (b) TROPOMI and OC-CCI, and (c) OLCI and OC-CCI K_d -blue for the time period 11 May to 9 June and gridded at 0.083° . (d) RMSD as provided in OC-CCI data set for same grid and time period.

Table 4.3.2: Comparison between TROPOMI against OLCI and OC-CCI K_d -blue, K_d -UVA and K_d -UVAB calculated on daily gridded data (0.083°) over time period 11 May to 9 June 2018. Given are slope a and intercept b from linear total-least-square regression, Pearson correlation coefficient r , bias, mean absolute error (MAE), and root mean square difference (RMSD).

	K_d	data set	a	b [m^{-1}]	r	bias [m^{-1}]	MAE [m^{-1}]	RMSD [m^{-1}]
TROPOMI <i>vs.</i> OLCI	blue	full	0.38	0.034	0.45	0.005	0.026	0.102
		masked	1.02	-0.002	0.77	0.001	0.015	0.028
TROPOMI <i>vs.</i> OC-CCI	blue	full	0.57	0.021	0.45	0.004	0.022	0.076
		masked	1.23	-0.015	0.74	0.003	0.015	0.027
OC-CCI <i>vs.</i> OLCI	blue	full	1.10	-0.004	0.68	0.002	0.015	0.085
		masked	0.86	0.009	0.92	0.002	0.009	0.017
TROPOMI <i>vs.</i> TROPOMI	blue <i>vs.</i> UVA	full	1.01	0.019	0.44	0.020	0.039	0.073
	masked	0.82	0.028	0.55	0.019	0.031	0.041	
TROPOMI <i>vs.</i> TROPOMI	blue <i>vs.</i> UVAB	full	0.69	0.054	0.53	0.037	0.051	0.071
	masked	0.99	0.040	0.64	0.039	0.045	0.052	

4.4 Discussion

4.4.1 VRS retrievability

The VRS signal in TROPOMI-measured backscattered radiances can be successfully identified using DOAS. Spatial patterns of VRS fit factors are consistent with distribution patterns of Chla, the main driver for light attenuation in the open ocean. Absolute values of VRS fit factors retrieved from TROPOMI data are in reasonable agreement with those retrieved from simulated backscattered radiances shown by the successful conversion to K_d using the RTM-based LUTs. The conversion yielded better results for the UV and short-blue than for the blue fit window. A simple additive correction was necessary here.

The requirement of an additive correction factor that brings together retrieved fit factors with model predictions is a typical DOAS problem (Irie et al., 2015; Seo et al., 2019). Peters et al. (2014) pointed out that theoretical VRS pseudo-absorption spectra are not ideal for compensating VRS structures in actual DOAS measurements of clear waters. Such a mismatch could explain the requirement of a correction term. If this is the case, the effect of this mismatch on the DOAS retrieval is dependent on fit window, since we did not observe an obvious need for a correction of VRS fit factors in the short-blue and UV fit windows. Discrepancies between retrieved VRS fit factors on satellite and simulated backscattered radiances have been already encountered for the sensors GOME-2, OMI, and SCIAMACHY in study 1, chapter 3. In study 1, this discrepancy was reduced by including cross sections in the DOAS fit for GOME-2 and SCIAMACHY which account for spectral features caused by instrumentation. The DOAS VRS fit on OMI data showed no sensitivity to empirical cross sections. We checked if such empirical cross sections calculated from fit residuals over cloudy scenes - which are essentially VRS-free scenes - improve the situation for TROPOMI. No impact on VRS fit factors was found. We therefore suggest a different reason for the required offset correction. While performing DOAS fits on simulated data, a correlation with O_4 was observed that is strongest in the blue fit window, weaker in the short-blue fit window and weakest in the UV fit window. This correlation behaves differently for fits of actual satellite scenes. DOAS retrievals targeting O_4 also often require additive correction factors, caused by an insufficient quality of the O_4 absorption cross section (Spinei et al., 2015). The effect of O_4 on the VRS retrieval should be further investigated to obtain a correction which is independent from other K_d products.

4.4.2 Ultraviolet K_d product quality

We relied on in-situ match-up analysis for the evaluation of the K_d -UV product quality, because no equivalent K_d -UV product is currently available from multispectral satellite sensors. Match-up analysis was not feasible for older hyperspectral sensors due to large ground pixel sizes. Before TROPOMI was launched, OMI had the best spatial resolution with 13 km by 24 km at nadir. The spatial resolution has dramatically increased with TROPOMI to 3.5 km by 7 km at nadir in 2018. This is still a large pixel size for comparison with point measurements, yet the results show a decent agreement between match-ups of hyperspectral and in-situ K_d . Since the number of stations was small, a loose criterion was used to search for match-ups. The resulting number of match-ups is large considering that almost half of the stations could be matched, but overall low. The information drawn from the in-situ data comparison should not be over-interpreted, especially regarding the correlation coefficient.

TROPOMI ultraviolet K_d products are promising shown by comparison to this in-situ data set. Overall, there is good agreement between the TROPOMI and in-situ K_d , when considering the small amount of match-ups. Quality of the in-situ K_d at short wavelengths is limited. The TriOS sensor only measures down to 320 nm and its measurement accuracy appears to decrease towards this lower end of the spectral range as observed also by other users (Nicolaus et al., 2010). Consequently, the in-situ K_d -UVAB has a spectral mismatch to the TROPOMI K_d -UVAB. Evaluated from the RTM simulations, the in-situ K_d -UVAB is expected to be about 5 to 10% lower than the satellite K_d -UVAB due to this spectral mismatch, which would imply an even larger underestimation of K_d -UVAB by TROPOMI. Potential biases of TROPOMI K_d -UVAB need to be checked in the future with high-quality radiometric measurements in the UV spectral range.

The ratio between K_d -UVA and K_d -UVAB is larger than 1 for high- K_d waters, which is potentially related to the observed underestimation of TROPOMI K_d -UVAB for higher K_d values (multiplicative bias). K_d -UVAB should always be larger than K_d -UVA from a theoretical point of view considering that CDOM absorption decreases exponentially with wavelength. A decreasing K_d with decreasing wavelength in the UV is backed up by field data (Baker and Smith, 1982; Conde et al., 2000). An exception might be waters with extremely low CDOM concentrations for which hardly any difference was observed between K_d at 310 and 465 nm (Højerslev and Aas, 1991). The multiplicative bias becomes important in CDOM-rich or productive areas in the open ocean. For $K_d < 0.3 \text{ m}^{-1}$, covering large parts of the open ocean, K_d -UVA and K_d -UVAB both are reasonable estimators for UV light penetration as concluded from the in-situ comparison.

In addition to systematic biases, spatial patterns differ between the two K_d -UV prod-

ucts. Daily comparisons of the gridded products with K_d -blue showed a lower correlation with K_d -UVA than with K_d -UVAB. This observation contrasts the analysis of the spectral relationships between K_d at different wavelengths derived from the in-situ $K_d(\lambda)$. However, quality of the in-situ measurements decreases with wavelength, naturally causing the correlation coefficient to decrease with wavelength. Other studies found also a decreasingly robust relationship with wavelength between K_d in the UV range and optical properties in the VIS range (Johannessen et al., 2003; Vasilkov et al., 2005; Smyth, 2011). A very robust relationship between K_d at 310 and 465 nm with correlation 0.998 was found in low-CDOM waters (Højerslev and Aas, 1991). It is therefore not generally clear how robustly the K_d -UV are related to K_d -blue in different parts of the ocean. Light attenuation in the UV is mainly determined by CDOM and mycosporine-like amino acid (MAA) absorption. Based on its origin, CDOM has different absorption characteristics. VIS absorption is much stronger for humic substances with less steep spectral slope as opposed to mostly protein degrading substances of marine origin (Nelson and Siegel, 2002). MAA production depends on UV irradiation and species composition (Vernet et al., 1994) and mainly influence K_d -UVAB due to MAA absorption peaks at 330 to 340 nm (for influence on K_d -UVA, see also discussion in Wang et al., 2021). Since the link between optical properties in different spectral regions of the UV-VIS is not robust from a biogeochemical perspective, it is necessary to directly infer spectral information on light penetration, highlighting the importance of this study. By covering three spectral regions, the TROPOMI K_d products can give insight on CDOM origin and MAA production. The algorithm sensitivity analysis has shown that the K_d -UV retrievals are only moderately sensitive to the chosen RTM parameterization. Changes in K_d -UV caused by sufficiently large changes in CDOM and phytoplankton absorption should therefore be resolvable.

More in-situ data are necessary to thoroughly evaluate K_d -UV performance. A larger data set could then also be used for estimating if correction terms for the K_d -UV are necessary (similar to K_d -blue) and for quantifying these correction terms.

4.4.3 Blue K_d product quality

TROPOMI K_d -blue agrees well with OLCI and OC-CCI K_d -blue. Differences between the TROPOMI, OLCI, and OC-CCI K_d -blue products are of the same order of magnitude as the uncertainties given for the OC-CCI data set. Higher agreement between the two multispectral K_d -blue data sets than between multi- and hyperspectral ones has to be put into perspective, considering different ground pixel sizes of the sensors. In addition, a perfect correlation between multi- and hyperspectral products is not expected due to

the uncertainty associated with the wavelength conversion. We therefore want to stress the importance of direct retrievals of K_d at other wavelengths. However, we are confident that the comparison between the hyperspectral and multispectral K_d -blue is robust in the oligotrophic waters of the study area because wavelength conversion was calculated from in-situ data measured in exactly these waters in the time period of the study. Evaluating the offset correction term from comparison with OLCI K_d -blue for small values (K_d -blue $< 0.15 \text{ m}^{-1}$) is meaningful. Systematic biases between the data sets cannot be evaluated independently, but comparing them was possible with respect to regional differences, discrepancies for K_d -blue values above 0.15 m^{-1} , and random errors.

K_d -blue product quality is especially good in clear water regions, but reduced in areas where K_d -blue $> 0.3 \text{ m}^{-1}$. As pointed out in study 1, chapter 3, the strength of the hyperspectral algorithm lies in low- K_d waters since the VRS signal is highest here. The PhytoDOAS retrieval uncertainty increases with increasing K_d . In some cases, the hyperspectral algorithm seems to fail for high- K_d scenes causing obvious regional discrepancies in the TROPOMI K_d -blue product, as in the waters around Newfoundland. Not only the general DOAS retrieval uncertainty plays a role for the performance in productive areas, also the model setup. Because the model was set up for case-1 waters, the K_d -blue product is only valid for open ocean scenarios. For coastal applications, the model has to be adjusted accordingly. The multispectral algorithms have already been adapted for high- K_d waters. The semi-analytical algorithm by Lee et al. (2005a) has shown to perform well in coastal areas (Lee et al., 2005b) and inland waters (Gomes et al., 2018) whereas the OK2-555 algorithm by Morel et al. (2007a) only covers case-1 waters.

A north-south trend was observed for the Gyres with OC-CCI and OLCI agreeing on lower values in the Northern than in the Southern Gyre in contrast to TROPOMI. Similar behaviour was observed for SCIAMACHY and OMI in chapter 3. While in case of SCIAMACHY the latitudinal trend was attributed to polarization effects, the SZA angle dependence of OMI VRS retrievals did not match the SZA dependence as predicted by the model. From experience with building the 3 dimensional LUT for TROPOMI, additionally including the VZA, we conclude that also for TROPOMI the SZA and VZA dependence of theoretical VRS fit factors as predicted by the RTM is not aligned with that of satellite-retrieved VRS fit factors. Since angular dependencies are largely controlled by surface roughness, it might be worthwhile to extend the LUT with wind speed as an input parameter available from climatologies. However, the false angular dependency might also be a DOAS-retrieval related problem, e.g., caused by an angle-dependent correlation with O_4 .

The TROPOMI K_d -blue product outperforms other hyperspectral K_d -blue products.

The product quality is higher in more productive waters than for SCIAMACHY, OMI, and GOME-2. In chapter 3, the K_d -blue products were limited from these three older hyperspectral sensors to below 0.15 m^{-1} . For these reduced data sets, correlations with OC-CCI K_d -blue around 0.65 were achieved. Since metrics were given for these sensors for daily comparisons of almost one year of data, monthly metrics obtained here cannot be compared one to one. However, TROPOMI K_d -blue correlation with the multispectral K_d -blue is above 0.7 for the reduced data set including values up to 0.3 m^{-1} . The scatter plots presented in chapter 3 show that the hyperspectral K_d -blue already diverges from the OC-CCI K_d -blue in this K_d regime. Partially, this improvement is caused by the much lower ground pixel size of TROPOMI, which is closer to the multispectral satellite footprints, and thus reduces the representation error between the data sets. Smaller ground pixel sizes also reduce the inhomogeneity in satellite scenes improving fit quality. The improved DOAS fit quality of TROPOMI compared to its heritage sensors has also been found for UV-VIS retrievals of atmospheric trace gases (e.g., Seo et al., 2019; van Geffen et al., 2020). The spread in the scatter plots appearing as a “butterfly shape” was first observed by Dinter et al. (2015) for SCIAMACHY and has appeared in all comparisons between hyper- and multispectral K_d products so far. A systematic difference in the method or sensor measurement technique seems to cause a behavior where multispectral algorithms find high K_d values for scenes for which the hyperspectral K_d is low and vice versa. Hardly any high- K_d scenes occur in the data sets where hyper- and multispectral K_d are in agreement. This behavior was discussed in Dinter et al. (2015) and chapter 3 and attributed to low retrieval sensitivity for high- K_d scenes causing one wing of the distribution and to cloud contamination and large deviations from the average ocean scenario prescribed in the model causing the other wing.

4.5 Conclusion

TROPOMI’s UV-VIS bands were successfully exploited for deriving K_d in the open ocean. This first application of TROPOMI data for oceanic retrievals yields promising results. Two novel K_d products in the UV (312.5 to 338.5 nm (UVAB) and 356.5 to 390 nm (UVA)) were presented showing decent agreement with K_d in-situ data. In addition, a K_d product in the blue was retrieved (390 to 423 nm) that showed a better performance than K_d -blue from SCIAMACHY, GOME-2 and OMI in earlier studies. K_d -blue agrees well with the wavelength-converted $K_d(490)$ products from the multispectral data sets OLCI and OC-CCI. Differences between the three K_d -blue products were found to be within the uncertainties of the OC-CCI data set.

The robust agreement of TROPOMI K_d products with multispectral data sets and the reasonable agreement with in-situ data show that VRS can be successfully retrieved using PhytoDOAS and converted to K_d using an RTM-based LUT. However, few retrieval issues were identified which could be investigated in more detail and, based on an algorithm sensitivity analysis, suggestions were made for improving the LUT in the future. A major issue was an empirical offset correction that had to be applied to the VRS fit factors going into the K_d -blue product. The TROPOMI K_d -blue product is therefore not independent from the OLCI wavelength-converted $K_d(490)$ product used as reference. A correlation with O_4 was found that might cause this offset. Finding a correction that aims at the origin of this problem and is independent from other K_d data sets is desirable.

This study presents the first direct satellite retrievals of K_d in the UV spectral range. We view the TROPOMI K_d products as gap-filling, providing information in wavelength regions not fully accessible with current and, to some extent, also planned ocean color sensors. TROPOMI K_d products for scenes with $K_d > 0.3 \text{ m}^{-1}$ should be treated with caution. Unfortunately, not all open ocean scenes can be covered with the presented TROPOMI data set since higher K_d values are typically found for, e.g., spring blooms in the high latitudes. However, valuable information can be drawn in large parts of the open ocean, including regions where UV dose rates are especially high. The uncertainties of TROPOMI K_d products need to be evaluated with larger in-situ data sets. This study therefore also stresses the need for collecting high-quality in-situ radiometric measurements in the UV spectral range. As a next step, a K_d time series over the TROPOMI recording time period can be derived and analyzed on global scales to investigate temporal and spatial stability of the products. Once thoroughly validated, TROPOMI K_d -UV data sets can be used, e.g., for modeling of photochemical reaction rates of climatically important chemical substances (Smyth, 2011) and for estimating UV dose rates in combination with mixed layer depth data and UV irradiance above surface (Vasilkov et al., 2001; Smyth, 2011). Based on this work, the presented approach can be adapted by adjusting the LUT to directly derive UV radiation in the ocean similar to Dinter et al. (2015). Intercomparison of the three spectral TROPOMI-derived K_d in the UV-VIS region can give insight on CDOM origin and production of UV-protective pigments by phytoplankton and be used as an indicator for UV-sensitive and optically interesting regions in the open ocean.

5 Potential of GOME-2 for monitoring coccolithophores in the Southern Ocean

5.1 Introduction

The Southern Ocean (SO) is a major carbon sink. About one fourth of the anthropogenic CO₂ released to the atmosphere has been taken up by the global oceans (Friedlingstein et al., 2019). Roughly 40% of this uptake occurred in the SO (Raven and Falkowski, 1999; Sabine et al., 2004; Khatiwala et al., 2009; Takahashi et al., 2009; Frölicher et al., 2015). CO₂ uptake is majorly due to physical processes, the so-called solubility pump. Through primary productivity of phytoplankton, carbon is bound organically. Vertical transport of this organically bound carbon to the ocean interior is responsible for about 10% of the oceanic uptake (Cox et al., 2000; Siegel et al., 2014). The efficiency of this biological carbon pump depends on the phytoplankton community structure. Phytoplankton species can be grouped according to their function in the biogeochemical cycles, so-called phytoplankton functional types (PFT) (Reynolds et al., 2002; Le Quéré et al., 2005). Dominating PFT in the SO are silicifying diatoms, dimethyl-sulfate producing *Phaeocystis* sp., and calcifying coccolithophores. Shifts in community structure due to global warming will effect carbon export efficiency and biogeochemical cycles with global consequences (Deppeler and Davidson, 2017).

The SO is considered to be dominated by microphytoplankton (20 - 200 μm) with blooms predominantly consisting of large diatoms and *Phaeocystis* sp. (Bathmann et al., 1997; Boyd, 2002; Poulton et al., 2007a). The role of coccolithophores was recognized through the observation of the Great Calcite Belt (GCB). The GCB is an area of elevated backscattering due to particulate inorganic carbon (PIC) evident in satellite observations. It stretches from 30°S to 60°S circling the SO with highest PIC concentrations found near the Patagonian Shelf and the Atlantic sector of the SO and decreased concentrations in Indian and Pacific sector (Balch et al., 2011). Coccolithophores produce calcite plates, coc-

coliths, which are attached to their cells or released into the water column. The shed coccoliths backscatter light efficiently such that waters with coccolithophore blooms are high-reflecting (Balch et al., 1996). Ship measurements have confirmed the presence of elevated surface reflectances due to PIC and associated coccolithophore presence (Balch et al., 2011, 2016). The GCB stretches over several fronts with the Subtropical Front marking the northern boundary. Coccolithophores are most abundant north of the Polar Front (Mohan et al., 2008), where they coexist with small lightly-silicified diatoms (Smith et al., 2017). Large heavily-silicified diatoms are generally more abundant south of the Polar Front (Froneman et al., 1995).

Large diatoms are associated with large carbon export rates through vertical transport to the deep ocean (Salter et al., 2007; Assmy et al., 2013). Calcification releases CO₂ which results in elevated partial CO₂ pressure (pCO₂) known as the carbonate counter pump. A decrease in coccolithophore concentrations can therefore lower pCO₂ and increase the uptake of atmospheric CO₂ by the ocean (solubility pump), but potentially also reduces the vertical carbon flux, because calcified shells generally sink quickly due to their weight (Riebesell et al., 2009; Müller et al., 2015; Balch et al., 2016). Effects of global warming in the GCB, including increased ocean acidification, warming sea surface temperatures, decreased salinity, shallower mixed layer depth, and increased ultraviolet and visible radiation, will change the phytoplankton community structure, but the effects on biogeochemical cycles and feedback to climate change are complex and not fully understood (Deppeler and Davidson, 2017). For a better understanding, long-term monitoring of phytoplankton community structure in the SO is necessary (IOCCG, 2015).

Satellite observations can provide long-term data sets with sufficient spatiotemporal resolution required for biogeochemical and climate modeling (e.g., Sathyendranath et al., 2019; IOCCG, 2020). Several approaches have been presented for determining phytoplankton community structure from space (e.g., Mouw et al., 2017). These methods differ in defining PFT. Some give information on size classes, while others group PFT with respect to taxa. For long-term studies of the community structure in the GCB, PFT products grouped according to taxa are necessary, ideally distinguishing between diatoms, coccolithophores and *Phaeocystis* sp.. The latter two are both in the same class, haptophytes, and have similar size and photosynthetic pigments (e.g., Nair et al., 2008), and therefore often not explicitly distinguished in remote sensing approaches. Approaches that provide Chlorophyll-a concentration (Chla) of these PFT are the abundance-based approach by Hirata et al. (2011) and the spectral-based approaches by Bracher et al. (2009) and Sadeghi et al. (2012a) as well as Xi et al. (2020). Hirata et al. (2011) exploit empirical relationships between in-situ marker pigments of PFT (using large High Performance Liquid Chromatography,

HPLC, data sets) and total Chla to derive Chla of diatoms and haptophytes as well as of five other PFT from the standard total Chla product obtained with Ocean Color (OC) satellite sensors. Such empirical relationships perform robustly on global scales, but have to be adjusted for regions as the *SO* (Soppa et al., 2014). It is unclear if the empirical relationships hold in future ocean conditions (e.g., IOCCG, 2014). Xi et al. (2020) use also an empirical approach which exploits the relationship between HPLC-measured marker pigments and empirical orthogonal functions of OC satellite-measured reflectances. The algorithm was further tuned by separation in sea surface temperature regimes (Xi et al., 2021). Chla of six PFT are determined including haptophytes and diatoms.

The spectral approach by Bracher et al. (2009) and Sadeghi et al. (2012a) is less empirical. Spectral differences in PFT absorption spectra caused by PFT-specific pigments are identified in satellite-measured backscattered radiances using Differential Optical Absorption Spectroscopy (PhytoDOAS). Unlike other PFT approaches, which use atmospherically corrected OC satellite data as input, this method has been applied to hyperspectral backscattered radiances measured at the top of atmosphere by SCIAMACHY (Scanning Imaging Absorption Spectrometer for Atmospheric Chartography), a sensor designed for atmospheric trace gas observations. Losa et al. (2017a) have established a 10 year time period of diatom, coccolithophore, and cyanobacteria Chla from SCIAMACHY data (2002 - 2012; Bracher et al., 2017). The spatial resolution of SCIAMACHY is much lower (30 by 60 km²) than for OC sensors. Losa et al. (2017a) have overcome this limitation by synergistically combining SCIAMACHY-derived PFT data with OC-PFT data using the approach by Hirata et al. (2011), combining the good spatial resolution of OC sensors with the high-resolved spectral information from SCIAMACHY.

Since SCIAMACHY measurements end in 2012 and longer observation periods are needed for studying climate change impacts, other SCIAMACHY-like sensors should be exploited for retrieving PFT Chla. In this study, the PhytoDOAS method was adapted to the Global Ozone Monitoring Experiment-2 (GOME-2) and its performance analyzed. This sensor is part of an operational mission with a series of satellites carrying the GOME-2 instrument which were launched in 2006 (MetOp-A), 2012 (MetOp-B), and 2018 (MetOp-C). GOME-2 data therefore cover a long time period and can bridge the time between SCIAMACHY and more recent and upcoming hyperspectral sensors such as TROPOMI onboard Sentinel-5P, for perspective creating a PFT data set spanning multiple decades. The Ozone Monitoring Instrument (OMI) can also fulfill this bridging task, however, OMI data quality has significantly decreased from 2008 due to a detector row anomaly (Schenkeveld et al., 2017) and OMI covers a smaller spectral range (only until 500 nm) which may hamper coccolithophore retrievals for which optimal fit windows for SCIAMACHY reached up

to 521 nm (Sadeghi et al., 2012a; Losa et al., 2017a).

Coccolithophore and diatom Chla are retrieved in the Atlantic and Indian sectors of the SO. The study focuses on the austral summer (October to March) of the years 2010/11 and 2011/12. Within the GCB project, measurements were taken by two ship expeditions within this time period and region to understand the phenomenon of the GCB. Several studies have used this data for connecting satellite-derived PIC, in-situ measured PIC, diatom and coccolithophore abundance and species composition, nutrients, carbon fluxes, carbon chemistry, and physical variables (Balch et al., 2016; Smith et al., 2017).

Objectives of this study are to assess the performance of PFT retrievals from GOME-2 and its suitability for long-term monitoring of diatoms and coccolithophores, the two key biomineralizing PFT in the GCB as one of the most biogeochemically important ocean regions. Quality of the data sets is determined by comparison with other satellite products, such as PIC, OC-PFT, and SCIAMACHY PFT data, and with in-situ data from the 2011/12 SO ship expeditions. The study area is focused on the Atlantic and Indian sector of the SO between 30° and 60°S (65°W-120°E, 30°- 65°S) and is referred to it as the SOAI region.

5.2 Methods

An overview of the algorithm for retrieving coccolithophore and diatom Chla from GOME-2 measured backscattered radiances can be found in Figure 5.2.1. The scheme also contains information on comparisons made with other satellite data products. All steps are explained in detail in the following. Data sets will be introduced first, followed by the PhytoDOAS retrieval. Next, a section is dedicated to the choice of optimal retrieval settings with respect to wavelength ranges. Various corrections are applied to the PhytoDOAS output in a post-processing step before PhytoDOAS outputs are converted to Chla. The conversion method is introduced first to give a better overview before corrections are explained in detail.

5.2.1 Data sets

GOME-2 data

Backscattered radiances and daily solar irradiances were taken from GOME-2 (Munro et al., 2016) hosted by MetOp-A satellite as satellite input data for PhytoDOAS method. Level 1 version 5.3 data were used. During the time period investigated in this study, spatial resolution was 40 km by 80 km for nadir ground pixels. The spatial resolution

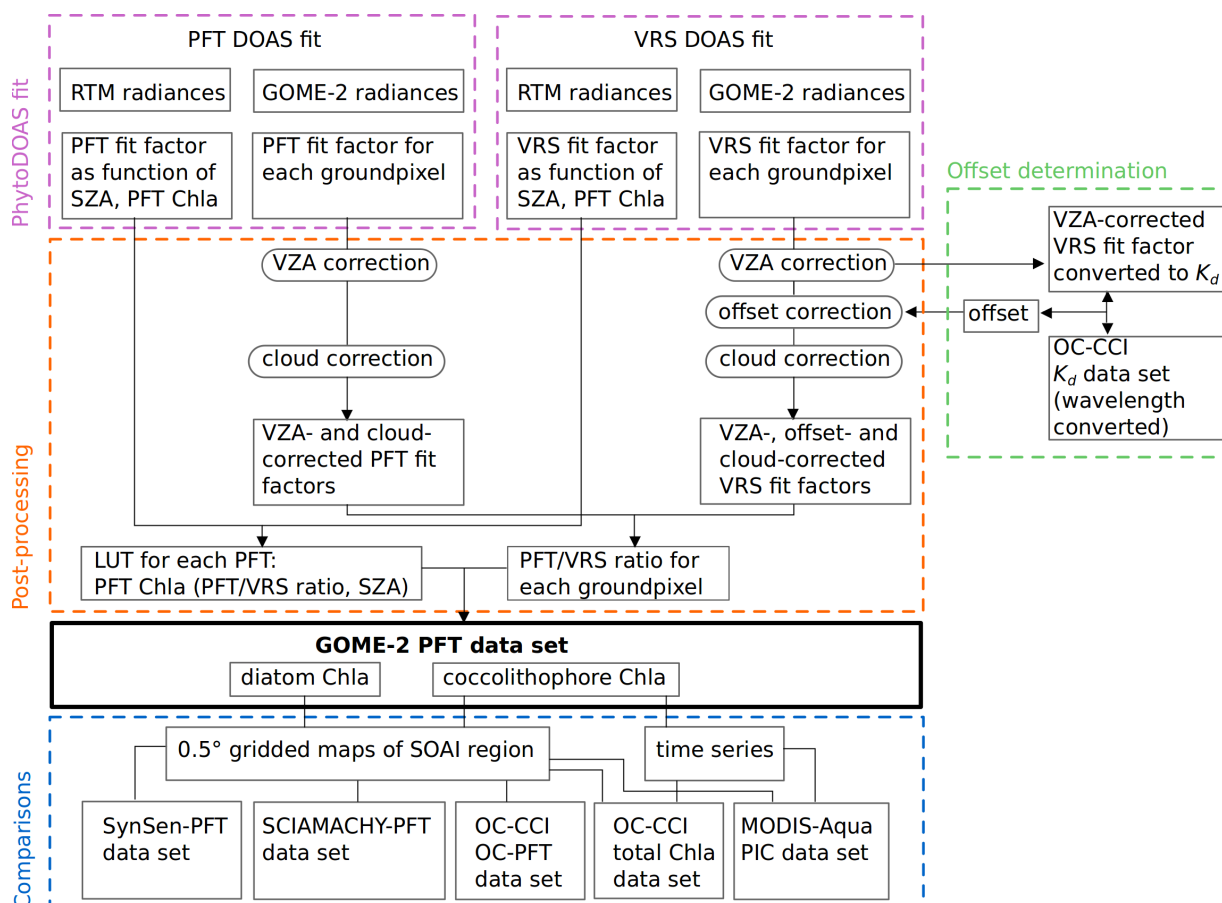


Figure 5.2.1: Schematic of the algorithm flow for deriving coccolithophore and diatom chlorophyll-a concentrations from GOME-2 backscattered radiances, including comparisons with other satellite products.

Table 5.2.1: Satellite data sets used for comparison with GOME-2 PFT results. Under product output, only variables from the data set used in this study are listed. Abbreviations used for the data sets throughout the study are listed under naming. The names SynSenPFT, SCIA-PD, and OC-PFT are used in combination with coccolithophore, haptophyte, and diatom Chla, respectively.

data set	algorithm	product output	unit	naming
SynSenPFT	SynSenPFT (Losa et al., 2017a)	coccolithophore, diatom Chla	mg/m ³	SynSenPFT
SCIAMACHY	PhytoDOAS v3.3 (Losa et al., 2017a)	coccolithophore, diatom Chla	mg/m ³	SCIA-PD
OC-CCI v2.0	OC-PFT v2 (Losa et al., 2017a)	haptophyte, diatom Chla	mg/m ³	OC-PFT
OC-CCI v3.1	blended (Jackson et al., 2017)	total Chla	mg/m ³	OC-CCI total Chla
OC-CCI v4.2	semi-analytic K_d (Lee et al., 2005a)	$K_d(490)$	m ⁻¹	OC-CCI K_d
MODIS-Aqua	PIC (Gordon et al., 2001; Balch et al., 2005)	PIC	mmol/m ³	MODIS PIC

was changed to 40 km by 40 km in 2013 at reduced coverage, because the instrument was operated in tandem with GOME-2 on MetOp-B. GOME-2A reaches global coverage in 1.5 days. Channel 3 (397 to 604 nm) was used for the retrieval, which has a spectral resolution of 0.51 nm. The instrument passes the equator at 9:30 am local time in descending node. Clouds were filtered based on the FRESCO+ product (Wang et al., 2008b). Only satellite pixels with solar zenith angle (SZA) < 70° were considered.

Satellite data sets for comparison

Several satellite data sets were used for comparison with GOME-2-derived PFT products. All data sets were regridded to 0.5° to match the chosen grid for GOME-2 PFT data.

SynSenPFT data, provided as daily files on 4 km sinusoidal grid, were downloaded from Pangaea (Losa et al., 2017b). Files contain concentrations for diatoms, coccolithophores, and cyanobacteria in mg/m³. The SynSenPFT product synergistically combines SCIAMACHY PhytoDOAS-PFT data version 3.3, also available on Pangaea as monthly gridded data (0.5°) (Bracher et al., 2017), and OC-PFT data calculated from OC-CCI total Chla product (version 2) based on (Hirata et al., 2011; Soppa et al., 2014). Both SynSenPFT input data products, SCIAMACHY PhytoDOAS-PFT and OC-CCI OC-PFT, were also used as single products in this study. Diatom concentrations are available for both, SCIAMACHY-PFT and OC-PFT data sets, whereas coccolithophore concentrations

are available from the SCIAMACHY-PFT and haptophytes concentrations from the OC-PFT data set.

PIC from MODIS-Aqua was downloaded as mapped daily data (4 km resolution) from <https://oceandata.sci.gsfc.nasa.gov/>. The algorithm for deriving PIC is a hybrid of a two band approach (Balch et al., 2005) and a three-band approach (Gordon et al., 2001). The two-band approach relates the total backscattering coefficient of calcite at 546 nm to the normalized water-leaving radiances at a blue and green wavelength via a LUT established from in-situ measurements. PIC is then calculated by dividing by the calcite-specific backscattering coefficient ($1.628 \text{ m}^2 \text{ mol}^{-1}$). The three-band approach is used when the two-band approach fails. It is usually more robust over high-reflecting waters and uses top-of-atmosphere (TOA) radiances at three wavelengths from 670 to 865 nm as input. TOA radiances are converted to reflectances and with an iterative procedure, contributions to the TOA reflectances by atmosphere-ocean system are estimated and the backscattering coefficient of calcite at 546 nm is derived. Conversion to PIC is then the same as in the two-band approach.

Total Chla was taken from the release version 3.1 (Sathyendranath et al., 2018) of OC-CCI data set (Sathyendranath et al., 2019) of the European Space Agency ESA (<http://www.esa-oceancolour-cci.org/>). Daily data files with 4 km resolution were taken. Total Chla is retrieved using a blended combination of several empirical band ratio algorithms (Jackson et al., 2017).

For correction of vibrational Raman scattering, the diffuse attenuation coefficient at 490 nm was used from OC-CCI version 4.2 (Sathyendranath et al., 2020). Daily data on a sinusoidal grid with 4 km resolution were used.

Different versions of OC-CCI products were used in this study mainly for historical reasons. At the time of release of the SynSenPFT product, only OC-CCI version 2 data were available. The total Chla product was mainly used for comparison with the here presented GOME-2 retrieval outputs and therefore a newer version of the OC-CCI data set was used. Compared to version 2, version 3.1 has increased data coverage and total Chla is derived with a superior blending approach. The newer version was therefore chosen. The correction of the vibrational Raman scattering was implemented at a later stage with the newest OC-CCI version being available at the time. Comparisons between OC-CCI total Chla and the SynSenPFT product are only made qualitatively. Furthermore, OC-CCI total Chla is also only used as a rough estimator for checking the reasonability of derived GOME-2 coccolithophore Chla and their phenology as well as derived GOME-2 diatom Chla and their spatial distribution. Differences between OC-CCI versions are small compared with the differences found in intercomparison of different data sets in this

study. Usage of different versions should therefore not influence any conclusions. Details on different OC-CCI versions and their intercomparison can be found in (Krasemann et al., 2017; Sathyendranath et al., 2019).

Time series processing

Time series were computed from GOME-2, PIC and total Chla satellite products. 7-day running composites were calculated for six 4° by 4° regions from the 0.5° gridded satellite products. For each day, all valid grid points within a given region were collected from the given date and from the three days prior and after this date. Six regions across the SOAI region were selected: Patagonian Shelf (62-58°W,50-46°S), North of South Georgia (42-38°W,52-48°S), Southwest of South Africa (6-10°E,42-38°S), North of Crozet Islands (46-50°E,46-42°S), South of Kerguelen Islands (71-75°E,54-50°S), Southwest of Western Australia (110-114°E,46-42°S).

In-situ data sets

In-situ data were taken from two research cruises in the SO (principal investigator: W. M. Balch, Bigelow Laboratory for Ocean Sciences, <https://www.bco-dmo.org/dataset/560357>). Data in the Atlantic sector of the SO were sampled in the time period 17 January to 17 February in 2011 with R/V Melville. Data in the Indian sector were collected in the time period 18 February to 20 March 2012 with R/V Roger Revelle. Samples were collected with CTD casts or taken from the ships non-contaminated seawater system. From this data set, coccolithophore cell counts were taken which were determined with optical microscopy as the number of birefringent plates and aggregates as well as chlorophyll-a determined via fluorometry (Balch et al., 2016). Only surface samples were considered. Samples at the minimum depth for each station were taken which ranged between 1.6 and 25.5 m.

5.2.2 PhytoDOAS

The Differential Optical Absorption Spectroscopy method was used for retrieving PFT (PhytoDOAS, Bracher et al., 2009; Sadeghi et al., 2012a) from backscattered radiances of the GOME-2 sensor. The overall fitting procedure followed Bracher et al. (2009). In the blue-green spectral range, PFT specific absorption spectra to the satellite-measured optical depth were fitted together with cross sections accounting for clear water and instrumental spectral features as well as relevant atmospheric absorption cross sections. Broadband features caused, e.g., by scattering or CDOM absorption were removed by additionally fitting a low order polynomial.

The clear water cross sections were determined in a pre-fit, in which only atmospheric absorbers were fitted to data from satellite scenes over a region in the South Pacific Gyre (110° to 130°E, 25° to 29°S), where Chla is very low (≈ 0.02 , e.g., Morel et al., 2007c). Residuals of these fits were analyzed in a principal component analysis (PCA). The first and second eigenvectors (EV) from the PCA combinedly describe liquid water absorption, vibrational Raman scattering (VRS), and spectral features caused by instrumentation. Figure 5.2.2 shows the first two EV as function of wavelength in the spectral range 425 to 495 nm. As comparison, a simulated clear water spectrum is shown that combines liquid water absorption and VRS. It was obtained from a residual of a DOAS fit on simulated backscattered radiances for an ocean scene without Chla (see section 5.2.3). Spectral features of this clear water spectrum can be recognized in the first and second eigenvectors.

In the main fit, the PFT fit factors were targeted. Following specific fit settings were chosen for both PFT:

- atmospheric absorption spectra: O₃, NO₂, O₄, H₂O (as in section 3.2.3),
- two eigenvectors from PCA of residuals in South Pacific Gyre region,
- a PFT specific absorption spectrum,
- a second-degree polynomial.

Coccolithophore and diatom fit factors were obtained in two separate fits, only fitting one PFT cross section at a time, a so-called single PFT-fit. Coccolithophores were fitted from 430 to 520 nm using an absorption cross section obtained from an *Emiliana huxleyi* culture as in Sadeghi et al. (2012a). *Emiliana huxleyi* dominates global coccolithophore abundance (Paasche, 2001). Diatoms were fitted from 425 to 495 nm using a specific absorption spectrum obtained in-situ during the EIFEX Atlantic Southern Ocean cruise as used in Bracher et al. (2009). Figure 5.2.3 shows the two spectra in comparison.

Choice of PFT fit window

Above described PhytoDOAS settings were based on fit window analyses performed beforehand. The GOME-2 visible channel 3 used for the PFT DOAS fits extends from 397 to 604 nm. It provides a larger variety of possible fit window settings for the PFT fits than possible for the SCIAMACHY sensor. SCIAMACHY PFT fit windows were limited to the spectral region of 424 to 525 nm (Bracher et al., 2009; Sadeghi et al., 2012a), only using a single spectral cluster (cluster 15 of channel 3) due to varying integration times of different clusters (Bovensmann et al., 1999). Sadeghi et al. (2012a) have introduced

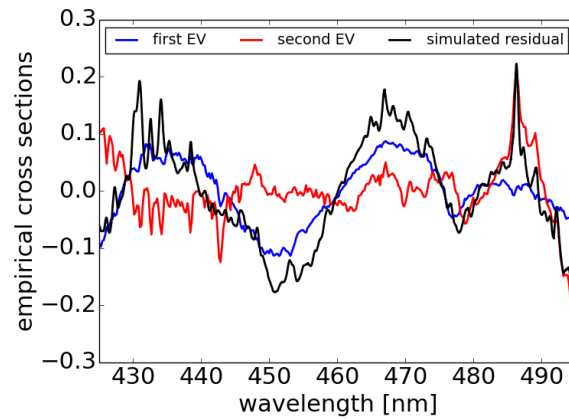


Figure 5.2.2: Empirical cross sections as function of wavelength. First (blue line) and second (red line) EV of PCA analysis of residuals over clear waters of the South Pacific Gyre are shown in comparison to a residual (black line) from a fit on simulated data that combines liquid water absorption and VRS.

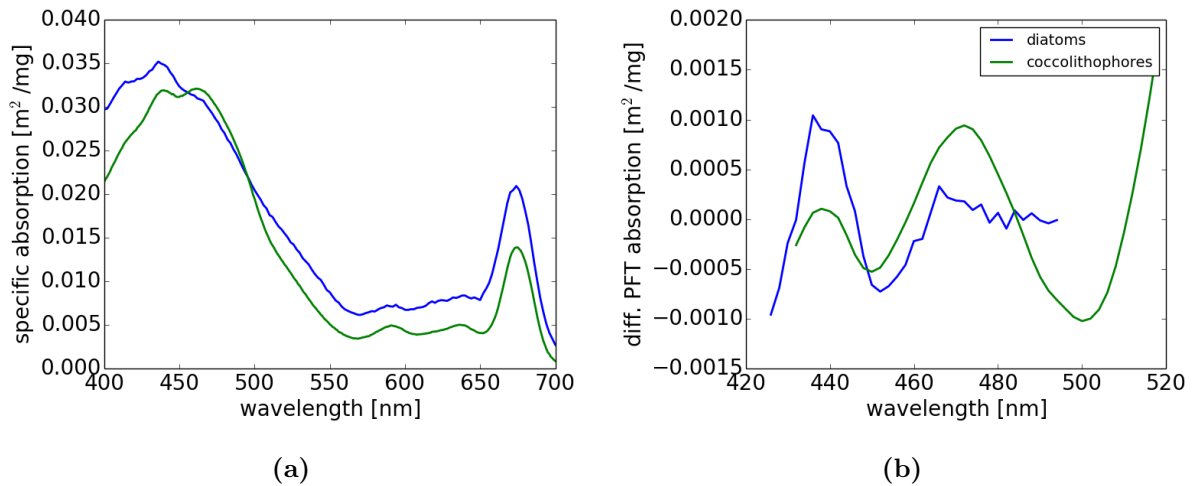


Figure 5.2.3: (a) Coccolithophore and diatom specific absorption spectra. (b) Differential PFT absorption spectra for coccolithophores and diatoms calculated by subtracting a fitted quadratic function to the specific absorption spectra in the wavelength ranges of the final fit window settings.

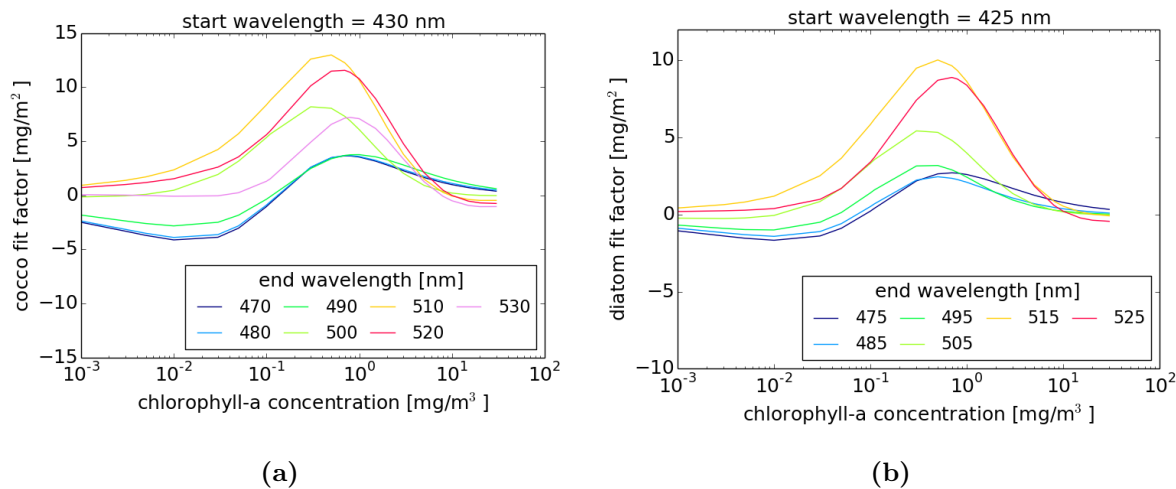


Figure 5.2.4: (a) Coccolithophore fit factors as function of Chla for a fix start wavelength of 430 nm and end wavelengths ranging between 470 and 530 nm. (b) Diatom fit factors as function of Chla for a fix start wavelength of 425 nm and end wavelengths ranging between 475 and 525 nm. PFT fit factors were retrieved from simulated TOA radiances using PhytoDOAS single-target fits.

the multi-target fit, i.e., the simultaneous fitting of several PFT absorption spectra in the PhytoDOAS fit, for retrieving coccolithophores as opposed to the single-target fit in [Bracher et al. \(2009\)](#), targeting diatoms and cyanobacteria separately. They determined optimal fit windows for the SCIAMACHY sensor by analyzing spectral similarities between PFT absorption spectra with the help of a fourth-derivative and orthogonality analysis of specific absorption spectra of different PFT with the focus on coccolithophores and diatoms. The optimal result was a triple fit (diatoms, coccolithophores, dinoflagellates) in the wavelength window 429 to 521 nm. Derivative analyses are a common tool for identifying spectral regions showing high variability/uniqueness in spectra that can be used for identifying PFT ([Lee et al., 2007](#); [Isada et al., 2015](#); [Wolanin et al., 2016](#)). [Wolanin et al. \(2016\)](#) investigated optimal wavelength regions for identifying coccolithophores, diatoms, and cyanobacteria. Several wavelength bands in the 400 to 520 nm region were identified as interesting for spectrally distinguishing coccolithophores and diatoms. They point out that the optimal wavelength regions for successfully differentiating certain PFT depends on the used method.

It was explored, if the spectral regions below 424 and above 525 nm are suitable for PFT retrievals using PhytoDOAS. Fit window analyses were done on simulated and satellite-measured backscattered radiances. Not only the correlation between certain PFT limits their retrieval, but also the correlation of absorption spectra of atmospheric gases or the

EV used in the PFT fit containing information on VRS and liquid water absorption. By performing single-target PFT fits on simulated and backscattered spectra, this correlation of PFT spectra with non-PFT spectra was investigated.

The fit window analysis with simulated backscattered radiances was performed using RTM settings as described below in section 5.2.3 and DOAS fit settings as described above, except that water vapor is not fitted (since it is not contained in the simulated atmosphere) and a theoretical clear water spectrum is fitted that combines VRS and liquid water absorption instead of empirically determined EV (see Figure 5.2.2). The fit window was varied with start wavelengths between 420 and 470 nm and end wavelengths between 470 and 570 nm with steps of 5 nm, restricting combinations to fit window lengths ≤ 100 nm.

Selected fit windows should fulfill two criteria. The relationship between PFT fit factors and PFT Chla should be monotonously increasing in the low Chla range. PFT fit factors will reach a maximum value for a medium PFT Chla. For larger Chla values, the PFT fit factors decrease because the signal from the ocean reaching the satellite drops. In combination with the VRS fit factors used as proxy for light penetration depth, the PFT/VRS fit factor ratio monotonously increases over a larger Chla range (see also section 5.2.3 for discussion). As a second criterion, PFT fit factors should be close to zero for ocean scenes without Chla. Non-zero fit factors hint at correlations between cross sections in the DOAS fit that should be avoided.

Almost all tested fit windows fulfill the two criteria. Examples are shown in Figure 5.2.4. Some fit windows with end wavelengths close to the edges of the tested range (smaller 500 nm and larger 540 nm) show unambiguous relationships between PFT fit factors and PFT Chla and/or large non-zero values for scenes without Chla. Results for diatoms and coccolithophores are similar. Small differences appear in shape of PFT fit factor to Chla relationship and larger differences in absolute PFT fit factor values. Since fit windows ending at wavelengths larger than 540 nm do not seem ideal, the fit window analysis on satellite-measured data was not carried out in this wavelength range. Fit windows ending below 500 nm, however, were tested also on satellite-measured data, since optimal fit windows in this wavelength range were found for diatom fits on SCIAMACHY-measured backscattered radiances before (Losa et al., 2017a).

The degree of the polynomial used in the DOAS fit also influences the choice of optimal fit window. Since PFT absorption spectra are rather broadband, a low polynomial degree should be chosen. Additionally to the second degree polynomial used in the final settings, a first degree polynomial was tested. The fit window analysis was repeated and showed that an unambiguous relationship between PFT fit factors and PFT Chla can be found

in significantly fewer fit windows (for both PFT). The fit window analysis on satellite-measured backscattered radiances was therefore only performed using a second-degree polynomial.

The fit window analysis on GOME-2-measured backscattered radiances was conducted in the wavelength range between 400 and 540 nm. Single diatom and coccolithophore DOAS fits with settings described above were tested as well as dual fits, i.e., fitting the diatom and coccolithophore spectrum simultaneously. Two blocks of wavelength combinations were tested. One covered the lower spectral range, start wavelengths ranging between 400 and 430 nm and end wavelengths between 485 nm and 520 nm, which included fit windows used for SCIAMACHY retrievals, but also the lower spectral range not tested with the SCIAMACHY sensor. The second block tested fit windows in the higher spectral range which are not covered by SCIAMACHY's cluster 15. Start wavelengths range between 430 and 460 nm and end wavelengths between 530 and 540 nm. Start and end wavelengths were varied in steps of 5 nm. Only combinations resulting in fit window lengths ≤ 100 nm were tested, because long fit windows are generally less suitable for DOAS (see section 2.11). Fit windows were tested using the global GOME-2 data set for January 2011.

As for the analysis on simulated radiances, fit factors close to zero in low Chla regions indicate low correlation of cross sections within the PhytoDOAS fit and therefore indicate promising fit window candidates. Figure 5.2.5 shows the median fit factor of those 10% of all ground pixels with the lowest fit factors in the global monthly data set. Results are shown for all fit window combinations and different fit settings, i.e., single vs. dual fit. Considering coccolithophore single fits first, fit windows from the block at the low spectral range yield fit factors becoming more negative with decreasing start and end wavelengths. Promising fit windows with fit factors close to zero are 430 to 510 nm and 430 to 520 nm. For the block at higher spectral range, promising combinations are 445 nm with 530 or 535 nm. Fit windows with start wavelength smaller than 445 nm have more negative fit factors and with start wavelength larger than 445 nm tend to yield fit factors slightly larger zero. For the coccolithophore dual fit, trends are generally similar, but for all combinations, the fit factors are shifted to more negative values resulting in an overall lower median value for the lowest 10%. Consequently, a fit window yielding a median close to zero is found at the high end of the spectral range, 460 to 530 nm.

Among the four promising fit windows for a coccolithophore single fit, the similarity of the fit results was tested by comparing the gridded fit factor maps (0.5°) on a daily basis against each other. Taking the fit window 430 to 520 nm as a reference, the correlation with results from the other three fit windows is larger than 0.97 and intercepts range between -0.2 and -0.32 mg/m^2 . Since no fundamental differences between the fit window candidates

were found, 430 to 520 nm was chosen as final fit window, because it is most similar to the coccolithophore fit window settings used for SCIAMACHY (427.5 to 521 nm) (Losa et al., 2017a). Losa et al. (2017a) used a dual fit, which were discarded for GOME-2, because correlation between the single and the dual fit for the 430 to 520 nm fit window was 0.9 in the SOAI region, but the dual fit introduced a negative offset to the fit factors, intercept of -2.26 mg/m^2 , slope of 1.03.

Diatom fit factors generally do not show as large non-zero fit factors as observed for the coccolithophore fits (in agreement with analysis on simulated data, Figure 5.2.4). Several fit window options are revealed. Fit windows from the block at the longer wavelength range are generally less suitable than those from the block at the shorter wavelength range. From the diatom single fit, it can be concluded that fit windows with start wavelength shorter 415 nm are not ideal and most fit windows with end wavelengths larger 505 nm. For the most suitable fit windows, start wavelengths between 415 and 430 nm and end wavelengths between 490 and 505 nm, the correlations of daily gridded diatom fit factors from the single fit and from the dual fit are high, larger 0.9. Since prior fit windows chosen for SCIAMACHY PFT fits lie within the optimal selection of fit windows for diatoms, a fit window was finally chosen that is similar to the diatom fit window in Losa et al. (2017a) for better direct comparison with retrieval performance of PhytoDOAS on SCIAMACHY-measured data. As final settings, a diatom single fit between 425 nm to 495 nm was chosen. Global diatom fit factor results are similar to diatom dual fit results in the longer wavelength range, 430 to 520 nm. The correlation is 0.87, slope 0.83, and intercept 0.38 mg/m^2 . As for SCIAMACHY, the short fit window used in Bracher et al. (2009) and Losa et al. (2017a) and the long fit window used in Sadeghi et al. (2012a) are both possible for diatom fits on GOME-2-measured data.

Concluding the search for optimal PhytoDOAS fit windows, both on simulated and on satellite-measured data, we found that the wavelength range covered by SCIAMACHY's spectral cluster 15 already contained the optimal fit windows for fitting coccolithophores and diatoms. The larger spectral range that GOME-2 offers did not help in discriminating coccolithophores and diatoms spectrally within the PhytoDOAS method. In accordance with Wolanin et al. (2016), it was found that shorter fit windows at the shorter wavelength range are more beneficial for fitting diatoms and the longer fit windows at the longer wavelength range are more suitable for fitting coccolithophores. As stated in Wolanin et al. (2016), fit windows with longer wavelengths than $\sim 520 \text{ nm}$ might be ideal for fitting cyanobacteria, which were not investigated in this study, but might be potentially well retrieved by exploiting the larger spectral range that GOME-2 offers.

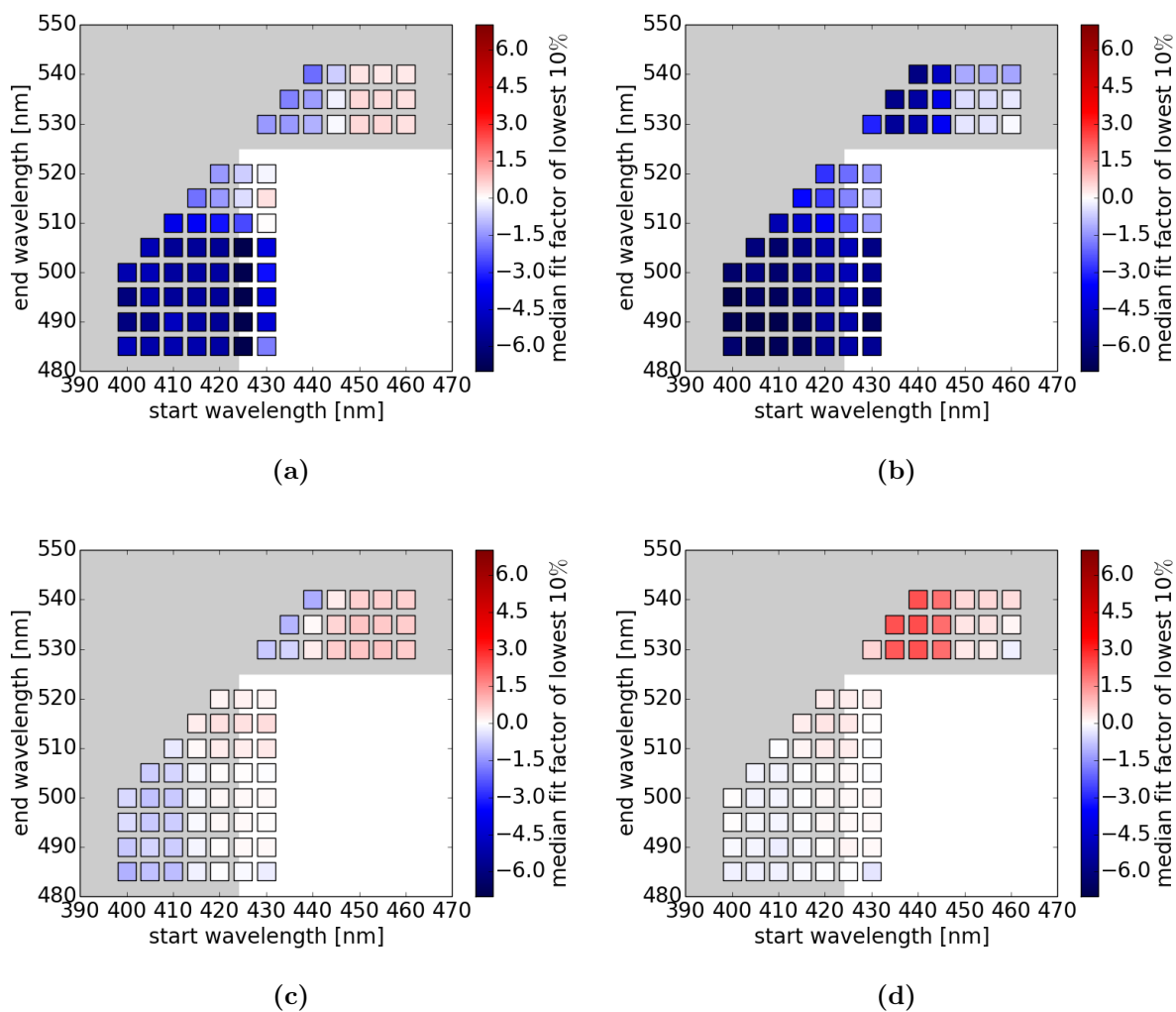


Figure 5.2.5: Median of lowest 10% of global PFT fit factors for January 2011 for different fit settings: (a) coccolithophore single fit, (b) coccolithophore dual fit, (c) diatom single fit, (d) diatom dual fit. Grey shaded area mark the spectral regions which are explorable with GOME-2’s visible channel 3, but not with SCIAMACHY’s spectral cluster 15.

5.2.3 Conversion to PFT Chla

PFT fit factors obtained from the PhytoDOAS fit are in units of mg/m^2 and need to be converted to PFT Chla by estimating the oceanic optical depth from which the satellite signal originates. As discussed in [Dinter et al. \(2015\)](#) and chapter [3](#), VRS can be used as a proxy for light penetration depth. For each satellite scene, PFT DOAS fits and a VRS DOAS fit were performed separately. Following [Losa et al. \(2017a\)](#), the ratio of PFT to VRS fit factors was calculated for scaling the PFT fit factor to the light penetration depth. This ratio was then converted using a LUT relating PFT/VRS fit factor ratio to PFT Chla as function of SZA.

Building of LUT

A relationship between PFT/VRS fit factor ratio and PFT Chla is required. First, the relationship between PFT fit factor and PFT Chla as well as between VRS fit factor and Chla were determined separately and then, in a second step, the two were combined by taking the PFT/VRS fit factor ratio for a given Chla. The relationship between VRS fit factors and Chla as function of SZA was determined for average open ocean scenarios using a standard phytoplankton absorption spectrum as in section [3.2.5](#). The relationship between PFT fit factor and PFT Chla was obtained from RTM simulations as described in the following.

The RTM SCIATRAN was used for simulating TOA radiances for the open ocean with water containing different PFT with various Chla ranging between 0 and $30 \text{ mg}/\text{m}^3$. Average open ocean scenarios were modeled as in chapters [3](#) and [4](#) with respect to, e.g., surface roughness, however, few changes were made:

- phytoplankton absorption coefficient a_{ph} : PFT specific absorption spectra a_{ph}^* were used to calculate the phytoplankton absorption coefficient at different Chla C , $a_{ph} = a_{ph}^* \cdot C$.
- liquid water absorption coefficient a_w : the spectrum by [Pope and Fry \(1997\)](#) was used instead of the more recent spectrum by [Mason et al. \(2016\)](#), because the latter one lead to ambiguous relationships between PFT fit factor and Chla for low Chla (more pronounced than in Figure [5.2.4](#) and for almost all fit windows), which was not evident in DOAS fits on satellite-measured backscattered radiances.
- CDOM absorption coefficient a_{CDOM} : the parameterization was not changed with respect to chapters [3](#) and [4](#), however, it is listed here explicitly, because it was used in combination with a different parameterization for phytoplankton absorption. a_{CDOM}

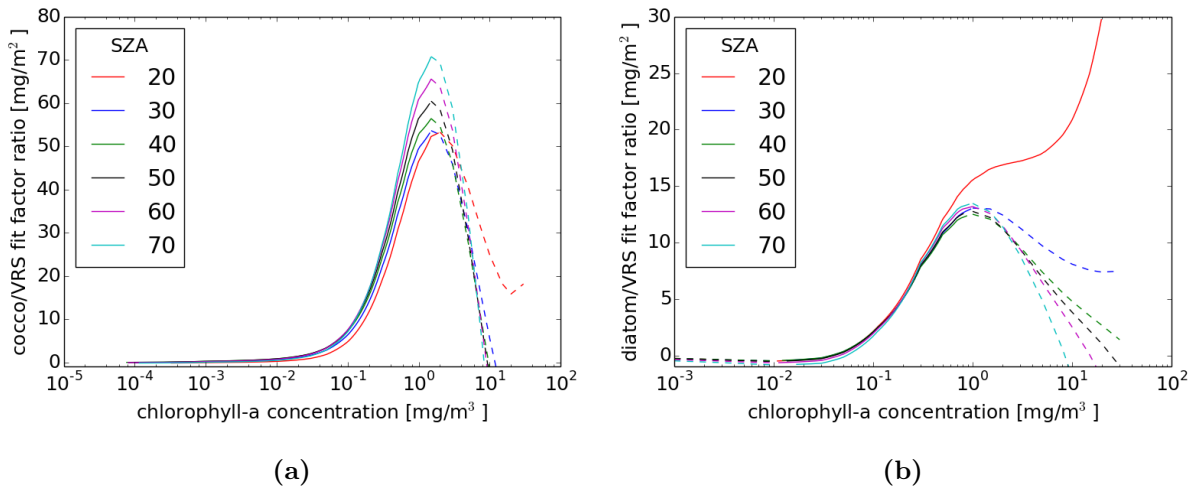


Figure 5.2.6: Look-up tables for converting PFT/VRS fit factor ratios to PFT chlorophyll-a concentration as function of SZA for (a) coccolithophores and (b) diatoms. Only a selection of simulated SZA is shown. Dotted curves show cut-off areas due to ambiguity of relationship between ratio and chlorophyll-a concentration.

was parameterized as in [Morel and Maritorena \(2001\)](#) using $a_{CDOM} = 0.2(a_w(\lambda_0) + 0.06C^{0.65}) \exp(-S(\lambda - \lambda_0))$ with $S = 0.014 \text{ nm}^{-1}$ and reference wavelength $\lambda_0 = 440 \text{ nm}$.

- particle scattering: was described by a Fournier-Forand scattering function as introduced in sections [2.9.6](#) and [3.2.5](#), however, instead of using the scattering coefficient as parameterized in [Gordon and Morel \(1983\)](#), the spectral variation of the attenuation coefficient c was parameterized as described in [Voss \(1992\)](#) as a power law $c = 0.39C^{0.57}(490/\lambda)^{0.5}$, since it is more recent. The exact choice of the parameterization does not have a significant influence on the resulting LUT.

As in chapter [4](#), a realistic atmosphere was modeled containing aerosols and all relevant trace gases except water vapor. Resulting LUT are displayed in [Figure 5.2.6](#) for a selection of simulated SZA. The LUT were cut off at high Chla (around 1 mg/m^3) when relationship between fit factor ratio and Chla become ambiguous. For the diatom LUT, the ratio also decreases slightly at the lower end of the Chla range, which was additionally cut off.

The LUT has to be used cautiously for ocean scenes with Chla larger 1 mg/m^3 . At this Chla value, the overall attenuation of the ocean is so high that the light path from which the signal originates reaches a critical value. The signal that reaches the satellite sensor drops unproportionally to the overall higher absorption in the ocean and lower PFT fit factors result. The VRS fit factor, which monotonously decreases with increasing Chla,

can not always compensate this behavior fully when the ratio of PFT to VRS fit factor is taken as the simulations show (also already observed for LUT built for SCIAMACHY PFT retrieval with slightly different RTM parameterization [Soppa et al., 2016b](#)). Since the overall attenuation determines the signal at the satellite and not just the contribution from a single PFT, absolute PFT Chla retrieved for ocean scenes with a total Chla value above 1 mg/m^3 should be double checked for consistency. In the Southern Ocean, total Chla above 1 mg/m^3 are found on the Patagonian Shelf, especially in the months of October and November, and in the vicinity of islands. No inconsistent behavior was observed that indicates that the results presented in the next section are majorly influenced by this effect.

5.2.4 Viewing zenith angle correction

Clouds shield the radiance signal from the ocean. DOAS retrievals of completely cloud-covered scenes are expected to yield fit factors of zero for oceanic reference spectra. Cloud-covered scenes were analyzed on a monthly basis. Non-zero fit factors were found and a distinct VZA dependence was observed. Figure [5.2.7](#) (a) shows coccolithophore, (c) diatom, and (d) VRS fit factors as function of VZA for cloudy scenes with cloud fraction larger 0.95 in the SOAI region for the month of December 2011. Non-zero fit factors are observed for all three variables. While fit factors are almost constant for positive VZA, linearly increasing trends with negative VZA are found for coccolithophore and VRS fit factors and a linearly decreasing trend for diatom fit factors. Figure [5.2.7](#) (b) shows coccolithophore fit factors from cloud-free scenes (cloud fraction < 0.05) in a region of the North Pacific Gyre (150° - 180° W, 15° - 25° N), where coccolithophore fit factors are also expected to be close to zero. A similar trend is observed, i.e., a linear increase of fit factors with negative VZA and nearly constant fit factors for positive VZA. The VZA effect is not only present over clouds, i.e., not caused by clouds, but rather appears as a global phenomenon. Negative VZA correspond to relative azimuth angles smaller 90° , corresponding to a viewing direction tilting towards the sun. Such a distinct VZA dependence was not found for VRS fit factors over cloudy scenes of other hyperspectral sensors (checked for TROPOMI). The observation is therefore instrument-specific and not a general physical effect inherent to the PhytoDOAS method. The origin of this effect is therefore difficult to examine and we have no explanation for it yet.

It was decided to correct the observed effect. A VZA-depending offset correction was determined that forces fit factors over clouds to zero. On a monthly basis, the VZA dependence was determined in the SOAI region over cloudy pixels (cloud fraction > 0.95). For each of the three oceanic variables, linear functions were determined describing the

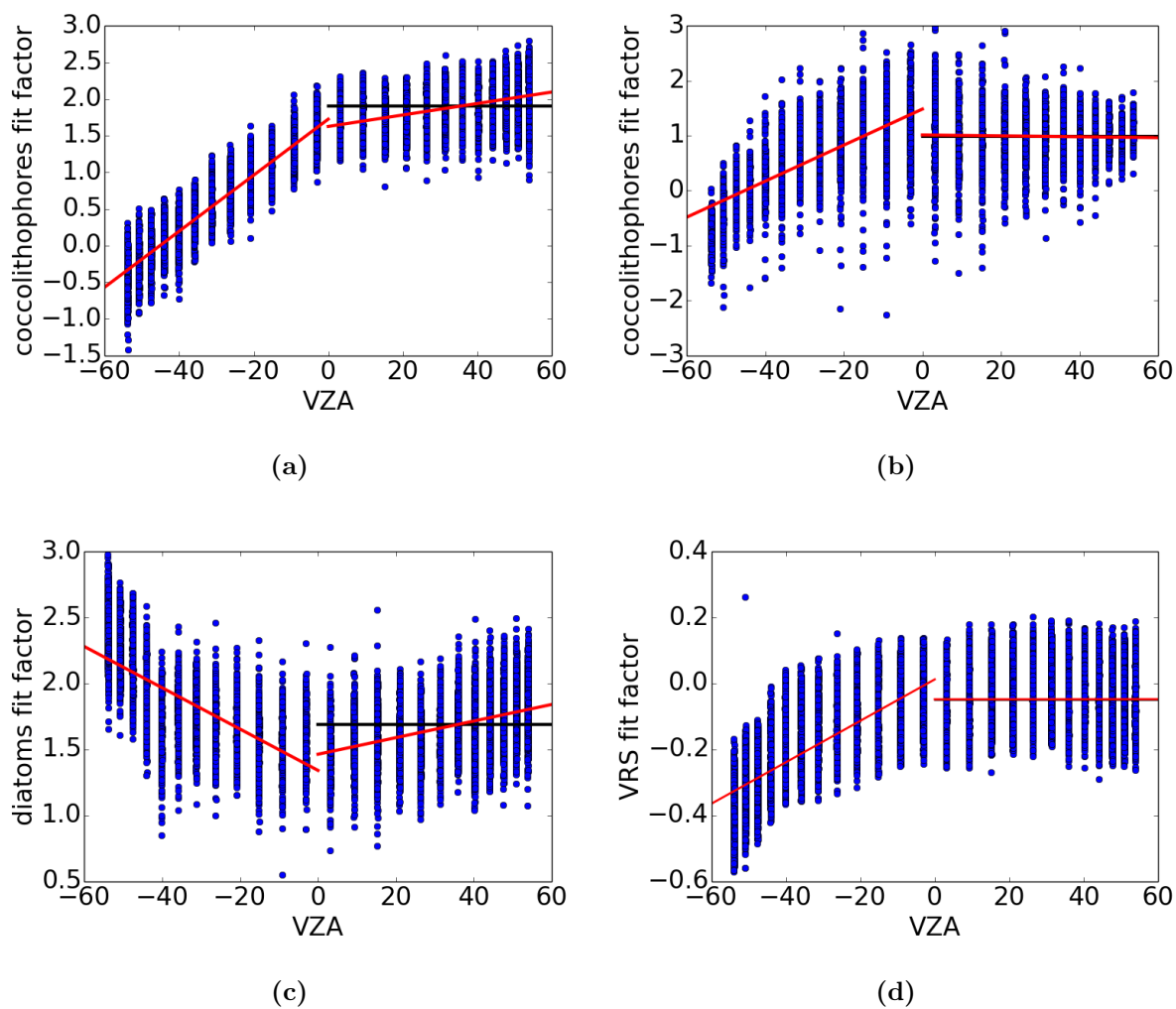


Figure 5.2.7: Coccolithophore fit factors as function of VZA (a) in the SOAI region over cloud-covered scenes (cloud fraction > 0.95) and (b) in the North Pacific Gyre (150° - 180° W, 15° - 25° N) over cloud-free scenes (cloud fraction < 0.05). (c) Diatom and (d) VRS fit factors in SOAI region over cloud-covered scenes. Linear functions used for correction of VZA-dependence are shown as red lines. Black lines show mean fit factor value for positive VZA.

VZA-dependence for positive and negative VZA separately (see Figure 5.2.7). Although the VZA dependence for positive VZA is almost constant, a linear description enabled a smoother transition of the correcting offsets at $VZA = 0^\circ$. Slopes varied slightly over time. For coccolithophores, a mean monthly slope of 0.02 ± 0.01 and intercept of $1.2 \pm 0.5 \text{ mg/m}^2$ was found for negative VZA and a slope of 0.006 ± 0.001 and intercept of $1.4 \pm 0.4 \text{ mg/m}^2$ for positive VZA for the investigated 12 months. The standard deviation is given as uncertainty. For diatoms, mean monthly slopes and intercept were -0.015 ± 0.004 and $1.3 \pm 0.2 \text{ mg/m}^2$ for negative VZA and 0.004 ± 0.002 and $1.4 \pm 0.2 \text{ mg/m}^2$ for positive VZA, respectively, and for VRS, 0.007 ± 0.002 and -0.006 ± 0.13 for negative VZA and $(-0.6 \pm 2) \cdot 10^{-4}$ and -0.08 ± 0.11 for positive VZA.

5.2.5 Offset correction

Since temporal biases in VRS fit factors were observed for GOME-2 (section 3.3.5), the quality of the VRS fit factors was checked by converting them into diffuse attenuation coefficients using a LUT as in chapter 3. The LUT was built from simulations that were also used for building the LUTs for converting PFT fit factors to PFT Chla. Resulting K_d were compared to wavelength-converted $K_d(490)$ from the OC-CCI data set (version 4.2.). The same wavelength conversion as in chapter 3 was used. Much higher GOME-2 K_d values than expected from the OC-CCI data set were obtained. An offset correction was applied to the VRS fit factors on a monthly basis similar to the correction made for the TROPOMI K_d product in the blue spectral range (section 4.2.3). The optimal additive offset for each month was determined by the value that yielded a slope close to one ($0.95 < \text{slope} < 1.05$) when GOME-2 K_d was compared to OC-CCI K_d on a daily basis using 0.5° gridded data of the SOAI region as input. The comparison was limited to $K_d < 0.15 \text{ m}^{-1}$, for which agreement between GOME-2 and OC-CCI K_d is significantly higher than for larger K_d values (section 3.4.3). The slope becomes less meaningful for larger K_d values, because data sets diverge. Averaged over the investigated 12 months, the mean Pearson correlation coefficient between GOME-2 and OC-CCI K_d for this reduced data set is 0.51 ± 0.08 in the SOAI region. Correcting the VRS fit factors with an additive offset results in slopes close to one, however, the GOME-2 K_d values are generally higher than those from OC-CCI. A mean intercept of $0.021 \pm 0.006 \text{ m}^{-1}$ is found for the 12 months. Optimal offsets vary from month to month and between the years, ranging between 0.15 and 0.27 with a mean additive offset of 0.21 ± 0.04 .

It is evident from the previous results in chapters 3 and 4 that the uncertainty in the VRS fit factor increases with increasing light attenuation. For waters with $K_d > 0.15 \text{ m}^{-1}$, large

uncertainties were found for the VRS-derived K_d . The uncertainty of K_d is influenced by the uncertainty in VRS fit factor and the uncertainty associated with the LUT conversion. Since their influence is challenging to separate, no filtering criterion is used to quality control VRS fit factors. The uncertainty in VRS fit factors has to be kept in mind. However, their influence on the conversion to PFT Chla might be less crucial than in the approach to derive K_d , since ratios of fit factors are generally more robust.

5.2.6 Cloud correction

Clouds shield the radiance signal below them, reducing the retrieved DOAS fit factors over partly cloudy scenes (Koelemeijer and Stammes, 1999). The Southern Ocean is a region of high cloud coverage. Due to the large pixel size of GOME-2 measurements, only low data coverage is achieved when applying a strict cloud filter (cloud fraction < 0.05). To overcome this major loss in information, a cloud correction was applied to keep partly cloudy pixels in the data set. The correction scheme follows a cloud correction introduced by Velders et al. (2001) and Richter and Burrows (2002) which was used for correcting DOAS-retrieved fit factors of tropospheric NO_2 . The signal of surface-near NO_2 was assumed to be completely shielded by clouds, which compares to the situation found for oceanic signals.

The cloud radiance fraction for a satellite scene was estimated with the help of the RTM SCIATRAN. Two different scenarios were simulated: a completely cloud covered scene represented by a surface height of 1 km and a surface albedo of 0.8 (same cloud albedo as assumed in FRESCO+ product) and a completely cloud-free scene with a surface albedo of 0.1 at a height of 0 km. The average ocean albedo is estimated to be lower (Li et al., 2018), however, results are rather insensitive to exact ocean albedo settings (0.07 was also tested). For both scenarios, different combinations of SZA, VZA, and relative azimuth were simulated. SZA range from 10° to 70° in steps of 5° , VZA from 0° to 60° in steps of 5° , and relative azimuth from 0° to 180° in steps of 10° . The model gave an output for TOA radiance as a function of SZA, VZA, and relative azimuth resulting in a LUT for a cloud-free and a completely cloud-covered case. The theoretical radiance for a satellite scene in case of a completely cloud-covered pixel L_{cloud} and in case of a cloud-free pixel L_{ocean} were obtained via interpolation using as input the SZA, VZA, and relative azimuth information of each satellite ground pixel. The cloud radiance fraction was then calculated as

$$f_{\text{cr}} = \frac{fL_{\text{cloud}}}{fL_{\text{cloud}} + (1 - f)L_{\text{ocean}}} \quad (5.2.1)$$

where f is the cloud fraction taken from the FRESCO+ cloud product (Wang et al., 2008b).

The fit factor was corrected using the cloud radiance fraction:

$$S_{\text{corr}} = S \frac{1}{1 - f_{\text{cr}}}. \quad (5.2.2)$$

Only ground pixels with f_{cr} smaller than 0.5 were corrected, so that pixels were kept in the data set only if more than half of the radiance information at the TOA originates from the ocean. This threshold corresponds to a cloud fraction of about 0.16 depending on viewing geometry.

5.3 Results

First, benefits of the applied cloud correction are presented. Next, GOME-2-derived PFT results are compared to other satellite products. From this comparison, the diatom concentrations derived from GOME-2 were found to show insufficient data quality. The study proceeds only with investigations on the coccolithophore concentrations. These are first compared to in-situ data. A time series analysis follows, where the phenology is investigated. In this study the term “bloom” does not follow any strict definition of a phytoplankton bloom with respect to Chla levels, but rather refers to “above average concentrations” in a certain region.

5.3.1 Benefits of cloud correction

For illustrating the effect of the cloud correction, different cloud filter and cloud correction scenarios for VZA-corrected coccolithophore fit factors in the SOAI region are shown in Figure 5.3.1 for the month of February 2011. Figure 5.3.1 (A) illustrates the coverage and magnitude of fit factors when only almost cloud-free scenes are selected, cloud fraction < 0.05 . Besides in the very North and close to Patagonia, data coverage is sparse. Including also scenes with higher cloud fractions (up to 0.16), increases the coverage, but reduces the mean fit factor as seen in Figure 5.3.1 (B). Figure 5.3.1 (C) shows the coccolithophore fit factors after cloud correction which permits correction of partly cloudy scenes with cloud fractions up to ~ 0.16 . The selection of ground pixels shown in (B) and (C) is similar, however, mean coccolithophore fit factors are higher after cloud correction. The cloud-corrected fit factor magnitudes are in line with the magnitudes observed in the cloud-free case (A). The applied cloud correction scheme successfully corrects the influence of

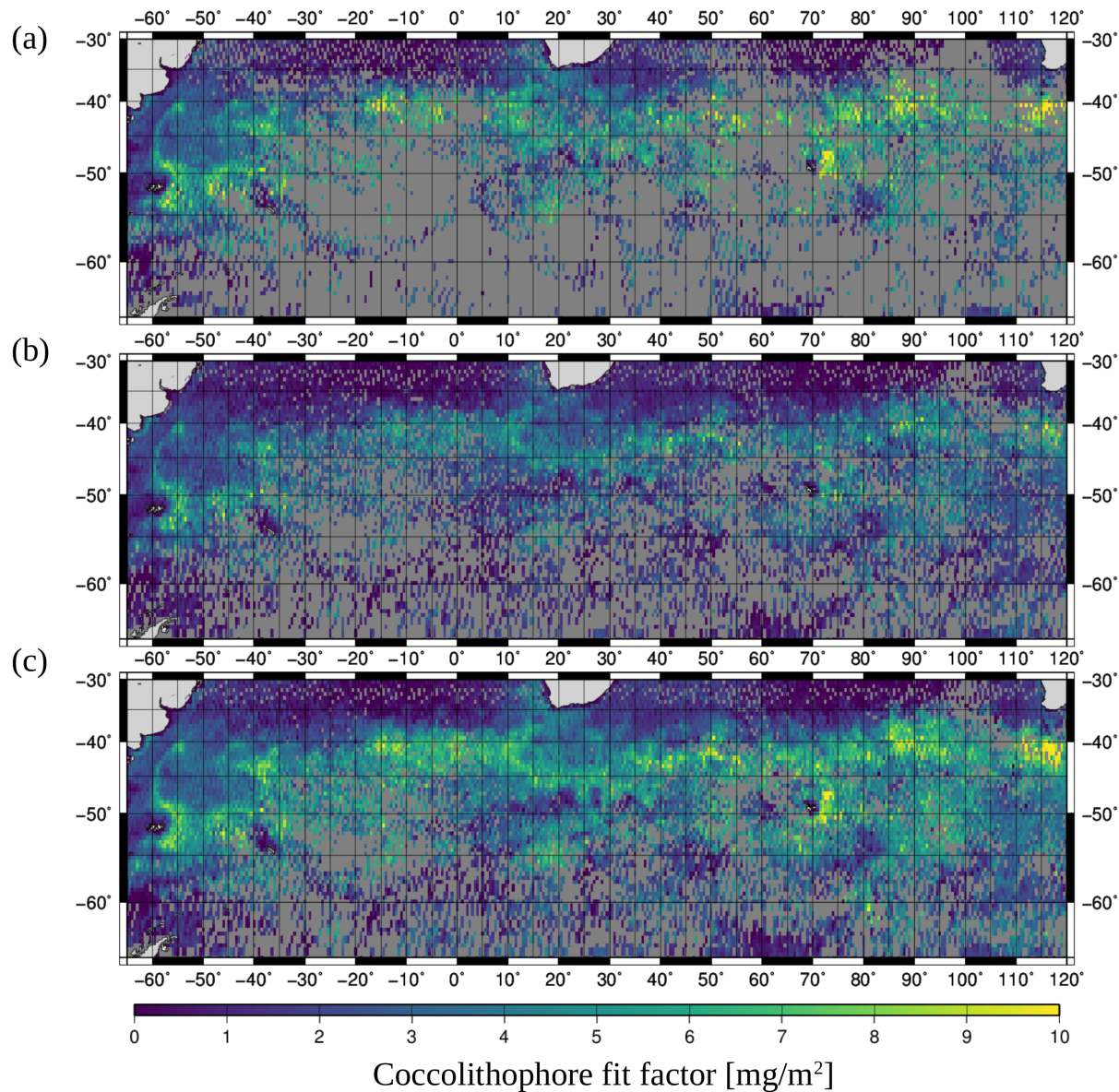


Figure 5.3.1: VZA-corrected coccolithophore fit factors in SOAI region gridded to 0.5° for February 2011. (A) A strict filter with cloud fraction < 0.05 was used to select only cloud-free scenes. (B) Partially clouded scenes are included with cloud fractions < 0.16 . (C) VZA-corrected coccolithophore fit factors after cloud correction which roughly permits correction of ground pixels with cloud fractions < 0.16 .

clouds. The coverage is significantly increased. Averaged over the investigated 12 months, the monthly coverage increases from a fraction of 0.52 ± 0.04 for the cloud-free case (cloud fraction < 0.05) to 0.76 ± 0.04 when cloud correction is applied. The mean daily coverage for the 12 months increases from 0.04 ± 0.01 to 0.09 ± 0.02 . All further analysis are performed on cloud corrected data.

5.3.2 Satellite product comparisons

Coccolithophores

Different satellite products were intercompared in the SOAI region. Figures 5.3.2 and 5.3.3 show the GOME-2 coccolithophore Chla in comparison to PIC from MODIS-Aqua, SynSenPFT coccolithophore Chla and its two input data sets, the SCIA-PD coccolithophore Chla and OC-PFT haptophytes Chla in the time periods 17 Jan to 17 Feb 2011 and 18 Feb to 20 Mar 2012, respectively. All data products were gridded to 0.5° . Naturally, the worse spatial resolution and coverage of the hyperspectral compared to the multispectral sensors becomes apparent immediately. Features in the SCIA-PD product appear sharper than those in the GOME-2 data caused by slightly better spatial resolution, but the product seems significantly patchier, i.e. high and low coccolithophore concentrations alternate on small scales. Generally, patterns appear similar, but the correlation between the hyperspectral sensors, considering the monthly gridded averages, is rather low with Pearson correlation coefficient of $r = 0.38$ for 2011 and 0.32 for 2012 (see also Table 5.3.2 for region-specific correlation coefficients). All correlations presented are calculated based on gridded monthly means. A comparison on a monthly basis enhances the representation error between different sensors which has to be kept in mind. Daily comparisons, however, yielded results only covering very few areas of high data coverage within the SOAI region and were therefore regarded as even less representative.

The magnitude of coccolithophore Chla is similar in all four PFT satellite products, however, the SCIA-PD data set reaches a bit higher values than the others. The hyperspectral sensors (and consequently also SynSenPFT product) detect higher coccolithophore Chla than the OC-PFT product in the open ocean areas of the SOAI regions far away from land masses. For the hyperspectral sensors, the highest values in these open ocean areas are of similar magnitude as the high values on the Patagonian Shelf. OC-PFT and the MODIS PIC product show a larger contrast between Patagonian Shelf and open ocean areas, with highest values clearly found on the Patagonian Shelf.

Since coccolithophores are calcifying organisms, PIC can be considered as a proxy for coccolithophore presence (Balch et al., 2011, 2016). The following focuses on intercom-

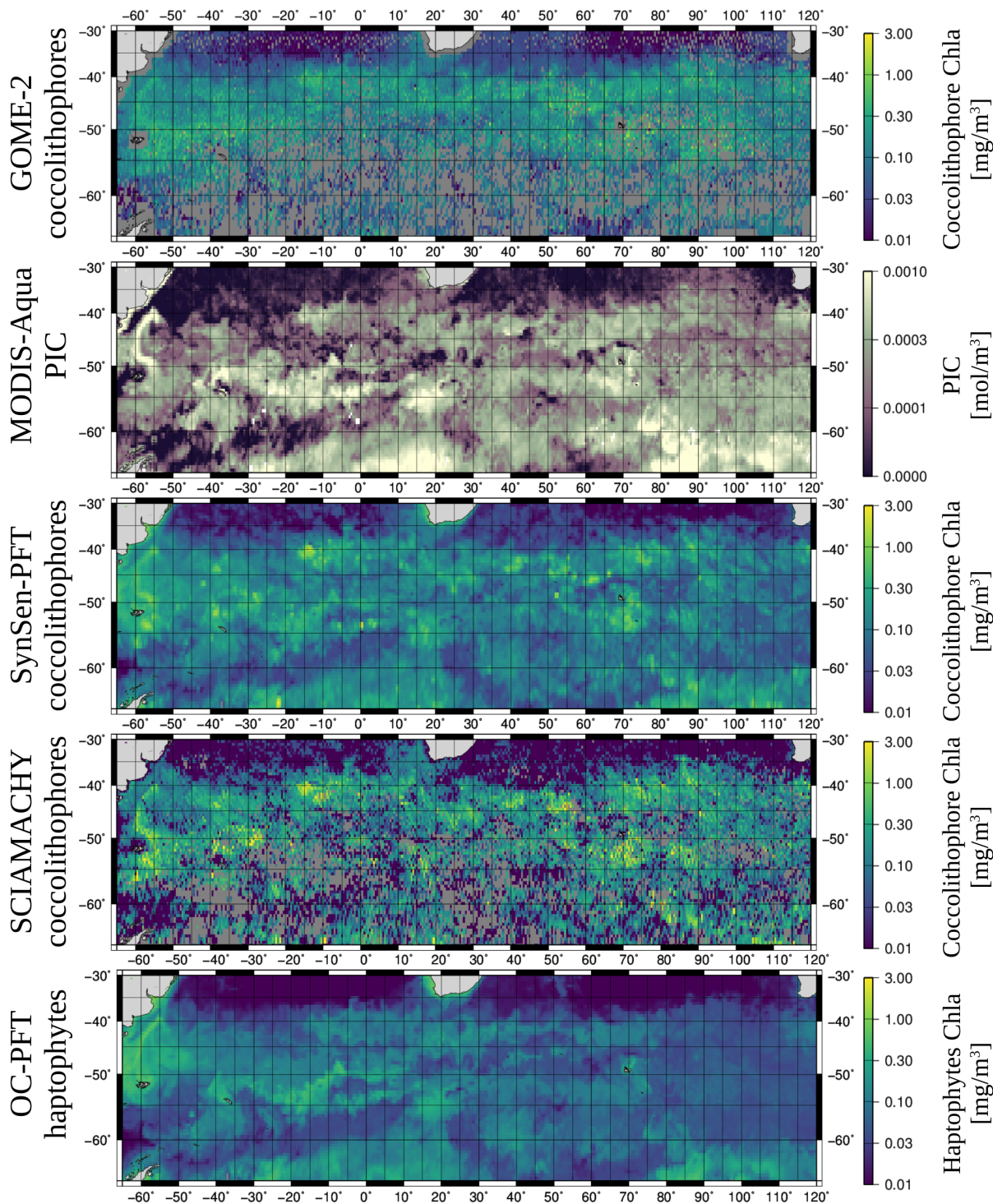


Figure 5.3.2: GOME-2-retrieved coccolithophore Chla in comparison to MODIS PIC, SynSenPFT and SCIA-PD coccolithophore Chla, and OC-PFT haptophytes Chla for the time period 17 January to 17 February 2011. All data sets are gridded to 0.5° .

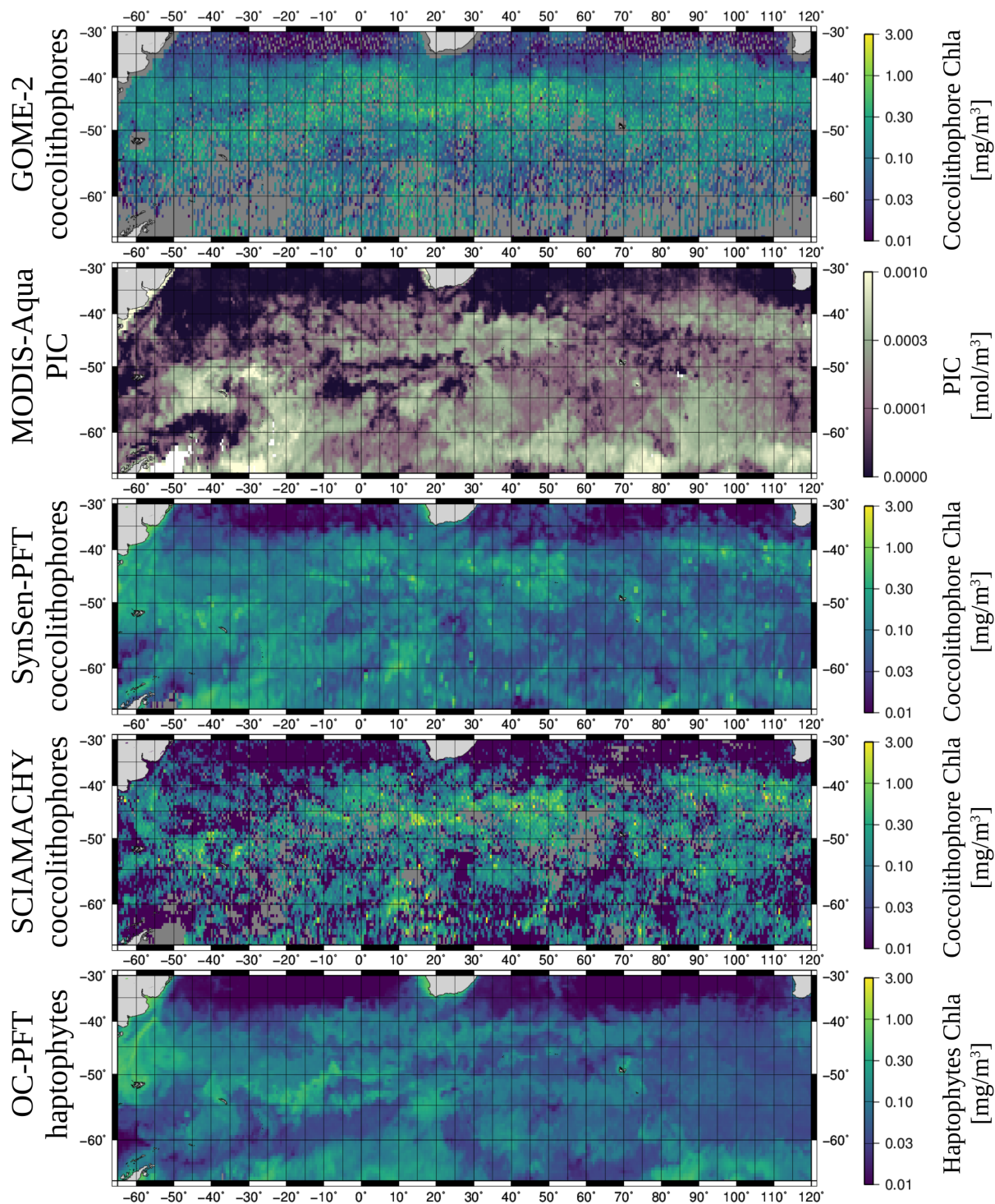


Figure 5.3.3: GOME-2-retrieved coccolithophore Chla in comparison to MODIS PIC, SynSenPFT and SCIA-PD coccolithophore Chla, and OC-PFT haptophytes Chla for the time period 18 February to 20 March 2012. All data sets are gridded to 0.5°.

parison between MODIS PIC and the coccolithophore/haptophytes data sets. Results are separated in north and south of the Polar Front, because coccolithophores are thought to be most abundant north of the Polar Front (Mohan et al., 2008) and hyperspectral data coverage significantly differs on the northern and southern side of the front. The Polar Front roughly coincides with 50°S (Balch et al., 2016). North of 50°S, where the coverage of the hyperspectral sensors is decent, GOME-2 and SCIAMACHY identify similar areas of high coccolithophore Chla which are in good agreement with patterns of elevated MODIS PIC concentrations. The OC-PFT product does not show enhanced haptophytes Chla for some of these features where MODIS PIC is high, e.g., around 45°S, 40°E and 40°S, 90°W (2011), 45°S, 30-50°W and 40°S, 90-110°W (2012). SynSenPFT coccolithophore patterns generally agree well with MODIS PIC. South of 50°S, intercomparison of hyper- and multispectral data sets is difficult, because the coverage of the hyperspectral sensors is low. In 2012, the coverage is a bit better in this area and a few features can also be identified in the hyperspectral data sets. A high MODIS PIC concentration between Falkland Islands and South Georgia is visible in terms of high coccolithophore Chla in the GOME-2 and SCIA-PD, but not in the OC-PFT data set. Enhanced MODIS PIC concentrations between 10° and 20°W and roughly 50° and 60°S coincide with high coccolithophore Chla values in all of the four other data sets. Roughly estimated from the few measurements South of 50°S, hyperspectral data sets generally seem to show lower coccolithophore Chla in the South than in the North, especially the GOME-2 data set.

For quantifying the similarity in patterns, Pearson correlation coefficients were calculated between MODIS PIC and the four other satellite data sets based on the monthly gridded data in subregions of the SOAI region (see Table 5.3.1). The SOAI region was subdivided into three major areas, referred to as the Patagonian region (30-60°S, 50-65°E), the Northern SOAI region (30-50°S, 50°E-120°W), and the Southern SOAI region (50-65°S, 50°E-120°W). For the latter two, correlation coefficients were also calculated for two reduced regions excluding the area South of 60°S for the Southern SOAI region, and the area North of 35°S for the Northern SOAI region, to exclude the influence of the extremely low coverage in the South (GOME-2 in 2012) and the low Chla areas in the North.

As already recognized from visual inspection, correlations between MODIS PIC and the four PFT satellite data sets are high in the Northern SOAI region ($r = 0.4 - 0.63$), considering that different variables and monthly means are intercompared and spatiotemporal resolution varies among products. GOME-2 reaches higher correlation than SCIA-PD and even exceeds OC-PFT correlation with PIC, which is remarkable considering the high representation error due to much lower sampling by the GOME-2 sensor. For the Patagonian region, correlations between MODIS PIC and SynSenPFT as well as OC-PFT are sim-

ilarly high as in the Northern SOAI region. Correlations between MODIS PIC and the hyperspectral coccolithophore Chla are significantly decreased, especially for SCIA-PD, for which even slightly negative correlations are found. In the Southern SOAI region, again, correlations are similarly high as in the Northern SOAI region for SynSenPFT and OC-PFT. Correlations with OC-PFT tend to be slightly higher whereas correlations with SynSenPFT are slightly lower in the South than in the North. For the hyperspectral data sets, correlations with MODIS PIC are low, which is, however, difficult to interpret due to low data coverage. The reduced Northern and Southern SOAI region show similar trends. Excluding the low Chla region from the Northern area, on which all sensors agree, reduces the correlation coefficient, which is especially true for the 2012 OC-PFT product. Excluding the low coverage area from the Southern SOAI region, increases correlations slightly for the hyperspectral sensors (Table 5.3.1, regions labeled with small). No clear trend is observed for OC-PFT and SynSenPFT.

Diatoms

Figures 5.3.4 and 5.3.5 show the GOME-2 diatom Chla in comparison to SynSenPFT, SCIA-PD, and OC-PFT diatom Chla and total Chla from OC-CCI for the time periods 17 Jan to 17 Feb 2011 and 18 Feb to 20 Mar 2012, respectively. Diatom Chla data sets are shown in comparison to a total Chla data set, because high total Chla is usually associated with diatom presence (assumption of abundance-based approaches, e.g., Hirata et al., 2011) and because the total Chla product gives a general idea of expected Chla ranges in the SOAI region. Hyperspectral diatom data sets are noisy compared to multispectral products and also compared to the hyperspectral coccolithophore data sets. Ranges of diatom Chla vary strongly among different sensors. GOME-2 diatom Chla values are lowest among all satellite data sets. Only in some areas, maximum Chla values of similar size as maximum values in the OC-PFT and SynSenPFT product can be seen. OC-PFT, SynSenPFT, and GOME-2 diatom Chla are generally lower than OC-CCI total Chla. In contrast, maximum SCIA-PD diatom Chla values are roughly a factor of three higher than maximum values of the total Chla product. GOME-2 and SCIA-PD diatom data are generally dissimilar. Comparing the gridded monthly mean, only a Pearson correlation coefficient of 0.08 is reached for 2011 and 0.04 for 2012. Pearson correlation coefficients with respect to the Northern, Southern, and Patagonian region can be found in Table 5.3.2.

GOME-2 diatom Chla hardly show any distinct patterns. Elevated concentrations around 0.1 to 0.3 mg/m³ are seen ubiquitously. Lower concentrations are found in the low Chla areas in the North. Distinct features of higher diatom Chla (~3 mg/m³) are only seen in 2012 west of the Falkland Islands and in the Indian sector at latitudes as of Kerguelen

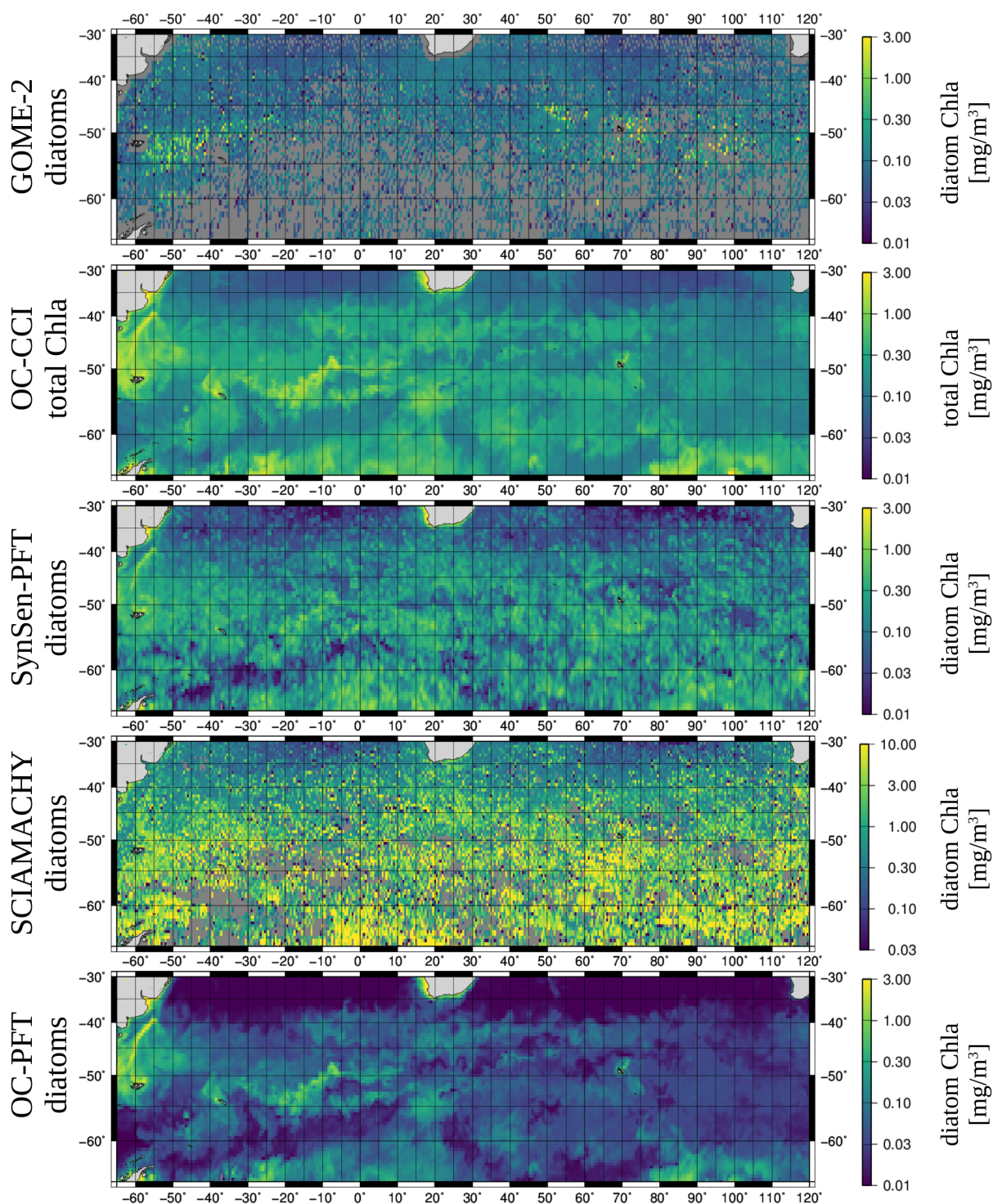


Figure 5.3.4: GOME-2-retrieved diatom Chl a in comparison to OC-CCI total Chl a and SynSenPFT, SCIA-PD, and OC-PFT diatom Chl a for the time period 17 January to 17 February 2011. All data sets are gridded to 0.5°. Note that color scales vary between different panels due to large differences in Chl a ranges.

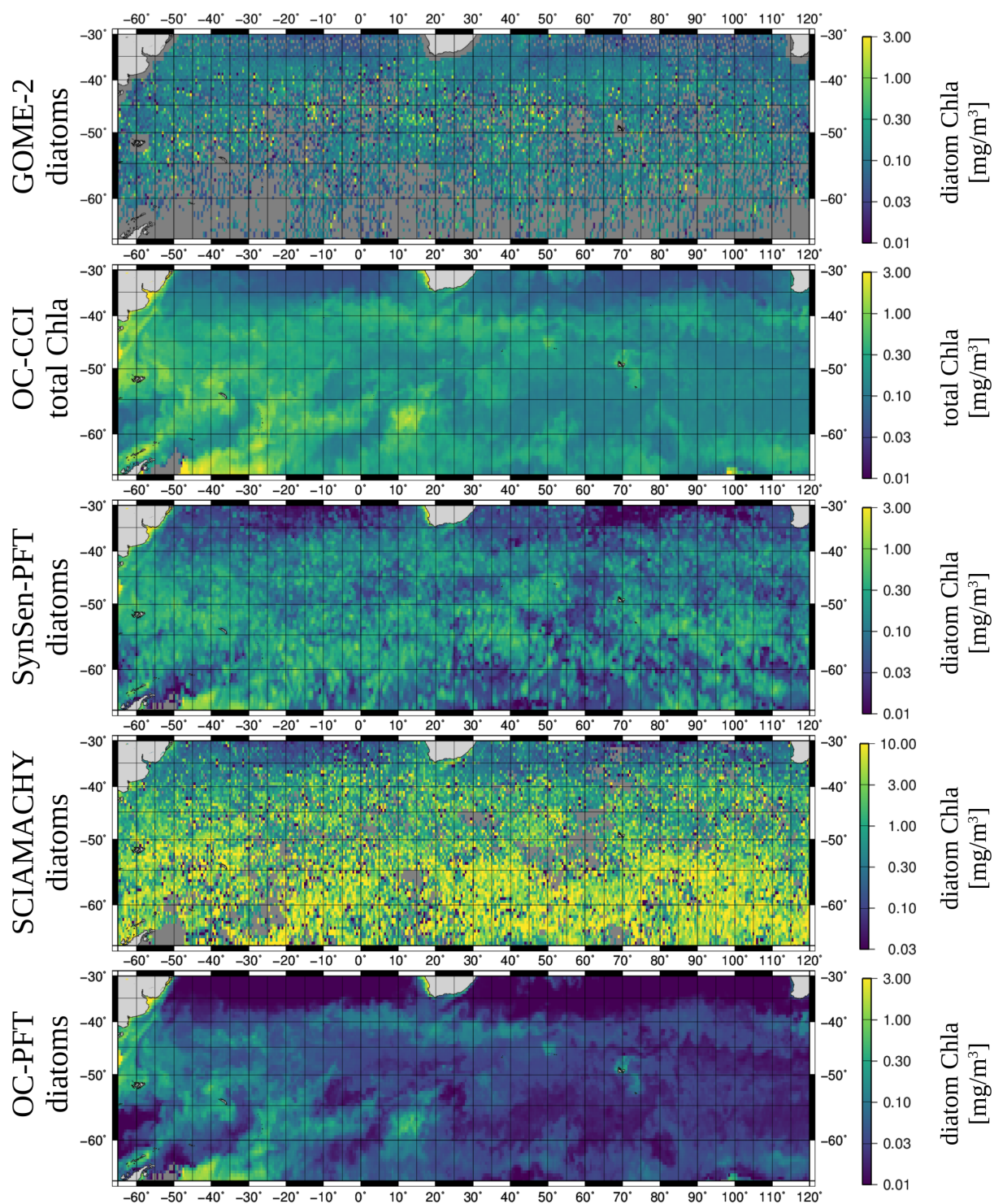


Figure 5.3.5: GOME-2-retrieved diatom Chla in comparison to OC-CCI total Chla and SynSenPFT, SCIA-PD, and OC-PFT diatom Chla for the time period 18 February to 20 March 2012. All data sets are gridded to 0.5° . Note that color scales vary between different panels due to large differences in Chla ranges.

Islands. However, these features are not visible as high Chla areas in the total Chla product. North of the Falkland Islands, where total Chla values are at its maximum in the SOAI region, diatom Chla is low in the GOME-2 data set.

In the SCIA-PD product, diatoms are ubiquitously present throughout the SOAI region. Low diatom concentrations are only seen in the low Chla areas in the North. Diatom Chla increases southwards. In contrast to the total Chla product which shows distinct areas of low Chla contrasting areas of high Chla South of 50°S, high diatom Chla is seen in the SCIA-PD product spreading almost homogeneously over the entire SOAI region South of 50°S. SCIAMACHY detects high diatom Chla North of the Falkland Islands (2011) where OC-CI total Chla is at its maximum, however, also South of the Falkland Islands (2011 and 2012) where only low Chla values are expected from the total Chla product.

The OC-PFT diatom product shows similar patterns as the total Chla product, since it is derived from it, but more contrast. The SynSen product appears noisy and elevated diatom concentrations are present throughout the SOAI region due to the influence of the SCIAMACHY sensor on the data product. Patterns of high diatom Chla appear slightly more similar to the total Chla product in the Atlantic sector than in the Indian sector.

Table 5.3.1: Pearson correlation coefficients between MODIS PIC and coccolithophore or haptophytes Chla from GOME-2, SCIA-PD, SynSenPFT, and OC-PFT, respectively, gridded to 0.5° and averaged over time periods 17 January to 17 February 2011 and 18 February to 20 March 2012. Nan values were excluded.

Region	GOME-2		SCIA-PD		OC-PFT		SynSenPFT	
	2011	2012	2011	2012	2011	2012	2011	2012
Northern SOAI	0.63	0.56	0.40	0.55	0.56	0.52	0.63	0.62
Northern SOAI (small)	0.55	0.47	0.36	0.40	0.51	0.31	0.57	0.52
Southern SOAI	0.16	0.18	0.20	0.14	0.67	0.46	0.53	0.38
Southern SOAI (small)	0.22	0.23	0.28	0.22	0.61	0.56	0.51	0.51
Patagonian	0.39	0.20	-0.03	-0.07	0.47	0.51	0.50	0.57

Table 5.3.2: Pearson correlation coefficients between GOME-2 and SCIA-PD coccolithophore and diatom Chla, respectively, gridded to 0.5° and averaged over time periods 17 January to 17 February 2011 and 18 February to 20 March 2012. Nan values were excluded.

Region	coccolithophores		diatoms	
	2011	2012	2011	2012
SOAI	0.38	0.32	0.08	0.04
Northern SOAI	0.44	0.41	0.09	0.07
Southern SOAI	0.23	0.14	0.01	0.01
Patagonian	0.49	0.30	0.15	0.04

5.3.3 In-situ comparison

Comparison with in-situ data focused on the GOME-2 coccolithophore data, since the GOME-2 diatom data quality appears insufficient from the satellite comparisons. Figure 5.3.6 (a) shows GOME-2 coccolithophore Chla averaged for the Atlantic sector over the time period 17 Jan to 17 Feb 2011 and for the Indian sector over the time period 18 Feb to 20 Mar 2012 to match the time periods and cruise tracks (shown as line on top of the 0.5° gridded data) of the 2011 R/V Melville and 2012 R/V Roger Revelle cruises. For comparison, Figure 5.3.6 (b) shows the coccolithophore abundance sampled during these two cruises (239 samples). Close agreement between in-situ and GOME-2 coccolithophore data is not expected, since a monthly mean gridded to 0.5° is intercompared with in-situ point measurements. In addition, data sets are given in different units and their conversion underlies large natural variability (Daniels et al., 2014). However, in-situ coccolithophore cell counts provide the only direct information on coccolithophore presence in this time period and region, making a qualitative comparison of the two data types worthwhile. The in-situ data set gives a rough idea of where coccolithophores can be expected in the SOAI region in this time period. The spatial distribution of GOME-2 coccolithophore Chla along the cruise tracks generally agrees well with patterns of the in-situ coccolithophore cell counts. Similar areas of high and low coccolithophore abundance are identified by in-situ cell counts and GOME-2 coccolithophore data. Coccolithophore concentrations are high on the Patagonian Shelf, North of South Georgia, in the Atlantic sector and North of Crozet Islands and South of Kerguelen Islands in the Indian sector. Uniform presence of coccolithophores along the eastern transects in the Indian sector (East of 80°E) are seen in in-situ cell counts and in the GOME-2 product. Low coccolithophore concentrations are found in-situ and by GOME-2 in areas North of 35° and close to 60°S . The transect between 10° and 30°W can not be intercompared due to too low coverage in the GOME-2

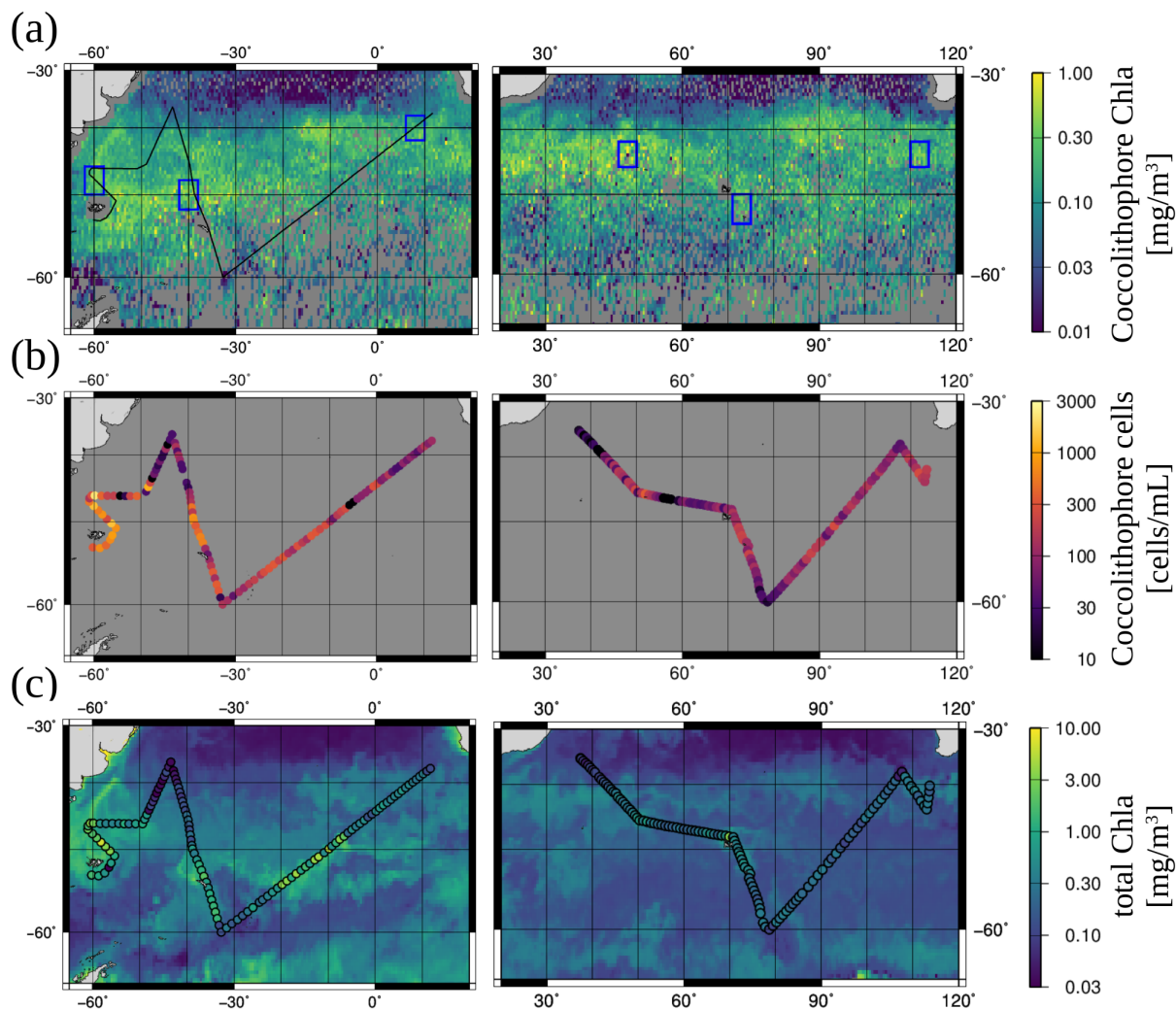


Figure 5.3.6: (a) GOME-2 coccolithophore Chla gridded to 0.5° in the Atlantic sector for the time period 17 Jan to 17 Feb 2011 and in the Indian sector for the time period 18 Feb to 20 Mar 2012. Black lines show the cruise tracks of R/V Melville and R/V Roger Revelle in 2011 and 2012, respectively. Blue rectangles mark the regions in which time series were computed, section 5.3.4. (b) Coccolithophore cell counts sampled in-situ. (c) OC-CCI total Chla gridded to 0.5° for same time periods as in (a). In-situ-sampled total Chla is shown overlaid as circles. Note that different color scales are used in (a) and (c) due to the large difference in range.

data set.

Following Poulton et al. (2013) and Smith et al. (2017), the cell count data was converted to concentrations in terms of chlorophyll-a using 0.2 pgChla/cell (Haxo, 1985) as conversion factor, which is a rather conservative value for *E. huxleyi* (e.g. 0.3 pgChla/cell (Daniels et al., 2014)). Since the conversion factor underlies large variability depending on species (Daniels et al., 2014), derived coccolithophore Chla from cell counts are only considered here as a rough estimator for expected concentration ranges. At the Patagonian Shelf, where *E. huxleyi* is dominating (Smith et al., 2017), in-situ coccolithophore Chla reach up to 0.5 mg/m³. The range of GOME-2 derived coccolithophore Chla is with 0-1 mg/m³ reasonable.

In-situ sampled total Chla matches well the monthly OC-CCI total Chla values as shown in Figure 5.3.6 (c). In-situ Chla is slightly higher than OC-CCI total Chla, especially apparent for the maximum values. Underestimation of total Chla in the Southern Ocean by globally-derived empirical Chla algorithms is a known issue (Johnson et al., 2013; IOCCG, 2015), e.g., the IOCCG (2015) finds an underestimation by a factor of two for version 6 of the ocean chlorophyll four-band algorithm (OC4v6, Werdell and Bailey, 2005, used in OC-CCI version 2). The OC-CCI total Chla product can be well used for comparison of spatial distributions and phenology, however, a possible underestimation needs to be kept in mind for further analysis. The range of in-situ total Chla in the Indian sector is 0.06-0.9 mg/m³ except for one data point. Since multiple PFT contribute to the total Chla signal (in-situ evidence for diatoms see Figure 3 in Balch et al., 2016), observed total Chla ranges indicate an overestimation of GOME-2 coccolithophore Chla in the Indian sector.

Balch et al. (2016) also determined the integrated calcification and photosynthesis of numerous discrete surface-water samples distributed along the cruise tracks. The integrated calcification over integrated photosynthesis ratio (see Figure 2 F in Balch et al., 2016) is high mostly in areas where total Chla is rather low, but GOME-2 coccolithophore Chla and MODIS PIC are rather high (transects East of 80° and North-South transect between ~30-45°W). Consequently, coccolithophores contribute significantly to the overall biomass in these areas supporting the correct identification of coccolithophores in these areas by GOME-2.

5.3.4 Time series

The temporal evolution of GOME-2 coccolithophore Chla in comparison to OC-CCI total Chla and MODIS PIC was investigated over the course of the austral summer in 2010/2011 and 2011/12. Time series from beginning of October until the end of March of coccol-

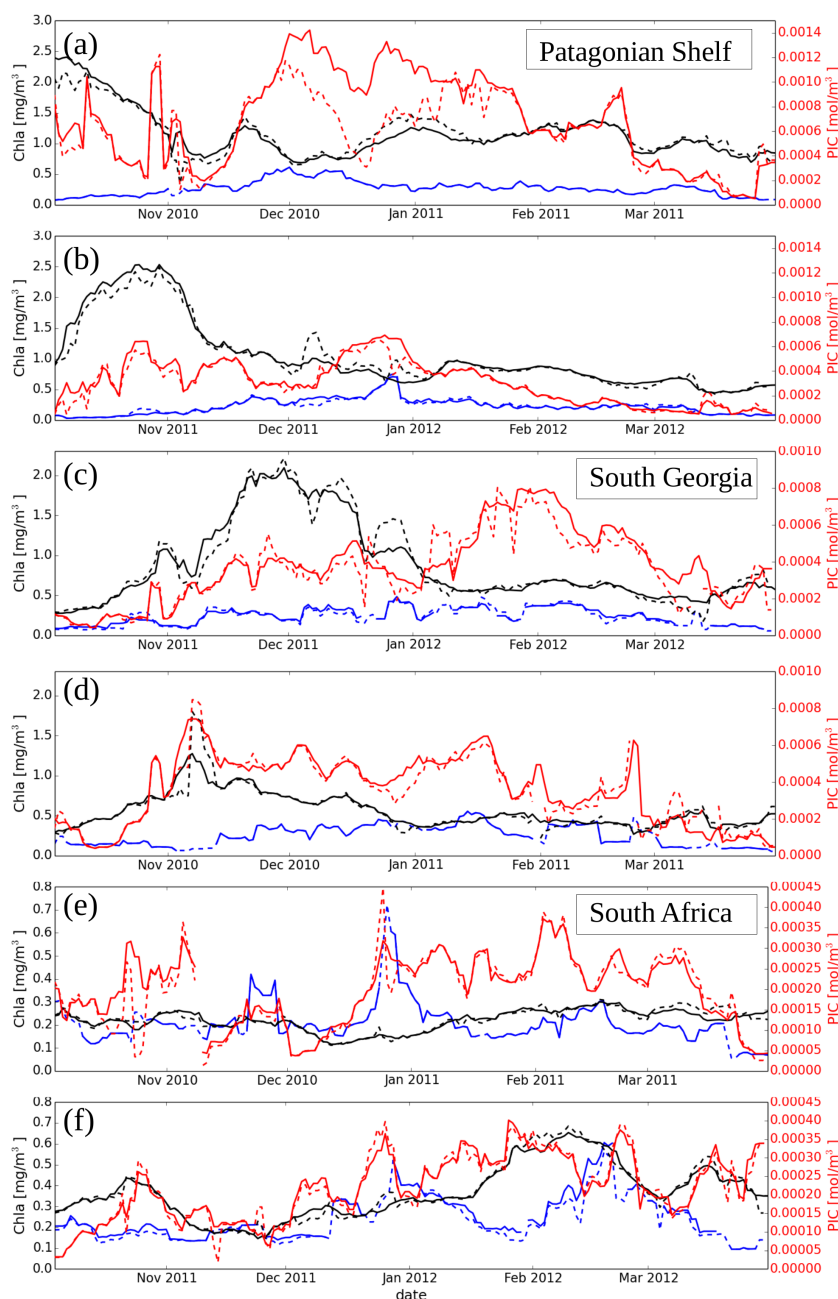


Figure 5.3.7: Time series of 7-day running composites computed from GOME-2 coccolithophore Chla (blue), MODIS-Aqua PIC (red), and OC-CCI total Chla (black) data sets in three regions of the Atlantic sector: (a), (b) Patagonian Shelf; (c), (d) North of South Georgia; (e), (f) Southwest of South Africa; for the time periods from beginning of October until end of March for 2010/11 and 2011/12, respectively. For MODIS-Aqua PIC and OC-CCI total Chla, dashed lines show the 7-day running composites based on the geocoordinates of the grid cells contained in the corresponding GOME-2 coccolithophore composite for each date. Time periods with dashed lines in the GOME-2 coccolithophore time series indicate composites calculated from less than 10 grid points. Regions are marked as blue rectangles in Figure 5.3.6.

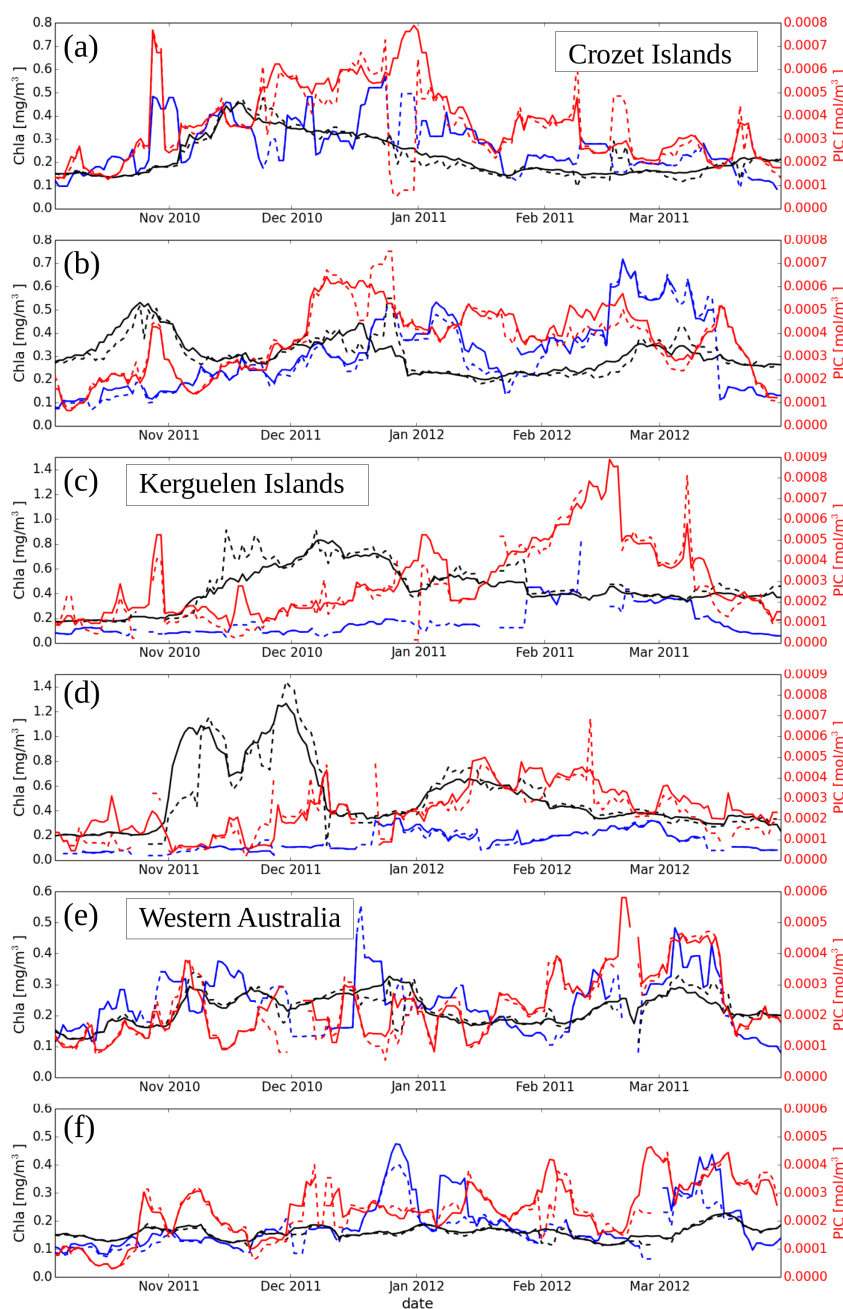


Figure 5.3.8: Time series of 7-day running composites computed from GOME-2 coccolithophore (blue), MODIS-Aqua PIC (red), and OC-CCI total Chla (black) data sets in three regions of the Indian sector: (a), (b) North of Crozet Islands; (c), (d) South of Kerguelen Islands; (e), (f) Southwest of Western Australia; for the time periods from beginning of October until end of March for 2010/11 and 2011/12, respectively. For MODIS-Aqua PIC and OC-CCI total Chla, dashed lines show the 7-day running composites based on the geocoordinates of the grid cells contained in the corresponding GOME-2 coccolithophore composite for each date. Time periods with dashed lines in the GOME-2 coccolithophore time series indicate composites calculated from less than 10 grid points. Regions are marked as blue rectangles in Figure 5.3.6

ithophore Chla from GOME-2, total Chla from OC-CCI, and PIC from MODIS-Aqua are shown in Figure 5.3.7 and Figure 5.3.8 as 7-day running composites for three regions in the Atlantic sector and three regions in the Indian sector, respectively, as introduced in section 5.2.1. 7-day temporal and $4^\circ \times 4^\circ$ spatial variability can be large within these regions as estimated from the standard deviation of the total Chla composites. Averaged over the full time series, the mean standard deviation of each composite is 25% to 60% of the mean total Chla value of each composite, with the higher value range obtained for regions showing strong seasonal cycles. To reduce the influence of the GOME-2 spatial coverage on the time series comparison, composites for MODIS PIC and OC-CCI total Chla were additionally calculated only selecting grid cells with coordinates as present in the corresponding GOME-2 composite (shown as dashed lines). This selection criterion only has a weak influence on the time series. General temporal trends remain. The total Chla time series is smoother than the PIC and especially the GOME-2 time series, which both show high frequency features due to lower data coverage. The focus lies on broad temporal patterns here.

Four regions show distinct bloom dynamics as visible from the pronounced maxima in total Chla: Patagonian Shelf, North of South Georgia, North of Crozet Islands, and South of Kerguelen Islands. Bloom dynamics are similar in the same region for different years, however, bloom maxima can be shifted by a month indicating a rather large interannual variability on this regional scale. Total Chla peaks within October to December. The total Chla maximum is followed by a maximum in PIC and coccolithophore concentration located within the months December through March. Overall temporal trends in PIC and coccolithophore Chla agree in these months, although local maxima and minima are not strictly correlated and PIC often peaks before coccolithophore Chla. For the months of October and November, pronounced high PIC values are observed which are usually associated with the total Chla maximum in the bloom regions of the Atlantic sector. Coccolithophore concentrations are low in these months and regions.

The two northern regions, Southwest of South Africa and of Australia, show low total Chla values in the OC-CCI data set during the entire austral summer with no clear bloom patterns except for the region Southwest of South Africa in the summer 2011/2012. The OC-CCI total Chla maximum is observed mid February. MODIS PIC and GOME-2 coccolithophore Chla peak around the same time. In 2010/2012, a peak in GOME-2 coccolithophore Chla of short duration at the end of December might explain the persisting high MODIS PIC values seen from January to March. This feature is not visible in the total Chla product, however might be suppressed by dynamics of other PFT that decline at the same time. In the area Southwest of Australia, the weak temporal variability in

OC-CCI total Chla is nicely followed by MODIS PIC and GOME-2 coccolithophore Chla, indicating that the fraction of coccolithophores in the phytoplankton community is roughly constant over time.

Of all time series, there is an interesting feature appearing twice which is visible in the regions Southwest of South Africa and South of the Kerguelen Islands in 2011/2012. Peaks in GOME-2 coccolithophore Chla are anticorrelated with the OC-CCI total Chla peak. The first GOME-2 coccolithophore peak appears at the beginning of January and decreases when OC-CCI total Chla starts to rise. GOME-2 coccolithophore Chla rises to a second peak at the end of February/beginning of March when OC-CCI total Chla has almost reached its maximum (Southwest of South Africa) or is already at its decline (South of Kerguelen Islands). The MODIS PIC concentration remains high after the first GOME-2 coccolithophore peak. No local minimum is seen. The temporal evolution of PIC in comparison to coccolithophore Chla can give insight into residence times of calcite in the upper ocean as discussed in section [5.4.4](#).

5.4 Discussion

First, the GOME-2 diatom retrieval is discussed shortly, followed by an extensive discussion of the more promising GOME-2 coccolithophore retrieval. Coccolithophore identification by GOME-2 is discussed in terms of presence and absence and, next, their quantification in terms of chlorophyll-a concentration. A discussion on coccolithophore phenology and its connection to PIC follows. The discussion proceeds with illustrating the GOME-2 coccolithophore monitoring capabilities in the Southern Ocean and the benefits of the presented data.

5.4.1 Diatom identification

Retrieving diatoms from GOME-2-measured backscattered radiances using PhytoDOAS yields a diatom data set of poor quality in the SO. The diatom data set is noisier than the coccolithophore data set and spatial correlation with OC-CCI total Chla is low. Noise in combination with false spatial distribution indicates that the PhytoDOAS method has difficulties to identify diatom absorption in GOME-2-measured optical depths and to separate it successfully from absorption spectra of other atmospheric and oceanic contributions or spectral instrumental artifacts. Results on diatom Chla were dissimilar to those found for SCIA-PD, indicating that the influence of spectral instrumental artifacts plays a significant role for the retrieval outcome.

SCIA-PD showed diatom Chla increasing towards the South which is in agreement with current knowledge on the diatom distribution in the SO (e.g., [Alvain et al., 2008](#); [Soppa et al., 2016a](#)). Maximum values for SCIA-PD diatom Chla are about a factor three higher than maximum values in the OC-CCI total Chla product. Considering, that total Chla is generally underestimated by empirical band algorithms in the Southern Ocean ([Johnson et al., 2013](#)), the range of diatom Chla is reasonable. However, SCIA-PD diatoms are ubiquitously present in the South which is not expected from the spatial distribution seen in the OC-CCI total Chla product. SCIA-PD diatom Chla therefore appear overestimated on average. [Losa et al. \(2017a\)](#) pointed out an overestimation of diatom Chla derived from SCIAMACHY on the global scale. The high data coverage in SCIA-PD compared to the GOME-2 data set indicates that a less strict cloud filter is used for SCIA-PD and there might be a small cloud contamination in the SCIA-PD products (also discussed in section [5.4.5](#)). GOME-2-derived diatom fit factors showed large positive values over clouds compared to the diatom fit factor range over cloud-free ocean scenes. Assuming a similar behavior for the retrieval on SCIAMACHY data, overestimation and ubiquitous presence of diatoms across the SO could partially be attributed to influence from clouds. It might be worthwhile to check, if similar results can be achieved for GOME-2 and SCIAMACHY when the exact same fit settings are used for GOME-2 and a stricter cloud filter is applied for SCIAMACHY. The retrieval might be more sensitive to small changes, e.g., in fit window, than expected from retrievals on simulated backscattered radiances.

5.4.2 Coccolithophore identification

Coccolithophore presence or absence can be successfully identified in GOME-2-measured backscattered radiances using the PhytoDOAS method. High correlation with MODIS PIC and good spatial agreement with in-situ coccolithophore cell counts indicate that presence of coccolithophores is correctly indicated in the GOME-2 coccolithophore data set north of 50°S. Less agreement between MODIS PIC and GOME-2 coccolithophore Chla was found for the Patagonian area, however, in-situ and time series data show that GOME-2 results are reasonable. Unfortunately, the large satellite foot print of the GOME-2 sensor and low coverage due to clouds in the SO region in combination with limited in-situ coccolithophore data sets (usually also in different units) do not permit a true validation of the GOME-2 product.

An issue for PFT retrievals is the correlation between specific absorption spectra of different PFT that cause their false identification. Although the fit window was identified as optimal for the retrieval of coccolithophores, a non-zero correlation between PFT ab-

sorption spectra remains as analyzed in [Sadeghi et al. \(2012a\)](#). Correlation between PFT spectra is mainly caused by chlorophyll-a as absorbing pigment, present in every PFT. [Wolanin et al. \(2015c\)](#) have analyzed the effect of constant or covarying background concentrations of other PFT on the coccolithophore PhytoDOAS retrieval with settings as in [Losa et al. \(2017a\)](#). Constant background concentrations of 0.05 mg/m³ for diatoms or 0.005 mg/m³ for cyanobacteria can lead to an error of 50% in retrieved coccolithophore concentrations. Covarying background concentration of 20% diatoms or 2% cyanobacteria can cause an error around 20%. Usually, an underestimation of the retrieved coccolithophore concentration is observed. From the time series analysis, confidence is gained that false PFT identification is not a major issue for the GOME-2 coccolithophore product. At the OC-CCI total Chla maxima, GOME-2 coccolithophore Chla is usually low and similar to concentrations outside of the total Chla maxima. The temporal evolution is independent of OC-CCI total Chla. Presence of phytoplankton does not automatically cause elevated or decreased coccolithophore fit factors due to correlation of spectra.

Presence of *Phaeocystis* sp. might cause residual coccolithophore concentrations in GOME-2 data set. Most PFT algorithms do not differentiate between coccolithophores and *Phaeocystis* sp. since they belong to the same phytoplankton class, the haptophytes. Remote sensing PFT algorithms are usually empirically developed based on large global HPLC data sets ([IOCCG, 2014](#)). HPLC data is used to determine PFT Chla of the phytoplankton community found in a water sample, based on absorption pigments which are typically found in certain PFT. Variability in HPLC pigment data is usually not high enough to enable discrimination of coccolithophores from *Phaeocystis* sp. ([Kramer and Siegel, 2019](#)). Due to the high similarity in pigment composition, PhytoDOAS will likely have difficulties to spectrally distinguish coccolithophores from *Phaeocystis* sp.. Elevated coccolithophore Chla in the GOME-2 product might be caused by *Phaeocystis* sp. which are known to form strong blooms in the South of the Southern Ocean ([El-Sayed et al., 1983](#); [Fryxell and Kendrick, 1988](#)). GOME-2 data coverage is very low below 60°S, but the few data show elevated coccolithophore Chla. Also PIC and the other PFT satellite products investigated in this study show high values South of 60°S. Coccolithophores are usually found north of the Polar Front ([Mohan et al., 2008](#)). A steep decline in coccolithophore concentration has been found going southwards ([Balch et al., 2016](#)). Coccolithophores can be detected in-situ as far South as 61°S across Drake Passage ([Charalampopoulou et al., 2016](#)), 70°S in the Weddell Sea ([Winter et al., 1999](#)), and 65°S of Australia ([Cubillos et al., 2007](#)). From what is known about coccolithophores, it is unlikely that intense coccolithophore blooms form South of 60°S. The high signal in MODIS PIC in the South can possibly be caused by enhanced reflectance due to diatom frustules ([Balch et al., 2005](#)),

storm-induced bubbles (Randolph et al., 2014), whitecaps and foam (Dierssen, 2019), or glacial flour (Dierssen et al., 2002). The GOME-2 coccolithophore Chla in the South is not so high as for the other satellite products (SCIA-PD, SynSenPFT, OC-PFT) which indicates that presence of *Phaeocystis* sp. only moderately causes overestimation of coccolithophore Chla when derived with GOME-2. This study was not designed to check the question how well PhytoDOAS can distinguish coccolithophores from *Phaeocystis* sp.. To tackle this question in the future, GOME-2 coccolithophore results could be investigated for specific times and regions for which in-situ evidence of *Phaeocystis* sp. blooms exists (e.g. Poulton et al., 2007a), however, in-situ observations need to fall within the GOME-2 mission time.

5.4.3 Coccolithophore quantification

Coccolithophore quantification is a challenge using the PhytoDOAS method in combination with a LUT approach. As estimated from in-situ data, GOME-2 derived coccolithophore Chla are realistic on the Patagonian Shelf, but seem to be overestimated in all other open ocean areas of the SOAI region, especially in the Indian sector. Sadeghi et al. (2012b) also found overestimated coccolithophore Chla by SCIAMACHY close to New Zealand and suggested that it is caused by a different coccolithophore species dominating these waters. Since the magnitudes of specific absorption spectra are variable depending on species, using a single specific absorption spectrum as reference in the PhytoDOAS fit can lead to a wrong estimation of coccolithophore Chla. Smith et al. (2017) found an increase in coccolithophore diversity moving eastward from Patagonian Shelf. At the Patagonian Shelf, *E. huxleyi* is dominating. Coccolithophore diversity could therefore explain why retrieved concentrations fit best at the Patagonian Shelf and are overestimated elsewhere.

The LUT had to be cut off at a value of around 1 mg/m^3 . In section 5.2.3, it was already pointed out that results have to be interpreted carefully for waters with total Chla larger 1 mg/m^3 . The overall consistency of coccolithophore Chla results found in all analysis indicates that the retrieval produces reasonable results for most SO scenes that are in the critical Chla range. It is not clear where the critical value lies exactly due to natural variability of the phytoplankton absorption and likely different sensitivities of the retrieval on simulated data compared to satellite-measured data. However, GOME-2 coccolithophore data on the Patagonian Shelf in the months October to November, when total Chla is highest, should be treated carefully.

One source of error in conversion with the LUT lies in the differences in simulations used for PFT and for VRS retrievals. Simulations for VRS reference spectra and backscattered

radiances on which VRS retrieval were performed to map a relationship between VRS fit factor and Chla differ slightly from those used for finding a relationship between PFT and Chla. Since the two are matched with respect to Chla when the LUT is built relating the ratio of the two fit factors to Chla, a mismatch arises, because Chla is the same in the scenarios, but optical depth of the water slightly differs mainly due to the use of a different water absorption spectrum. Simulations for VRS were not recalculated to match those for PFT, but kept as in chapter 3, because of high computation times. The mismatch is not regarded as the main source for the overestimation for two reasons. Sadeghi et al. (2012b) also observe an overestimation in a similar area. Second, the coccolithophore fit factors already appear to be too high when comparing them only with the PFT part of the LUT, i.e. the PFT fit factors resulting from PhytoDOAS fits on simulated radiances. Nevertheless, simulations should be recalculated in future.

Obtaining realistic physical quantities from PhytoDOAS-retrieved fit factors using a LUT has already been in a challenge in chapters 3 and 4. Correlations with atmospheric spectra and spectral artifacts caused by instrumentation have been suggested as one source of error. As in chapter 4, the VRS fit factor had to be offset-corrected which indicates a mismatch between retrievals performed on satellite data and retrievals performed on model data. Without correction, coccolithophore Chla would be even higher. However, offset-corrected K_d values were higher for GOME-2 than for OC-CCI which can also lead to a general overestimation of coccolithophore Chla. This bias between the data sets was not correctable using a simple additive offset. Unfortunately, often the fit behavior can not be well predicted by results obtained on simulated data. As an example, a strong VZA dependence of the fit factors was seen which is not in agreement with modeled VZA dependence. Empirical conversion functions could be explored for newer hyperspectral sensors, e.g., TROPOMI, which have better spatial resolution.

5.4.4 Coccolithophore phenology

The coccolithophore phenology as observed in the time series of GOME-2 coccolithophore Chla is consistent with typical coccolithophore seasonal cycles. GOME-2 coccolithophore Chla peaks generally after the OC-CCI total Chla product in austral summer, December to March, which is in line with the general hypothesis that coccolithophore blooms follow diatom blooms, when surface waters are nutrient depleted and stratification increases (Holigan et al., 1993a,b). This hypothesis is supported by seasonal cycles of coccolithophores in the SO, which are often estimated from PIC satellite observations. E.g., following the total Chla peak in November, Signorini et al. (2006) found that MODIS PIC concentrations

start rising in November and peak in January.

Maxima in GOME-2 coccolithophore Chla roughly coincide with maxima in MODIS PIC concentration. A clear succession of the MODIS PIC signal following the GOME-2 coccolithophore signal is not observed. The MODIS PIC product has been validated by matchup comparison with ship measurements of PIC from several cruises in the Atlantic Ocean and the GCB (Balch et al., 2016). The RMS error was determined as $\pm 11\%$. Since the MODIS PIC product is robust, it was used in this study for evaluating the GOME-2 coccolithophore retrieval performance. The two products are expected to agree in first order. PIC is a proxy for coccolithophores due to their calcification activities, however, PIC can maintain in the surface waters after coccolithophore blooms died (Balch et al., 2007; Poulton et al., 2007b). The GOME-2 product, on the other hand, is only expected to detect living coccolithophores, since it targets the absorption of pigments involved in photosynthesis (Sadeghi et al., 2012a,b). Additionally, the calcification rates in a coccolithophore bloom underly natural variability. It has been observed that coccolithophores tend to increase calcification when growth rates slow and shed coccoliths due to cell stress and cell death (Paasche, 2001; Müller et al., 2008). From these insights on the relationship between PIC and coccolithophores, the MODIS PIC signal is expected to follow the GOME-2 coccolithophore signal, because it captures the late coccolithophore bloom state (Tyrrell and Merico, 2004). In the time series analyzed in this study, MODIS PIC often even peaks before GOME-2 coccolithophore Chla. Sadeghi et al. (2012b) investigated the temporal evolution of mean monthly MODIS PIC in comparison to mean monthly SCIAMACHY-derived coccolithophore Chla and found a general correlation between the two, however, were not able to resolve a clear succession of SCIAMACHY coccolithophore and MODIS PIC concentrations. This study finds similar behaviour for a higher temporal resolution, however, differences in temporal and spatial scales between the data sets and variability within the investigated regions remain large and might not enable to resolve such clear temporal trends.

Clear discrepancies between GOME-2 coccolithophore Chla and MODIS PIC signal were found in the months of October and November in areas with high total Chla maxima during these months. Most cruises that sampled for coccolithophore abundance on the Patagonian Shelf and vicinity took place later in the season, in December (Holligan et al., 2010; Poulton et al., 2013), January/February (Balch et al., 2016; Charalampopoulou et al., 2016), and March (Balch et al., 2011) (also see Table 1 in Holligan et al., 2010). Jacques and Panouse (1991) found presence of coccolithophores even further South, West of the Antarctic Peninsula, at the end of November. Hardly any in-situ data are present for coccolithophore abundance on the Patagonian Shelf in austral spring, however, from

observations by [Jacques and Panouse \(1991\)](#), higher coccolithophore concentrations are possible in these latitudes at this time of the year. The relative height of the MODIS PIC spring peak in the here presented time series analysis appears too high compared to the summer peak. [Signorini et al. \(2006\)](#) did not observe such a MODIS PIC feature in their analysis of the Patagonian Shelf for the season 2004/2005. Their mixed layer depths temporal evolution also indicates that environmental conditions are not favorable for coccolithophores in October and start to become favorable in November. A look at the environmental conditions during the austral summers of 2010/2011 and 2011/12 presumably helps to answer the question, if PIC concentrations in these months are associated with coccolithophores (not indicated by the GOME-2 product, however, since total Chla is especially high for this area and time of the year, the GOME-2 product might not be reliable) or have a different cause, contamination of the PIC algorithm by high total Chla ([Mitchell et al., 2017](#)), high opal concentrations ([Balch et al., 2005](#)), etc.

The time series analysis showed examples where two GOME-2 coccolithophore Chla maxima were observed in a time period for which MODIS PIC only showed one broad maximum. The two GOME-2 coccolithophore Chla maxima anticorrelated with a peak in OC-CCI total Chla. It is hypothesized that the coccolithophores start to grow, are outcompeted by other PFT leading to a peak in total Chla, and then start to grow again after, e.g., nutrient conditions are unfavorable for those other PFT. The PIC concentration stays high due to coccoliths that reside in surface waters while the coccolithophore bloom declines and reforms. By comparison of MODIS PIC and GOME-2 coccolithophore Chla, residence times of PIC in surface waters and coccolith to coccolithophore ratios could be estimated under different environmental conditions and bloom stages, when spatiotemporal differences between data sets are carefully accounted for. A spread in PIC turnover times of 7 to 50 days has been estimated from several cruises ([Balch et al., 2007](#)). Average global PIC turnover times have been estimated to be shorter, ~ 7 days ([Hopkins et al., 2019](#)), and are comparable to short turnover times (3-7 days) found in-situ ([Poulton et al., 2006](#)). Higher turnover times of 15 days have been estimated for the high latitudes ([Hopkins et al., 2019](#)). Lags between GOME-2 coccolithophore and MODIS PIC concentrations found in the presented time series analysis lie within these temporal ranges of observed and predicted turnover times.

5.4.5 Monitoring coccolithophores in the Southern Ocean

The GOME-2 coccolithophore data set is suitable for monitoring coccolithophores in the Southern Ocean Atlantic and Indian sectors north of the Polar Front including the Patag-

onian Shelf. Phenology and spatial distribution are correctly reproduced and can be used, e.g., as guideline for modelers working on reproducing coccolithophore seasonal cycles and spatial patterns in the Southern Ocean. Absolute coccolithophore Chla should be treated with caution, as well as relative coccolithophore Chla when different regions are intercompared, especially if total Chla is larger $1\text{mg}/\text{m}^3$. Similar to other PFT remote sensing products (e.g., [Brewin et al., 2017](#); [Xi et al., 2021](#)), GOME-2-derived coccolithophore Chla is associated with high uncertainties. For instance, [Xi et al. \(2021\)](#) present haptophyte Chla ranges roughly between 0.1 to $0.5\text{ mg}/\text{m}^3$ in the SOAI region with per pixel uncertainties ranging between 50% to 100%. GOME-2 coccolithophore Chla should be used carefully, e.g., for estimating total coccolithophore biomass.

Monitoring of PFT requires sufficient data coverage which has been improved in this study by using a cloud correction method. The developed cloud correction scheme for GOME-2-derived oceanic quantities increased the coverage in the SO significantly and was key for analyzing time series in multiple regions and broadscale spatial distribution. Despite these advances, coverage remains an issue for the GOME-2 coccolithophore data set even north of 50°S . Coverage is limited in some areas north of 50°S , e.g., low coverage was found for the transect between $0\text{-}30^\circ\text{W}$. In-situ data showed a cooccurrence of coccolithophores and diatoms in this area ([Balch et al., 2016](#)), making it an interesting location for a time series analysis. When computed, the GOME-2 time series had too many data gaps and was too noisy (and therefore not shown) to obtain any valuable information.

An opportunity to overcome poor spatiotemporal resolution of hyperspectral products is a combination with multispectral products as synergistically performed for the SynSenPFT product ([Losa et al., 2017a](#)). As analyzed in this study, SynSenPFT coccolithophore Chla compared well in comparison to MODIS PIC. Correlations with MODIS PIC north of 50°S were highest among the PFT data sets. It exceeded the correlation between MODIS PIC and the two input products, SCIA-PD coccolithophore and OC-PFT haptophytes product, which indicates that the Kalman-type filtering, used for optimal interpolation in the SynSenPFT method, successfully combines the input products yielding an overall improved data set in the SOAI region. It is acknowledged here, that the OC-PFT product targets haptophytes and not coccolithophores and therefore lower correlations with the MODIS PIC product are naturally expected. The SynSenPFT approach can also be applied to GOME-2 data in combination with a multispectral PFT product, which has been tested with an older version of the GOME-2 PFT data and showed promising results ([Losa et al., 2018](#)). However, when hyperspectral data coverage is low as in the SO, the synergistic product will be completely dominated by the multispectral product. An extension of the SynSenPFT method to include information from spatial and temporal averaging can im-

prove the situation as suggested in [Losa et al. \(2017a\)](#). As the comparison between MODIS PIC and OC-PFT has shown, OC-PFT can not predict high coccolithophore abundance where Chla is low, since it assumes a rigid relationship between the two variables. High PIC concentrations, but low total Chla have also been investigated in field-measurements of a large-scale coccolithophore bloom in the northeast Atlantic Ocean ([Fernández et al., 1993](#)). [Palacz et al. \(2013\)](#) have found that total Chla is a rather weak estimator for predicting coccolithophores and suggested that modeling coccolithophore biomass should possibly not be based on total Chla. For a synergistic coccolithophore product in the SO, it might therefore be better to not use an abundance-based, but a spectral-based PFT product as multispectral input data set, e.g., [Xi et al. \(2020\)](#). The mentioned multispectral data sets only give haptophytes as output and do not distinguish between coccolithophores and *Phaeocystis* sp.. The multispectral data sets could be analyzed to separate coccolithophores from *Phaeocystis* sp., e.g., based on their ecological preferences ([Palacz et al., 2013](#)), or even by extending the SynSenPFT approach to include biogeochemical modeling as suggested in [Losa et al. \(2017a\)](#). Complete spectral discrimination of these two PFT within the PhytoDOAS method is also challenging. However, using in-situ data and PFT models, *Phaeocystis* sp. influence on the coccolithophore data set could be quantified.

Studying the influence of climate change on phytoplankton community structure requires long-term data sets ([Cadée and Hegeman, 2002](#); [Suikkanen et al., 2013](#)) spanning about 40 years ([Henson et al., 2010](#)). GOME-2 data series, using all three MetOP satellites, ranges from 2006 to date and will presumably continue at least until 2023 based on designed mission life time ([EUMETSAT, 2017](#)), but probably even longer, considering that MetOP A and B vastly exceeded their designed mission life times. A 20 year data set can be realistically expected from the GOME-2 instruments. Further extension of the time series requires merging with other hyperspectral sensors (e.g., [Hilboll et al., 2013](#); [Coldewey-Egbers et al., 2015](#); [Heue et al., 2016](#)), which additionally increases coverage in overlapping mission time periods. SCIAMACHY, which started recording measurements in 2002, is a potential candidate for such a merged product. For the SOAI region, intercomparison of the SCIA-PD and the GOME-2 coccolithophore product showed only moderate agreement, hampering merging of data sets from the two sensors. The SCIA-PD coccolithophore product showed a higher data coverage in the study area than the GOME-2 product, although no cloud correction was used. SCIAMACHY has a smaller spatial resolution than GOME-2 (30 by 60 km² as opposed to 40 by 80 km²). It only reaches global coverage within 6 days as opposed to 1.5 days for GOME-2. Due to the large swath of GOME-2, groundpixels at the edges are very large and usually screened out, because often not cloud-free. Cloud filtering techniques are not directly comparable between the two sensors, but it appears likely that

the reflectance threshold used for filtering clouds in the SCIA-PD product is not as strict as the filter criterion used for GOME-2. The cloud correction method used in this study can in principle be applied to any other PhytoDOAS-derived product and consequently be used for increasing SCIAMACHY data coverage. Cloud contamination, if present in the SCIA-PD product, does not seem to have a large impact on the coccolithophore product, because general features are very similar compared to the other satellite products. Different cloud filtering criteria and representation error due to different sampling times can explain low agreement between SCIA-PD and GOME-2 coccolithophore products found in this study. However, insufficient agreement between sensors for merging has also been found for PhytoDOAS-derived diffuse attenuation coefficients on the global scale in chapter 3 for an earlier mission year (2007). Further analyses are needed and corrections might have to be applied prior to merging.

Satellite time series need to be stable in time for trend analyses which can be impaired, e.g., by sensor degradation (Lacan and Lang, 2011; Dikty et al., 2012; Munro et al., 2016). Problematic non-physical seasonal cycles in DOAS-derived atmospheric and oceanic quantities from GOME-2 backscattered radiances have been observed (Lerot et al., 2010, section 3.3.5) and associated with seasonally changing spectral features in GOME-2 recorded solar spectra caused by the diffuser plate as for the GOME instrument (Richter and Wagner, 2001). Within the limited time period studied here, no such behavior appeared after offset-correcting VRS fit factors with the help of the OC-CCI K_d product. Investigating long-term stability of the GOME-2 coccolithophore Chla was out of the scope of this study. The temporal stability needs to be checked, when full mission period is processed in the future.

5.4.6 Benefits of GOME-2 coccolithophore Chla data

Although long-term monitoring of coccolithophores in the SO is an overall goal, valuable insights on SO coccolithophores and their relationship with PIC can be already drawn from the here presented two year data set and from the whole GOME-2 A time period data product, which should be producible based on this study without further changes to the method. The comparison between MODIS PIC and the GOME-2 coccolithophore Chla, also in relation to OC-CCI total Chla product, yielded important results and raised interesting research questions.

Spatial variability in PIC can be explained to a large extent by presence of living coccolithophores. High correlations between GOME-2-derived coccolithophores and MODIS PIC across the Atlantic and Indian sectors of the GCB indicate that the MODIS PIC

signal is indeed caused by living coccolithophores over large scales supporting the GCB hypothesis. Furthermore, temporal variability is different for coccolithophores and PIC. Coccolithophore phenology can only be roughly inferred from PIC on temporal scales on the order of months. Examples have been found in the time series analysis, for which only one persistent coccolithophore bloom would be deduced from MODIS PIC, while the GOME-2 coccolithophore data set shows two blooms. Differences in the GOME-2 coccolithophore and MODIS PIC time series could be exploited for inferring residence times of PIC in surface waters. How long PIC remains in surface waters is interesting, because short PIC turnover times in combination with high particulate organic carbon (POC) turnover times are postulated to indicate regions of high carbon export (Balch et al., 2007). Generally, interesting regions and times of the year for further studies on understanding PIC and coccolithophores in the SO and their remote-sensing can be identified by discrepancies between PIC and coccolithophore Chla identified in the MODIS-Aqua and GOME-2 data, respectively. Comparison of GOME-2 coccolithophore product to OC-CCI total Chla also has further implications. Generally, a high degree of independence was observed between the two data sets which substantiates the hypothesis that total Chla is not a good estimator for coccolithophore abundance (Palacz et al., 2013) (in the SO).

Next to PIC and total Chla, GOME-2 coccolithophore Chla can be compared to time series of environmental conditions such as mixed layer depth, sea surface temperature, photosynthetically available radiation, surface velocity, and nutrients from other satellite or model products similar to Sadeghi et al. (2012b) to further understand coccolithophore phenology, e.g., identify optimal growth conditions. GOME-2 coccolithophore Chla data offers the potential of studying phenology in the SO over broad spatial scales and seasonal cycles (spring and summer months) which can not be realized with ship campaigns in this remote area. From the full GOME-2 A time period, also the influence of climate oscillations on coccolithophores could be investigated (e.g., as done for diatoms in Soppa et al., 2016a).

5.5 Conclusion

This study evaluated monitoring capabilities of the GOME-2 sensor for two key PFT in the Southern Ocean, coccolithophores and diatoms. PhytoDOAS retrieval performance on GOME-2-measured hyperspectral data was assessed by comparison with PFT products, total Chla, and PIC from other satellite sensors, as well as in-situ data. The study area focused on the GCB in the Atlantic and Indian sector for the austral summer in 2010/11 and 2011/12.

The standard PhytoDOAS approach was extended by implementing corrections which increased temporal stability and coverage of resulting GOME-2 PFT data sets. A cloud correction scheme was applied for the first time to oceanic parameters retrieved with DOAS. It roughly doubled coverage in the often cloud-covered SO and was essential for investigating PFT spatial distributions over large scales and time series. It is suggested to use it where necessary also for improving coverage of other PhytoDOAS data sets from different hyperspectral sensors.

The study focus was shifted to coccolithophores, because the retrieved diatom product did not show sufficient data quality for, e.g., studying coexistence of the two PFT in the SO. Although chosen fit settings were similar to previous retrievals on SCIAMACHY data, results were dissimilar, indicating that sensitivity to exact fit settings and instrumentation specific spectral features is high.

Identification of coccolithophores works well using PhytoDOAS. The spatial distribution and temporal evolution of retrieved coccolithophore concentrations generally agree well with MODIS PIC and does not follow the OC-CCI total Chla signal. Quantification of coccolithophores using PhytoDOAS in combination with a LUT approach is challenging. Absolute values of GOME-2 coccolithophore Chla are associated with higher uncertainties and should be treated especially carefully if total Chla exceeds 1 mg/m^3 . Quantifying uncertainties by validation with in-situ data was not feasible due to the lack in in-situ data quantity and provision of in-situ data in units differing from those retrieved by satellites as well as due to the comparably poor spatiotemporal resolution of the GOME-2 sensor. Rough evaluation with in-situ data showed good agreement with GOME-2 coccolithophore spatial distribution and reasonable coccolithophore Chla on the Patagonian Shelf. Towards the Indian sector, an overestimation of GOME-2 coccolithophore Chla is observed, possibly reflecting coccolithophore species diversity in specific absorption (Sadeghi et al., 2012b).

Despite the much coarser spatiotemporal resolution of the GOME-2 coccolithophore data sets compared to typical ocean color products, this study illustrated its value for answering important research questions and identifying new areas of research. High agreement between GOME-2 coccolithophore Chla and MODIS PIC supports the GCB hypothesis that high-reflecting waters in the SO are associated with living coccolithophores. Just as interesting are the differences between the two data sets. Temporal variability is generally larger in GOME-2 coccolithophore Chla than in the MODIS PIC product showing a potential for estimating PIC residence times in surface waters. These results stress the need for coccolithophore products as uncertainties are introduced when coccolithophore phenology is inferred from PIC. Support was found in the GOME-2 coccolithophore Chla data that total Chla is not a good estimator for coccolithophore abundance and spectral-based

approaches appear therefore more suitable for coccolithophore identification from satellite data than abundance-based approaches.

Regarding long-term monitoring of coccolithophores in the SO, GOME-2 data sets cover a long time period, but extension of this time period by merging with other hyperspectral sensors such as SCIAMACHY might be difficult and require further corrections. Possibilities were discussed for synergistically combining (Losa et al., 2017a) GOME-2 data with multispectral data to obtain improved data coverage and spatial resolution. As most promising, the combination with a spectral-based approach applied to multispectral OC data was identified as well as the assessment of *Phaeocystis* sp. influence on the data set by including knowledge on ecological preferences.

6 Concluding remarks

Main conclusions and applications of the work presented within the main three studies of this thesis are summarized. The three studies are then combinedly discussed with respect to the overarching hypotheses of this thesis.

6.1 Summary of main conclusions and applications

The first OC retrievals from the DOAS-type sensors GOME-2, OMI, and TROPOMI in the blue and/or ultraviolet spectral range were presented based on the Differential Optical Absorption Spectroscopy method (PhytoDOAS). Filling-in by Vibrational Raman scattering was successfully identified in backscattered radiances measured by all three sensors (as well as SCIAMACHY). A diffuse attenuation coefficient (K_d -blue) was derived from VRS for the blue spectral range (390 to 423 nm). Robust agreement with the operationally-provided diffuse attenuation coefficient from common OC data sets was found after wavelength-converting it. Intersensor differences were found for the DOAS-type sensors in terms of spatial and temporal biases which hamper the merging of data sets from different sensors and highlight the importance of accurate calibration of level-1 radiances for OC applications. Derived K_d -blue provides an independent data set based on a completely different approach as compared to those used on multispectral sensors. In contrast to the multispectral approaches, the PhytoDOAS retrieval uncertainty is lowest for the clearest waters. Hyperspectral K_d -blue are potentially more accurate here. To substantiate this statement, extensive validation with in-situ data are needed in the future. At present, such a validation was not feasible, as the work was limited by existing in-situ data sets and the spatial resolution of DOAS-type satellite sensors, which was only recently improved.

The first direct derivation of diffuse attenuation coefficients from satellite measurements in the ultraviolet spectral range was presented in this work. Two novel diffuse attenuation products in the UV for the wavelength ranges 312.5 to 338.5 nm and 356.5 to 390 nm were shown to have potential based on comparison with field measurements. These K_d coefficients in the UV can be used to better estimate shortwave radiation penetration and heat budgets. Comparison of K_d at three shortwave spectral ranges can provide insight

on CDOM and UV-absorbing phytoplankton pigments. For all VRS retrievals, the light availability, which is important for estimating primary productivity as well as photodamage or other photochemical processes, can also be directly obtained from VRS through a modified LUT. UV dose rates can be directly inferred without going through a multistep approach of considering atmosphere, surface and underwater properties separately.

Coccolithophore Chla was successfully retrieved from GOME-2 measurements in the Southern Ocean by including knowledge on VRS retrievals from the first two studies. Comparison with other satellite products and field measurements showed that the spatial distribution and phenology of GOME-2-derived coccolithophore Chla are well represented, but absolute coccolithophore Chla values are also associated with higher uncertainties. An overestimation of coccolithophore Chla was identified for most parts of the Atlantic and Indian sectors. High similarity between GOME-2 coccolithophore Chla and MODIS-Aqua particulate inorganic carbon was found which strengthens the Great Calcite Belt hypothesis. Elevated reflectances in the Southern Ocean are indeed caused by living coccolithophores. Comparison of the two data sets furthermore showed areas of high and low PIC residence times; the latter indicate areas of possible high carbon export rates. GOME-2 coccolithophore Chla showed a high degree of independence from total Chla in the Southern Ocean, which substantiates the hypothesis that the total chlorophyll-a concentration is not a good descriptor for coccolithophore biomass. Retrieved diatom Chla from GOME-2 revealed to be insufficient in data quality.

6.2 Hypothesis I: OC variables in the blue-green spectral range can be retrieved from multiple SCIAMACHY-like satellite sensors

The PhytoDOAS method is generally suitable for retrieving OC variables from SCIAMACHY-like satellite sensors. The filling-in of Vibrational Raman Scattering was spectrally identified in backscattered radiances measured by GOME-2, SCIAMACHY, OMI, and TROPOMI. VRS is highest in clear water regions where underwater light paths are long and many VRS events occur. The spatial distribution of VRS in the global oceans showed patterns that closely resemble those of phytoplankton biomass for all sensors. Phytoplankton are the main driver for underwater light depths in the open ocean. When Chla is low, VRS is high and vice versa. The amount of VRS can be connected to descriptors of the underwater light field. The light availability and the diffuse attenuation coefficient around 400 nm had been successfully derived for SCIAMACHY from VRS data prior to this work. This analysis

was extended in this thesis from one month to nearly one year of SCIAMACHY data. The approach was adapted and applied for the first time to GOME-2 and OMI satellite data for the same time period. The resulting K_d -blue was compared to operationally-provided K_d at 490 nm from multispectral sensors, which was wavelength-converted before analysis. Robust agreement was found when the 11-month data sets were gridded to the same spatial resolution and compared on a daily basis. Pearson correlation coefficients were around 0.65 for low K_d values ($< 0.15 \text{ m}^{-1}$). Similarly, the method was adapted for TROPOMI. One month of TROPOMI K_d data were compared to the wavelength-converted K_d from multispectral sensors and to in-situ data. An even higher correlation coefficient was found for the comparisons with multispectral data sets for a larger K_d range ($< 0.3 \text{ m}^{-1}$), which was in decent agreement with in-situ data.

With respect to PFT retrieval capabilities of DOAS-type sensors, derived coccolithophore Chla from GOME-2 backscattered radiances showed robust results for the Atlantic and Indian sectors of the Southern Ocean. Monthly gridded GOME-2 coccolithophore Chla showed remarkably high correlations with MODIS-Aqua PIC, a proxy for coccolithophores, despite the large representation error between the data sets. The time series of GOME-2 coccolithophore Chla for two austral summers showed temporal evolutions that were in agreement with both MODIS-Aqua PIC and with what is known about coccolithophore phenology in the Southern Ocean from other studies. GOME-2 coccolithophore Chla was mostly independent in time and space from total Chla, which provides further confidence that coccolithophores can be discriminated from other phytoplankton by the PhytoDOAS method. Identification of diatoms did not work well for the GOME-2 sensor in the Southern Ocean for the chosen fit settings. A wide range of fit settings was tested on simulated radiances prior to this application, but the fit settings were not exhaustively tested. Sensitivity of the PhytoDOAS fit with respect to specific settings might be different for fits on actual satellite data. It is therefore only concluded that diatom fits are more challenging than coccolithophore fits for the GOME-2 sensor. Spectral channels of OMI and TROPOMI are shorter. Identified optimal fit windows for coccolithophores are not included. PFT fits on OMI data have shown promising results and were presented at conferences (see list of publications at beginning of document), but the conversion of the fit factors to PFT Chla remained a major issue. PFT retrievals were therefore focused on GOME-2 data and not further pursued for OMI data in this thesis. This thesis can not conclusively state whether PFT retrievals of similar quality are possible for OMI and TROPOMI. It is also possible that only certain PFT are retrievable from certain sensors.

Overall, PhytoDOAS retrievals perform best for open ocean where Chla is only moderately high. K_d -blue retrievals were restricted to sites where $K_d < 0.15 \text{ m}^{-1}$ for SCIA-

MACHY, GOME-2, and OMI and $<0.3\text{ m}^{-1}$ for TROPOMI. These thresholds correspond to a Chla value of about 2 mg/m^3 and 6.5 mg/m^3 , respectively, in the average open ocean standard scenario simulated with RTM for a SZA of 40° and a VZA of 0° . For PFT fits, PhytoDOAS retrieval uncertainty is lowest for a PFT Chla value of about 1 mg/m^3 , which is reached for lower PFT Chla, if other PFT are present. Derived PFT Chla in the current data set for waters with total Chla $> 1\text{ mg/m}^3$ need to be treated cautiously, because an unambiguous assignment of PFT fit factor to PFT Chla concentration via LUT is not possible at this stage.

Limitations of the PhytoDOAS retrieval were identified for its current state in combination with signal-to-noise ratios and calibration quality of backscattered radiances from current DOAS-type sensors. Accurate quantification of OC variables from DOAS-type sensors is a challenge. For instance, a general overestimation of TROPOMI-derived K_d -blue was observed and of GOME-2 derived coccolithophore Chla. Additionally, even for open ocean scenes with low PhytoDOAS retrieval uncertainty, a fraction of K_d -blue values were found to be associated with high uncertainties for all sensors. Two predominant sources of error were identified: (1) calibration of level 1 radiances and (2) RTM assumptions. Several temporal and spatial biases were found in the PhytoDOAS-derived data sets, which did not appear for all sensors, but rather were identified to be sensor-specific. Based on these results, it is clear that PhytoDOAS retrievals are rather sensitive to instrumental spectral artifacts introduced by insufficient calibration of the level 1 data. Specific RTM settings also influence the quality of the results. An average scenario was chosen for determining a VRS reference spectrum which causes poor fit quality for ocean sites that distinctly differ from the average condition. Conversion of PhytoDOAS fit factors to physical values using a LUT introduces additional uncertainty, because assumptions have to be made in the forward model. The dimensionality of the LUT can be increased to account for the influence of various parameters on the retrieval results, e.g., a parameterization with respect to wind speed and aerosols can be added, and these variables are then taken from ancillary data sets. For the shortest wavelengths, ozone concentration had the largest influence on the retrieval, whereas in the visible, aerosols had the largest influence, followed by the influence of wind speed. However, some parameters remain unknown, because they underlie high natural variability, such as the phytoplankton absorption.

6.3 Hypothesis II: OC variables from multiple SCIAMACHY-like sensors can be merged to create a long time series

Retrieved OC variables from multiple DOAS-type sensors showed dissimilarities which impede merging the data sets in their current stage. Sensor-specific biases were found in space and time. Partial explanations were found for some of these biases. For example, the spectral influence of SCIAMACHY's polarization sensitivity caused a north-south trend, and the spectral influence of GOME-2's diffuser structures caused a seasonal trend. Although these causes were at least partially identified, the biases could not be corrected fully by modifying the PhytoDOAS fit accordingly. For OMI and TROPOMI, no specific spectral artifacts caused by instrumentation could be identified. However, results for these two sensors also showed unexpected behavior, which requires corrections. Biases can lead to artificial trends in time series created by merging different sensors' data sets and therefore ought to be removed beforehand. At this stage, intricate corrections would be necessary for each sensor. In the third study, for example, multiple corrections steps were applied to reach sufficient data quality. Such corrections are difficult to develop accurately if they rely on ancillary data. Analytical corrections, incorporated into the PhytoDOAS fit, and empirical corrections, based on in-situ data, are optimal. Since analytical corrections showed only limited success and empirical corrections are not feasible due to both ground pixel sizes and limitations of in-situ data sets, comparable OC variables from multispectral sensors were used for corrections in this work. An independent solution is ideal for this scenario. Improved calibration of level-1 radiances is predicted to make most corrections redundant.

6.4 Hypothesis III: Ultraviolet-visible bands of SCIAMACHY-like sensors can be exploited for the retrieval of novel ultraviolet OC products

Ultraviolet and visible bands of the DOAS-type sensor TROPOMI were successfully exploited for retrieving new OC variables: two ultraviolet K_d in the spectral ranges 312.5-338.5 nm and 356.5-390 nm. Within a feasibility study of one month of TROPOMI data, the quality of the two ultraviolet K_d derived from VRS in the UV-VIS spectral bands was investigated. Comparison with in-situ data showed promising results. Solar radia-

tion is lower in the UV than in the visible spectral range, and its attenuation is generally higher in the atmosphere and for many open ocean conditions. UV radiances measured by satellites are therefore generally lower. In accordance with reasonable VRS DOAS fit results in the UV on SCIAMACHY backscattered radiances found prior to this work, it is concluded that signal-to-noise ratios of TROPOMI are sufficient for accurately detecting VRS in the wavelength range 349 to 450 nm. K_d can be derived from VRS up to a value of $K_d \approx 0.3 \text{ m}^{-1}$ with current retrieval settings. Sensitivity analysis showed that the retrieval is rather insensitive to the RTM parameterization of, e.g., CDOM, phytoplankton, and water absorption, which underlie high natural variability or have not been measured with high accuracy yet. A derivation of OC variables with the PhytoDOAS method in combination with a LUT approach is therefore possible in the UV. Better knowledge of UV parameterization can improve the retrieval accuracy, but is not a requirement to be able to resolve changes in CDOM absorption and UV-absorbing phytoplankton pigment production, for example. The potential of retrievals on TROPOMI data for ultraviolet K_d was illustrated here. Further potential is seen for developing an operational retrieval based on this work to establish new OC products.

6.5 Outlook

This work found general applicability of PhytoDOAS to data from SCIAMACHY-like sensors for OC retrievals. However, some limitations were identified. In the following section, some suggestions are made on how to improve the PhytoDOAS fit quality and overcome some of the existing limitations.

A primary requirement for more accurate OC PhytoDOAS retrievals is an improvement of calibration of level-1 backscattered radiances. The instrumental influence was observed to be small for the TROPOMI sensor. One way to move forward would be to concentrate on the TROPOMI sensor, as the calibration of this sensor is expected to increase in the near future with the release of the second version of level-1b processor (Ludewig et al., 2020). The spatial resolution of TROPOMI is the best among the current DOAS-type sensors for comparison with field measurements. Towed and underway systems, which are actively improving for in-situ measurements (e.g., Chase et al., 2013; Liu et al., 2019; Bracher et al., 2020), can further reduce the spatial representation error between satellite ground pixels and field measurements. Provided that calibration is sufficient, comparison with large in-situ data sets would enable investigation of the retrieval behavior with respect to physical instead of instrumental effects. A deeper understanding of the physical processes in the PhytoDOAS method for different environmental conditions can be obtained. Empirically,

insight can be gained on how the DOAS-retrieved fit factors relate to the physical variables under different conditions to check the validity of the LUT. Replacement of RTM-based LUT by empirically derived LUT could be a strategy in the event that improved calibration does not lead to a reduced mismatch in fit factor behavior observed on satellite-recorded and simulated data.

As a next step, the uncertainty in the LUT should be reduced by increasing its dimensionality. Increasing the computational effort for a multidimensional LUT is only worthwhile if the calibration of level-1 radiances is sufficient and the influence of instrumental artifacts on the retrieval is reduced. Only then can the parameterization in the LUT actually mimic the behavior of PhytoDOAS fits on satellite-measured radiances in dependence of different environmental parameters. From the retrieval sensitivity analysis, several factors were identified as larger sources of uncertainty (depending on the spectral range), including wind speed, ozone concentration, and aerosol loading. These variables could be incorporated in the LUT as a first step. Ancillary data sets taken as input data require sufficient quality. A first attempt could be to take the data from climatologies, which are more robust. Further, oceanic absorption coefficients, e.g., CDOM absorption, could be taken from multispectral OC data to refine the LUT, given that uncertainties of the ancillary data sets are sufficiently low.

Modifications to the PhytoDOAS retrieval could also be tested for reducing the retrieval uncertainty. The VRS reference spectrum is calculated for a certain Chla and for certain viewing geometries and environmental parameters, which leads to higher uncertainties in the DOAS fit the more the satellite scenario differs from the reference scenario. An iterative approach could be used, similar to DOAS retrievals for SO₂ (e.g., [Richter, 2009](#)). The VRS reference spectrum could be adjusted after each iterative step to the approximate Chla inferred from the VRS fit result. Improving the VRS fit at high Chla may also increase the Chla range in which PFT Chla can be retrieved unambiguously with the LUT approach based on the PFT/VRS fit factor ratio. For reducing the spectral mismatch introduced due to viewing geometries, multiple reference spectra can be calculated to cover the full range of viewing geometries. Depending on the viewing geometry of each satellite ground pixel, the suitable VRS reference spectrum can be taken for the fit. Altogether, improvements to the DOAS retrieval aim at improving the accuracy of retrieved OC variables required by the user community for, e.g., climate modeling, as formulated in [Frouin et al. \(2018\)](#) and [Sathyendranath et al. \(2019\)](#).

Bibliography

- Acarreta, J. R., De Haan, J. F., and Stammes, P. (2004). Cloud pressure retrieval using the O₂-O₂ absorption band at 477 nm. *Journal of Geophysical Research: Atmospheres*, 109(D5):D05204.
- Aliwell, S. R., Van Roozendaal, M., Johnston, P. V., Richter, A., Wagner, T., Arlander, D. W., Burrows, J. P., Fish, D. J., Jones, R. L., Tørnkvist, K. K., Lambert, J.-C., Pfeilsticker, K., and Pundt, I. (2002). Analysis for BrO in zenith-sky spectra: An intercomparison exercise for analysis improvement. *Journal of Geophysical Research: Atmospheres*, 107(D14):4199.
- Alvain, S., Moulin, C., Dandonneau, Y., and Loisel, H. (2008). Seasonal distribution and succession of dominant phytoplankton groups in the global ocean: A satellite view. *Global Biogeochemical Cycles*, 22(3):GB3001.
- Alvarado, L. M. A., Richter, A., Vrekoussis, M., Hilboll, A., Kalisz Hedegaard, A. B., Schneising, O., and Burrows, J. P. (2020). Unexpected long-range transport of glyoxal and formaldehyde observed from the Copernicus Sentinel-5 Precursor satellite during the 2018 Canadian wildfires. *Atmospheric Chemistry and Physics*, 20(4):2057–2072.
- Andreae, M. O. and Merlet, P. (2001). Emission of trace gases and aerosols from biomass burning. *Global Biogeochemical Cycles*, 15(4):955–966.
- Artlett, C. P. and Pask, H. M. (2015). Optical remote sensing of water temperature using Raman spectroscopy. *Optics Express*, 23(25):31844–31856.
- Ashraf, P. M., Shaju, S. S., Gayatri, D., Minu, P., and Meenakumari, B. (2013). In situ time series estimation of downwelling diffuse attenuation coefficient at Southern Bay of Bengal. *Journal of the Indian Society of Remote Sensing*, 41(3):725–730.
- Assmy, P., Smetacek, V., Montresor, M., Klaas, C., Henjes, J., Strass, V. H., Arrieta, J. M., Bathmann, U., Berg, G. M., Breitbarth, E., Cisewski, B., Friedrichs, L., Fuchs, N., Herndl, G. J., Jansen, S., Krägfesky, S., Latasa, M., Peeken, I., Röttgers, R.,

- Scharek, R., Schüller, S. E., Steigenberger, S., Webb, A., and Wolf-Gladrow, D. (2013). Thick-shelled, grazer-protected diatoms decouple ocean carbon and silicon cycles in the iron-limited Antarctic Circumpolar Current. *Proceedings of the National Academy of Sciences*, 110(51):20633–20638.
- Aurin, D., Mannino, A., and Lary, D. (2018). Remote sensing of CDOM, CDOM spectral slope, and dissolved organic carbon in the global ocean. *Applied Sciences*, 8:2687.
- Austin, R. W. and Petzold, T. J. (1981). The determination of the diffuse attenuation coefficient of sea water using the Coastal Zone Color Scanner. In Gower, J. F. R., editor, *Oceanography from Space*, pages 239 – 256. Springer US, Boston, MA.
- Austin, R. W. and Petzold, T. J. (1986). Spectral dependence of the diffuse attenuation coefficient of light in ocean waters. *Optical Engineering*, 25:471–479.
- Austin, R. W. and Petzold, T. J. (1990). Spectral dependence of the diffuse attenuation coefficient of light in ocean waters: a reexamination using new data. In Spinrad, R. W., editor, *Ocean Optics X*, volume 1302, pages 79 – 93. International Society for Optics and Photonics, SPIE.
- Babin, M., Stramski, D., Ferrari, G. M., Claustre, H., Bricaud, A., Obolensky, G., and Hoepffner, N. (2003). Variations in the light absorption coefficients of phytoplankton, nonalgal particles, and dissolved organic matter in coastal waters around Europe. *Journal of Geophysical Research: Oceans*, 108(C7):3211.
- Bai, K., Chang, N.-B., Yu, H., and Gao, W. (2016). Statistical bias correction for creating coherent total ozone record from OMI and OMPS observations. *Remote Sensing of Environment*, 182:150–168.
- Baker, K. S. and Smith, R. C. (1980). Quasi-Inherent Characteristics Of The Diffuse Attenuation Coefficient For Irradiance. In Duntley, S. Q., editor, *Ocean Optics VI*, volume 0208, pages 60 – 63. International Society for Optics and Photonics, SPIE.
- Baker, K. S. and Smith, R. C. (1982). Bio-optical classification and model of natural waters. *Limnology and Oceanography*, 27(3):500–509.
- Balch, W. M., Kilpatrick, K. A., Holligan, P., Harbour, D., and Fernández, E. (1996). The 1991 coccolithophore bloom in the central North Atlantic. 2. Relating optics to coccolith concentration. *Limnology and Oceanography*, 41(8):1684–1696.

- Balch, W. M., Gordon, H. R., Bowler, B. C., Drapeau, D. T., and Booth, E. S. (2005). Calcium carbonate measurements in the surface global ocean based on Moderate-Resolution Imaging Spectroradiometer data. *Journal of Geophysical Research: Oceans*, 110(C7):C07001.
- Balch, W. M., Drapeau, D., Bowler, B., and Booth, E. (2007). Prediction of pelagic calcification rates using satellite measurements. *Deep Sea Research Part II: Topical Studies in Oceanography*, 54(5):478–495.
- Balch, W. M., Drapeau, D. T., Bowler, B. C., Lyczkowski, E., Booth, E. S., and Alley, D. (2011). The contribution of coccolithophores to the optical and inorganic carbon budgets during the Southern Ocean Gas Exchange Experiment: New evidence in support of the “Great Calcite Belt” hypothesis. *Journal of Geophysical Research: Oceans*, 116(C4):C00F06.
- Balch, W. M., Bates, N. R., Lam, P. J., Twining, B. S., Rosengard, S. Z., Bowler, B. C., Drapeau, D. T., Garley, R., Lubelczyk, L. C., Mitchell, C., and Rauschenberg, S. (2016). Factors regulating the Great Calcite Belt in the Southern Ocean and its biogeochemical significance. *Global Biogeochemical Cycles*, 30(8):1124–1144.
- Barnes, R. A. and Holmes, A. W. (1993). Overview of the SeaWiFS ocean sensor. In Barnes, W. L., editor, *Sensor Systems for the Early Earth Observing System Platforms*, volume 1939, pages 224 – 232. International Society for Optics and Photonics, SPIE.
- Barnes, W. L. and Salomonson, V. V. (1992). MODIS: a global imaging spectroradiometer for the Earth Observing System. In Pearson, J. E., editor, *Optical Technologies for Aerospace Sensing: A Critical Review*, volume 10269, pages 280 – 302. International Society for Optics and Photonics, SPIE.
- Bartlett, J. S., Voss, K. J., Sathyendranath, S., and Vodacek, A. (1998). Raman scattering by pure water and seawater. *Applied Optics*, 37(15):3324–3332.
- Basu, S. and Mackey, K. R. M. (2018). Phytoplankton as key mediators of the biological carbon pump: Their responses to a changing climate. *Sustainability*, 10(3):869.
- Bathmann, U., Scharek, R., Klaas, C., Dubischar, C., and Smetacek, V. (1997). Spring development of phytoplankton biomass and composition in major water masses of the Atlantic sector of the Southern Ocean. *Deep Sea Research Part II: Topical Studies in Oceanography*, 44(1):51–67.

- Beaulieu, C., Henson, S. A., Sarmiento, J. L., Dunne, J. P., Doney, S. C., Rykaczewski, R. R., and Bopp, L. (2013). Factors challenging our ability to detect long-term trends in ocean chlorophyll. *Biogeosciences*, 10(4):2711–2724.
- Behrens, L. K., Hilboll, A., Richter, A., Peters, E., Alvarado, L. M. A., Kalisz Hedegaard, A. B., Wittrock, F., Burrows, J. P., and Vrekoussis, M. (2019). Detection of outflow of formaldehyde and glyoxal from the African continent to the Atlantic Ocean with a MAX-DOAS instrument. *Atmospheric Chemistry and Physics*, 19(15):10257–10278.
- Bezy, J.-L., Delwart, S., Gourmelon, G., Baudin, G., Bessudo, R., and Sontag, H. (1997). Medium-resolution imaging spectrometer (MERIS). In Fujisada, H., Calamai, G., and Sweeting, M. N., editors, *Advanced and Next-Generation Satellites II*, volume 2957, pages 31 – 41. International Society for Optics and Photonics, SPIE.
- Bidigare, R. R., Ondrusek, M. E., Morrow, J. H., and Kiefer, D. A. (1990). In-vivo absorption properties of algal pigments. In Spinrad, R. W., editor, *Ocean Optics X*, volume 1302, pages 290 – 302. International Society for Optics and Photonics, SPIE.
- Bischel, W. K. and Black, G. (1983). Wavelength dependence of Raman scattering cross sections from 200–600 nm. *AIP Conference Proceedings*, 100(1):181–187.
- Blankenship, R. E. (2002). Photosynthetic Pigments: Structure and Spectroscopy. In Blankenship, R. E., editor, *Molecular Mechanisms of Photosynthesis*, chapter 4, pages 42–60. Blackwell Science Ltd, Oxford.
- Blum, M., Rozanov, V. V., Burrows, J. P., and Bracher, A. (2012). Coupled ocean-atmosphere radiative transfer model in the framework of software package SCIA-TRAN: Selected comparisons to model and satellite data. *Advances in Space Research*, 49(12):1728–1742.
- Bonan, G. B. and Doney, S. C. (2018). Climate, ecosystems, and planetary futures: The challenge to predict life in Earth system models. *Science*, 359(6375):eaam8328.
- Bovensmann, H., Burrows, J. P., Buchwitz, M., Frerick, J., Noël, S., Rozanov, V. V., Chance, K. V., and Goede, A. P. H. (1999). SCIAMACHY: Mission objectives and measurement modes. *Journal of the Atmospheric Sciences*, 56(2):127–150.
- Boyd, P. W. (2002). Environmental factors controlling phytoplankton processes in the Southern Ocean. *Journal of Phycology*, 38(5):844–861.

- Boyd, P. W., Claustre, H., Levy, M., Siegel, D. A., and Weber, T. (2019). Multi-faceted particle pumps drive carbon sequestration in the ocean. *Nature*, 568(7752):327–335.
- Bracher, A. and Wiencke, C. (2000). Simulation of the effects of naturally enhanced UV radiation on photosynthesis of Antarctic phytoplankton. *Marine Ecology Progress Series*, 196:127–141.
- Bracher, A., Vountas, M., Dinter, T., Burrows, J. P., Röttgers, R., and Peeken, I. (2009). Quantitative observation of cyanobacteria and diatoms from space using PhytoDOAS on SCIAMACHY data. *Biogeosciences*, 6(5):751–764.
- Bracher, A., Dinter, T., Wolanin, A., Rozanov, V. V., Losa, S. N., and Soppa, M. A. (2017). Global monthly mean chlorophyll a surface concentrations from August 2002 to April 2012 for diatoms, coccolithophores and cyanobacteria from PhytoDOAS algorithm version 3.3 applied to SCIAMACHY data, link to NetCDF files in ZIP archive. PANGAEA. In supplement to: Losa et al. (2017a). <https://doi.org/10.1594/PANGAEA.870486>.
- Bracher, A., Xi, H., Dinter, T., Mangin, A., Strass, V., von Appen, W.-J., and Wiegmann, S. (2020). High resolution water column phytoplankton composition across the Atlantic Ocean from ship-towed vertical undulating radiometry. *Frontiers in Marine Science*, 7:235.
- Brewin, R. J., Sathyendranath, S., Müller, D., Brockmann, C., Deschamps, P.-Y., Devred, E., Doerffer, R., Fomferra, N., Franz, B., Grant, M., Groom, S., Horseman, A., Hu, C., Krasemann, H., Lee, Z., Maritorena, S., Mélin, F., Peters, M., Platt, T., Regner, P., Smyth, T., Steinmetz, F., Swinton, J., Werdell, J., and White, G. N. (2015). The Ocean Colour Climate Change Initiative: III. A round-robin comparison on in-water bio-optical algorithms. *Remote Sensing of Environment*, 162:271–294.
- Brewin, R. J. W., Ciavatta, S., Sathyendranath, S., Jackson, T., Tilstone, G., Curran, K., Airs, R. L., Cummings, D., Brotas, V., Organelli, E., Dall’Olmo, G., and Raitso, D. E. (2017). Uncertainty in ocean-color estimates of chlorophyll for phytoplankton groups. *Frontiers in Marine Science*, 4:104.
- Bricaud, A., Morel, A., and Prieur, L. (1981). Absorption by dissolved organic matter of the sea (yellow substance) in the UV and visible domains. *Limnology and Oceanography*, 26(1):43–53.
- Bricaud, A., Claustre, H., Ras, J., and Oubelkheir, K. (2004). Natural variability of

- phytoplanktonic absorption in oceanic waters: Influence of the size structure of algal populations. *Journal of Geophysical Research: Oceans*, 109(C11):C11010.
- Brillouin, L. (1922). Diffusion de la lumière et des rayons X par un corps transparent homogène - Influence de l'agitation thermique. *Annales de Physique*, 9(17):88–122.
- Buiteveld, H., Hakvoort, J. H. M., and Donze, M. (1994). Optical properties of pure water. In Jaffe, J. S., editor, *Ocean Optics XII*, volume 2258, pages 174 – 183. International Society for Optics and Photonics, SPIE.
- Burrows, J. P., Weber, M., Buchwitz, M., Rozanov, V., Ladstätter-Weißmayer, A., Richter, A., DeBeek, R., Hoogen, R., Bramstedt, K., Eichmann, K.-U., Eisinger, M., and Perner, D. (1999). The Global Ozone Monitoring Experiment (GOME): Mission concept and first scientific results. *Journal of the Atmospheric Sciences*, 56(2):151–175.
- Burrows, J. P., Platt, U., and Borrell, P. (2011). Tropospheric Remote Sensing from Space. In Burrows, J. P., Platt, U., and Borrell, P., editors, *The Remote Sensing of Tropospheric Composition from Space*, pages 1–66. Springer-Verlag, Heidelberg.
- Cadée, G. C. and Hegeman, J. (2002). Phytoplankton in the Marsdiep at the end of the 20th century; 30 years monitoring biomass, primary production, and Phaeocystis blooms. *Journal of Sea Research*, 48(2):97–110.
- Carpenter, L. J., Archer, S. D., and Beale, R. (2012). Ocean-atmosphere trace gas exchange. *Chemical Society Reviews*, 41:6473–6506.
- Chance, K. and Kurucz, R. L. (2010). An improved high-resolution solar reference spectrum for earth's atmosphere measurements in the ultraviolet, visible, and near infrared. *Journal of Quantitative Spectroscopy and Radiative Transfer*, 111(9):1289–1295.
- Chandrasekhar, S. (1960). *Radiative Transfer*. Dover Publications, New York.
- Charalampopoulou, A., Poulton, A., Bakker, D., Lucas, M., Stinchcombe, M., and Tyrrell, T. (2016). Environmental drivers of coccolithophore abundance and calcification across Drake Passage (Southern Ocean). *Biogeosciences*, 13:5917–5935.
- Chase, A., Boss, E., Zaneveld, R., Bricaud, A., Claustre, H., Ras, J., Dall'Olmo, G., and Westberry, T. K. (2013). Decomposition of in situ particulate absorption spectra. *Methods in Oceanography*, 7:110–124.

- Chauhan, P., Sahay, A., Rajawat, A., and Nayak, S. (2003). Remote sensing of diffuse attenuation coefficient (K490) using IRS-P4 Ocean Colour Monitor (OCM) sensor. *Indian Journal of Marine Sciences*, 32:279–284.
- Coldewey-Egbers, M., Loyola, D. G., Koukouli, M., Balis, D., Lambert, J.-C., Verhoelst, T., Granville, J., van Roozendaal, M., Lerot, C., Spurr, R., Frith, S. M., and Zehner, C. (2015). The GOME-type Total Ozone Essential Climate Variable (GTO-ECV) data record from the ESA Climate Change Initiative. *Atmospheric Measurement Techniques*, 8(9):3923–3940.
- Conde, D., Aubriot, L., and Sommaruga, R. (2000). Changes in UV penetration associated with marine intrusions and freshwater discharge in a shallow coastal lagoon of the Southern Atlantic Ocean. *Marine Ecology Progress Series*, 207:19–31.
- Corson, M. R., Korwan, D. R., Lucke, R. L., Snyder, W. A., and Davis, C. O. (2008). The Hyperspectral Imager for the Coastal Ocean (HICO) on the International Space Station. In *IGARSS 2008 - 2008 IEEE International Geoscience and Remote Sensing Symposium*, volume 4, pages IV–101 – IV–104.
- Couto, A. B., Brotas, V., Mélin, F., Groom, S., and Sathyendranath, S. (2016). Inter-comparison of OC-CCI chlorophyll-a estimates with precursor data sets. *International Journal of Remote Sensing*, 37(18):4337–4355.
- Cox, P. M., Betts, R. A., Jones, C. D., Spall, S. A., and Totterdell, I. J. (2000). Acceleration of global warming due to carbon-cycle feedbacks in a coupled climate model. *Nature*, 408:184–187.
- Cruz, R. A., Marcano, A., Jacinto, C., and Catunda, T. (2009). Ultrasensitive thermal lens spectroscopy of water. *Optics Letters*, 34(12):1882–1884.
- Cubillos, J., Wright, S., Nash, G., de Salas, M., Griffiths, B., Tilbrook, B., Poisson, A., and Hallegraeff, G. (2007). Calcification morphotypes of the coccolithophorid *Emiliania huxleyi* in the Southern Ocean: changes in 2001 to 2006 compared to historical data. *Marine Ecology Progress Series*, 348:47–54.
- Cullen, J. J. and Neale, P. J. (1994). Ultraviolet radiation, ozone depletion, and marine photosynthesis. *Photosynthesis Research*, 39:303–320.
- Curtis, D. B., Meland, B., Aycibin, M., Arnold, N. P., Grassian, V. H., Young, M. A., and Kleiber, P. D. (2008). A laboratory investigation of light scattering from representative

- components of mineral dust aerosol at a wavelength of 550 nm. *Journal of Geophysical Research: Atmospheres*, 113(D8):D08210.
- Daniels, C. J., Sheward, R. M., and Poulton, A. J. (2014). Biogeochemical implications of comparative growth rates of *Emiliania huxleyi* and *Coccolithus* species. *Biogeosciences*, 11(23):6915–6925.
- de Lima Ribeiro, A. and Pask, H. (2020). Remote sensing of natural waters using a multichannel, lidar-compatible Raman spectrometer and blue excitation. *Frontiers in Marine Science*, 7:43.
- Deppeler, S. L. and Davidson, A. T. (2017). Southern Ocean phytoplankton in a changing climate. *Frontiers in Marine Science*, 4:40.
- Desiderio, R. A. (2000). Application of the Raman scattering coefficient of water to calculations in marine optics. *Applied Optics*, 39(12):1893–1894.
- Dierssen, H. M., Smith, R. C., and Vernet, M. (2002). Glacial meltwater dynamics in coastal waters west of the Antarctic peninsula. *Proceedings of the National Academy of Sciences*, 99(4):1790–1795.
- Dierssen, H. M. and Randolph, K. (2013). Remote Sensing of Ocean Color. In Orcutt, J., editor, *Earth System Monitoring: Selected Entries from the Encyclopedia of Sustainability Science and Technology*, pages 439–472. Springer New York, New York, NY.
- Dierssen, H. M. (2019). Hyperspectral measurements, parameterizations, and atmospheric correction of whitecaps and foam from visible to shortwave infrared for Ocean Color remote sensing. *Frontiers in Earth Science*, 7:14.
- Dikty, S., Richter, A., Weber, M., Noël, S., Bovensmann, H., Wittrock, F., and Burrows, J. P. (2012). GOME-2 on MetOp-A support for analysis of GOME-2 in-orbit degradation and impacts on level 2 data products final report. Technical report, Institute of Environmental Physics, Institute of Remote Sensing, University of Bremen FB1.
- Dinter, T., Rozanov, V. V., Burrows, J. P., and Bracher, A. (2015). Retrieving the availability of light in the ocean utilising spectral signatures of vibrational Raman scattering in hyper-spectral satellite measurements. *Ocean Science*, 11(3):373–389.
- Dirksen, R., Dobber, M., Voors, R., Kleipool, Q., van den Oord, G., and Levelt, P. (2017). In-flight calibration of the ozone monitoring instrument. In Armandillo, E., Costeraste,

- J., and Karafolas, N., editors, *International Conference on Space Optics – ICSO 2006*, volume 10567, pages 513 – 519. International Society for Optics and Photonics, SPIE.
- Doron, M., Babin, M., Mangin, A., and Hembise, O. (2007). Estimation of light penetration, and horizontal and vertical visibility in oceanic and coastal waters from surface reflectance. *Journal of Geophysical Research: Oceans*, 112(C6):C06003.
- Einstein, A. (1910). Theorie der Opaleszenz von homogenen Flüssigkeiten und Flüssigkeitsgemischen in der Nähe des kritischen Zustandes. *Annalen der Physik*, 338(16):1275–1298.
- El-Sayed, S. Z., Biggs, D. C., and Holm-Hansen, O. (1983). Phytoplankton standing crop, primary productivity, and near-surface nitrogenous nutrient fields in the Ross Sea, Antarctica. *Deep Sea Research Part A. Oceanographic Research Papers*, 30(8):871–886.
- Eldridge, R. G. (1967). Water vapor absorption of visible and near infrared radiation. *Applied Optics*, 6(4):709–713.
- EUMETSAT (2017). GOME-2 Factsheet, EUM/OPS/DOC/10/1299, issue v4D, 27. April 2017. Technical report, EUMETSAT.
- EUMETSAT (2021). Recommendations for Sentinel-3 OLCI Ocean Colour product validations in comparison with in situ measurements – Matchup Protocols, EUM/SEN3/DOC/19/1092968, issue v7, 17. May 2021. Technical report, EUMETSAT.
- Evans, R. H. and Gordon, H. R. (1994). Coastal zone color scanner “system calibration”: A retrospective examination. *Journal of Geophysical Research: Oceans*, 99(C4):7293–7307.
- Falkowski, P., Scholes, R. J., Boyle, E., Canadell, J., Canfield, D., Elser, J., Gruber, N., Hibbard, K., Högberg, P., Linder, S., Mackenzie, F. T., Moore III, B., Pedersen, T., Rosenthal, Y., Seitzinger, S., Smetacek, V., and Steffen, W. (2000). The global carbon cycle: A test of our knowledge of Earth as a system. *Science*, 290(5490):291–296.
- Falkowski, P. G., Katz, M. E., Knoll, A. H., Quigg, A., Raven, J. A., Schofield, O., and Taylor, F. J. R. (2004). The evolution of modern eukaryotic phytoplankton. *Science*, 305(5682):354–360.
- Faris, G. W. and Copeland, R. A. (1997). Wavelength dependence of the Raman cross section for liquid water. *Applied Optics*, 36(12):2686–2688.

- Feldman, G., Kuring, N., Ng, C., Esaias, W., McClain, C., Elrod, J., Maynard, N., Endres, D., Evans, R., Brown, J., Walsh, S., Carle, M., and Podesta, G. (1989). Ocean color: Availability of the global data set. *Eos, Transactions American Geophysical Union*, 70(23):634–641.
- Fenchel, T. (1988). Marine plankton food chains. *Annual Review of Ecology and Systematics*, 19(1):19–38.
- Fernández, E., Boyd, P., Holligan, P. M., and Harbour, D. S. (1993). Production of organic and inorganic carbon within a large-scale coccolithophore bloom in the northeast Atlantic Ocean. *Marine Ecology Progress Series*, 97(3):271–285.
- Fichot, C. G., Sathyendranath, S., and Miller, W. L. (2008). SeaUV and SeaUVC: Algorithms for the retrieval of UV/Visible diffuse attenuation coefficients from ocean color. *Remote Sensing of Environment*, 112(4):1584–1602.
- Field, C. B., Behrenfeld, M. J., Randerson, J. T., and Falkowski, P. (1998). Primary production of the biosphere: Integrating terrestrial and oceanic components. *Science*, 281(5374):237–240.
- Fleischmann, O. C., Hartmann, M., Burrows, J. P., and Orphal, J. (2004). New ultraviolet absorption cross-sections of BrO at atmospheric temperatures measured by time-windowing Fourier transform spectroscopy. *Journal of Photochemistry and Photobiology A: Chemistry*, 168(1):117–132.
- Flores-Anderson, A. I., Griffin, R., Dix, M., Romero-Oliva, C. S., Ochaeta, G., Skinner-Alvarado, J., Ramirez Moran, M. V., Hernandez, B., Cherrington, E., Page, B., and Barreno, F. (2020). Hyperspectral Satellite Remote Sensing of Water Quality in Lake Atitlán, Guatemala. *Frontiers in Environmental Science*, 8:7.
- Fournier, G. R. and Forand, J. L. (1994). Analytic phase function for ocean water. In Jaffe, J. S., editor, *Ocean Optics XII*, volume 2258, pages 194 – 201. International Society for Optics and Photonics, SPIE.
- Fournier, G. R. and Jonasz, M. (1999). Computer-based underwater imaging analysis. In Gilbert, G. D., editor, *Airborne and In-Water Underwater Imaging*, volume 3761, pages 62 – 70. International Society for Optics and Photonics, SPIE.
- Fraunhofer, J. (1817). Bestimmung des Brechungs- und des Farbenzerstreungs-Vermögens verschiedener Glasarten, in Bezug auf die Vervollkommnung achromatischer Fernröhre. *Annalen der Physik*, 56(7):264–313.

- Friedlingstein, P., Jones, M. W., O'Sullivan, M., Andrew, R. M., Hauck, J., Peters, G. P., Peters, W., Pongratz, J., Sitch, S., Le Quéré, C., Bakker, D. C. E., Canadell, J. G., Ciais, P., Jackson, R. B., Anthoni, P., Barbero, L., Bastos, A., Bastrikov, V., Becker, M., Bopp, L., Buitenhuis, E., Chandra, N., Chevallier, F., Chini, L. P., Currie, K. I., Feely, R. A., Gehlen, M., Gilfillan, D., Gkritzalis, T., Goll, D. S., Gruber, N., Gutekunst, S., Harris, I., Haverd, V., Houghton, R. A., Hurtt, G., Ilyina, T., Jain, A. K., Joetzjer, E., Kaplan, J. O., Kato, E., Klein Goldewijk, K., Korsbakken, J. I., Landschützer, P., Lauvset, S. K., Lefèvre, N., Lenton, A., Lienert, S., Lombardozzi, D., Marland, G., McGuire, P. C., Melton, J. R., Metzl, N., Munro, D. R., Nabel, J. E. M. S., Nakaoka, S.-I., Neill, C., Omar, A. M., Ono, T., Peregon, A., Pierrot, D., Poulter, B., Rehder, G., Resplandy, L., Robertson, E., Rödenbeck, C., Séférian, R., Schwinger, J., Smith, N., Tans, P. P., Tian, H., Tilbrook, B., Tubiello, F. N., van der Werf, G. R., Wiltshire, A. J., and Zaehle, S. (2019). Global Carbon Budget 2019. *Earth System Science Data*, 11(4):1783–1838.
- Frölicher, T. L., Sarmiento, J. L., Paynter, D. J., Dunne, J. P., Krasting, J. P., and Winton, M. (2015). Dominance of the Southern Ocean in anthropogenic carbon and heat uptake in CMIP5 models. *Journal of Climate*, 28(2):862–886.
- Froneman, P., McQuaid, C., and Perissinotto, R. (1995). Biogeographic structure of the microphytoplankton assemblages of the south Atlantic and Southern Ocean during austral summer. *Journal of Plankton Research*, 17(9):1791–1802.
- Frouin, R., Schwindling, M., and Deschamps, P.-Y. (1996). Spectral reflectance of sea foam in the visible and near-infrared: In situ measurements and remote sensing implications. *Journal of Geophysical Research: Oceans*, 101(C6):14361–14371.
- Frouin, R. and Iacobellis, S. F. (2002). Influence of phytoplankton on the global radiation budget. *Journal of Geophysical Research: Atmospheres*, 107(D19):ACL 5–1–ACL 5–10.
- Frouin, R., Ramon, D., Boss, E., Jolivet, D., Compiègne, M., Tan, J., Bouman, H., Jackson, T., Franz, B., Platt, T., and Sathyendranath, S. (2018). Satellite radiation products for ocean biology and biogeochemistry: Needs, state-of-the-art, gaps, development priorities, and opportunities. *Frontiers in Marine Science*, 5:3.
- Fry, E. S. (2000). Visible and near-ultraviolet absorption spectrum of liquid water: comment. *Applied Optics*, 39(16):2743–2744.
- Fryxell, G. A. and Kendrick, G. A. (1988). Austral spring microalgae across the Weddell

- Sea ice edge: spatial relationships found along a northward transect during AMERIEZ 83. *Deep Sea Research Part A. Oceanographic Research Papers*, 35(1):1–20.
- GCOS (2011). Systematic observation requirements from satellite-based data products for climate 2011 update. supplemental details to the satellite-based component of the “Implementation Plan for the Global Observing System for Climate in Support of the UNFCCC”; no. 154. Technical report, World Meteorological Organisation (WMO): Geneva, Switzerland.
- GCOS (2016). GCOS 2016 implementation plan. Technical report, World Meteorological Organisation (WMO): Geneva, Switzerland.
- Giardino, C., Brando, V. E., Gege, P., Pinnel, N., Hochberg, E., Knaeps, E., Reusen, I., Doerffer, R., Bresciani, M., Braga, F., Foerster, S., Champollion, N., and Dekker, A. (2019). Imaging Spectrometry of Inland and Coastal Waters: State of the Art, Achievements and Perspectives. *Surveys in Geophysics*, 40(3):401–429.
- Goericke, R. and Repeta, D. J. (1993). Chlorophylls a and b and divinyl chlorophylls a and b in the open subtropical North Atlantic Ocean. *Marine Ecology Progress Series*, 101(3):307–313.
- Gomes, A., Bernardo, N., Carmo, A., Rodrigues, T., and Alcântara, E. (2018). Diffuse attenuation coefficient retrieval in CDOM dominated inland water with high chlorophyll-a concentrations. *Remote Sensing*, 10:1063.
- Gordon, H. R. and McCluney, W. R. (1975). Estimation of the Depth of Sunlight Penetration in the Sea for Remote Sensing. *Applied Optics*, 14(2):413–416.
- Gordon, H. R., Smith, R. C., Ronald, J., and Zaneveld, V. (1980). Introduction to ocean optics. In Duntley, S. Q., editor, *Ocean Optics VI*, volume 0208, pages 14 – 55. International Society for Optics and Photonics, SPIE.
- Gordon, H. R., Clark, D. K., Brown, J. W., Brown, O. B., Evans, R. H., and Broenkow, W. W. (1983). Phytoplankton pigment concentrations in the Middle Atlantic Bight: comparison of ship determinations and CZCS estimates. *Applied Optics*, 22(1):20–36.
- Gordon, H. R. and Morel, A. Y. (1983). *Remote Assessment of Ocean Color for Interpretation of Satellite Visible Imagery: a Review*, volume 4. Springer-Verlag, New York.
- Gordon, H. R. and Wang, M. (1994a). Influence of oceanic whitecaps on atmospheric correction of ocean-color sensors. *Applied Optics*, 33(33):7754–7763.

- Gordon, H. R. and Wang, M. (1994b). Retrieval of water-leaving radiance and aerosol optical thickness over the oceans with SeaWiFS: a preliminary algorithm. *Applied Optics*, 33(3):443–452.
- Gordon, H. R., Boynton, G. C., Balch, W. M., Groom, S. B., Harbour, D. S., and Smyth, T. J. (2001). Retrieval of coccolithophore calcite concentration from SeaWiFS Imagery. *Geophysical Research Letters*, 28(8):1587–1590.
- Gorshelev, V., Serdyuchenko, A., Weber, M., Chehade, W., and Burrows, J. P. (2014). High spectral resolution ozone absorption cross-sections – Part 1: Measurements, data analysis and comparison with previous measurements around 293 K. *Atmospheric Measurement Techniques*, 7(2):609–624.
- Grainger, J. F. and Ring, J. (1962). Anomalous Fraunhofer Line Profiles. *Nature*, 193:762.
- Gregg, W. W. and Casey, N. W. (2010). Improving the consistency of ocean color data: A step toward climate data records. *Geophysical Research Letters*, 37(4):L04605.
- Groom, S., Sathyendranath, S., Ban, Y., Bernard, S., Brewin, R., Brotas, V., Brockmann, C., Chauhan, P., Choi, J.-k., Chuprin, A., Ciavatta, S., Cipollini, P., Donlon, C., Franz, B., He, X., Hirata, T., Jackson, T., Kampel, M., Krasemann, H., Lavender, S., Pardo-Martinez, S., Mélin, F., Platt, T., Santoleri, R., Skakala, J., Schaeffer, B., Smith, M., Steinmetz, F., Valente, A., and Wang, M. (2019). Satellite Ocean Colour: Current status and future perspective. *Frontiers in Marine Science*, 6:485.
- Gross, E. (1930). Change of wave-length of light due to elastic heat waves at scattering in liquids. *Nature*, 126(3171):201–202.
- Guanter, L., Kaufmann, H., Segl, K., Foerster, S., Rogass, C., Chabrillat, S., Kuester, T., Hollstein, A., Rossner, G., Chlebek, C., Straif, C., Fischer, S., Schrader, S., Storch, T., Heiden, U., Mueller, A., Bachmann, M., Mühle, H., Müller, R., Habermeyer, M., Ohndorf, A., Hill, J., Buddenbaum, H., Hostert, P., Van der Linden, S., LeitÄLo, P. J., Rabe, A., Doerffer, R., Krasemann, H., Xi, H., Mauser, W., Hank, T., Locherer, M., Rast, M., Staenz, K., and Sang, B. (2015). The EnMAP Spaceborne Imaging Spectroscopy Mission for Earth Observation. *Remote Sensing*, 7(7):8830–8857.
- Guarini, R., Loizzo, R., Longo, F., Mari, S., Scopa, T., and Varacalli, G. (2017). Overview of the prisma space and ground segment and its hyperspectral products. In *2017 IEEE International Geoscience and Remote Sensing Symposium (IGARSS)*, pages 431 – 434.

- Guenther, A., Hewitt, C. N., Erickson, D., Fall, R., Geron, C., Graedel, T., Harley, P., Klinger, L., Lerdau, M., Mckay, W. A., Pierce, T., Scholes, B., Steinbrecher, R., Tallamraju, R., Taylor, J., and Zimmerman, P. (1995). A global model of natural volatile organic compound emissions. *Journal of Geophysical Research: Atmospheres*, 100(D5):8873–8892.
- Haltrin, V. I. and Kattawar, G. W. (1993). Self-consistent solutions to the equation of transfer with elastic and inelastic scattering in oceanic optics: I. Model. *Applied Optics*, 32(27):5356–5367.
- Hare, D. E. and Sorensen, C. M. (1990). Raman spectroscopic study of dilute H₂O in the temperature range – 31.5 to 160°C. *The Journal of Chemical Physics*, 93(10):6954–6961.
- Harris, G. P. (1986). *Phytoplankton ecology: structure, function and fluctuation*. Springer, Berlin.
- Haxo, F. T. (1985). Photosynthetic action spectrum of the coccolithophorid, *Emiliana huxleyi* (haptophyceae): 19' hexanoyloxyfucoxanthin as antenna pigment. *Journal of Phycology*, 21(2):282–287.
- Hays, G. C., Richardson, A. J., and Robinson, C. (2005). Climate change and marine plankton. *Trends in Ecology & Evolution*, 20(6):337–344.
- Henriksen, P., Riemann, B., Kaas, H., Sørensen, H. M., and Sørensen, H. L. (2002). Effects of nutrient-limitation and irradiance on marine phytoplankton pigments. *Journal of Plankton Research*, 24(9):835–858.
- Hense, I., Stemmler, I., and Sonntag, S. (2017). Ideas and perspectives: climate-relevant marine biologically driven mechanisms in Earth system models. *Biogeosciences*, 14(2):403–413.
- Henson, S. A., Sarmiento, J. L., Dunne, J. P., Bopp, L., Lima, I., Doney, S. C., John, J., and Beaulieu, C. (2010). Detection of anthropogenic climate change in satellite records of ocean chlorophyll and productivity. *Biogeosciences*, 7(2):621–640.
- Heue, K.-P., Coldewey-Egbers, M., Delcloo, A., Lerot, C., Loyola, D., Valks, P., and van Roozendaal, M. (2016). Trends of tropical tropospheric ozone from 20 years of European satellite measurements and perspectives for the Sentinel-5 Precursor. *Atmospheric Measurement Techniques*, 9(10):5037–5051.

- Hewson, W., Bösch, H., Barkley, M. P., and De Smedt, I. (2013). Characterisation of GOME-2 formaldehyde retrieval sensitivity. *Atmospheric Measurement Techniques*, 6(2):371–386.
- Hilboll, A., Richter, A., and Burrows, J. P. (2013). Long-term changes of tropospheric NO₂ over megacities derived from multiple satellite instruments. *Atmospheric Chemistry and Physics*, 13(8):4145–4169.
- Hilsenrath, E., Cebula, R. P., DeLand, M. T., Laamann, K., Taylor, S., Wellemeyer, C., and Bhartia, P. K. (1995). Calibration of the NOAA 11 solar backscatter ultraviolet (SBUV/2) ozone data set from 1989 to 1993 using in-flight calibration data and SSBUV. *Journal of Geophysical Research: Atmospheres*, 100(D1):1351–1366.
- Hirata, T., Hardman-Mountford, N., Brewin, R., Aiken, J., Barlow, R., Suzuki, K., Isada, T., Howell, E., Hashioka, T., Noguchi-Aita, M., et al. (2011). Synoptic relationships between surface Chlorophyll-a and diagnostic pigments specific to phytoplankton functional types. *Biogeosciences*, 8(2):311–327.
- Højerslev, N. and Aas, E. (1991). A relationship for the penetration of ultraviolet B radiation into the Norwegian Sea. *Journal of Geophysical Research: Oceans*, 96(C9):17003–17005.
- Holligan, P., Charalampopoulou, A., and Hutson, R. (2010). Seasonal distributions of the coccolithophore, *Emiliana huxleyi*, and of particulate inorganic carbon in surface waters of the Scotia Sea. *Journal of Marine Systems*, 82(4):195–205.
- Holligan, P. M., Fernández, E., Aiken, J., Balch, W. M., Boyd, P., Burkill, P. H., Finch, M., Groom, S. B., Malin, G., Muller, K., Purdie, D. A., Robinson, C., Trees, C. C., Turner, S. M., and van der Wal, P. (1993a). A biogeochemical study of the coccolithophore, *Emiliana huxleyi*, in the North Atlantic. *Global Biogeochemical Cycles*, 7(4):879–900.
- Holligan, P. M., Groom, S. B., and Harbour, D. S. (1993b). What controls the distribution of the coccolithophore, *Emiliana huxleyi*, in the North Sea? *Fisheries Oceanography*, 2(3–4):175–183.
- Hopkins, J., Henson, S. A., Poulton, A. J., and Balch, W. M. (2019). Regional characteristics of the temporal variability in the global particulate inorganic carbon inventory. *Global Biogeochemical Cycles*, 33(11):1328–1338.

- Hudson, N., Baker, A., and Reynolds, D. (2007). Fluorescence analysis of dissolved organic matter in natural, waste and polluted waters – a review. *River Research and Applications*, 23(6):631–649.
- IOCCG (2006). *Remote Sensing of Inherent Optical Properties: Fundamentals, Tests of Algorithms, and Applications*, volume No. 5 of *Reports of the International Ocean Colour Coordinating Group*. IOCCG, Dartmouth, Canada.
- IOCCG (2007). *Ocean-Colour Data Merging*, volume No. 6 of *Reports of the International Ocean Colour Coordinating Group*. IOCCG, Dartmouth, Canada.
- IOCCG (2008). *Why Ocean Colour? The Societal Benefits of Ocean-Colour Technology*, volume No. 7 of *Reports of the International Ocean Colour Coordinating Group*. IOCCG, Dartmouth, Canada.
- IOCCG (2013). *In-flight Calibration of Satellite Ocean-Colour Sensors*, volume No. 14 of *Reports of the International Ocean Colour Coordinating Group*. IOCCG, Dartmouth, Canada.
- IOCCG (2014). *Phytoplankton Functional Types from Space*, volume No. 15 of *Reports of the International Ocean Colour Coordinating Group*. IOCCG, Dartmouth, Canada.
- IOCCG (2015). *Ocean Colour Remote Sensing in Polar Seas*, volume No. 16 of *Reports of the International Ocean Colour Coordinating Group*. IOCCG, Dartmouth, Canada.
- IOCCG (2020). *Synergy between Ocean Colour and Biogeochemical/Ecosystem Models*, volume No. 19 of *Reports of the International Ocean Colour Coordinating Group*. IOCCG, Dartmouth, Canada.
- IPCC (2013). *Climate Change 2013 – The Physical Science Basis: Working Group I Contribution to the Fifth Assessment Report of the Intergovernmental Panel on Climate Change*. Stocker, T.F., D. Qin, G.-K. Plattner, M. Tignor, S.K. Allen, J. Boschung, A. Nauels, Y. Xia, V. Bex and P.M. Midgley, editors, Cambridge University Press, Cambridge, United Kingdom and New York, NY, USA, 1535 pp.
- IPCC (2014). *Climate Change 2014: Synthesis Report. Contribution of Working Groups I, II and III to the Fifth Assessment Report of the Intergovernmental Panel on Climate Change*. Core writing team R.K. Pachauri and L.A. Meyer, editors, IPCC, Geneva, Switzerland, 151 pp.

- IPCC (2019). *IPCC Special Report on the Ocean and Cryosphere in a Changing Climate*. Pörtner, H.-O. and Roberts, D. C. and Masson-Delmotte, V. and Zhai, P. and Tignor, M. and Poloczanska, E. and Mintenbeck, K. and Alegría, A. and Nicolai, M. and Okem, A. and Petzold, J. and B. Rama, B. and Weyer, N.M., editors, in press.
- Irie, H., Nakayama, T., Shimizu, A., Yamazaki, A., Nagai, T., Uchiyama, A., Zaizen, Y., Kagamitani, S., and Matsumi, Y. (2015). Evaluation of MAX-DOAS aerosol retrievals by coincident observations using CRDS, lidar, and sky radiometer in Tsukuba, Japan. *Atmospheric Measurement Techniques*, 8(7):2775–2788.
- Isada, T., Hirawake, T., Kobayashi, T., Nosaka, Y., Natsuike, M., Imai, I., Suzuki, K., and Saitoh, S.-I. (2015). Hyperspectral optical discrimination of phytoplankton community structure in Funka Bay and its implications for ocean color remote sensing of diatoms. *Remote Sensing of Environment*, 159:134–151.
- Jackson, T., Sathyendranath, S., and Mélin, F. (2017). An improved optical classification scheme for the Ocean Colour Essential Climate Variable and its applications. *Remote Sensing of Environment*, 203:152–161.
- Jacques, G. and Panouse, M. (1991). Biomass and composition of size fractionated phytoplankton in the Weddell-Scotia Confluence area. *Polar Biology*, 11(5):315–328.
- Jamet, C., Loisel, H., and Dessailly, D. (2012). Retrieval of the spectral diffuse attenuation coefficient $K_d(\lambda)$ in open and coastal ocean waters using a neural network inversion. *Journal of Geophysical Research: Oceans*, 117(C10):C10023.
- Jamet, C., Ibrahim, A., Ahmad, Z., Angelini, F., Babin, M., Behrenfeld, M. J., Boss, E., Cairns, B., Churnside, J., Chowdhary, J., Davis, A. B., Dionisi, D., Duforêt-Gaurier, L., Franz, B., Frouin, R., Gao, M., Gray, D., Hasekamp, O., He, X., Hostetler, C., Kalashnikova, O. V., Knobelspiesse, K., Lacour, L., Loisel, H., Martins, V., Rehm, E., Remer, L., Sanhaj, I., Stamnes, K., Stamnes, S., Victori, S., Werdell, J., and Zhai, P.-W. (2019). Going Beyond Standard Ocean Color Observations: Lidar and Polarimetry. *Frontiers in Marine Science*, 6:251.
- Jin, X., Gruber, N., Dunne, J. P., Sarmiento, J. L., and Armstrong, R. A. (2006). Diagnosing the contribution of phytoplankton functional groups to the production and export of particulate organic carbon, CaCO_3 , and opal from global nutrient and alkalinity distributions. *Global Biogeochemical Cycles*, 20(2):GB2015.

- Jochum, M., Yeager, S., Lindsay, K., Moore, K., and Murtugudde, R. (2010). Quantification of the Feedback between Phytoplankton and ENSO in the Community Climate System Model. *Journal of Climate*, 23(11):2916–2925.
- Johannessen, S. C., Miller, W. L., and Cullen, J. J. (2003). Calculation of UV attenuation and colored dissolved organic matter absorption spectra from measurements of ocean color. *Journal of Geophysical Research: Oceans*, 108(C9):3301.
- Johnsen, G., Samset, O., Granskog, L., and Sakshaug, E. (1994). In vivo absorption characteristics in 10 classes of bloom-forming phytoplankton: taxonomic characteristics and responses to photoadaptation by means of discriminant and HPLC analysis. *Marine Ecology Progress Series*, 105:149–157.
- Johnson, R., Strutton, P. G., Wright, S. W., McMinn, A., and Meiners, K. M. (2013). Three improved satellite chlorophyll algorithms for the Southern Ocean. *Journal of Geophysical Research: Oceans*, 118(7):3694–3703.
- Joiner, J., Bhartia, P. K., Cebula, R. P., Hilsenrath, E., McPeters, R. D., and Park, H. (1995). Rotational Raman scattering (Ring effect) in satellite backscatter ultraviolet measurements. *Applied Optics*, 34(21):4513–4525.
- Joiner, J., Vasilkov, A. P., Flittner, D. E., Gleason, J. F., and Bhartia, P. K. (2004). Retrieval of cloud pressure and oceanic chlorophyll content using Raman scattering in GOME ultraviolet spectra. *Journal of Geophysical Research: Atmospheres*, 109(D1):D01109.
- Joiner, J. and Vasilkov, A. P. (2006). First results from the OMI rotational Raman scattering cloud pressure algorithm. *IEEE Transactions on Geoscience and Remote Sensing*, 44(5):1272–1282.
- Joiner, J., Yoshida, Y., Guanter, L., and Middleton, E. M. (2016). New methods for the retrieval of chlorophyll red fluorescence from hyperspectral satellite instruments: simulations and application to GOME-2 and SCIAMACHY. *Atmospheric Measurement Techniques*, 9(8):3939–3967.
- Kara, A. B., Hurlburt, H. E., Rochford, P. A., and O’Brien, J. J. (2004). The impact of water turbidity on interannual sea surface temperature simulations in a layered global ocean model. *Journal of Physical Oceanography*, 34(2):345–359.
- Karl, D., Bidigare, R., and Letelier, R. (2001). Long-term changes in plankton community structure and productivity in the North Pacific Subtropical Gyre: The domain shift

- hypothesis. *Deep Sea Research Part II: Topical Studies in Oceanography*, 48(8):1449–1470.
- Kattawar, G. W., Young, A. T., and Humphreys, T. J. (1981). Inelastic scattering in planetary atmospheres. I - The Ring effect, without aerosols. *Astrophysical Journal*, 243:1049–1057.
- Kattawar, G. W. and Xu, X. (1992). Filling in of Fraunhofer lines in the ocean by Raman scattering. *Applied Optics*, 31(30):6491–6500.
- Khatiwala, S., Primeau, F., and Hall, T. (2009). Reconstruction of the history of anthropogenic CO₂ concentrations in the ocean. *Nature*, 462:346–349.
- King, M. D., Platnick, S., Menzel, W. P., Ackerman, S. A., and Hubanks, P. A. (2013). Spatial and Temporal Distribution of Clouds Observed by MODIS Onboard the Terra and Aqua Satellites. *IEEE Transactions on Geoscience and Remote Sensing*, 51(7):3826–3852.
- Kirchhoff, G. (1860). Ueber das Verhältniss zwischen dem Emissionsvermögen und dem Absorptionsvermögen der Körper für Wärme und Licht. *Annalen der Physik*, 185(2):275–301.
- Kirk, J. T. O. (1994). *Light and Photosynthesis in Aquatic Ecosystems*. Cambridge University Press, Cambridge, second edition.
- Kishino, M., Takahashi, M., Okami, N., and Ichimura, S. (1985). Estimation of the spectral absorption coefficients of phytoplankton in the sea. *Bulletin of Marine Science*, 37:634–642.
- Kneizys, F. X., Shettle, E., Abreu, L. W., Chetwynd, J., and Anderson, G. (1988). Users guide to LOWTRAN 7. Technical report, Air Force Geophysics Laboratory AFGL.
- Koelemeijer, R. B. A. and Stammes, P. (1999). Validation of Global Ozone Monitoring Experiment cloud fractions relevant for accurate ozone column retrieval. *Journal of Geophysical Research: Atmospheres*, 104(D15):18801–18814.
- Kondilenko, I. I., Korotkov, P. A., Klimenko, V. A., and Demyanenko, O. P. (1977). Transverse crosssection of Raman scattering of the ν_1 vibration of the water molecule in the liquid and gaseous state. *Optical Spectroscopy (USSR)*, 43:384–386.

- Kostadinov, T. S., Siegel, D. A., and Maritorena, S. (2009). Retrieval of the particle size distribution from satellite ocean color observations. *Journal of Geophysical Research: Oceans*, 114(C9):C09015.
- Kou, L., Labrie, D., and Chylek, P. (1993). Refractive indices of water and ice in the 0.65- to 2.5- μm spectral range. *Applied Optics*, 32(19):3531–3540.
- Kramer, S. J. and Siegel, D. A. (2019). How can phytoplankton pigments be best used to characterize surface ocean phytoplankton groups for ocean color remote sensing algorithms? *Journal of Geophysical Research: Oceans*, 124(11):7557–7574.
- Krasemann, H., Müller, D., Mélin, F., Valente, A., Jackson, T., and Grant, M. (2017). Product Validation and Inter-comparison Report, D4.1 PVIR, Ocean Colour Climate Change Initiative – Phase Two. Version 3.0.2. Technical report, European Space Agency.
- Kratzer, S., Brockmann, C., and Moore, G. (2008). Using MERIS full resolution data to monitor coastal waters – A case study from Himmerfjärden, a fjord-like bay in the northwestern Baltic Sea. *Remote Sensing of Environment*, 112(5):2284–2300.
- Kröckel, L. and Schmidt, M. A. (2014). Extinction properties of ultrapure water down to deep ultraviolet wavelengths. *Optical Materials Express*, 4(9):1932–1942.
- Krutz, D., Müller, R., Knodt, U., Günther, B., Walter, I., Sebastian, I., Säuberlich, T., Reulke, R., Carmona, E., Eckardt, A., Venus, H., Fischer, C., Zender, B., Arloth, S., Lieder, M., Neidhardt, M., Grote, U., Schrandt, F., Gelmi, S., and Wojtkowiak, A. (2019). The instrument design of the DLR Earth Sensing Imaging Spectrometer (DE-SIS). *Sensors*, 19(7).
- Kühl, S., Pukite, J., Deutschmann, T., Platt, U., and Wagner, T. (2008). SCIAMACHY limb measurements of NO₂, BrO and OCIO. Retrieval of vertical profiles: Algorithm, first results, sensitivity and comparison studies. *Advances in Space Research*, 42(10):1747–1764.
- Lacan, A. and Lang, R. (2011). Investigation on GOME-2 throughput degradation, final report, EUM/LEO/REP/09/0732, issue 1.1, 16 July 2011. Technical report, EUMETSAT.
- Lampel, J., Frieß, U., and Platt, U. (2015). The impact of vibrational Raman scattering of air on DOAS measurements of atmospheric trace gases. *Atmospheric Measurement Techniques*, 8(9):3767–3787.

- Landau, L. D. and Placzek, G (1934). Struktur der unverschobenen Streulinie. *Physikalische Zeitschrift der Sowjetunion*, 5:172–173.
- Langford, V. S., McKinley, A. J., and Quickenden, T. I. (2001). Temperature dependence of the visible-near-infrared absorption spectrum of liquid water. *The Journal of Physical Chemistry A*, 105(39):8916–8921.
- Larouche, P., Max, J.-J., and Chapados, C. (2008). Isotope effects in liquid water by infrared spectroscopy. II. Factor analysis of the temperature effect on H₂O and D₂O. *The Journal of Chemical Physics*, 129(6):064503.
- Le Quéré, C., Harrison, S. P., Colin Prentice, I., Buitenhuis, E. T., Aumont, O., Bopp, L., Claustre, H., Cotrim Da Cunha, L., Geider, R., Giraud, X., Klaas, C., Kohfeld, K. E., Legendre, L., Manizza, M., Platt, T., Rivkin, R. B., Sathyendranath, S., Uitz, J., Watson, A. J., and Wolf-Gladrow, D. (2005). Ecosystem dynamics based on plankton functional types for global ocean biogeochemistry models. *Global Change Biology*, 11(11):2016–2040.
- Lee, Z., Carder, K. L., and Arnone, R. A. (2002). Deriving inherent optical properties from water color: a multiband quasi-analytical algorithm for optically deep waters. *Applied Optics*, 41(27):5755–5772.
- Lee, Z., Du, K.-P., and Arnone, R. (2005a). A model for the diffuse attenuation coefficient of downwelling irradiance. *Journal of Geophysical Research: Oceans*, 110(C2):C02016.
- Lee, Z., Darecki, M., Carder, K. L., Davis, C. O., Stramski, D., and Rhea, W. J. (2005b). Diffuse attenuation coefficient of downwelling irradiance: An evaluation of remote sensing methods. *Journal of Geophysical Research: Oceans*, 110(C2):C02017.
- Lee, Z., Carder, K., Arnone, R., and He, M. (2007). Determination of primary spectral bands for remote sensing of aquatic environments. *Sensors*, 7(12):3428–3441.
- Lee, Z., Hu, C., Shang, S., Du, K., Lewis, M., Arnone, R., and Brewin, R. (2013). Penetration of uv-visible solar radiation in the global oceans: Insights from ocean color remote sensing. *Journal of Geophysical Research: Oceans*, 118(9):4241–4255.
- Lerot, C., Stavrakou, T., De Smedt, I., Müller, J.-F., and Van Roozendaal, M. (2010). Glyoxal vertical columns from GOME-2 backscattered light measurements and comparisons with a global model. *Atmospheric Chemistry and Physics*, 10(24):12059–12072.

- Lerot, C., Van Roozendaal, M., Spurr, R., Loyola, D., Coldewey-Egbers, M., Kochenova, S., van Gent, J., Koukouli, M., Balis, D., Lambert, J.-C., Granville, J., and Zehner, C. (2014). Homogenized total ozone data records from the European sensors GOME/ERS-2, SCIAMACHY/Envisat, and GOME-2/MetOp-A. *Journal of Geophysical Research: Atmospheres*, 119(3):1639–1662.
- Leser, H., Hönninger, G., and Platt, U. (2003). MAX-DOAS measurements of BrO and NO₂ in the marine boundary layer. *Geophysical Research Letters*, 30(10):1537.
- Levelt, P. F., van den Oord, G. H. J., Dobber, M. R., Malkki, A., Visser, H., de Vries, J., Stammes, P., Lundell, J. O. V., and Saari, H. (2006). The ozone monitoring instrument. *IEEE Transactions on Geoscience and Remote Sensing*, 44(5):1093–1101.
- Lewis, M. R., Carr, M.-E., Feldman, G. C., Esaias, W., and McClain, C. (1990). Influence of penetrating solar radiation on the heat budget of the equatorial Pacific Ocean. *Nature*, 347:543–545.
- Li, X., Fan, X., Yan, H., Li, A., Wang, M., and Qu, Y. (2018). Mapping global ocean surface albedo from satellite observations: Models, algorithms, and datasets. *The International Archives of the Photogrammetry, Remote Sensing and Spatial Information Sciences*, XLII-3:967–970.
- Lichtenberg, G., Kleipool, Q., Krijger, J. M., van Soest, G., van Hees, R., Tilstra, L. G., Acarreta, J. R., Aben, I., Ahlers, B., Bovensmann, H., Chance, K., Gloudemans, A. M. S., Hoogeveen, R. W. M., Jongma, R. T. N., Noël, S., PETERS, A., Schrijver, H., Schrijvers, C., Sioris, C. E., Skupin, J., Slijkhuis, S., Stammes, P., and Wuttke, M. (2006). SCIAMACHY Level 1 data: calibration concept and in-flight calibration. *Atmospheric Chemistry and Physics*, 6(12):5347–5367.
- Liebing, P., Krijger, M., Snel, R., Bramstedt, K., Noël, S., Bovensmann, H., and Burrows, J. P. (2018). In-flight calibration of SCIAMACHY’s polarization sensitivity. *Atmospheric Measurement Techniques*, 11(1):265–289.
- Liou, K. N. (2002). *An Introduction to Atmospheric Radiation*. Academic Press, second edition.
- Litchman, E., de Tezanos Pinto, P., Edwards, K. F., Klausmeier, C. A., Kremer, C. T., and Thomas, M. K. (2015). Global biogeochemical impacts of phytoplankton: a trait-based perspective. *Journal of Ecology*, 103(6):1384–1396.

- Liu, Y., Boss, E., Chase, A., Xi, H., Zhang, X., Röttgers, R., Pan, Y., and Bracher, A. (2019). Retrieval of phytoplankton pigments from underway spectrophotometry in the Fram Strait. *Remote Sensing*, 11(3):318.
- Longhurst, A., Sathyendranath, S., Platt, T., and Caverhill, C. (1995). An estimate of global primary production in the ocean from satellite radiometer data. *Journal of Plankton Research*, 17(6):1245–1271.
- Losa, S. N., Soppa, M. A., Dinter, T., Wolanin, A., Oelker, J., and Bracher, A. (2017b). Global chlorophyll a surface concentrations for diatoms, coccolithophores and cyanobacteria as the synergistic SynSenPFT product combined PhytoDOAS and OC-PFT for the period of time August 2002 - April 2012, links to NetCDF files. PANGAEA. In supplement to: Losa et al. (2017a). <http://dx.doi.org/10.5285/9c334fbe6d424a708cf3c4cf0c6a53f5>.
- Losa, S. N., Soppa, M. A., Dinter, T., Wolanin, A., Brewin, R. J. W., Bricaud, A., Oelker, J., Peeken, I., Gentili, B., Rozanov, V., and Bracher, A. (2017a). Synergistic Exploitation of Hyper- and Multi-Spectral Precursor Sentinel Measurements to Determine Phytoplankton Functional Types (SynSenPFT). *Frontiers in Marine Science*, 4:203.
- Losa, S. N., Oelker, J., Soppa, M. A., Losch, M., Dutkiewicz, S., Dinter, T., Richter, A., Rozanov, V. V., Burrows, J. P., and Bracher, A. (2018). Investigating the phytoplankton diversity in the Great Calcite Belt: perspective from modelling and satellite retrievals. In *Extended Abstract*, Dubrovnik (Croatia), 7 October 2018 - 12 October 2018. Ocean Optics Conference XXIV.
- Ludewig, A., Kleipool, Q., Bartstra, R., Landzaat, R., Leloux, J., Loots, E., Meijering, P., van der Plas, E., Rozemeijer, N., Vonk, F., and Veeffkind, P. (2020). In-flight calibration results of the TROPOMI payload on board the Sentinel-5 Precursor satellite. *Atmospheric Measurement Techniques*, 13(7):3561–3580.
- Marshall, B. R. and Smith, R. C. (1990). Raman scattering and in-water ocean optical properties. *Applied Optics*, 29(1):71–84.
- Mason, J. D., Cone, M. T., and Fry, E. S. (2016). Ultraviolet (250–550 nm) absorption spectrum of pure water. *Applied Optics*, 55(25):7163–7172.
- Maxwell, J. C. (1865). VIII. A dynamical theory of the electromagnetic field. *Philosophical Transactions of the Royal Society of London*, 155:459–512.

- McCree, K. (1981). Photosynthetically Active Radiation. In Lange, O., Nobel, P., Osmond, C., and Ziegler, H., editors, *Earth System Monitoring: Selected Entries from the Encyclopedia of Sustainability Science and Technology*, volume 12/A. Springer, Berlin, Heidelberg.
- McLinden, C. A., McConnell, J. C., Strong, K., McDade, I. C., Gattinger, R. L., King, R., Solheim, B., Llewellyn, E. J., and Evans, W. J. F. (2002). The impact of the OSIRIS grating efficiency on radiance and trace-gas retrievals. *Canadian Journal of Physics*, 80(4):469–481.
- Meier, A. C., Schönhardt, A., Bösch, T., Richter, A., Seyler, A., Ruhtz, T., Constantin, D.-E., Shaiganfar, R., Wagner, T., Merlaud, A., Van Roozendaal, M., Belegante, L., Nicolae, D., Georgescu, L., and Burrows, J. P. (2017). High-resolution airborne imaging DOAS measurements of NO₂ above Bucharest during AROMAT. *Atmospheric Measurement Techniques*, 10(5):1831–1857.
- Mélin, F. (2016). Impact of inter-mission differences and drifts on chlorophyll-a trend estimates. *International Journal of Remote Sensing*, 37(10):2233–2251.
- Miller, A. J., Alexander, M. A., Boer, G. J., Chai, F., Denman, K., Erickson, David J., I., Frouin, R., Gabric, A. J., Laws, E. A., Lewis, M. R., Liu, Z., Murtugudde, R., Nakamoto, S., Neilson, D. J., Norris, J. R., Ohlmann, J. C., Perry, R. I., Schneider, N., Shell, K. M., and Timmermann, A. (2003). Potential feedbacks between Pacific Ocean ecosystems and interdecadal climate variations. *Bulletin of the American Meteorological Society*, 84(5):617–634.
- Mitchell, C., Hu, C., Bowler, B., Drapeau, D., and Balch, W. M. (2017). Estimating particulate inorganic carbon concentrations of the global ocean from Ocean Color measurements using a reflectance difference approach. *Journal of Geophysical Research: Oceans*, 122(11):8707–8720.
- Mobley, C. D. (1994). *Light and Water: Radiative Transfer in Natural Waters*. Academic Press.
- Mobley, C. D., Sundman, L. K., and Boss, E. (2002). Phase function effects on oceanic light fields. *Applied Optics*, 41(6):1035–1050.
- Mobley, C. D. and Sundman, L. K. (2013). HydroLight 5.2 - EcoLight 5.2 technical documentation. Technical report, Sequoia Scientific, Inc.

- Mobley, C. D., Boss, E., and Roesler, C. (2021). Ocean Optics Web Book, <http://www.oceanopticsbook.info/>, accessed: 15.03.2021.
- Mohan, R., Mergulhao, L. P., Guptha, M., Rajakumar, A., Thamban, M., AnilKumar, N., Sudhakar, M., and Ravindra, R. (2008). Ecology of coccolithophores in the Indian sector of the Southern Ocean. *Marine Micropaleontology*, 67(1):30–45.
- Morel, A. and Prieur, L. (1977). Analysis of variations in ocean color. *Limnology and Oceanography*, 22(4):709–722.
- Morel, A. (1988). Optical modeling of the upper ocean in relation to its biogenous matter content (case I waters). *Journal of Geophysical Research: Oceans*, 93(C9):10749–10768.
- Morel, A. (1991). Light and marine photosynthesis: a spectral model with geochemical and climatological implications. *Progress in Oceanography*, 26(3):263–306.
- Morel, A. and Gentili, B. (1993). Diffuse reflectance of oceanic waters. II. Bidirectional aspects. *Applied Optics*, 32(33):6864–6879.
- Morel, A. and Antoine, D. (1994). Heating rate within the upper ocean in relation to its bio-optical state. *Journal of Physical Oceanography*, 24(7):1652–1665.
- Morel, A. and Gentili, B. (1996). Diffuse reflectance of oceanic waters. III. Implication of bidirectionality for the remote-sensing problem. *Applied Optics*, 35(24):4850–4862.
- Morel, A. and Maritorena, S. (2001). Bio-optical properties of oceanic waters: A reappraisal. *Journal of Geophysical Research: Oceans*, 106(C4):7163–7180.
- Morel, A., Antoine, D., and Gentili, B. (2002). Bidirectional reflectance of oceanic waters: accounting for Raman emission and varying particle scattering phase function. *Applied Optics*, 41(30):6289–6306.
- Morel, A., Huot, Y., Gentili, B., Werdell, P. J., Hooker, S. B., and Franz, B. A. (2007a). Examining the consistency of products derived from various ocean color sensors in open ocean (Case 1) waters in the perspective of a multi-sensor approach. *Remote Sensing of Environment*, 111(1):69–88.
- Morel, A., Claustre, H., Antoine, D., and Gentili, B. (2007b). Natural variability of bio-optical properties in case 1 waters: attenuation and reflectance within the visible and near-UV spectral domains, as observed in South Pacific and Mediterranean waters. *Biogeosciences*, 4(5):913–925.

- Morel, A., Gentili, B., Claustre, H., Babin, M., Bricaud, A., Ras, J., and Tièreche, F. (2007c). Optical properties of the “clearest” natural waters. *Limnology and Oceanography*, 52(1):217–229.
- Mouw, C. B., Hardman-Mountford, N. J., Alvain, S., Bracher, A., Brewin, R. J. W., Bricaud, A., Ciotti, A. M., Devred, E., Fujiwara, A., Hirata, T., Hirawake, T., Kostadinov, T. S., Roy, S., and Uitz, J. (2017). A consumer’s guide to satellite remote sensing of multiple phytoplankton groups in the global ocean. *Frontiers in Marine Science*, 4:41.
- Mueller, J. (2000). SeaWiFS algorithm for the diffuse attenuation coefficient, K(490), using water-leaving radiances at 490 and 555 nm. In *SeaWiFS postlaunch technical report series, volume 11. Sea-WiFS postlaunch calibration and validation analyses, part 3*, pages 24–27. NASA Goddard Space Flight Center, Greenbelt, Maryland.
- Müller, M. N., Antia, A. N., and LaRoche, J. (2008). Influence of cell cycle phase on calcification in the coccolithophore *Emiliania huxleyi*. *Limnology and Oceanography*, 53(2):506–512.
- Müller, M. N., Trull, T. W., and M., H. G. (2015). Differing responses of three Southern Ocean *Emiliania huxleyi* ecotypes to changing seawater carbonate chemistry. *Marine Ecology Progress Series*, 531:81–90.
- Munro, R., Lang, R., Klaes, D., Poli, G., Retscher, C., Lindstrot, R., Huckle, R., Lacan, A., Grzegorski, M., Holdak, A., Kokhanovsky, A., Livschitz, J., and Eisinger, M. (2016). The GOME-2 instrument on the Metop series of satellites: instrument design, calibration, and level 1 data processing – an overview. *Atmospheric Measurement Techniques*, 9(3):1279–1301.
- Nair, A., Sathyendranath, S., Platt, T., Morales, J., Stuart, V., Forget, M.-H., Devred, E., and Bouman, H. (2008). Remote sensing of phytoplankton functional types. *Remote Sensing of Environment*, 112(8):3366–3375.
- Nelson, N. B. and Siegel, D. A. (2002). Chapter 11 - Chromophoric DOM in the Open Ocean. In Hansell, D. A. and Carlson, C. A., editors, *Biogeochemistry of Marine Dissolved Organic Matter*, pages 547 – 578. Academic Press, San Diego.
- Newnham, D. A. and Ballard, J. (1998). Visible absorption cross sections and integrated absorption intensities of molecular oxygen (O₂ and O₄). *Journal of Geophysical Research: Atmospheres*, 103(D22):28801–28815.

- Nicolaus, M., Hudson, S. R., Gerland, S., and Munderloh, K. (2010). A modern concept for autonomous and continuous measurements of spectral albedo and transmittance of sea ice. *Cold Regions Science and Technology*, 62(1):14–28.
- Nieke, J., Borde, F., Mavrocordatos, C., Berruti, B., Delclaud, Y., Riti, J. B., and Garnier, T. (2012). The Ocean and Land Colour Imager (OLCI) for the Sentinel 3 GMES Mission: status and first test results. In Shimoda, H., Xiong, X., Cao, C., Gu, X., Kim, C., and Kumar, A. S. K., editors, *Earth Observing Missions and Sensors: Development, Implementation, and Characterization II*, volume 8528, pages 49 – 57. International Society for Optics and Photonics, SPIE.
- Noël, S., Bovensmann, H., Skupin, J., Wuttke, M., Burrows, J., Gottwald, M., and Krieg, E. (2003). The SCIAMACHY calibration/monitoring concept and first results. *Advances in Space Research*, 32(11):2123–2128.
- Noxon, J. F. (1975). Twilight enhancement in $O_2(b^1\Sigma_g)$ airglow emission. *Journal of Geophysical Research (1896-1977)*, 80(10):1370–1373.
- O’Connor, C. L. and Schlupf, J. P. (1967). Brillouin scattering in water: The Landau-Placzek ratio. *The Journal of Chemical Physics*, 47(1):31–38.
- Oelker, J., Richter, A., Dinter, T., Rozanov, V. V., Burrows, J. P., and Bracher, A. (2019). Global diffuse attenuation derived from vibrational Raman scattering detected in hyperspectral backscattered satellite spectra. *Optics Express*, 27(12):A829–A855.
- Oelker, J., Losa, S. N., Richter, A., and Bracher, A. (2021). TROPOMI-retrieved under-water light attenuation in three spectral regions in the ultraviolet and blue. *Frontiers in Marine Science*. Manuscript was resubmitted on 01 October 2021.
- Ohlmann, J. C., Siegel, D. A., and Gautier, C. (1996). Ocean mixed layer radiant heating and solar penetration: A global analysis. *Journal of Climate*, 9(10):2265–2280.
- Okamura, Y., Yamada, Y., Urabe, T., Ando, S., and Tanaka, K. (2019). In-orbit observation of the Second Generation Global Imager (SGLI) and study towards follow-on imaging radiometer. In *IGARSS 2019 - 2019 IEEE International Geoscience and Remote Sensing Symposium*, pages 5792–5795.
- OMI (2005). OMI/Aura level 1b 5 year averaged solar irradiance (OMI-Aura.L1-GLOBAL-OMTMIRRYA_2005m0101t0000-syear-rPDS01_v003-2007m0716t145802.he4).

- O'Reilly, J. E., Maritorena, S., Mitchell, B. G., Siegel, D. A., Carder, K. L., Garver, S. A., Kahru, M., and McClain, C. (1998). Ocean color chlorophyll algorithms for SeaWiFS. *Journal of Geophysical Research: Oceans*, 103(C11):24937–24953.
- O'Reilly, J. E. and Werdell, P. J. (2019). Chlorophyll algorithms for ocean color sensors - OC4, OC5 & OC6. *Remote Sensing of Environment*, 229:32–47.
- Orlando, J. J., Tyndall, G. S., Moortgat, G. K., and Calvert, J. G. (1993). Quantum yields for nitrate radical photolysis between 570 and 635 nm. *J. Phys. Chem.*, 97(42):10996–11000.
- Paasche, E. (2001). A review of the coccolithophorid *Emiliana huxleyi* (Prymnesiophyceae), with particular reference to growth, coccolith formation, and calcification-photosynthesis interactions. *Phycologia*, 40(6):503–529.
- Palacz, A. P., John, M. A. S., Brewin, R. J. W., Hirata, T., and Gregg, W. W. (2013). Distribution of phytoplankton functional types in high-nitrate, low-chlorophyll waters in a new diagnostic ecological indicator model. *Biogeosciences*, 10(11):7553–7574.
- Passow, U. and Carlson, C. (2012). The biological pump in a high CO₂ world. *Marine Ecology Progress Series*, 470:249–271.
- Pastel, M., Pommereau, J.-P., Goutail, F., Richter, A., Pazmiño, A., Ionov, D., and Portafaix, T. (2014). Construction of merged satellite total O₃ and NO₂ time series in the tropics for trend studies and evaluation by comparison to NDACC SAOZ measurements. *Atmospheric Measurement Techniques*, 7(10):3337–3354.
- Perner, D. and Platt, U. (1979). Detection of nitrous acid in the atmosphere by differential optical absorption. *Geophysical Research Letters*, 6(12):917–920.
- Peters, C., Pechtl, S., Stutz, J., Hebestreit, K., Hönninger, G., Heumann, K. G., Schwarz, A., Winterlik, J., and Platt, U. (2005). Reactive and organic halogen species in three different European coastal environments. *Atmospheric Chemistry and Physics*, 5(12):3357–3375.
- Peters, E. (2013). *Improved MAX-DOAS measurements and retrievals focused on the marine boundary layer*. Dissertation, University of Bremen.
- Peters, E., Wittrock, F., Richter, A., Alvarado, L. M. A., Rozanov, V. V., and Burrows, J. P. (2014). Liquid water absorption and scattering effects in DOAS retrievals over oceans. *Atmospheric Measurement Techniques*, 7(12):4203–4221.

- Placzek, G. (1934). *Rayleigh-Streuung und Raman-Effekt*. Akademische Verlagsgesellschaft, Leipzig.
- Platt, T. (1986). Primary production of the ocean water column as a function of surface light intensity: algorithms for remote sensing. *Deep Sea Research Part A. Oceanographic Research Papers*, 33(2):149–163.
- Platt, U., Perner, D., and Pätz, H. W. (1979). Simultaneous measurement of atmospheric CH₂O, O₃, and NO₂ by differential optical absorption. *Journal of Geophysical Research: Oceans*, 84(C10):6329–6335.
- Platt, U. and Stutz, J. (2008). *Differential Optical Absorption Spectroscopy*. Springer, Berlin, Heidelberg.
- Pope, R. M. and Fry, E. S. (1997). Absorption spectrum (380–700 nm) of pure water. II. Integrating cavity measurements. *Applied Optics*, 36(33):8710–8723.
- Poulton, A. J., Sanders, R., Holligan, P. M., Stinchcombe, M. C., Adey, T. R., Brown, L., and Chamberlain, K. (2006). Phytoplankton mineralization in the tropical and subtropical Atlantic Ocean. *Global Biogeochemical Cycles*, 20(4):GB4002.
- Poulton, A. J., Mark Moore, C., Seeyave, S., Lucas, M. I., Fielding, S., and Ward, P. (2007a). Phytoplankton community composition around the Crozet Plateau, with emphasis on diatoms and Phaeocystis. *Deep Sea Research Part II: Topical Studies in Oceanography*, 54(18):2085–2105.
- Poulton, A. J., Adey, T. R., Balch, W. M., and Holligan, P. M. (2007b). Relating coccolithophore calcification rates to phytoplankton community dynamics: Regional differences and implications for carbon export. *Deep Sea Research Part II: Topical Studies in Oceanography*, 54(5):538–557.
- Poulton, A. J., Painter, S. C., Young, J. R., Bates, N. R., Bowler, B., Drapeau, D., Lyczskowski, E., and Balch, W. M. (2013). The 2008 *Emiliana huxleyi* bloom along the Patagonian Shelf: Ecology, biogeochemistry, and cellular calcification. *Global Biogeochemical Cycles*, 27(4):1023–1033.
- Priour, L. and Sathyendranath, S. (1981). An optical classification of coastal and oceanic waters based on the specific spectral absorption curves of phytoplankton pigments, dissolved organic matter, and other particulate materials. *Limnology and Oceanography*, 26(4):671–689.

- Quickenden, T. I. and Irvin, J. A. (1980). The ultraviolet absorption spectrum of liquid water. *The Journal of Chemical Physics*, 72(8):4416–4428.
- Randolph, K., Dierssen, H. M., Twardowski, M., Cifuentes-Lorenzen, A., and Zappa, C. J. (2014). Optical measurements of small deeply penetrating bubble populations generated by breaking waves in the Southern Ocean. *Journal of Geophysical Research: Oceans*, 119(2):757–776.
- Raven, J. A. and Falkowski, P. G. (1999). Oceanic sinks for atmospheric CO₂. *Plant, Cell & Environment*, 22(6):741–755.
- Rayleigh, F. R. S. (1899). XXXIV. On the transmission of light through an atmosphere containing small particles in suspension, and on the origin of the blue of the sky. *The London, Edinburgh, and Dublin Philosophical Magazine and Journal of Science*, 47(287):375–384.
- Remer, L. A., Kleidman, R. G., Levy, R. C., Kaufman, Y. J., Tanré, D., Mattoo, S., Martins, J. V., Ichoku, C., Koren, I., Yu, H., and Holben, B. N. (2008). Global aerosol climatology from the MODIS satellite sensors. *Journal of Geophysical Research: Atmospheres*, 113(D14):D14S07.
- Reynolds, C. S., Huszar, V., Kruk, C., Naselli-Flores, L., and Melo, S. (2002). Towards a functional classification of the freshwater phytoplankton. *Journal of Plankton Research*, 24(5):417–428.
- Richter, A. (1997). *Measurements of stratospheric trace species above Bremen, 53N using absorption spectroscopy*. Dissertation, University of Bremen.
- Richter, A. and Wagner, A. (2001). Diffuserplate spectral structures and their influence on GOME slant columns. Technical report, Institute of Environmental Physics, University of Bremen; Institute of Environmental Physics, University of Heidelberg.
- Richter, A. and Burrows, J. (2002). Tropospheric NO₂ from GOME measurements. *Advances in Space Research*, 29(11):1673–1683.
- Richter, A. (2009). Algorithm Theoretical Basis Document for the GOME-2 Rapid Volcanic SO₂ product. Technical report, Insitute of Environmental Physics, University of Bremen.
- Richter, A., Begoin, M., Hilboll, A., and Burrows, J. P. (2011). An improved NO₂ retrieval for the GOME-2 satellite instrument. *Atmospheric Measurement Techniques*, 4(6):1147–1159.

- Richter, A. and Wagner, T. (2011). Solar Backscattered Radiation: UV, Visible and Near IR – Trace Gases. In Burrows, J. P., Platt, U., and Borrell, P., editors, *The Remote Sensing of Tropospheric Composition from Space*, pages 67 – 122. Springer-Verlag, Heidelberg.
- Riebesell, U., Körtzinger, A., and Oschlies, A. (2009). Sensitivities of marine carbon fluxes to ocean change. *Proceedings of the National Academy of Sciences*, 106(49):20602–20609.
- Roesler, C. S., Perry, M. J., and Carder, K. L. (1989). Modeling in situ phytoplankton absorption from total absorption spectra in productive inland marine waters. *Limnology and Oceanography*, 34(8):1510–1523.
- Romanov, N. P. and Shuklin, V. S. (1975). Raman scattering cross section of liquid water. *Optical Spectroscopy (USSR)*, 38:646–648.
- Rothman, L. S., Gordon, I. E., Babikov, Y., Barbe, A., Benner, D. C., Bernath, P. F., Birk, M., Bizzocchi, L., Boudon, V., Brown, L. R., Campargue, A., Chance, K., Cohen, E. A., Coudert, L. H., Devi, V. M., Drouin, B. J., Fayt, A., Flaud, J.-M., Gamache, R. R., Harrison, J. J., Hartmann, J.-M., Hill, C., Hodges, J. T., Jacquemart, D., Jolly, A., Lamouroux, J., Roy, R. J. L., Li, G., Long, D. A., Lyulin, O. M., Mackie, C. J., Massie, S. T., Mikhailenko, S., Müller, H. S. P., Naumenko, O. V., Nikitin, A. V., Orphal, J., Perevalov, V., Perrin, A., Polovtseva, E. R., Richard, C., Smith, M. A. H., Starikova, E., Sung, K., Tashkun, S., Tennyson, J., Toon, G. C., Tyuterev, V., and Wagner, G. (2013). The HITRAN2012 molecular spectroscopic database. *Journal of Quantitative Spectroscopy and Radiative Transfer*, 130:4–50.
- Röttgers, R., McKee, D., and Utschig, C. (2014). Temperature and salinity correction coefficients for light absorption by water in the visible to infrared spectral region. *Optics Express*, 22(21):25093–25108.
- Ročanov, A., Köhl, S., Doicu, A., McLinden, C., Pukite, J., Bovensmann, H., Burrows, J. P., Deutschmann, T., Dorf, M., Goutail, F., Grunow, K., Hendrick, F., von Hobe, M., Hrechanyy, S., Lichtenberg, G., Pfeilsticker, K., Pommereau, J. P., Van Roozendaal, M., Stroh, F., and Wagner, T. (2011). BrO vertical distributions from SCIAMACHY limb measurements: comparison of algorithms and retrieval results. *Atmospheric Measurement Techniques*, 4(7):1319–1359.
- Ročanov, V. V., Ročanov, A. V., Kokhanovsky, A. A., and Burrows, J. P. (2014). Radiative transfer through terrestrial atmosphere and ocean: Software package SCIATRAN. *Journal of Quantitative Spectroscopy and Radiative Transfer*, 133:13–71.

- Rozanov, V. V., Dinter, T., Rozanov, A. V., Wolanin, A., Bracher, A., and Burrows, J. P. (2017). Radiative transfer modeling through terrestrial atmosphere and ocean accounting for inelastic processes: Software package SCIATRAN. *Journal of Quantitative Spectroscopy and Radiative Transfer*, 194:65–85.
- Ruddick, K., Neukermans, G., Vanhellemont, Q., and Jolivet, D. (2014). Challenges and opportunities for geostationary ocean colour remote sensing of regional seas: A review of recent results. *Remote Sensing of Environment*, 146:63–76.
- Sabine, C. L., Feely, R. A., Gruber, N., Key, R. M., Lee, K., Bullister, J. L., Wanninkhof, R., Wong, C. S., Wallace, D. W. R., Tilbrook, B., Millero, F. J., Peng, T.-H., Kozyr, A., Ono, T., and Rios, A. F. (2004). The oceanic sink for anthropogenic CO₂. *Science*, 305(5682):367–371.
- Sadeghi, A., Dinter, T., Vountas, M., Taylor, B. B., Altenburg-Soppa, M and Peeken, I., and Bracher, A. (2012a). Improvement to the PhytoDOAS method for identification of coccolithophores using hyper-spectral satellite data. *Ocean Science*, 8(6):1055–1070.
- Sadeghi, A., Dinter, T., Vountas, M., Taylor, B., Altenburg-Soppa, M., and Bracher, A. (2012b). Remote sensing of coccolithophore blooms in selected oceanic regions using the PhytoDOAS method applied to hyper-spectral satellite data. *Biogeosciences*, 9(6):2127–2143.
- Saiz-Lopez, A., Plane, J. M. C., and Shillito, J. A. (2004). Bromine oxide in the mid-latitude marine boundary layer. *Geophysical Research Letters*, 31(3):L03111.
- Salter, I., Lampitt, R. S., Sanders, R., Poulton, A., Kemp, A. E., Boorman, B., Saw, K., and Pearce, R. (2007). Estimating carbon, silica and diatom export from a naturally fertilised phytoplankton bloom in the Southern Ocean using PELAGRA: A novel drifting sediment trap. *Deep Sea Research Part II: Topical Studies in Oceanography*, 54(18):2233–2259.
- Sander, R., Keene, W. C., Pszenny, A. A. P., Arimoto, R., Ayers, G. P., Baboukas, E., Caine, J. M., Crutzen, P. J., Duce, R. A., Hönninger, G., Huebert, B. J., Maenhaut, W., Mihalopoulos, N., Turekian, V. C., and Van Dingenen, R. (2003). Inorganic bromine in the marine boundary layer: a critical review. *Atmospheric Chemistry and Physics*, 3(5):1301–1336.
- Sathyendranath, S., Platt, T., Caverhill, C. M., Warnock, R. E., and Lewis, M. R. (1989).

Remote sensing of oceanic primary production: computations using a spectral model. *Deep Sea Research Part A. Oceanographic Research Papers*, 36(3):431–453.

Sathyendranath, S., Gouveia, A. D., Shetye, S. R., Ravindran, P., and Platt, T. (1991). Biological control of surface temperature in the Arabian Sea. *Nature*, 349(3):54–56.

Sathyendranath, S. and Platt, T. (1993). Underwater light field and primary production: Application to remote sensing. In Barale, V. and Schlittenhardt, P. M., editors, *Ocean Colour: Theory and Applications in a Decade of CZCS Experience*, pages 79 – 93. Springer Netherlands, Dordrecht.

Sathyendranath, S. (2011). User Requirements Document, D 1.1, Ocean Colour Climate Change Initiative – Phase One. Version 1.11. Technical report, European Space Agency.

Sathyendranath, S., Grant, M., Brewin, R. J. W., Brockmann, C., Brotas, V., Chuprin, A., Doerffer, R., Dowell, M., Farman, A., Groom, S., Jackson, T., Krasemann, H., Lavender, S., Martinez Vicente, V., Mazeran, C., Mélin, F., Moore, T. S., Müller, D., Platt, T., Regner, P., Roy, S., Steinmetz, F., Swinton, J., Valente, A., Zühlke, M., Antoine, D., Arnone, R., Balch, W. M., Barker, K., Barlow, R., Bélanger, S., Berthon, J.-F., Beşiktepe, Ş., Brando, V. E., Canuti, E., Chavez, F., Claustre, H., Crout, R., Feldman, G., Franz, B., Frouin, R., García-Soto, C., Gibb, S. W., Gould, R., Hooker, S., Kahru, M., Klein, H., Kratzer, S., Loisel, H., McKee, D., Mitchell, B. G., Moisan, T., Muller-Karger, F., O’Dowd, L., Ondrusek, M., Poulton, A. J., Repecaud, M., Smyth, T., Sosik, H. M., Taberner, M., Twardowski, M., Voss, K., Werdell, J., Wernand, M., and Zibordi, G. (2018). ESA Ocean Colour Climate Change Initiative (Ocean_Colour_cci): Version 3.1 Data. Centre for Environmental Data Analysis, 04 July 2018. <http://dx.doi.org/10.5285/9c334fbe6d424a708cf3c4cf0c6a53f5>.

Sathyendranath, S., Brewin, R. J. W., Brockmann, C., Brotas, V., Calton, B., Chuprin, A., Cipollini, P., Couto, A. B., Dingle, J., Doerffer, R., Donlon, C., Dowell, M., Farman, A., Grant, M., Groom, S., Horseman, A., T, J., Krasemann, H., Lavender, S., Martinez-Vicente, V., Mazeran, C., Mélin, F., Moore, T. S., Müller, D., Regner, P., Roy, S., Steele, C., Steinmetz, F., Swinton, J., Taberner, M., Thompson, A., Valente, A., Zühlke, M., Brando, V., Feng, H., Feldman, G., Franz, B., Frouin, R., Gould, J. R., Hooker, S. B., Kahru, M., Kratzer, S., Mitchell, B. G., Muller-Karger, F., Sosik, H. M., Voss, K. J., Werdell, J., and Platt, T. (2019). An ocean-colour time series for use in climate studies: the experience of the Ocean-Colour Climate Change Initiative (OC-CCI). *Sensors*, 19:4285.

- Sathyendranath, S., Jackson, T., Brockmann, C., Brotas, V., Calton, B., Chuprin, A., Clements, O., Cipollini, P., Danne, O., Dingle, J., Donlon, C., Grant, M., Groom, S., Krasemann, H., Lavender, S., Mazeran, C., Mélin, F., Moore, T., Müller, D., Renger, P., Steinmetz, F., Steele, C., Swinton, J., Valente, A., Zühlke, M., Feldman, G., Franz, B., Frouin, R., Werdell, J., and Platt, T. (2020). ESA Ocean Colour Climate Change Initiative (Ocean_Colour_cci): Global chlorophyll-a data products gridded on a sinusoidal projection, Version 4.2. Centre for Environmental Data Analysis. <https://catalogue.ceda.ac.uk/uuid/99348189bd33459cbd597a58c30d8d10>.
- Schenkeveld, V. M. E., Jaross, G., Marchenko, S., Haffner, D., Kleipool, Q. L., Rozemeijer, N. C., Veefkind, J. P., and Levelt, P. F. (2017). In-flight performance of the Ozone Monitoring Instrument. *Atmospheric Measurement Techniques*, 10(5):1957–1986.
- Schlesinger, M. E. and Ramankutty, N. (1994). An oscillation in the global climate system of period 65–70 years. *Nature*, 367(6465):723–726.
- Schönhardt, A., Richter, A., Wittrock, F., Kirk, H., Oetjen, H., Roscoe, H. K., and Burrows, J. P. (2008). Observations of iodine monoxide columns from satellite. *Atmospheric Chemistry and Physics*, 8(3):637–653.
- Seegers, B. N., Stumpf, R. P., Schaeffer, B. A., Loftin, K. A., and Werdell, P. J. (2018). Performance metrics for the assessment of satellite data products: an ocean color case study. *Optics Express*, 26(6):7404–7422.
- Seo, S., Richter, A., Blechschmidt, A.-M., Bougoudis, I., and Burrows, J. P. (2019). First high-resolution BrO column retrievals from TROPOMI. *Atmospheric Measurement Techniques*, 12(5):2913–2932.
- Serdyuchenko, A., Gorshelev, V., Weber, M., Chehade, W., and Burrows, J. P. (2014). High spectral resolution ozone absorption cross-sections – Part 2: Temperature dependence. *Atmospheric Measurement Techniques*, 7(2):625–636.
- Shang, S., Lee, Z., and Wei, G. (2011). Characterization of MODIS-derived euphotic zone depth: Results for the China Sea. *Remote Sensing of Environment*, 115(1):180–186.
- Shell, K. M., Frouin, R., Nakamoto, S., and Somerville, R. C. J. (2003). Atmospheric response to solar radiation absorbed by phytoplankton. *Journal of Geophysical Research: Atmospheres*, 108(D15):4445.

- Shen, M., Duan, H., Cao, Z., Xue, K., Loisel, S., and Yesou, H. (2017). Determination of the downwelling diffuse attenuation coefficient of lake water with the Sentinel-3A OLCI. *Remote Sensing*, 9:1246.
- Siegel, D. A., Maritorena, S., Nelson, N. B., Hansell, D. A., and Lorenzi-Kayser, M. (2002). Global distribution and dynamics of colored dissolved and detrital organic materials. *Journal of Geophysical Research: Oceans*, 107(C12):3228.
- Siegel, D. A., Buesseler, K. O., Doney, S. C., Sailley, S. F., Behrenfeld, M. J., and Boyd, P. W. (2014). Global assessment of ocean carbon export by combining satellite observations and food-web models. *Global Biogeochemical Cycles*, 28(3):181–196.
- Signorini, S. R., Garcia, V. M. T., Piola, A. R., Garcia, C. A. E., Mata, M. M., and McClain, C. R. (2006). Seasonal and interannual variability of calcite in the vicinity of the Patagonian shelf break (38°S–52°S). *Geophysical Research Letters*, 33(16):L16610.
- Simpson, W. R., von Glasow, R., Riedel, K., Anderson, P., Ariya, P., Bottenheim, J., Burrows, J., Carpenter, L. J., Frieß, U., Goodsite, M. E., Heard, D., Hutterli, M., Jacobi, H.-W., Kaleschke, L., Neff, B., Plane, J., Platt, U., Richter, A., Roscoe, H., Sander, R., Shepson, P., Sodeau, J., Steffen, A., Wagner, T., and Wolff, E. (2007). Halogens and their role in polar boundary-layer ozone depletion. *Atmospheric Chemistry and Physics*, 7(16):4375–4418.
- Sinha, R. P. and Häder, D.-P. (2002). UV-induced DNA damage and repair: a review. *Photochemical & Photobiological Sciences*, 1:225–236.
- Sinnhuber, B.-M., Sheode, N., Sinnhuber, M., Chipperfield, M. P., and Feng, W. (2009). The contribution of anthropogenic bromine emissions to past stratospheric ozone trends: a modelling study. *Atmospheric Chemistry and Physics*, 9(8):2863–2871.
- Skupin, J., Noël, S., Wuttke, M. W., Gottwald, M., Bovensmann, H., Weber, M., and Burrows, J. P. (2005). SCIAMACHY solar irradiance observation in the spectral range from 240 to 2380 nm. *Advances in Space Research*, 35(3):370–375.
- Smith, H. E. K., Poulton, A. J., Garley, R., Hopkins, J., Lubelczyk, L. C., Drapeau, D. T., Rauschenberg, S., Twining, B. S., Bates, N. R., and Balch, W. M. (2017). The influence of environmental variability on the biogeography of coccolithophores and diatoms in the Great Calcite Belt. *Biogeosciences*, 14(21):4905–4925.
- Smith, R. C. and Baker, K. S. (1981). Optical properties of the clearest natural waters (200–800 nm). *Applied Optics*, 20(2):177–184.

- Smyth, T. J. (2011). Penetration of UV irradiance into the global ocean. *Journal of Geophysical Research: Oceans*, 116(C11):C11020.
- Solomon, S., Schmeltekopf, A. L., and Sanders, R. W. (1987). On the interpretation of zenith sky absorption measurements. *Journal of Geophysical Research: Atmospheres*, 92(D7):8311–8319.
- Solomon, S., Portmann, R. W., Sanders, R. W., Daniel, J. S., Madsen, W., Bartram, B., and Dutton, E. G. (1999). On the role of nitrogen dioxide in the absorption of solar radiation. *Journal of Geophysical Research: Atmospheres*, 104(D10):12047–12058.
- Soppa, M. A., Dinter, T., Taylor, B. B., and Bracher, A. (2013). Satellite derived euphotic depth in the Southern Ocean: Implications for primary production modelling. *Remote Sensing of Environment*, 137:198–211.
- Soppa, M. A., Hirata, T., Silva, B., Dinter, T., Peeken, I., Wiegmann, S., and Bracher, A. (2014). Global retrieval of diatom abundance based on phytoplankton pigments and satellite data. *Remote Sensing*, 6(10):10089–10106.
- Soppa, M. A., Völker, C., and Bracher, A. (2016a). Diatom phenology in the Southern Ocean: Mean patterns, trends and the role of climate oscillations. *Remote Sensing*, 8(5):420.
- Soppa, M. A., Dinter, T., Losa, S., Wolanin, A., and Bracher, A. (2016b). SY-4Sci Synergy R & D Study 4: Phytoplankton Functional Types (SynSenPFT): Algorithm Theoretical Base Document (ATBD). Technical report, Alfred Wegener Institute (AWI), Helmholtz Centre for Polar and Marine Research; Institute of Environmental Physics, University of Bremen.
- Spinei, E., Cede, A., Herman, J., Mount, G. H., Eloranta, E., Morley, B., Baidar, S., Dix, B., Ortega, I., Koenig, T., and Volkamer, R. (2015). Ground-based direct-sun DOAS and airborne MAX-DOAS measurements of the collision-induced oxygen complex, O₂O₂, absorption with significant pressure and temperature differences. *Atmospheric Measurement Techniques*, 8(2):793–809.
- Staehr, P. A. and Henriksen, P. and Markager, S. (2002). Photoacclimation of four marine phytoplankton species to irradiance and nutrient availability. *Marine Ecology Progress Series*, 238:47–49.
- Stavrakou, T., Müller, J.-F., De Smedt, I., Van Roozendael, M., Kanakidou, M., Vrekoussis, M., Wittrock, F., Richter, A., and Burrows, J. P. (2009). The continental source

- of glyoxal estimated by the synergistic use of spaceborne measurements and inverse modelling. *Atmospheric Chemistry and Physics*, 9(21):8431–8446.
- Sugihara, S., Kishino, M., and Okami, N. (1984). Contribution of Raman scattering to upward irradiance in the sea. *Journal of the Oceanographical Society of Japan*, 40(6):397–404.
- Suikkanen, S., Pulina, S., Engström-Öst, J., Lehtiniemi, M., Lehtinen, S., and Brutemark, A. (2013). Climate Change and Eutrophication Induced Shifts in Northern Summer Plankton Communities. *Plos One*, 8(6):1–10.
- Sullivan, J. M., Twardowski, M. S., Zaneveld, J. R. V., Moore, C. M., Barnard, A. H., Donaghay, P. L., and Rhoades, B. (2006). Hyperspectral temperature and salt dependencies of absorption by water and heavy water in the 400–750 nm spectral range. *Applied Optics*, 45(21):5294–5309.
- Sweeney, C., Gnanadesikan, A., Griffies, S. M., Harrison, M. J., Rosati, A. J., and Samuels, B. L. (2005). Impacts of shortwave penetration depth on large-scale ocean circulation and heat transport. *Journal of Physical Oceanography*, 35(6):1103–1119.
- Takahashi, T., Sutherland, S. C., Wanninkhof, R., Sweeney, C., Feely, R. A., Chipman, D. W., Hales, B., Friederich, G., Chavez, F., Sabine, C., Watson, A., Bakker, D. C., Schuster, U., Metzl, N., Yoshikawa-Inoue, H., Ishii, M., Midorikawa, T., Nojiri, Y., Körtzinger, A., Steinhoff, T., Hoppema, M., Olafsson, J., Arnarson, T. S., Tilbrook, B., Johannessen, T., Olsen, A., Bellerby, R., Wong, C., Delille, B., Bates, N., and de Baar, H. J. (2009). Climatological mean and decadal change in surface ocean pCO₂, and net sea-air CO₂ flux over the global oceans. *Deep Sea Research Part II: Topical Studies in Oceanography*, 56(8):554–577.
- Tanskanen, A., Määttä, A., Krotkov, N., Herman, J., Kaurola, J., Koskela, T., Karpetchko, A., Fioletov, V., and Bernhard, G. (2006). Surface ultraviolet irradiance from OMI. *IEEE TRANSACTIONS ON GEOSCIENCE AND REMOTE SENSING*, 44:1267–1271.
- Taylor, B. B., Torrecilla, E., Bernhardt, A., Taylor, M. H., Peeken, I., Röttgers, R., Piera, J., and Bracher, A. (2011). Bio-optical provinces in the eastern Atlantic Ocean and their biogeographical relevance. *Biogeosciences*, 8(12):3609–3629.
- Thalman, R. and Volkamer, R. (2013). Temperature dependent absorption cross-sections of O₂–O₂ collision pairs between 340 and 630 nm and at atmospherically relevant pressure. *Physical Chemistry Chemical Physics*, 15(37):15371–15381.

- Theys, N., De Smedt, I., van Gent, J., Danckaert, T., Wang, T., Hendrick, F., Stavrakou, T., Bauduin, S., Clarisse, L., Li, C., Krotkov, N., Yu, H., Brenot, H., and Van Roozendael, M. (2015). Sulfur dioxide vertical column DOAS retrievals from the Ozone Monitoring Instrument: Global observations and comparison to ground-based and satellite data. *Journal of Geophysical Research: Atmospheres*, 120(6):2470–2491.
- Trenberth, K. E. and Hurrell, J. W. (1994). Decadal atmosphere-ocean variations in the Pacific. *Climate Dynamics*, 9(6):303–319.
- Twardowski, M. S., Boss, E., Macdonald, J. B., Pegau, W. S., Barnard, A. H., and Zaneveld, J. R. V. (2001). A model for estimating bulk refractive index from the optical backscattering ratio and the implications for understanding particle composition in case I and case II waters. *Journal of Geophysical Research: Oceans*, 106(C7):14129–14142.
- Twardowski, M. S., Boss, E., Sullivan, J. M., and Donaghay, P. L. (2004). Modeling the spectral shape of absorption by chromophoric dissolved organic matter. *Marine Chemistry*, 89(1):69–88.
- Tyrrell, T. and Merico, A. (2004). *Emiliania huxleyi*: bloom observations and the conditions that induce them. In Thierstein, H. and Young, J., editors, *Coccolithophores*, pages 75–97. Springer, Berlin, Heidelberg.
- v. Smoluchowski, M. (1908). Molekular-kinetische Theorie der Opaleszenz von Gasen im kritischen Zustande, sowie einiger verwandter Erscheinungen. *Annalen der Physik*, 330(2):205–226.
- van der Does, M., Korte, L. F., Munday, C. I., Brummer, G.-J. A., and Stuut, J.-B. W. (2016). Particle size traces modern Saharan dust transport and deposition across the equatorial North Atlantic. *Atmospheric Chemistry and Physics*, 16(21):13697–13710.
- van Geffen, J. H. G. M. (2004). Wavelength calibration of spectra measured by the Global Ozone Monitoring Experiment: variations along orbits and in time. *Applied Optics*, 43(3):695–706.
- van Geffen, J. H. G. M., Eskes, H. J., Boersma, K. F., Maasakkers, J. D., and Veefkind, J. P. (2019). TROPOMI ATBD of the total and tropospheric NO₂ data products. Technical report, Royal Netherlands Meteorological Institute.
- van Geffen, J. H. G. M., Boersma, K. F., Eskes, H., Sneep, M., ter Linden, M., Zara, M., and Veefkind, J. P. (2020). S5P TROPOMI NO₂ slant column retrieval: method, sta-

- bility, uncertainties and comparisons with OMI. *Atmospheric Measurement Techniques*, 13(3):1315–1335.
- Vandaele, A., Hermans, C., Simon, P., Carleer, M., Colin, R., Fally, S., Mérienne, M., Jenouvrier, A., and Coquart, B. (1998). Measurements of the NO₂ absorption cross-section from 42 000 cm⁻¹ to 10 000 cm⁻¹ (238–1000 nm) at 220 K and 294 K. *Journal of Quantitative Spectroscopy and Radiative Transfer*, 59(3):171–184.
- Vasilkov, A., Krotkov, N., Herman, J., McClain, C., Arrigo, K., and Robinson, W. (2001). Global mapping of underwater UV irradiances and DNA-weighted exposures using Total Ozone Mapping Spectrometer and Sea-viewing Wide Field-of-view Sensor data products. *Journal of Geophysical Research*, 106:27205–27219.
- Vasilkov, A. P., Joiner, J., Gleason, J., and Bhartia, P. K. (2002a). Ocean Raman scattering in satellite backscatter UV measurements. *Geophysical Research Letters*, 29(17):14–18.
- Vasilkov, A. P., Herman, J. R., Krotkov, N. A., Kahru, M., Mitchell, B. G., and Hsu, C. (2002b). Problems in assessment of the ultraviolet penetration into natural waters from space-based measurements. *Optical Engineering*, 41(12):3019–3027.
- Vasilkov, A. P., Herman, J. R., Ahmad, Z., Kahru, M., and Mitchell, B. G. (2005). Assessment of the ultraviolet radiation field in ocean waters from space-based measurements and full radiative-transfer calculations. *Applied Optics*, 44(14):2863–2869.
- Veefkind, J., Aben, I., McMullan, K., Förster, H., de Vries, J., Otter, G., Claas, J., Eskes, H., de Haan, J., Kleipool, Q., van Weele, M., Hasekamp, O., Hoogeveen, R., Landgraf, J., Snel, R., Tol, P., Ingmann, P., Voors, R., Kruizinga, B., Vink, R., Visser, H., and Levelt, P. (2012). TROPOMI on the ESA Sentinel-5 Precursor: A GMES mission for global observations of the atmospheric composition for climate, air quality and ozone layer applications. *Remote Sensing of Environment*, 120:70–83.
- Velders, G. J. M., Granier, C., Portmann, R. W., Pfeilsticker, K., Wenig, M., Wagner, T., Platt, U., Richter, A., and Burrows, J. P. (2001). Global tropospheric NO₂ column distributions: Comparing three-dimensional model calculations with GOME measurements. *Journal of Geophysical Research: Atmospheres*, 106(D12):12643–12660.
- Vernet, M., Brody, E. A., Holm-Hansen, O., and Mitchell, B. G. (1994). The response of Antarctic phytoplankton to ultraviolet radiation: Absorption, photosynthesis, and taxonomic composition. In *Ultraviolet Radiation in Antarctica: Measurements and Biological Effects*, pages 143 – 158. American Geophysical Union (AGU).

- Vodacek, A. and Blough, N. V. (1997). Seasonal variation of CDOM in the Middle Atlantic Bight: terrestrial inputs and photooxidation. In Ackleson, S. G. and Frouin, R. J., editors, *Ocean Optics XIII*, volume 2963, pages 132 – 137. International Society for Optics and Photonics, SPIE.
- Volkamer, R., Spietz, P., Burrows, J., and Platt, U. (2005). High-resolution absorption cross-section of glyoxal in the UV–vis and IR spectral ranges. *Journal of Photochemistry and Photobiology A: Chemistry*, 172(1):35–46.
- Vonk, F. (2018). Input/output data specification for the TROPOMI L01b data processor. Technical report, Royal Netherlands Meteorological Institute.
- Voss, K. J. (1992). A spectral model of the beam attenuation coefficient in the ocean and coastal areas. *Limnology and Oceanography*, 37(3):501–509.
- Vountas, M., Rozanov, V., and Burrows, J. (1998). Ring effect: Impact of rotational Raman scattering on radiative transfer in Earth’s atmosphere. *Journal of Quantitative Spectroscopy and Radiative Transfer*, 60(6):943–961.
- Vountas, M., Richter, A., Wittrock, F., and Burrows, J. P. (2003). Inelastic scattering in ocean water and its impact on trace gas retrievals from satellite data. *Atmospheric Chemistry and Physics*, 3(5):1365–1375.
- Vountas, M., Dinter, T., Bracher, A., Burrows, J. P., and Sierk, B. (2007). Spectral studies of ocean water with space-borne sensor SCIAMACHY using Differential Optical Absorption Spectroscopy (DOAS). *Ocean Science*, 3(3):429–440.
- Vrekoussis, M., Wittrock, F., Richter, A., and Burrows, J. P. (2009). Temporal and spatial variability of glyoxal as observed from space. *Atmospheric Chemistry and Physics*, 9(13):4485–4504.
- Vrekoussis, M., Wittrock, F., Richter, A., and Burrows, J. P. (2010). GOME-2 observations of oxygenated VOCs: what can we learn from the ratio glyoxal to formaldehyde on a global scale? *Atmospheric Chemistry and Physics*, 10(21):10145–10160.
- Wagner, T., Leue, C., Pfeilsticker, K., and Platt, U. (2001). Monitoring of the stratospheric chlorine activation by Global Ozone Monitoring Experiment (GOME) OClO measurements in the austral and boreal winters 1995 through 1999. *Journal of Geophysical Research: Atmospheres*, 106(D5):4971–4986.

- Wagner, T., von Friedeburg, C., Wenig, M., Otten, C., and Platt, U. (2002). UV-visible observations of atmospheric O₄ absorptions using direct moonlight and zenith-scattered sunlight for clear-sky and cloudy sky conditions. *Journal of Geophysical Research: Atmospheres*, 107(D20):4424.
- Walrafen, G. E. (1966). Raman Spectral Studies of the Effects of Temperature on Water and Electrolyte Solutions. *The Journal of Chemical Physics*, 44(4):1546–1558.
- Walrafen, G. E. (1967). Raman Spectral Studies of the Effects of Temperature on Water Structure. *The Journal of Chemical Physics*, 47(1):114–126.
- Wang, G., Cao, W., Yang, D., and Xu, D. (2008a). Variation in downwelling diffuse attenuation coefficient in the northern South China Sea. *Chinese Journal of Oceanology and Limnology*, 26(3):323–333.
- Wang, M. (1999). Atmospheric correction of ocean color sensors: computing atmospheric diffuse transmittance. *Applied Optics*, 38(3):451–455.
- Wang, M. and Bailey, S. W. (2001). Correction of sun glint contamination on the SeaWiFS ocean and atmosphere products. *Applied Optics*, 40(27):4790–4798.
- Wang, M., Son, S., and Harding Jr., L. W. (2009). Retrieval of diffuse attenuation coefficient in the Chesapeake Bay and turbid ocean regions for satellite ocean color applications. *Journal of Geophysical Research: Oceans*, 114(C10):C10011.
- Wang, P., Stammes, P., van der A, R., Pinardi, G., and van Roozendaal, M. (2008b). FRESCO+: an improved O₂ A-band cloud retrieval algorithm for tropospheric trace gas retrievals. *Atmospheric Chemistry and Physics*, 8(21):6565–6576.
- Wang, W. and Zhao, J. (2014). Variation of diffuse attenuation coefficient of downwelling irradiance in the Arctic Ocean. *Acta Oceanologica Sinica*, 33(6):53–62.
- Wang, Y., Lee, Z., Wei, J., Shang, S., Wang, M., and Lai, W. (2021). Extending satellite ocean color remote sensing to the near-blue ultraviolet bands. *Remote Sensing of Environment*, 253:112228.
- Welsch, C., Swenson, H., Cota, S. A., DeLuccia, F., Haas, J. M., Schueler, C., Durham, R. M., Clement, J. E., and Ardanuy, P. E. (2001). VIIRS (Visible Infrared Imager Radiometer Suite): a next-generation operational environmental sensor for NPOESS. In *IGARSS 2001. Scanning the Present and Resolving the Future. Proceedings. IEEE*

2001 International Geoscience and Remote Sensing Symposium (Cat. No.01CH37217), volume 3, pages 1020 – 1022.

- Werdell, P. J. and Bailey, S. W. (2005). An improved in-situ bio-optical data set for ocean color algorithm development and satellite data product validation. *Remote Sensing of Environment*, 98(1):122–140.
- Werdell, P. J., Behrenfeld, M. J., Bontempi, P. S., Boss, E., Cairns, B., Davis, G. T., Franz, B. A., Gliese, U. B., Gorman, E. T., Hasekamp, O., Knobelspiesse, K. D., Mannino, A., Martins, J. V., McClain, C. R., Meister, G., and Remer, L. A. (2019). The Plankton, Aerosol, Cloud, Ocean Ecosystem Mission: status, science, advances. *Bulletin of the American Meteorological Society*, 100(9):1775–1794.
- Westberry, T. K., Boss, E., and Lee, Z. (2013). Influence of Raman scattering on ocean color inversion models. *Applied Optics*, 52(22):5552–5561.
- Winter, A., Elbrächter, M., and Krause, G. (1999). Subtropical coccolithophores in the Weddell Sea. *Deep Sea Research Part I: Oceanographic Research Papers*, 46(3):439–449.
- Wittrock, F., Richter, A., Oetjen, H., Burrows, J. P., Kanakidou, M., Myriokefalitakis, S., Volkamer, R., Beirle, S., Platt, U., and Wagner, T. (2006). Simultaneous global observations of glyoxal and formaldehyde from space. *Geophysical Research Letters*, 33(16):L16804.
- Wolanin, A., Rozanov, V., Dinter, T., and Bracher, A. (2015a). Detecting CDOM Fluorescence Using High Spectrally Resolved Satellite Data: A Model Study. In Lohmann, G., Meggers, H., Unnithan, V., Wolf-Gladrow, D., Notholt, J., and Bracher, A., editors, *Towards an Interdisciplinary Approach in Earth System Science: Advances of a Helmholtz Graduate Research School*, pages 109 – 121. Springer International Publishing, Cham.
- Wolanin, A., Rozanov, V. V., Dinter, T., Noël, S., Vountas, M., Burrows, J. P., and Bracher, A. (2015b). Global retrieval of marine and terrestrial chlorophyll fluorescence at its red peak using hyperspectral top of atmosphere radiance measurements: Feasibility study and first results. *Remote Sensing of Environment*, 166:243–261.
- Wolanin, A., Dinter, T., Soppa, M., and Bracher, A. (2015c). SY-4Sci Synergy R & D Study 4: Phytoplankton Functional Types (SynSenPFT): Report on using radiative transfer modelling to develop a correction scheme and investigate the sensitivity of the improved PhytoDOAS (version3.0) algorithm. Technical report, Alfred Wegener Institute (AWI),

Helmholtz Centre for Polar and Marine Research; Institute of Environmental Physics, University of Bremen.

- Wolanin, A., Soppa, M. A., and Bracher, A. (2016). Investigation of spectral band requirements for improving retrievals of phytoplankton functional types. *Remote Sensing*, 8(10).
- Xi, H., Losa, S. N., Mangin, A., Soppa, M. A., Garnesson, P., Demaria, J., Liu, Y., d'Andon, O. H. F., and Bracher, A. (2020). Global retrieval of phytoplankton functional types based on empirical orthogonal functions using CMEMS GlobColour merged products and further extension to OLCI data. *Remote Sensing of Environment*, 240:111704.
- Xi, H., Losa, S. N., Mangin, A., Garnesson, P., Bretagnon, M., Demaria, J., Soppa, M. A., Hembise Fanton d'Andon, O., and Bracher, A. (2021). Global chlorophyll a concentrations of phytoplankton functional types with detailed uncertainty assessment using multisensor ocean color and sea surface temperature satellite products. *Journal of Geophysical Research: Oceans*, 126(5):e2020JC017127.
- Xu, X. and Kattawar, G. W. (1994). Filling in of Fraunhofer lines in the ocean by Brillouin scattering. *Applied Optics*, 33(21):4835–4840.
- Yang, H. and Gordon, H. R. (1997). Remote sensing of ocean color: assessment of water-leaving radiance bidirectional effects on atmospheric diffuse transmittance. *Applied Optics*, 36(30):7887–7897.
- Zepp, R. G., Callaghan, T. V., and Erickson III, D. J. (2003). Interactive effects of ozone depletion and climate change on biogeochemical cycles. *Photochemical & Photobiological Sciences*, 2:51–61.
- Zepp, R. G., Erickson III, D. J., Paul, N. D., and Sulzberger, B. (2007). Interactive effects of solar UV radiation and climate change on biogeochemical cycling. *Photochemical & Photobiological Sciences*, 6:286–300.
- Zhang, T. and Fell, F. (2007). An empirical algorithm for determining the diffuse attenuation coefficient K_d in clear and turbid waters from spectral remote sensing reflectance. *Limnology and Oceanography: Methods*, 5(12):457–462.
- Zhang, X., Hu, L., and He, M.-X. (2009). Scattering by pure seawater: Effect of salinity. *Optics Express*, 17(7):5698–5710.

Zhang, Y., Wang, X., Wen, S., Herrmann, H., Yang, W., Huang, X., Zhang, Z., Huang, Z., He, Q., and George, C. (2016). On-road vehicle emissions of glyoxal and methylglyoxal from tunnel tests in urban Guangzhou, China. *Atmospheric Environment*, 127:55–60.

Acknowledgements

This thesis would not have been possible without the support of many people. I would like to thank every single one who contributed and helped along the way.

First of all, I have to thank Astrid Bracher for supervising my thesis and giving me the opportunity to work on two interesting projects with her. I am also most thankful to her for letting me join ship campaigns and gather field experience which I truly enjoy.

I thank John Burrows for having me as a PhD student at the Institute of Environmental Physics and being able to use all its infrastructure. Thank you for kindly agreeing to be the second reviewer for this thesis.

I thank all my PhD committee members, Astrid Bracher, John Burrows, Andreas Richter, and Svetlana Losa as well as Tilman Dinter, an almost permanent guest in our meetings, for their time and inspiring discussions.

Especially, I would like to thank Andreas Richter for his guidance and patience in answering all my physics-related questions and discuss DOAS results with me. I truly enjoyed working together with Svetlana Losa on two projects and value our scientific discussions. I am thankful for their mental support and mentoring which helped me to successfully complete this thesis.

I highly appreciate Janna Rückert, Marianna A. Soppa, Andreas Richter, Svetlana N. Losa, and Leonardo Alvarado for reading and commenting as well as Sasha Kramer and Tessa Penner for proof-reading parts of the thesis.

Heiko Schellhorn, Heiko Schröter, Stephanie Drath, and Geraldine Schmiechen owned themselves the title *hero of the day* once in a while. Thank you for all the IT and administrative support when in need.

I thank all colleagues at the Institute of Environmental Physics and the Alfred-Wegener-Institute for the inspiring working environment and helping me with scientific questions. I would like to highlight the support I received from Vladimir and Alexei Rozanov on SCIATRAN parameterizations, thank you. Just as valuable to me are the non-scientific chats I had at lunch times and other occasions with my colleagues and friends from Uni Bremen, especially Andreas M., Anne, Diana, Elpida, Hella, Jia, Kai-Uwe, Leonardo, Ola, Martin, Matthias, Thomas and Sven. I am happy to have been part of the Phytooptics

Group at the Alfred-Wegener-Institute. Thank you for all the scientific input and nice times we spent during conferences, campaigns, Christmas parties, kohltours, and our trip to Neuwerk.

I thank ESA for OC-CCI data, MERIS, SCIAMACHY, OLCI, and TROPOMI data; NASA Goddard Space Flight Center's Ocean Data Processing System (ODPS) for MODIS and SeaWiFs data. I thank everyone involved, from ship crew to principal investigator, for collecting, processing, and sharing the in-situ data used in this thesis.

I gratefully acknowledge funding by the Deutsche Forschungsgemeinschaft (DFG) within Priority Program SPP 1158 "Antarktis", project PhySyn with number Bu688-26-1. I appreciate funding by the European Space Agency within the frame of the Sentinel-5P + Innovation projects. Special thanks go to Marie-Helene Rio, project coordinator at ESA, for shaping the project focus on UV light attenuation with me and my co-authors and supporting our ideas. Financial support for conferences, a summer school, and soft skill courses was also received from the graduate school GLOMAR of MARUM, University of Bremen. Thank you for the nice course offers and structural guidance. Additional funding was received from the European Commission as a Joint Research Centre travel scholarship for attending the International Ocean Color Symposium 2016 in Lisbon. I am grateful for having had the chance to attend the Ocean Optics Summer Class in 2017 sponsored by NASA and the University of Maine. Special thanks go to the lecturers for sharing their expert knowledge, especially Emmanuel Boss, Curtis Mobley, Collin Roesler, and Ken Voss.

I am most grateful to have my family and friends who accompanied me along the way. I thank my parents for their life-long support and encouragement. I am grateful for my partner Simon. Thank you for all the good times we had in the last years and for sticking with me in the bad ones. Having Janna as a friend has been an enormous gift. Thank you for your endless support and making me feel less like a Martian on this planet.

Erklärung

Hiermit erkläre ich, dass ich die Arbeit ohne unerlaubte fremde Hilfe angefertigt habe, dass ich weiterhin keine anderen als die angegebenen Quellen und Hilfsmittel benutzt und die den benutzten Werken wörtlich oder inhaltlich entnommenen Stellen als solche kenntlich gemacht habe.

Julia Oelker

Bremen, den 29.06.2021